

# Aerodynamic Problems of Urban UAV Operations

A thesis submitted for the degree of  
**MPhil**

by  
**Sakbundit Kittiyoungkun**

Supervised by  
**Dr A. J. Saddington and Professor K. Knowles**

**Aeromechanical Systems Group**  
**Department of Engineering and Applied Science**

August 2010

## **Declaration**

No portion of the work presented in this thesis has been submitted in support of an application for another degree or qualification at this or any other University or Institution of Learning.

# Abstract

Unmanned Air Vehicles, UAVs are designed to operate without any onboard controllers. Consequently, they are considered to operate in a wide range of applications. Missions in undesirable conditions such as bad weather and/or highly unsteady gustiness could cause an unsuccessful operation. In many ways, aerodynamics is a key feature in the performance of UAVs such as influencing deformation vehicle, guidance and control. Two aspects of this research are, therefore, to understand flying conditions of UAVs in an urban environment and how the flying performance is affected by such conditions. The first objective relies on understanding air flow behaviour in the lower part of the urban environment which has the most important role on the response of UAVs. The second objective will be to look at the characteristics of a three-dimensional airfoil when it encounters an unsteady sinusoidal gust at different oscillation frequencies and freestream velocities.

As the first step of the studies on the aerodynamic problem of UAV operations in the lower part of an atmospheric boundary layer in an urban environment, the boundary layer thickness in a suitable wind tunnel facility were the first experimental results obtained. Experimental measurements of the mean velocity profile in a turbulent boundary layer were investigated for three different floor roughness conditions as well as a smooth wall condition. As a result, three different boundary layer thicknesses were then classified depending on the wall surface roughness and a combination with turbulence generators providing a maximum thickness of 280 mm at the centre of the tunnel test section. However, the experimental investigations into the turbulent boundary layer over a rough wall have shown that the boundary layer thickness is dependent on the surface roughness and is different from that obtained under the smooth wall condition.

An experimental study into a simulated urban flow regime was then carried out after the measurement of the boundary layer. Wind tunnel experiments on the air flow around a single and twin buildings including an investigation of the airflow between the gap of the buildings were obtained. Wind in the lower part of the atmospheric boundary layer is more a micro-scale problem which increases or decreases the wind speed induced by buildings nearby. The studies have found some strong concentrated vortices caused by the flow separation essentially independent

of the nature of the upstream flow and usually as a direct result of the building geometry and orientation. As the measurement location increased further downstream from the back of the buildings, the concentrated vortices were found to be weak and disappeared into the wake region.

Finally, an experiment was conducted using a sinusoidal gust generator to describe the effects of wind oscillation parameters such as oscillation amplitude, oscillation frequency and reduced frequency under static and dynamic conditions. An evaluation was made of the onset of dynamic stall due to rapid changes in angle of attack during an unsteady pitch motion. The NACA 23012 wing profile was tested at a fixed angle of attack condition with varying oscillation flow parameters. Results demonstrate that those parameters influence the dynamic stall and hysteresis loop based on lift coefficient and angle of attack.



# Acknowledgements

I would like to thank my supervisor, Dr Alistair Saddington for his time, excellent guidance and supervision throughout this course from the beginning since I started. I am also thankful to Professor Kevin Knowles for his time and excellent advice. Especially, thanks to Dr Mark Finnis for his valuable time and continuous assistance for laboratory set up and kind cooperation to progress experiments forwards. Finally, I thank Mr David Wasley for his technical and practical help with the experiments.



# Nomenclature

All units are in SI

## Alphanumeric

$\bar{u}$	Mean wind velocity,
$\bar{u}_1$	Mean wind velocity at a first point of interest,
$\bar{u}_2$	Mean wind velocity at a second point of interest,
$\frac{ac}{2}$	Position of axis of wing rotation from centre chord point,
$a$	Dimension along wind direction, semi-major axis of an ellipse,
$a$	Windward face length of a building,
$b$	Building length across wind direction, semi-minor axis of an ellipse,
$B_L$	Larger dimension in a windward face of a building,
$B_S$	Smaller dimension in a windward face of a building,
$C$	Area of an elliptical tunnel section = $\pi ab$ ,
$c$	Aerofoil chord length, A distance from centre of ellipse to either focus (= $\sqrt{a^2 - b^2}$ ),
$C_L$	Lift coefficient,
$C_{pdynamic}$	Dynamic pressure coefficient,
$C_{pstatic}$	Static pressure coefficient,
$C_{ptotal}$	Total pressure coefficient,
$C_{p\alpha}$	Pressure coefficient in pitch plane,

$C_{p\beta}$	Pressure coefficient in yaw plane,
$D$	Width of a building,
$d, H_d$	A displacement height from bottom of shear layer due to surrounding obstacles,
$d_u$	Displacement height,
$e$	Distance between centre of a circle and a windward face of a building, Unit vector,
$F(k), G(k)$	Theodorsen function values,
$h, H$	Building height,
$H_0$	An average level height of the rooftop of buildings,
$h_{mean}$	an average of canopy height,
$I_{x,y,z,xy,xz,yz}$	Moment of inertia about $ox, oy, oz, ox$ and $oy, ox$ and $oz, oy$ and $oz$ respectively,
$K$	Amplification factor,
$k$	Reduced frequency = $\frac{c\omega}{2U}$ ,
$K_{c,max}$	Maximum amplification factor in a corner stream at outer building corner,
$K_{pcl,max}$	Maximum amplification factor along a passage centreline,
$L$	Length of a building,
$L, M, N$	Rolling, pitching and yawing moment,
$l_g$	Gust wavelength,
$p, q, r$	Roll, pitch and yaw rate,
$R$	Radius of an influence area,
$S$	Building Interference Scale, Wing area,
$s$	semi-span of a wing,
$t$	Airfoil thickness, time,

$Tu$	Turbulence Intensity,
$u$	Velocity in longitudinal direction,
$U, V, W$	Axial, side and normal velocity,
$u'$	Fluctuating velocity in longitudinal direction,
$u_*, u_\tau$	Shear stress velocity,
$U_0, u_0, U_\infty, u_\infty$	Mean wind velocity,
$v$	Velocity in lateral direction,
$v'$	Fluctuating velocity in lateral direction,
$V_z, V_r, V_\theta$	Velocity components in Cylindrical Polar Coordinates,
$V_{local}$	Local mean wind velocity at a point of interest,
$V_{ref}$	Reference wind velocity measured without a building,
$W$	Street width, Maximum gust velocity,
$w$	Velocity in vertical direction, Passage width,
$w'$	Fluctuating velocity in vertical direction,
$w_g$	Gust velocity,
$X$	Distance in longitudinal direction,
$X, Y, Z$	Axial, side and normal force,
$X_0$	An upwind spacing between buildings,
$X_r$	Reattachment distance,
$Y$	Distance in lateral direction,
$Z$	Distance in vertical direction,
$z$	Height above the ground,
$z_0$	Surface roughness parameter,
$z_1$	Height above the ground of a first point of interest,
$z_2$	Height above the ground of a second point of interest,

$z_d$  Zero plane displacement,

## Greek Symbols

$\alpha$  An approaching flow direction, effective angle of attack produced by sinusoidal gust,

$\alpha_a$  Oscillation amplitude,

$\alpha_m$  Given mean angle of attack,

$\beta$  Yaw angle of five-hole probe,

$\delta$  Boundary layer thickness, Uncertainty,

$\delta^*$  Displacement thickness,

$\kappa$  von Karmann constant, 0.41,

$\lambda$  Density ratio of ground obstructions, Width of wind tunnel/height of wind tunnel,

$\mu$  Dynamic viscosity,

$\nu$  Kinematic viscosity,

$\omega$  Gust frequency, rotational speed,

$\phi$  Phase difference, Roll angle,

$\psi$  Yaw angle of a rid plane,

$\rho$  Fluid density,

$\sigma$  Root mean square of the fluctuated velocity,

$\theta$  Pitch angle, Momentum thickness,

$\xi$  Wave number,

## Abbreviations

ABL Atmospheric Boundary Layer,

CFD Computational Fluid Dynamics,

CL Canopy Layer,

IS	Inertial Sublayer,
LDA	Laser Doppler Anemometry,
LES	Large Eddy Simulation,
PIV	Particle Image Velocimetry,
RS	Roughness Sublayer,
SL	Surface Layer,
UAV	Unmanned Aerial Vehicle,





# Contents

<b>1</b>	<b>Introduction</b>	<b>1</b>
1.1	Objectives and project aims . . . . .	2
<b>2</b>	<b>Wind Environments around buildings</b>	<b>3</b>
2.1	Atmospheric boundary layer partition . . . . .	3
2.2	The factors affecting wind speed . . . . .	3
2.3	Flow regimes in Roughness Sublayer . . . . .	4
2.4	Flow structures at a roof level . . . . .	9
2.4.1	Flow in passages between parallel buildings . . . . .	9
2.4.2	Conical Vortex on buildings . . . . .	11
2.4.3	Downwash vortex at base of buildings . . . . .	13
2.5	Building geometry selection . . . . .	15
<b>3</b>	<b>Aerofoil section and nonlinear gust response</b>	<b>29</b>
3.1	Stall characteristic . . . . .	29
3.2	Stall behaviour . . . . .	30
3.3	Laminar separation bubble . . . . .	32
3.4	Lift Characteristics for low speed aerofoils . . . . .	32
3.5	Nonlinear gust response . . . . .	33
3.5.1	Flow patterns of dynamic stall . . . . .	34
3.5.2	Parametric studies on dynamic stall . . . . .	35
3.6	Aerofoil shape on Dynamic stall . . . . .	37
3.7	Three-dimensional effect on dynamic stall . . . . .	38
3.8	Present study . . . . .	38
<b>4</b>	<b>Boundary layer measurement</b>	<b>53</b>
4.1	Experimental apparatus and instrumentation . . . . .	53
4.2	Instrumentation . . . . .	54
4.3	Experimental procedures . . . . .	55
4.4	Preliminary test . . . . .	56
4.4.1	Empty wind tunnel . . . . .	56

## CONTENTS

4.4.2	Wind tunnel with roughness elements and spires . . . . .	57
4.5	Boundary layer profile relating to scale . . . . .	59
4.6	Conclusion . . . . .	60
<b>5</b>	<b>Five-hole probe</b>	<b>69</b>
5.1	Applications of Five-hole Probe and Calibration Process . . . . .	69
5.2	Probe Geometries and Description . . . . .	70
5.3	Calibration Procedures . . . . .	71
5.4	Calibration Results . . . . .	74
5.4.1	Reynolds number effect . . . . .	75
5.4.2	Probe sensitivity . . . . .	76
5.4.3	Uncertainty analysis . . . . .	77
5.5	Concluding remarks . . . . .	80
<b>6</b>	<b>Flow behind surface mounted bluff bodies</b>	<b>93</b>
6.1	Introduction . . . . .	93
6.2	Experimental apparatus and measurement technique . . . . .	94
6.2.1	Building geometry and boundary layer thickness . . . . .	94
6.2.2	Measurement technique . . . . .	96
6.3	Experimental results and discussion . . . . .	96
6.3.1	Single Building Configuration . . . . .	96
6.3.2	Twin Building Configuration . . . . .	98
6.4	Summary and conclusions . . . . .	100
<b>7</b>	<b>The lift of a wing due to a sinusoidal gust</b>	<b>119</b>
7.1	Introduction . . . . .	119
7.2	Experimental Description . . . . .	120
7.2.1	Apparatus . . . . .	120
7.2.2	Experimental measurements . . . . .	120
7.3	Experimental results and discussion . . . . .	121
7.3.1	No gust excitation (static condition) . . . . .	121
7.3.2	Single harmonic excitation . . . . .	124
7.4	Conclusions . . . . .	129
<b>8</b>	<b>Conclusions and recommendations</b>	<b>145</b>
8.1	Conclusions . . . . .	145
8.2	Recommendations . . . . .	147
<b>A</b>	<b>Classification of Structural Shapes</b>	<b>159</b>

## CONTENTS

<b>B</b>	<b>Vector Resolution for Five-hole Probe Calibration Modes</b>	<b>161</b>
B.1	For "yaw-pitch mode" for probe calibration . . . . .	161
B.2	For "pitch-yaw mode" for probe calibration . . . . .	165
<b>C</b>	<b>Pressure Coefficient plots in 3-dimensions</b>	<b>169</b>
<b>D</b>	<b>Flow fields around buildings of rectangular shape</b>	<b>181</b>
<b>E</b>	<b>Wind tunnel of elliptic section</b>	<b>201</b>



# List of Figures

2.1	wind flow layer in the rural and urban environment [9]. . . . .	16
2.2	wind flow layer in the rural and urban environment [37]. . . . .	17
2.3	Contour of streamlines for high-rise building [38]. . . . .	17
2.4	Types of airflow dependent on length to height ratio [35] . . . . .	18
2.5	Flow visualisation of wind flow around a single narrow building [39]	18
2.6	High wind speeds around tall building with flow visualisation [39] .	19
2.7	Streamlines of the mean flow by LES [8] . . . . .	19
2.8	Schematic orientation of twin buildings [8, 14] . . . . .	20
2.9	Isolated roughness flow [40] . . . . .	20
2.10	General flow field [40] . . . . .	20
2.11	Wake interference flow when $W/H = 1$ [14, 38] . . . . .	21
2.12	Skimming flow [11, 40] . . . . .	21
2.13	Threshold aspect ratio of $(H/W)$ and $(L/W)$ [16] . . . . .	22
2.14	Characteristics canyon geometries to produce three different flow regimes [41] . . . . .	22
2.15	Threshold values for transition flow patterns [41] . . . . .	23
2.16	Buildings configuration of flow between parallel buildings [18] . . .	23
2.17	Influence areas of three different building types [35] . . . . .	24
2.18	Flow visualisation for three different flow patterns [42] . . . . .	24
2.19	CFD contour of a ratio local mean velocity to reference mean velocity without building at the same point of interest at different passage widths [18] . . . . .	25
2.20	Double conical vortex [43, 44] . . . . .	26
2.21	Inverted conical vortex formation procedure near the corner of tall building [26] . . . . .	26
2.22	Flow over building at glancing angle [26] . . . . .	26
2.23	Standing vortex system at different angle of attacks [33] . . . . .	27
3.1	Types of stall [46]. . . . .	39
3.2	Types of stall comparison [48]. . . . .	40
3.3	Thin aerofoil stall [45] . . . . .	41

## LIST OF FIGURES

3.4	Laminar separation pattern [69, 70] . . . . .	42
3.5	Diagram of different flow conditions for short and long separation bubbles, where $R_c$ is Reynolds number based on chord length [70] .	43
3.6	Simulated vortex shedding at different time [57] . . . . .	44
3.7	Schematic of the lift coefficient plot and flow morphology under dynamic motion [47] . . . . .	45
3.8	Normal force on NACA 0012 [56] . . . . .	46
3.9	Effect of reduced frequency on unsteady lift of an oscillating NACA 0012 [47] . . . . .	47
3.10	Effect of oscillation amplitude on NACA 0012 at constant mean angle of attack at $15^\circ$ [56] . . . . .	48
3.11	Effect of mean angle of attack on unsteady lift of an oscillating NACA 0012 at $M = 0.4$ and $k = 0.075$ [47] . . . . .	49
3.12	Effect of Reynolds number and Mach number on the unsteady lift of an oscillating NACA 0012 aerofoil [47, 56] . . . . .	50
3.13	Effect of aerofoil shape on dynamic stall [58] . . . . .	51
3.14	Unsteady lift on a finite semi-span swept wing at $Ma = 0.2$ [58] . .	52
4.1	Schematic of a closed section wind tunnel used for experiments. . .	62
4.2	Instrumental set-up . . . . .	62
4.3	Probe alignment and distance to surface [71] . . . . .	62
4.4	Centre line with different sample rates . . . . .	63
4.5	Empty wind tunnel in the spanwise locations at frequency 20 Hz . .	63
4.6	Boundary layer profiles with elliptical wedges but without surface roughness . . . . .	64
4.7	Boundary layer profiles with elliptical wedges and with surface roughness . . . . .	64
4.8	Profiles of mean velocity at various spanwise locations . . . . .	65
4.9	Comparison between three different set up methods . . . . .	65
4.10	Experimental result compare with ESDU methods to define the profile characteristics . . . . .	66
4.11	Simulated atmospheric boundary layer in an urban area . . . . .	67
5.1	Schematic diagram of forward facing Pyramid five-hole pressure probe [76] . . . . .	81
5.2	Schematic diagram of five-hole probe in 2 dimensions (Unit in mm)	81
5.3	Schematic diagram of five-hole probe in 3 dimensions . . . . .	82
5.4	Pitch and yaw angles pressure coefficient at $Re = 340$ . . . . .	83
5.5	Pitch and yaw angles pressure coefficient at $Re = 340$ at $\alpha = \pm 20^\circ$ and $\beta = \pm 20^\circ$ . . . . .	83
5.6	Pitch and yaw angles pressure coefficient at $Re = 565$ . . . . .	84

LIST OF FIGURES

5.7 Pitch and yaw angles pressure coefficient at  $Re = 565$  at  $\alpha = \pm 20^\circ$  and  $\beta = \pm 20^\circ$  . . . . . 84

5.8 Pitch and yaw angles pressure coefficient at  $Re = 790$  . . . . . 85

5.9 Pitch and yaw angles pressure coefficient at  $Re = 790$  at  $\alpha = \pm 20^\circ$  and  $\beta = \pm 20^\circ$  . . . . . 85

5.10 Yaw angle calibration at  $Re = 340$  . . . . . 86

5.11 Pitch angle calibration at  $Re = 340$  . . . . . 86

5.12 Yaw angle calibration at  $Re = 565$  . . . . . 87

5.13 Pitch angle calibration at  $Re = 565$  . . . . . 87

5.14 Yaw angle calibration at  $Re = 790$  . . . . . 88

5.15 Pitch angle calibration at  $Re = 790$  . . . . . 88

5.16 Pressure port no. 1 response to pitch and yaw motions . . . . . 89

5.17 Pressure port no. 2 response to pitch and yaw motions . . . . . 89

5.18 Pressure port no. 3 response to pitch and yaw motions . . . . . 90

5.19 Pressure port no. 4 response to pitch and yaw motions . . . . . 90

5.20 Pressure port no. 5 response to pitch and yaw motions . . . . . 91

6.1 Wake generators and roughness elements . . . . . 103

6.2 Estimated measurement locations based on tuft flow . . . . . 104

6.3 Measurements at different longitudinal locations behind building models . . . . . 105

6.4 Velocity field without buildings at test section . . . . . 106

6.5 Velocity field behind a single building at  $X/H = 0.75$  . . . . . 107

6.6 Velocity field behind a single building at  $X/H = 1.0$  . . . . . 108

6.7 Velocity field behind a single building at  $X/H = 1.5$  . . . . . 109

6.8 Vector plot in Y-Z plane behind a single building at  $X/H = 0.75$ . Positive velocity indicates upward velocity. Negative velocity indicates downward velocity. . . . . 110

6.9 Vector plot in Y-Z plane behind a single building at  $X/H = 1.0$ . Positive velocity indicates upward velocity. Negative velocity indicates downward velocity. . . . . 111

6.10 Vector plot in Y-Z plane behind a single building at  $X/H = 1.5$ . Positive velocity indicates upward velocity. Negative velocity indicates downward velocity. . . . . 112

6.11 Velocity field behind twin buildings at  $X/H = 0.75$  . . . . . 113

6.12 Velocity field behind twin buildings at  $X/H = 1.0$  . . . . . 113

6.13 Velocity field behind twin buildings at  $X/H = 1.5$  . . . . . 114

6.14 Time averaged velocity vector behind twin buildings at  $X/H = 0.75$ . Only one building on the right is shown here. . . . . 115

6.15 Time averaged velocity vector behind twin buildings at  $X/H = 1.0$ . Only one building on the right is shown here. . . . . 116

LIST OF FIGURES

6.16 Time averaged velocity vector behind twin buildings at  $X/H = 1.5$ .  
Only one building on the right is shown here. . . . . 117

6.17 Time averaged velocity vector from Tutar and Ogus [88] in x-z  
plane with  $w/H = 0.6$ . . . . . 118

7.1 Schematic of the 3–component mechanical balance . . . . . 133

7.2 Average lift coefficients against angle of attack at freestream velocity of 30 m/s and theoretical inviscid static lift calculated based on thin aerofoil theory with the angles of attack from  $-6^\circ \leq \alpha \leq 21^\circ$  at  $Re = 3.34 \times 10^5$  and vane oscillation amplitude  $\pm 8^\circ$ . . . . . 134

7.3 Average lift coefficients against angle of attack at freestream velocity of 30 m/s and theoretical inviscid static lift calculated based on thin aerofoil theory with the angles of attack from  $-6^\circ \leq \alpha \leq 21^\circ$  at  $Re = 3.34 \times 10^5$  and vane oscillation amplitude  $\pm 4^\circ$ . . . . . 134

7.4 Average lift coefficients against angle of attack at freestream velocity of 30 m/s and theoretical inviscid static lift calculated based on thin aerofoil theory with the angles of attack from  $-6^\circ \leq \alpha \leq 21^\circ$  at  $Re = 3.34 \times 10^5$  and vane oscillation limit  $0^\circ - 4^\circ$ . . . . . 135

7.5 Average lift coefficients against angles of attack at  $Re = 1.11 \times 10^5$  and Vane oscillation amplitude  $\pm 8^\circ$ . . . . . 135

7.6 Static lift coefficients at different Reynolds numbers. . . . . 136

7.7 Lift coefficients at  $12^\circ$  at  $Re = 1.11 \times 10^5$ . . . . . 136

7.8 Static pressure distribution for NACA23012  $Re = 1.11 \times 10^5$ ,  $\alpha = 0^\circ$  where solid lines represent results included viscosity and dash lines represent results without viscosity. . . . . 137

7.9 Static pressure distribution for NACA23012  $Re = 3.34 \times 10^5$ ,  $\alpha = 0^\circ$  where solid lines represent results included viscosity and dash lines represent results without viscosity. . . . . 137

7.10 Static pressure distribution for NACA23012  $Re = 1.11 \times 10^5$ ,  $\alpha = 3^\circ$  where solid lines represent results included viscosity and dash lines represent results without viscosity. . . . . 138

7.11 Static pressure distribution for NACA23012  $Re = 3.34 \times 10^5$ ,  $\alpha = 3^\circ$  where solid lines represent results included viscosity and dash lines represent results without viscosity. . . . . 138

7.12 Effects of mean angle variation at a constant oscillation amplitude of  $\pm 8^\circ$  and reduced frequency of 0.02 . . . . . 139

7.13 Time history of lift coefficients for the NACA 23012 . . . . . 140

7.14 Effects of the lift coefficients at a constant mean angle of attack and reduced frequency of 0.02 with variation in oscillation amplitude . 141

7.15 Effects of reduced frequency on the lift coefficients at constant mean angle of attack and oscillation amplitude of  $8^\circ$  . . . . . 142



## LIST OF FIGURES

7.16 Effects of Reynolds numbers on the lift coefficients at constant reduced frequency and constant oscillation amplitude of $8^\circ$ . . . . .	143
A.1 Vortex shedding from different bluff body shapes [96] . . . . .	160
B.1 . . . . .	162
B.2 . . . . .	163
B.3 . . . . .	164
B.4 . . . . .	165
B.5 . . . . .	166
C.1 Typical calibration plot for pressure coefficient in pitch motion at $Re = 340$ . . . . .	169
C.2 Typical calibration plot for pressure coefficient in pitch motion at $Re = 565$ . . . . .	170
C.3 Typical calibration plot for pressure coefficient in pitch motion at $Re = 790$ . . . . .	171
C.4 Typical calibration plot for pressure coefficient in yaw motion at $Re = 340$ . . . . .	172
C.5 Typical calibration plot for pressure coefficient in yaw motion at $Re = 565$ . . . . .	173
C.6 Typical calibration plot for pressure coefficient in yaw motion at $Re = 790$ . . . . .	174
C.7 Typical calibration plot for static pressure coefficient at $Re = 340$ . . . . .	174
C.8 Typical calibration plot for static pressure coefficient at $Re = 565$ . . . . .	175
C.9 Typical calibration plot for static pressure coefficient at $Re = 790$ . . . . .	175
C.10 Average pressure coefficient contour dependent upon $\alpha$ and $\beta$ . . . . .	176
C.11 Static pressure coefficient at $Re = 565$ . . . . .	176
C.12 Static pressure coefficient at $Re = 790$ . . . . .	177
C.13 Effect of probe sensitivity from port no.1 at $Re = 565$ . . . . .	177
C.14 Effect of probe sensitivity from port no.2 at $Re = 565$ . . . . .	178
C.15 Effect of probe sensitivity from port no.1 at $Re = 790$ . . . . .	178
C.16 Effect of probe sensitivity from port no.2 at $Re = 790$ . . . . .	179
D.1 Velocity field behind a single building at $X/H = 0.75$ . . . . .	181
D.2 Velocity field behind a single building at $X/H = 1.0$ . . . . .	182
D.3 Velocity field behind a single building at $X/H = 1.5$ . . . . .	183
D.4 Vector plot in Y-Z plane behind a single building at $X/H = 0.75$ . . . . .	184
D.5 Vector plot in Y-Z plane behind a single building at $X/H = 1.0$ . . . . .	184
D.6 Vector plot in Y-Z plane behind a single building at $X/H = 1.5$ . . . . .	185
D.7 Velocity field behind twin buildings at $X/H = 0.75$ . . . . .	185
D.8 Velocity field behind twin buildings at $X/H = 1.0$ . . . . .	186

LIST OF FIGURES

D.9 Velocity field behind twin buildings at  $X/H = 1.5$  . . . . . 186

D.10 Vertical and lateral velocity gradients at  $X/H = 0.75$  downstream  
behind a single building configuration . . . . . 187

D.11 Vertical and lateral velocity gradients at  $X/H = 1.0$  downstream  
behind a single building configuration . . . . . 188

D.12 Vertical and lateral velocity gradients at  $X/H = 1.5$  downstream  
behind a single building configuration . . . . . 189

D.13 Vertical velocity gradient plots at three locations downstream be-  
hind twin buildings configuration . . . . . 190

D.14 Lateral velocity gradient plots at three locations downstream behind  
twin buildings configuration . . . . . 191

D.15 Change in flow angularity in U-V velocity components at  $X/H = 0.75$  192

D.16 Change in flow angularity in U-V velocity components at  $X/H = 1.0$  193

D.17 Change in flow angularity in U-V velocity components at  $X/H = 1.5$  194

D.18 Change in flow angularity in U-V velocity components at  $X/H =$   
 $0.75$  behind twin buildings. Only half of the plane of measurement  
is shown here. . . . . 195

D.19 Change in flow angularity in U-V velocity components at  $X/H =$   
 $1.0$  behind twin buildings. Only half of the plane of measurement  
is shown here. . . . . 196

D.20 Change in flow angularity in U-V velocity components at  $X/H =$   
 $1.5$  behind twin buildings. Only half of the plane of measurement  
is shown here. . . . . 197

D.21 Change in flow angularity in U-V velocity components at  $X/H = 0.75$  198

D.22 Change in flow angularity in U-V velocity components at  $X/H = 1.0$  198

D.23 Change in flow angularity in U-V velocity components at  $X/H = 1.5$  199

E.1 Elements of an elliptic . . . . . 202

E.2 Elements of an elliptic [97] . . . . . 203

E.3 Correction factor plot for a rigid tunnel walls [97] . . . . . 203

E.4 Correction factor plot for an open tunnel [97] . . . . . 204

# List of Tables

2.1	Further explanation of Figure 2.6 . . . . .	6
2.2	The flow regimes associated with building ratio [9, 10, 14, 15] . . . . .	8
5.1	The uncertainties for $Re = 340$ . . . . .	79
5.2	The uncertainties for $Re = 565$ . . . . .	79
5.3	The uncertainties for $Re = 790$ . . . . .	79
7.1	Comparison of experimental results and calculated result . . . . .	132
B.1	yaw-pitch mode . . . . .	165
B.2	Pitch-yaw mode . . . . .	167
E.1	The correction factor $\delta_1$ and $\delta_2$ for a rigid walls tunnel [97] . . . . .	204
E.2	The correction factor $\delta_3$ and $\delta_4$ for an open tunnel [97] . . . . .	205



# Chapter 1

## Introduction

For more than half a century, there have been a number of investigations and studies of wind flow over an urban environment, in which the general conclusion is that the flows are complex and three dimensional. Many works related to turbulence describe the behaviour of the flow over the urban area with a terrain roughness. The significant roles of the turbulent flow are mainly investigated in a region called the atmospheric boundary layer (*ABL*). The atmospheric boundary layer region can expand to a few hundred metres above the ground or up to a thousand metres above the ground depending on characteristics of the terrain such as surface roughness and the orientation of buildings. The atmospheric boundary layer is complicated due to a combination of many influences. Rotation of the Earth, buoyancy forces, surface drag forces, and the geometry of topographic features [1] all influence the atmospheric boundary layer.

Nowadays much research into fluid dynamics and wind engineering are more or less specifically interested in the characteristics of the boundary layer either in theory or using experimental methods. Therefore in order to understand the roles of the boundary layer, a close connection between theory and experiment will be considered. Investigations into man-made structures or bluff bodies, such as tall and low-rise buildings and bridges, have been the main subject of wind engineering in order to remove the large impact of wind-loading on such structures. Such studies not only consider the effect of the aerodynamic behaviour below roof top level but also focus on the outcome of such flow characteristics, for example vortex shedding, wakes and flow separation. Natural wind flow can be imitated in a long test section wind tunnel by introducing surface roughness over a test section floor to produce turbulent flow and boundary layer over the test section. The simulation of an atmospheric boundary layer in a wind tunnel involves a combination of flow mixing devices, such as spires, to generate the neutral flow stratification for a specific model at any scale. A standard conceptual framework for studying the flow in

urban environments is to consider the flow characteristics induced by bluff bodies. Most structures are civil engineering structures such as buildings, bridges and other structures built to withstand natural forces. One of the most common effects of the flow around bluff bodies is flow separation and vortex shedding formation near sharp edges of the bodies. Therefore, an observation of a relationship of the flow in an urban environment and aerodynamic characteristics produced by bluff bodies will be presented in order to understand the flow behaviour for different configurations. For the study of such consequences, it is desirable to select an appropriate model scale with the correct wind tunnel size in order to be able to investigate the flow conditions similar to the natural wind conditions. In many reviews of techniques used in boundary layer flow generation, model scale selection depends on the length of the wind tunnel test section and the most desirable scale should not be smaller than 1 : 600 [2].

## 1.1 Objectives and project aims

Research on aerodynamic problems of flying UAVs in an urban environment will be conducted in two different parts. The first part is to observe the characteristics and behaviour of a simulated atmospheric boundary layer. Determination and explanation of the effects of gusts induced by low altitude buildings in the urban environment is then required. However, in order to understand the flying behaviour of UAVs in real wind conditions at various urban configurations, an experimental model of unsteady aerodynamic gusts will be constructed. The flow field study in the urban environment in this research is significantly focusing on the flow around single- and twin-building configurations to provide an understanding of the flow induced by the buildings and its behaviour.

The second part of the research will be looking at the performance of a three-dimensional UAV wing planform in a simulated gust. The main objectives of the research are to investigate and identify certain parameters affecting the performance of UAVs flying in the turbulent flow region at low-rise building level up to a few hundred metres above the ground by using relevant results obtained from the experiments. An appearance of mixed laminar and turbulent flows is generally believed to be a key feature that impact the aerodynamic performance of aircraft operating at low Reynolds numbers range.

# Chapter 2

## Wind Environments around buildings

### 2.1 Atmospheric boundary layer partition

Characteristics of a boundary layer developed in the urban area are different from a turbulent boundary layer developed over an homogeneous rough surface. The boundary layer can be divided into two main layers: the internal and external layers, where the flow in the external layer is not influenced by the effect of surface roughness. Surface Layer (*SL*) is a lower portion of the internal layer which extends up to 10% of the boundary layer thickness. In addition, the flow in this particular region is strongly controlled by obstacles on the ground. The Surface Layer is also separated into two sub-layers called Inertial Sublayer (*IS*) and Roughness Sublayer (*RS*) as in Figure 2.1

Moreover, Canopy Layer (*CL*) is also a part of the lower region of the internal layer. The characteristics of the external layer do not have any effects on the Canopy Layer because the canopy flow is strongly manipulated by the distribution of the buildings and the street geometry. It is interesting to note that the flow bounded in the Canopy Layer appears to be dependent on incoming flow properties. Therefore, many research studies into air pollutant dispersal and wind loading on a structure are concerned with the flow pattern in the Canopy Layer.

### 2.2 The factors affecting wind speed

Gradient wind is the wind at a particular height above the earth surface and is not affected by the earth surface roughness such as cities, mountains, hills, tall buildings and other obstructions. The drag force caused by these obstacles reduces as the height above the earth increases and when the first value of the wind speed reaches

the gradient wind value, the height is called gradient height. At the gradient height ( $h$ ) the horizontal drag force induced by obstacles becomes negligible. In fact, if the wind flows above a fetch (a distance that uniform terrain roughness extends upwind) of at least 100 km of flat and uniform terrain before approaching towns or city areas, the atmospheric boundary layer is still in equilibrium with the primary surface i.e. the wind speed profile does not change with an increase of the fetch in the upwind direction. A change in terrain roughness downwind of the uniform fetch causes the new boundary layer to initiate and the flow inside this internal layer is not in equilibrium.

### 2.3 Flow regimes in Roughness Sublayer

In the Roughness Sublayer, the flow characteristics depend on the distribution of the buildings and the buildings' aspect ratio. This ratio is based on an average building height to an average street width,  $H/W$ . Before focusing on the effects of the flow fields around twin buildings, the flow patterns around an isolated high-rise building should be considered.

When the wind direction is perpendicular to a building as displayed in Figure 2.3, the flow field around an isolated high-rise building would be complex.

For a single bluff body, a vortex system extends over the entire length of the windward face to form an unsteady horseshoe vortex system in front of the building. The unsteady horseshoe vortex system is formed in front of the obstacle in a separation zone and sweeps downstream along the obstacle sides. Owing to experiments of Baker [3] and Nigro [4], it should be noted that the unsteady horseshoe vortex can be seen in front of the obstacle when  $Re > 2800$  where Reynolds number is dependent on a dimension of a wall-mounted building. Martinuzzi and Tropea [5] concluded that streamwise vortices in a shear layer are the factor to influence flow field around three-dimensional obstacles. The point where stagnation occurs is usually on a symmetry plane on a windward face, a short distance upwind of a building at  $(2/3) < (Z/W) < (3/4)$ . Martinuzzi and Tropea [5] also suggested that the shape and form of separation over the roof-top level and aft of a building depend on the relative boundary layer thickness,  $(\delta/H)$ . Below the stagnation point the oncoming flow is swept sideways and downwards to ground level and outwards along the flow direction. Above this point, the flow separates sideways and upwards and does not reattach on the rooftop level. Considering the wind flowing downwards, as the flow approaches the bottom of the building, pressure increases. As the wind behaviour generally takes the shortest way, the wind starts to move downwards as it approaches the ground. This generates a large circulation vortex in front of the building [6] as seen in Figure 2.3 although the vortex cannot be seen properly. However, behind the building the recirculation regions of an adverse pressure gradi-



ent are formed generating another free stagnation point downstream near the point where  $Z/H$  is approximately  $1/2 - 2/3$ . Not only is reverse flow observed near the top edge of the leeward side but it is observed at the sides of the building also. Depending on the ratio of length to height of a building as seen in Figure 2.4, three different flow fields are determined:

1. Tall building,  $h > 1.25a$ , where "a" is windward width and "h" is height of the building. The main airflow is swept along the side of the building due to the narrow windward facade but the recirculation vortices are present in front of and behind the building over small areas displayed in Figure 2.3 and Figure 2.5. However, a peak in velocity exists from downstream corner of the building.
2. Tall building of transitional type,  $0.33a \leq h \leq 1.25a$ . Flow moves downwards due to the stagnation point at heights as high as 70 – 80% of the building, resulting in a strong vortex in the front near the base of the building, with the flow deviating to the lower pressure regions; upwards, downwards and sideways. The standing vortex in Figure 2.6 on the ground located in front of the building is another result from the flow deviating downwards. The standing vortex causes some of the air at the building corners to merge with the oncoming flow into the downstream jet. Moreover, a recirculation region is also induced behind the building due to the pressure difference in the wake region. Within this zone, the velocity gradient is very high including high speed rotational vortices. Beyond this area, the flow is undisturbed at some distance downstream as indicated by a reattachment line.
3. Long face,  $a > 3h$ . In this case, the vortex system in front of the building is less dominant. A reverse air flow on the leeward side is induced if the flow is perpendicular to the windward face. For wind directions between  $30^\circ$  and  $60^\circ$ , an "overrolling vortex" is possible behind the building.

The flow structures in a flow over a wall-mounted cube investigated by Meinders [7] and Krajnovic [8] showed comparable patterns near the base of the obstacle. The horseshoe vortex is generated at the front face and an arc-shaped vortex is found behind the cube. Also the flow separates at the side faces and near the rooftop level resulting in flow recirculation areas near the side edges and downstream behind the cube. The horseshoe vortex is deflected downstream along both sides of the obstacle and further downstream leading to the vortex strength weakening. In the wake region behind the cube, an arc-type vortex is formed and gradually grows towards the leeward side of the obstacle as shown in Figure 2.7 according to width-to-height ratio of the building. Figure 2.8a shows three different flows classified which can be

Number	Flow Descriptions
0	undisturbed wind
1, 2	air flow over and around the building
3, 4	air flow in front of the building is partly deflected above and aside
5	the larger part of the air flow in front of the building deflected downwards
6	vortices in front of the building
7	stagnation point in front of the building
8	wind speed increased at corners of the building
9	broad jet streams with increased velocity next to the building
10, 14	reversed air flow regions behind the building
11	stagnation point behind the building
12	flow direction behind stagnation point
13	standing vortices behind the building
15	upwind-directed air streams behind the building
16	small rotating vortices
17	edge of the “influence area”

TABLE 2.1 Further explanation of Figure 2.6

used to explain the flow behaviour in an urban environment. These three different types are determined by the interaction of the vortex generation between upwind and downwind buildings:

#### 1. Isolated Roughness.

This is the flow behaviour for which buildings are well apart and the aspect ratio,  $W/H$ , is greater than 3.30 [9]. A recirculation vortex behind the upwind building is formed due to the flow separation near the top edge of the upwind building. On the other hand, Chang and Meroney [10] described that the isolated roughness flow occurs when the aspect ratio,  $W/H$ , is greater than 5. Farhadi and Sedighi [11] also supported that the separated flow at the leading edge of the windward building generates a vortex on top of the building and the flow behind this vortex is forced to form a secondary recirculation in front of the downwind building. A profile from the upwind building deflects downwards to the ground before the circulation vortex meets a bolster vortex in front of the downwind building but the interaction between the two vortices is weak because the building separation is large. Separation flow on the rooftop of the downwind building is investigated since each building acts as if they are an individual building. The effects of the flow field such as separation of the upwind building do not influence the flow field in the downwind building area. However, the wind flow behind the upwind building creates enhancement of the vortex in front of the downwind building as

the procedures of how the vortex created are explained earlier in an isolated building case. It is interesting to note that in a region behind the leeward edge of the downwind building the flow introduces a reverse flow but does not attach to the leeward edge.

## 2. Wake Interference.

For the wake interference flow case, Ricciardelli and Polimeno [9] suggested that this flow pattern occurs when  $1.54 < W/H < 3.30$  or  $0.3 < H/W < 0.65$  with an aerodynamic interference between buildings and happens because of the small distance between the buildings. On the other hand, Chang and Meroney [10] provided that the building ratio in this case,  $W/H$  is between 1.2 and 5. Consequently, the downwind building interrupts the recirculation vortex before readjustment takes place. Separation flow happens at the rooftop level of the upwind building and the wind flow behind the upwind building is curled down to create a low pressure recirculating flow region between two buildings. The flow separation cannot be observed near the top windward edge of the downwind building. This indicates that the space, and the ratio of  $W/H$  between the two buildings, influence the upwind building to produce a high level of turbulence that retards the separation flow on both rooftop and sides of the downwind building. However, the circulation and the bolster vortices can still interact. It is very interesting to note that as a threshold value of wake interference flow to isolated roughness flow is reached, a main vortex which expands from the leeward side of the upstream building starts breaking down, replaced by two individual co-rotative vortices [12]

## 3. Skimming Flow.

If the distance between buildings gets smaller,  $W/H < 1.54$  [9] and  $W/H < 1.2$  [10] the flow above the roof top level cannot penetrate into the canyon leaving a stable vortex trapped in between the buildings. Because the spacing between the buildings is very narrow, the majority of the flow flows over the rooftop level of the buildings leaving some of the air flow trapped in between the buildings [6]. The trapped vortex rotates slowly and provides a shelter between the buildings. Martinuzzi and Havel [13] also suggested a separated shear layer from the windward building reattaches on the side-walls of the downward building. Farhadi and Sedighi [11] concluded that the ratio of  $W/H$  has a small influence on turbulence level in front of the windward building and above the gap between the two buildings. However, they provided that in the inter-obstacle region the level of turbulence increases as the ratio of  $W/H$  is larger. In this case, an average canopy height,  $h_{mean}$ , can be defined which divides the Surface Layer ( $SL$ ) into an upper layer and a

lower layer, called Canopy Layer (*CL*). The displacement height  $d_u$ , at which elevation of the mean wind speed profile tends to zero, is also identified in the skimming flow case as well as the average canopy height. The displacement height seems to be in the range of  $(2/3)h_{mean}$  to  $(3/4)h_{mean}$  [9]. The skimming flow region contains two different vortex structures in a gap between buildings either one main vortex structure or multi-vortex structures. In very narrow canyons ( $W/H < 0.6 - 0.7$ ) one or two additional stretched and weak vortices are found in a lower part of the canyons depending on the ratio of  $W/H$ . This results in a large reduction of the horizontal mean wind speed producing a shelter effect at a region near ground level [12].

Authors	Skimming flow	Wake interference	Isolated roughness
Ricciardelli and Polimeno	$W/H < 1.54$	$1.54 < W/H < 3.33$	$W/H > 3.33$
Chang and Meroney	$W/H < 1.2$	$1.2 < W/H < 5.00$	$W/H > 5.00$
Baik and Kim	$W/H < 2.00$	$W/H > 2.50$	–
Kovar-Panskus et al	$W/H < 2.00$	$W/H > 2.00$	–

TABLE 2.2 The flow regimes associated with building ratio [9, 10, 14, 15]

Consequently, the building ratios ( $W/H$ ) from the literature are summarised in Table 2.2. There is another significant point to focus on recommended by Oke [16]. He pointed out another ratio and explained that the three different flow patterns are a combination of two different ratios of  $(H/W)$  and  $(L/W)$  (where  $L$  is the length of the building perpendicular to the oncoming flow) as shown in Figure 2.13, for a transition point from skimming flow to wake interference flow, the threshold value becomes independent on the length of the building,  $L$ , when  $L/H > 2$ . In contrast, from wake interference to isolated roughness flow the threshold is still dependent on the building length.

Hunter [17] concluded threshold values,  $(H/W)$  for a change of flow patterns of a cube geometry for a transition from skimming flow to wake interference flow is in between 0.71 – 0.74. Changing flow regime from wake interference flow to isolated roughness flow, both simulation and a value from Oke [16] are confirmed at  $(H/W = 0.6)$ . On the other hand, the threshold values were completely different for both simulation and Oke's experiment when  $(L/W > 1.0)$  as displayed in Figure 2.15

## 2.4 Flow structures at a roof level

### 2.4.1 Flow in passages between parallel buildings

Flow in passages between parallel buildings is one of the most significant flow patterns in the lower level of the atmospheric boundary layer study. In common, passages between buildings are omnipresent, and different types of passages induce a significant increase and/or decrease in wind speeds between the buildings causing uncomfortable wind flow at pedestrian level. In the past, many wind tunnel experiments have been conducted and focused on the wind flow between parallel alongside buildings. Most recently, numerical simulation is applied to provide more understanding of the flow in specific conditions and in more complicated cases.

At pedestrian-level wind speed, there are three disparate flow regimes along the passage centre line depending on building parameter,  $w/S$  where  $w$  is the passage width and  $S$  is the building influence scale:

$$S = (B_L B_S^2)^{1/3} \quad (2.1)$$

The building influence scale is established to determine the flow recirculation area on building roofs where  $B_L$  and  $B_S$  are the larger and smaller height and width dimensions of the buildings in the windward facade respectively. More importantly, the parameter is defined that when  $B_L$  is larger than  $8B_S$ , then  $B_L$  equivalent to  $8B_S$  is to be used.

Based on the building parameter,  $w/S$ , three different flows at pedestrian level are distinguished and indicated by another three parameters called "amplification factors":

$$K = \frac{V_{local}}{V_{ref}} \quad (2.2)$$

in which  $V_{local}$  is local mean velocity at point of interest and  $V_{ref}$  is reference mean velocity measured without building(s) under consideration.

1. Resistance flow ( $w/S < 0.125$ ) is usually originated in narrow passages where flow resistance in the passages is high resulting in the ratio of maximum amplification factor in a corner stream to a passage centreline,  $K_{pcl,max}/K_{c,max}$  and is approximately equal to one or even smaller (see experiment by Blocken [18]). In terms of shear layer interaction, the separate shear layers from the inner leading edges of the buildings collide with each other, forming a large-scale vortex [19]. However if the passage gap is very narrow compared with the dimension of the windward facade, flow separation is not detected near the passage entrance. It indicates that the flow pattern resembles as if the two buildings act as one building of similar shape.

2. Interaction flow ( $0.125 < w/S < 1.25$ ). Flow separation from two corners at the passage entrance interrelates and combines together into a single stream. The flow interaction results in the ratio of  $K_{pcl,max}/K_{c,max}$  greater than one and the single stream expands downstream to a considerable distance from the building exit. At a location of approximately 20% from the passage entrance, the maximum wind velocity amplification is observed. However, the amplification value varies with wind direction with an area near the passage entrance more significantly affected by adverse wind conditions than other areas of the passage [20]. Sakamoto and Haniu [19] suggested the negative pressure in the inner side of the building is greater than the outer side due to the fact that flow velocity in the gap is faster than the outer one. Also, flow in the gap suppresses a separated shear flow from a corner of the building leading to a periodical roll up in the gap causing the flow around the building to be asymmetrical. As the value of building parameter becomes close to 1.25, a small vortex forms behind the building on the side of the biased flow. On the other hand, a large-scale vortex also forms further downstream on the unbiased side.
  
3. Isolated flow ( $w/S > 1.25$ ), the gap between buildings is too large therefore there is no interaction in the passage. The ratio of  $K_{pcl,max}/K_{c,max}$  is more or less equal to one, due to no flow interaction. However at the passage corners, flow separations are clearly present because each building behaves as if they are an individual block to interact with the upstream flow. In the isolated flow, it can be concluded that if the buildings are completely outside the influence area (explained in the next paragraph) no interaction will take place. In other words, if the influence areas do not overlap, there will be no interaction between the buildings and the periodic rolling up from separated shear flow in the inner corner of the gap begins to push back in the rear region. The flow in the gap between the two buildings does not show unstable biased flow any longer.

Lawson [6] suggested that a passage gap for both  $w/S < 0.125$  and  $w/S > 1.25$  cases, the buildings do not introduce a significantly accelerated flow through them. The most important parameter to determine such flow patterns in the passage between two parallel buildings is an "influence area". The influence area is an area covered by a radius "R" by drawing a circle passing through two stagnation points in front and aft of an individual building. The windward dimensions, length and height, of the building are dominant key factors to evaluate the radius R. As mentioned earlier in a flow pattern around a single building, three different types of building are classified.

### 2.4.2 Conical Vortex on buildings

Another significant parameter of the flow characteristics is the vortex shedding induced by buildings. These vortices are investigated in strong wind conditions related to flow separation and the local pressure changing at sharp edges. The change in local pressure is composed of a local peak suction which is induced by large and strong conical vortices at the roofs and the edges when the wind flow crashes into buildings at any directions. Two types of suction can be found; on a roof top of low-rise building and on a side of high-rise building. A pair of conical vortices is a cause of the local suction in the former case. Kawai [21,22] suggested that the peak suction occasionally occurs near the leading edge or the corner of the walls and roofs when the wind approaches from an oblique angle in highly turbulent flow. Moreover, he suggested the large suction is also created beside the leading edge close to a roof corner and it is induced by a pair of conical vortices persuaded by the flow separation from the leading edge.

Conical vortices related to the peak suction can be established in two different types, moving and non-moving vortices. The non-moving type, in Figure 2.20 appear on a flat roof at an oblique angle and they are the same type of conical vortex formed near a corner of the high-rise building producing the large suction in a glimpsing angle [21]. This type of conical vortex decays and grows alternatively depending on the wind direction and the approaching wind speed. However, the conical vortex on the flat roof is unstable even in a smooth flow. As the angle of an approaching wind increases, the vortex is found to grow larger. It is confirmed that the mean vortex core position gets closer to an edge of a flat roof building when the turbulence level gets higher; also the mean position of the vortex core relative to an edge of a building differs with the mean angle of an approaching flow [23]. However, it is very important to note by Yoshihito et al [24] (1998) that the conical vortex formed over a flat roof building has been considered to consist of a pair of vortices with directions of rotation that are opposite. The authors also found an interesting phenomenon in that the conical vortex does not appear with a pair of vortices but sometimes with a form of a single vortex instead. The conical vortex phenomenon when one side conical vortex exists but another side disappears is randomly repeated with each other is called "switching phenomenon". To elaborate this phenomenon in uniform flow, it can be explained in terms of an interaction between two different vortices. When a vortex called "vortex  $\alpha$ " which has its axis vertical to a leading corner of the roof, and is believed that it is induced by an unsteady stagnation point in uniform flow on a side of the cubic-type building is formed, "vortex  $\alpha$ " interacts with a conical vortex generated on the same side of "vortex  $\alpha$ ". The interaction of the two vortices results in the recovery of a negative pressure on the side of building due to vortex formation. On the other hand, if the strong conical vortex is originated from the other side of the building roof, the

negative pressure becomes larger on that side. If the negative pressure on one side changes in turn, it results in a switching of negative pressure in uniform flow. However in the turbulent case, an approaching flow is not symmetrical on both sides of the cubic building then the location of the stagnation point on a side of the building is stably random. Consequently, the switching of the negative pressure due to the interaction of two vortices is difficult to observe [25]. The other type of vortex, in Figure 2.21 and Figure 2.22 is a moving conical vortex and is complemented by vortex shedding. Local severe suction near the building side could be developed due to separated shear flow around the building. Okuda et al [26] observed the flow behaviour by focusing on the distribution of wind pressures on the side surface of a prism which indicates a building and flow visualisation against an angle of attack of an approaching flow. There were two cases which Okuda suggested could be a sequence of the conical vortex formation. In the case of an approaching flow at  $\alpha = 0^\circ$  to  $5^\circ$ , the vortex formed at a lower side of the building. The other case at a glancing angle where  $\alpha = 10^\circ$  to  $15^\circ$ , the vortex developed at the upper side near the roof of building. In the former case where  $\alpha = 0^\circ$  to  $5^\circ$  a separated shear flow is curled up to form a cylindrical vortex at a lower part of the building which is called an inverted conical vortex. The formation of this vortex instigates at a height of  $3/4$  of the height of the building according to the separation shear layer rolling up. Subsequently the vortex moves downwards to form a conical vortex at a downward corner of the building to induce the large peak suction at an oblique angle. The inverted conical vortex is inclined at an angle of  $60^\circ$  to the leeward relative to the downward windward corner. The separated shear layer profile on the side is an influence factor to generate the inverted conical vortex to stretch and incline more and more. Then the vortex discards along the flow direction and merges into the wake region causing the large suction to become less powerful. H.Kawai [22], however, still believed that the strength of the conical vortex in the smooth flow is larger than in the turbulent flow. In the case of turbulent flow, the vortices are more flat and the locations to form such vortices are closer to the roof surface. Comparison with calculated and measured flow fields from Davies et al [27] indicated that there was a small recirculation region formed behind a block. A spiral motion investigation was first checked by releasing very small seeding near the recirculation region behind the block observing that the seeding moved towards a symmetry plane of the flow, then moved closely to the block and dispersed away in a spiral motion gradually increasing in height. As the spiral motion increased in height, the vortex left near a side at a top region of the block. Castro and Robin [28] also observed similar flow behaviour even though their experiment was focusing on an effect of a flow field around a surface mounted cube. The recirculation region in the case of Castro and Robin formed at a side of the cube. They applied similar flow technique to Davies' by releasing the seeding near the ground in a rear recirculation area. The origin of the spiral region was observed to start at a side of the cube and disappear at the top



edge near the symmetry plane of the flow behind the cube. Another two views of the computed and measured results are from Woo et al [29] and Melbourne [30]. These two cases also used the seeding to examine the recirculation region and its origin. The vortex/recirculation region in these cases appeared to originate from behind the block and sweep outwards to a side and moved upwards to the top roof. The recirculation region left the block near the top leeward side of the block. Sizes of the spiral were wider, longer and flatter than the the case of Castro and Robin. Note that the wind direction of these four flow patterns was perpendicular to a front face of the block model. When the approaching flow attacks the building at glancing angle,  $\alpha = 10^\circ$  to  $15^\circ$  the separated shear flow is split into the upper and lower parts by the upper windward corner, the lower part is reattached onto the upper part region on the building. The separated flow is rolled inside in an arc shape to form a standing conical vortex which causes another local severe suction. A turning radius of the vortex is small near the corner where it is generated. At the windward upper corner, the suction appears to be strong. It is always observed that the largest suction appears at this corner. Surprisingly, the flow inside the standing vortex rotates for a few turns and is shed to a wake region behind the building in the middle point of the leeward side. Moreover, some of the upper separated shear flow is curved up from a side between the front and the top edges to combine with another conical vortex generated by the upper windward corner as shown in Figure 2.22. Okuda et al [31] also recommended that when the wind direction does not change and the approaching velocity is constant, the amount of air flow into the standing vortex is equivalent to the quantity of air flow out of the vortex. Consequently, the standing vortex is fixed on the upper windward corner and the fluctuating suction is zero. On the other hand, if the wind direction is suddenly changed the origin of the standing vortex is still at the upper windward corner although the vortex is stretched into a thinner shape towards the leeward region. This immediate change results in the local suction becoming very strong and the turning curvature is less. In contrast, if the wind direction changed to another direction away from the glancing angle the suction does not happen at the upper windward corner anymore. However, it is important to bear in mind that the standing conical vortex is originally formed at the upper region vicinity to the upper windward corner, unlike the inverted conical vortex which is generally formed at the lower windward corner.

### 2.4.3 Downwash vortex at base of buildings

Here again, another high wind velocity caused by high ground level near a tall building base is about to be illustrated. A construction of tall buildings in an area close to a low-rise building varies the flow velocity as three different flow fields are investigated:

1. The first flow separation is influenced by a pressure distribution on a windward face which relates to local dynamic pressure. As the oncoming flow approaches the building, it slows down and finally comes to rest at a stagnation point which can be as high as 80% of the building height. As the height of the building is high up, the ambient wind speed is faster; therefore the rise of pressure is greater [6]. This results in increasing total pressure with increasing height of building. Below the stagnation point, the flow is forced to flow vertically downwards. The downward flow then forms into a standing vortex system at the base of the tall building leading to increasing high wind speed in low region. A distribution of two buildings with a low-rise building in front is said to be critical in terms of flow field condition. The configuration of upstream building in front of the tall building generates an augmented vortex in front of the tall building resulting in high wind velocity near pedestrian level [32]. Becker et al [33] also carried out visualisation experiments to understand more of the flow topology around a block model, representing a building, in two different boundary layer conditions with oncoming free-stream perpendicular to the windward face of the model. They explained that in front of the building, there was no fundamental change of the characteristics of the horseshoe vortex system on each side and in front of the building for both boundary layer conditions. They found that in a boundary layer flow field the separated vortices on side of the obstacle moved closer to the side and produced smaller recirculation region behind the building.
2. Another flow separation is caused by pressure differences between low and high wake regions. A relatively high pressure region is at the windward face of the tall building and low pressure region is at leeward and sides of the building. The connection of regions of different pressures around corners induces local flows with vortices of varying intensity. At this low pressure region, the pressure seems to be dependent on free stream velocity above the boundary layer. It can be summed up that the taller the building, the less pressure in the wake region but the higher the induced velocity around corners and behind the building.
3. The other flow structure observed behind the building is in a form of a standing vortex. As flow angle increases, one of the vortex footprints moves closer to a side of the building. According to an investigation of Becker et al [33] the characteristics of this standing vortex reaches the backside of the building at a flow angle of  $\alpha = 45^\circ$  and standing at the rooftop level at  $\alpha = 60^\circ$ . A study from Kranojvic et al [8] by using LES method suggested that the back vortices are not upright but they are tilted with respect to the vertical axis. They also confirmed the flow structure by oil-film flow visualisation and observed

the vortex topology from smoke visualisation. The dependence on oncoming flow angle of attack of flow structure is displayed in Figure 2.23

## 2.5 Building geometry selection

A building geometry has been chosen from the literature review of the wind environments around buildings and experimental results obtained from boundary layer thickness measurements in Chapter 4. The estimated boundary layer thickness at the centre of the test section is 235 mm. Hence, the building model height should not be more than 235 mm in order to fully immerse it in the boundary layer. A factor to determine the building geometry is based on Schofield and Logan [34]. They described that the flow field around surface-mounted obstacles is mainly influenced by the parameters; obstacle height ( $H$ ), boundary layer thickness ( $\delta$ ) and wall shear velocity ( $u_\tau$ ). They indicated the ratio of the obstacle height-to-boundary layer thickness is the most important parameter influencing the flow characteristics around the building. If  $H/\delta$  is larger than 0.80, the boundary layer separates near the windward face of the building creating the strong vortex system near the sharp edged corners. Also the reattachment point behind the obstacle is further than in case of  $H/\delta < 0.80$  where the boundary layer separates early. When the boundary layer separates early, the horseshoe vortex cannot be detected. Another factor to determine a choice of the building geometry is discomfort areas based on W. J. Beranek investigations [35]. The air flow around a transitional building type on the windward side, see Figure 2.17, is greatly transported downwards and significantly swept sideways creating a large area of reverse flow on the back of the building. Based on the boundary layer measurements which will be discussed later in Chapter 4 and the information from literatures review, the building height was then selected to be 200 mm, where the width and the length of the building are chosen arbitrarily. Hence, the geometry of the building to provide a potential of the overall of the air flow pattern is given by the following dimensions;  $L \times H \times W = 200 \times 200 \times 100$  (mm). The geometry indicates the ratio of  $H/\delta = 0.85$  which is the ratio where the flow separates closer to the windward face causing the horseshoe circulation vortex generated closer to the base of the building, and the building dimensions represent the transitional building type, see Figure 2.17.

For a twin-building experiment, the building models with the same dimensions,  $L \times H \times W = 200 \times 200 \times 100$  (mm), were used. Passage width between the buildings was determined based on simulated results of Cemeliet et al [18] and Ishizaki [36]. To obtain interaction flow between two buildings sitting side-by-side with the wind speed in the gap reaching the maximum value, a separation distance between the two buildings is dependent on the buildings geometry. For the building

geometry of  $L \times H \times W = 200 \times 200 \times 100$  (mm), the maximum values of a relative wind speed,  $U/U_{ref}$  at different altitude were obtained when the width of the gap is approximately  $0.6H$ .

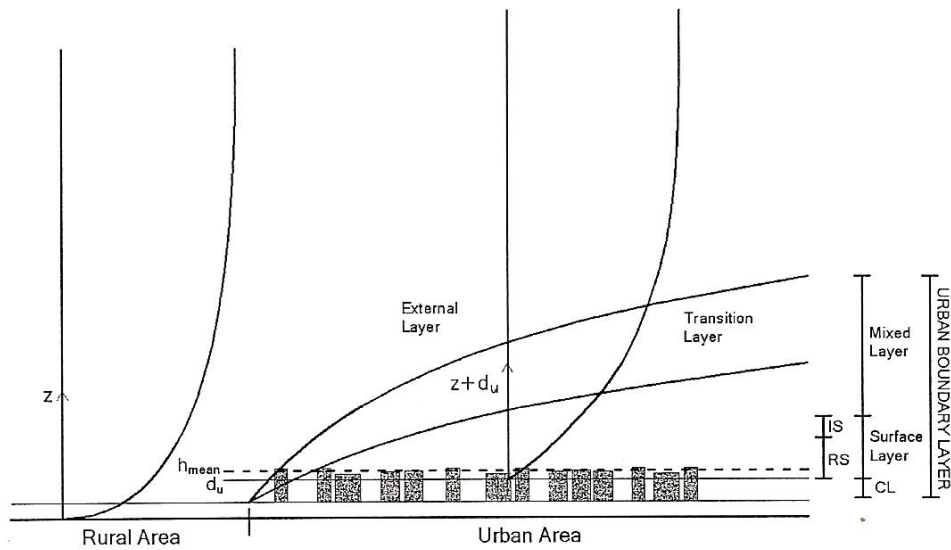


FIGURE 2.1 wind flow layer in the rural and urban environment [9].

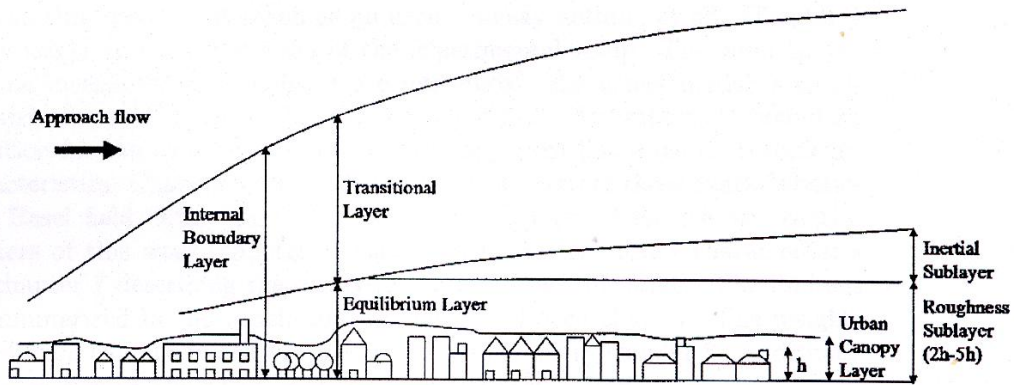


FIGURE 2.2 wind flow layer in the rural and urban environment [37].

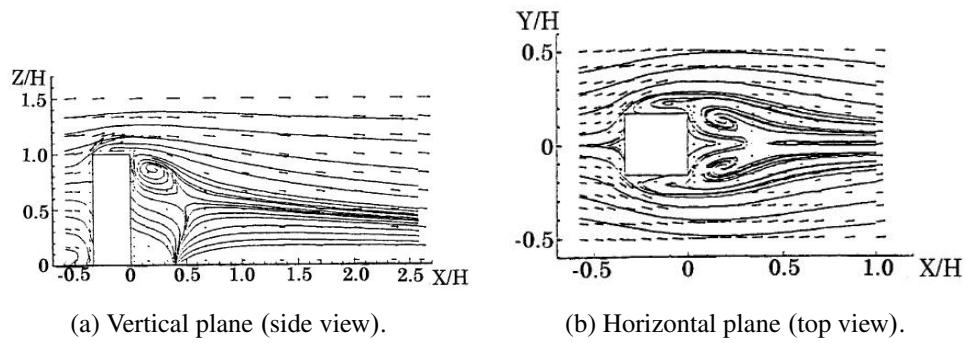


FIGURE 2.3 Contour of streamlines for high-rise building [38].

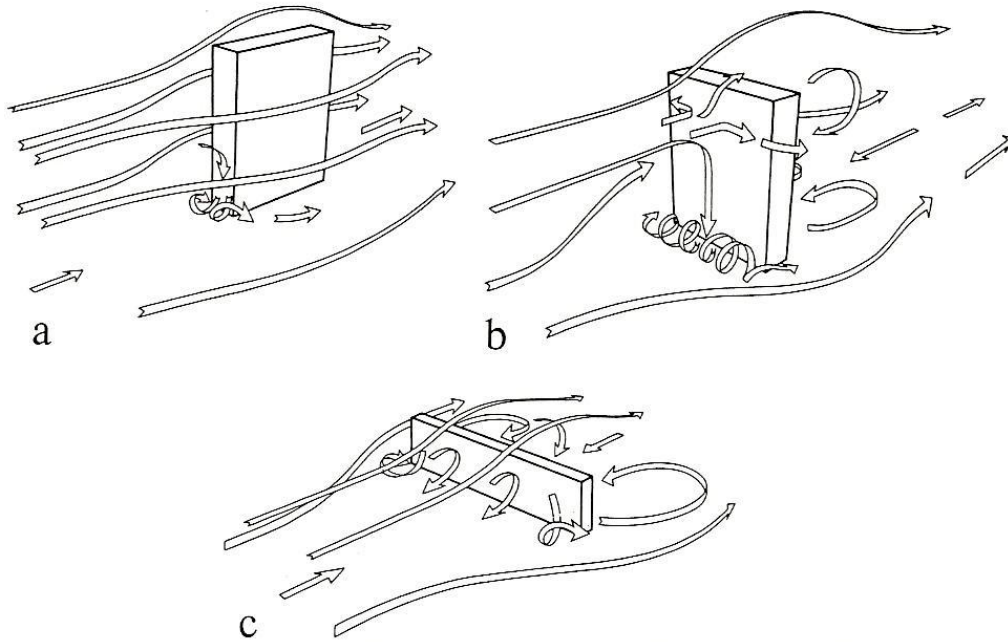


FIGURE 2.4 Types of airflow dependent on length to height ratio [35]

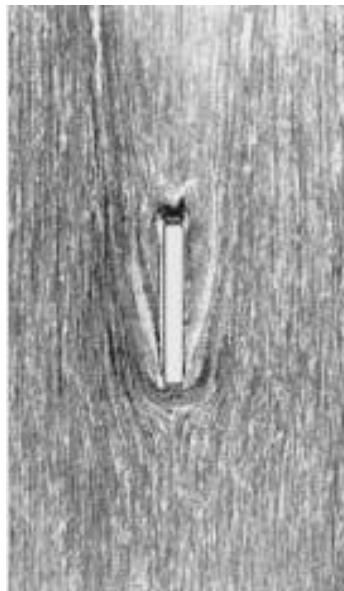


FIGURE 2.5 Flow visualisation of wind flow around a single narrow building [39]

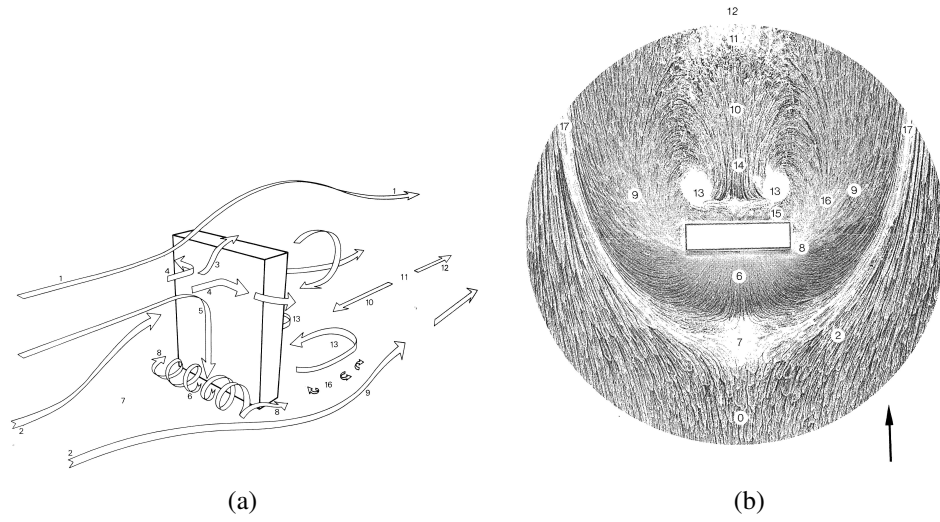


FIGURE 2.6 High wind speeds around tall building with flow visualisation [39]

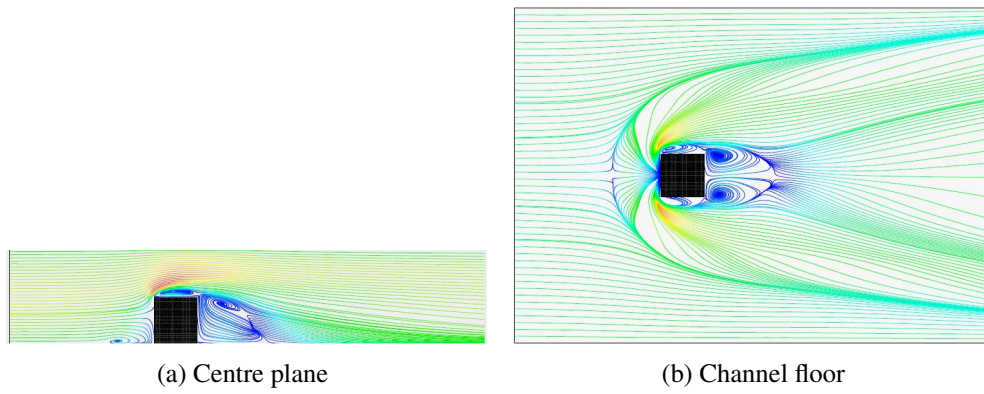


FIGURE 2.7 Streamlines of the mean flow by LES [8]

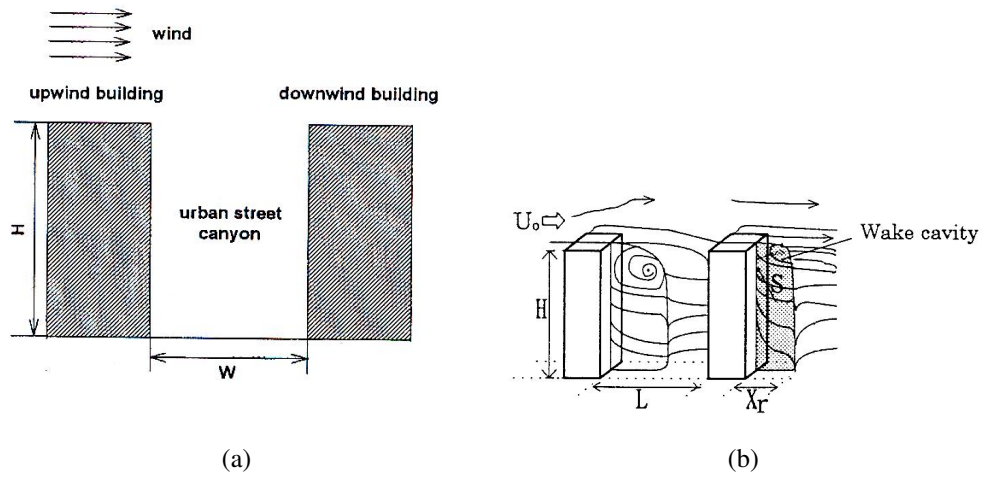


FIGURE 2.8 Schematic orientation of twin buildings [8, 14]

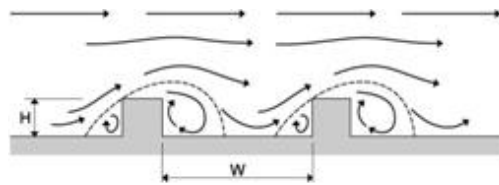


FIGURE 2.9 Isolated roughness flow [40]

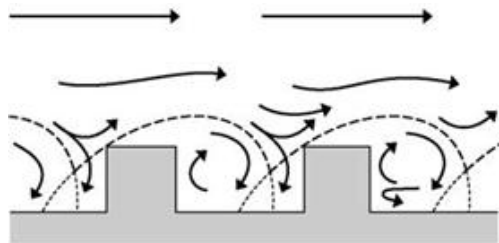


FIGURE 2.10 General flow field [40]



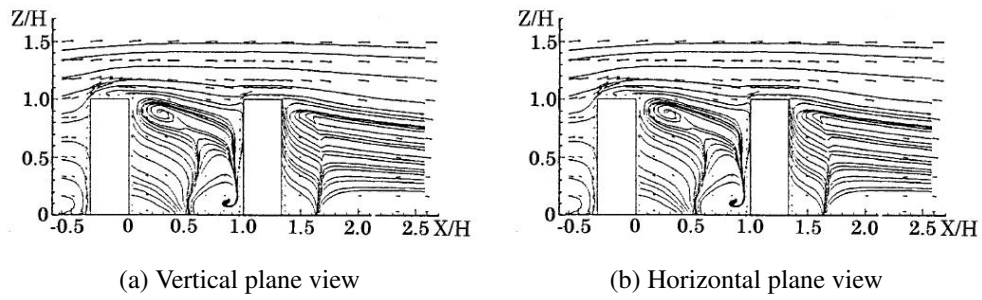


FIGURE 2.11 Wake interference flow when  $W/H = 1$  [14,38]

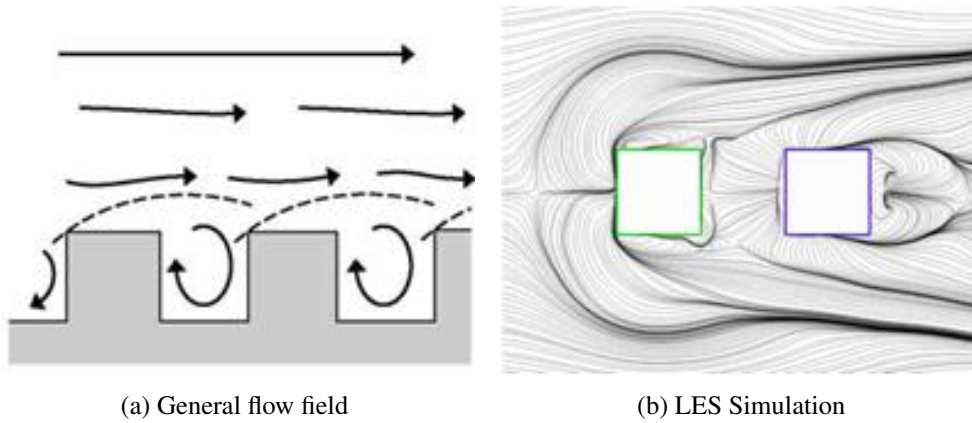


FIGURE 2.12 Skimming flow [11,40]

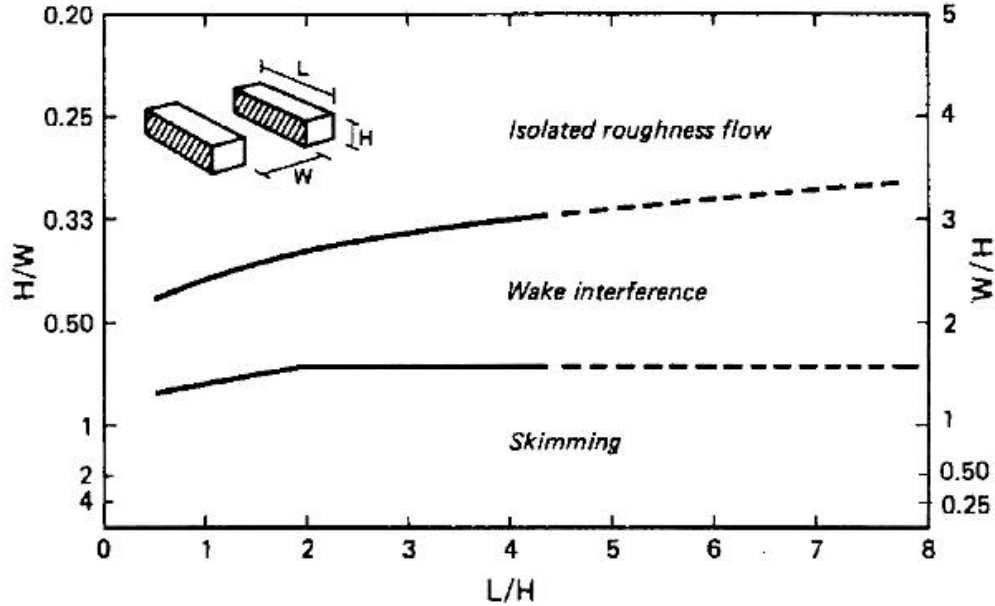


FIGURE 2.13 Threshold aspect ratio of  $(H/W)$  and  $(L/W)$  [16]

Modelled urban canyon geometries and anticipated flow regimes

$L/H$ ratios	Width of canyon (m)	$H/W$ ratios	Type of flow regime anticipated
Cubic canyon 1 (20 m/20 m)	20	1.0	skimming flow
	27	0.74	transition to wake interference
	40	0.5	wake interference
	50	0.4	transition to isolated roughness
	60	0.33	isolated roughness
Short canyon 3 (60 m/20 m)	20	1.0	skimming flow
	40	0.5	wake interference
	60	0.33	transition to isolated roughness
	80	0.25	isolated roughness
Medium-length canyon 5 (100 m/20 m)	20	1.0	skimming flow
	34	0.6	transition to isolated roughness
	40	0.5	wake interference
	60	0.33	wake interference
	100	0.2	isolated roughness
Long canyon 7 (140 m/20 m)	140	0.14	isolated roughness
	20	1.0	skimming
	40	0.5	wake interference
	74	0.27	transition to isolated roughness
	100	0.2	isolated roughness
	140	0.14	isolated roughness

FIGURE 2.14 Characteristics canyon geometries to produce three different flow regimes [41]

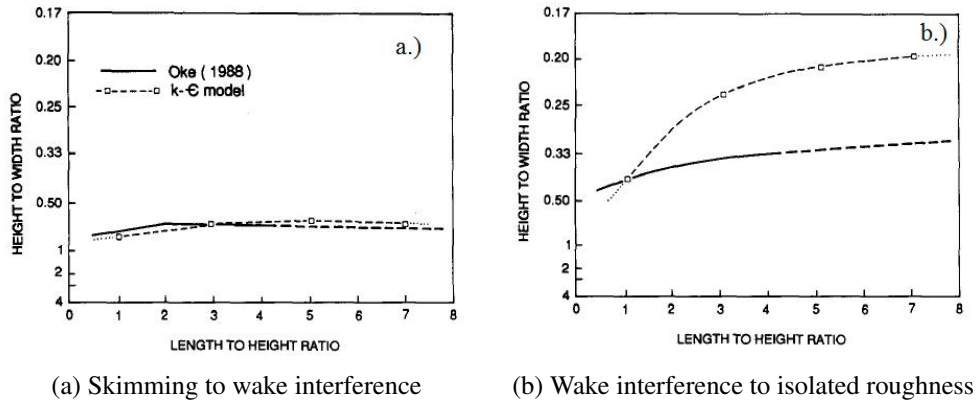


FIGURE 2.15 Threshold values for transition flow patterns [41]

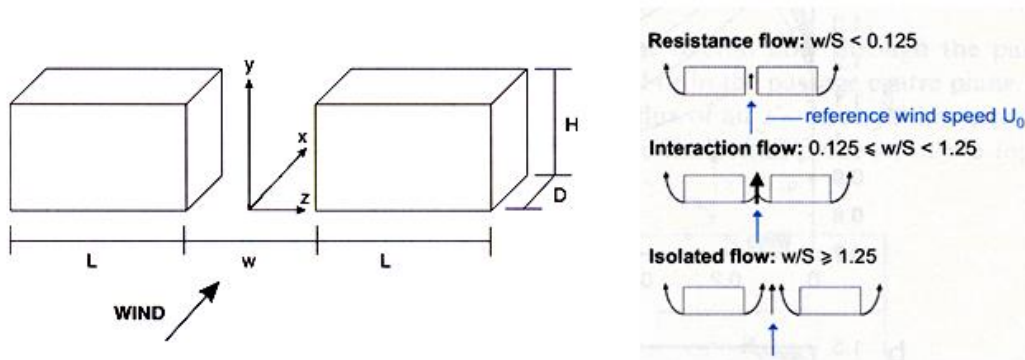


FIGURE 2.16 Buildings configuration of flow between parallel buildings [18]

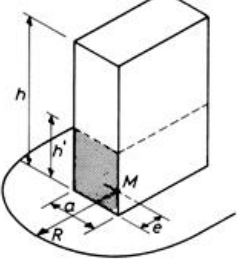
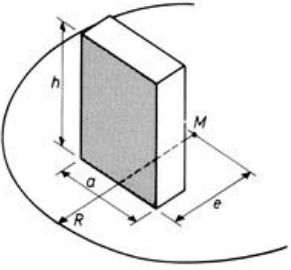
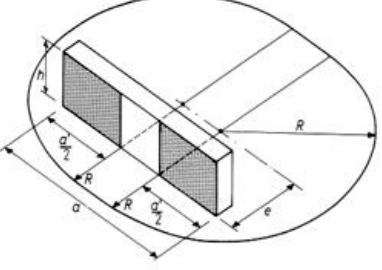
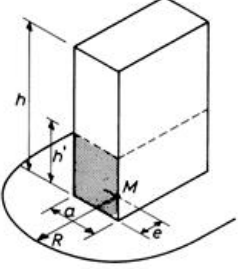
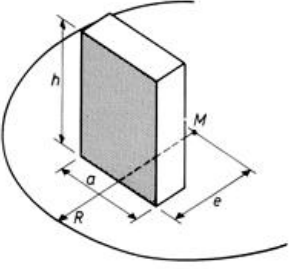
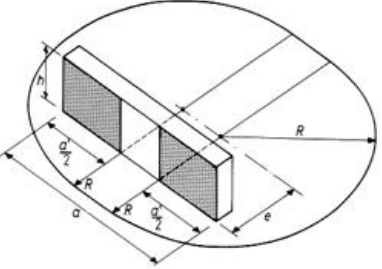
$h > 1.25a$ Tall building	$0.33a < h < 1.25a$ Transitional building	$a > 3h$ Long building
		
$R = 1.6\sqrt{ah'} = 1.8a$  $h' = 1.25a$ 	$R = 1.6\sqrt{ah}$ 	$R = 1.6\sqrt{ah} = 2.8h$  $a' = 3h$ 

FIGURE 2.17 Influence areas of three different building types [35]

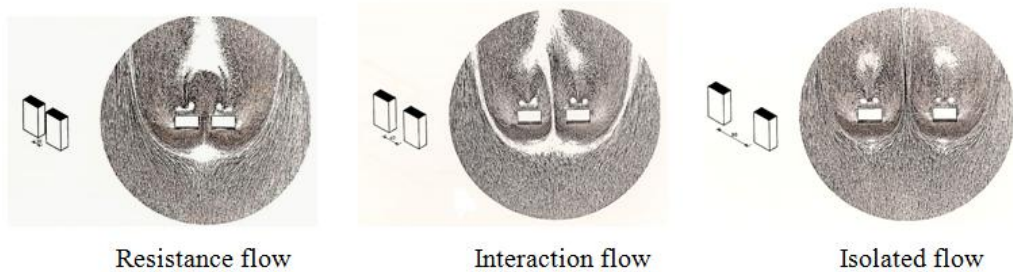


FIGURE 2.18 Flow visualisation for three different flow patterns [42]

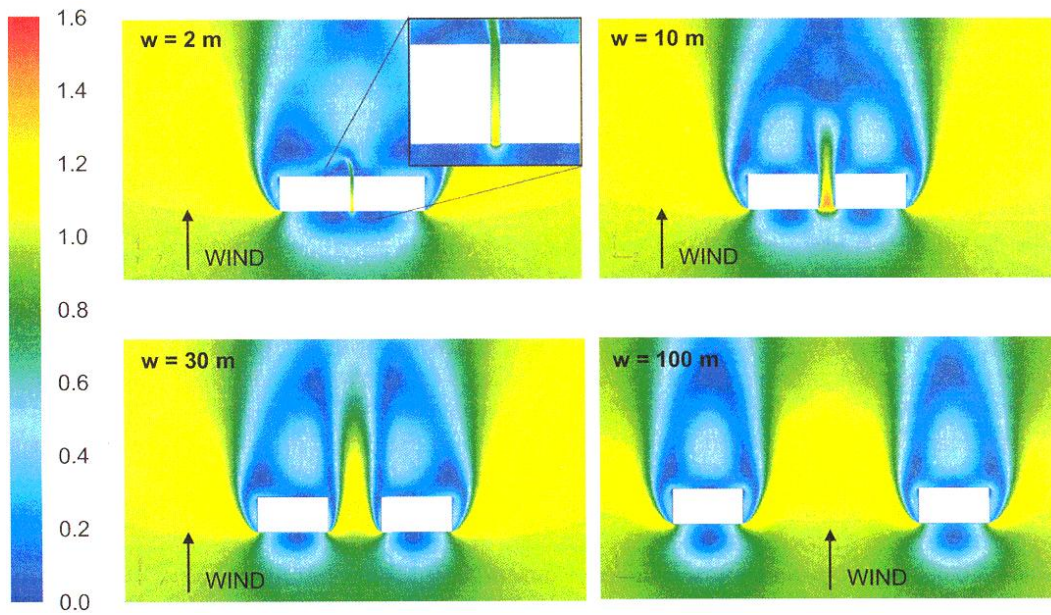


FIGURE 2.19 CFD contour of a ratio local mean velocity to reference mean velocity without building at the same point of interest at different passage widths [18]

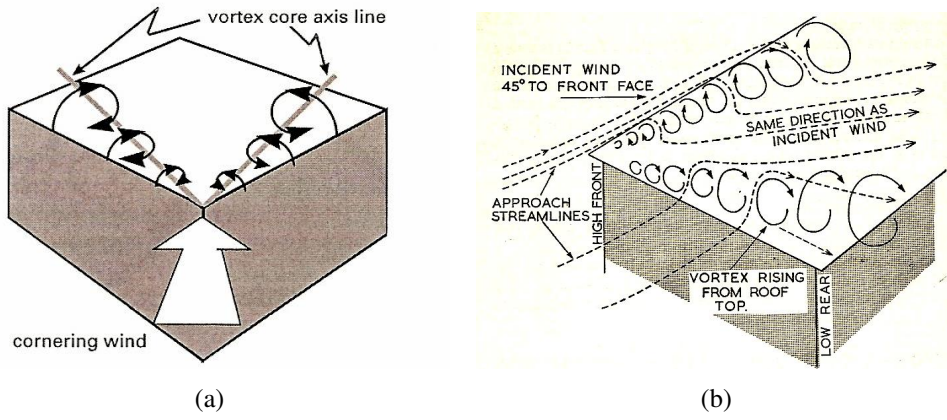


FIGURE 2.20 Double conical vortex [43,44]

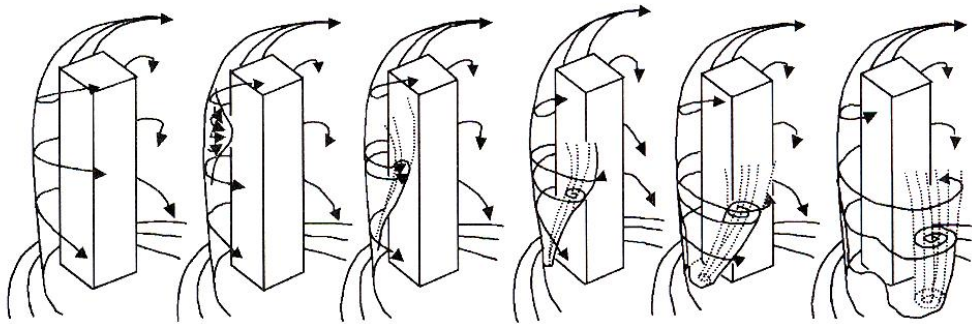


FIGURE 2.21 Inverted conical vortex formation procedure near the corner of tall building [26]

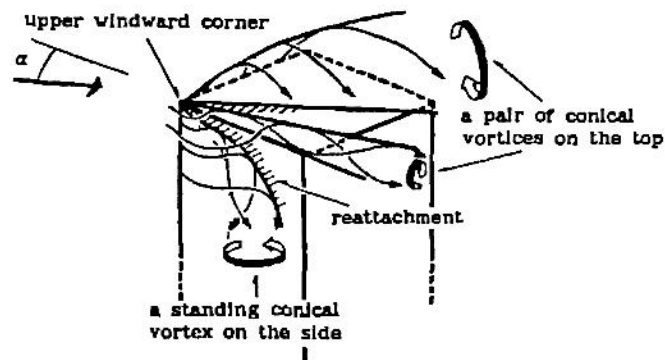


FIGURE 2.22 Flow over building at glancing angle [26]



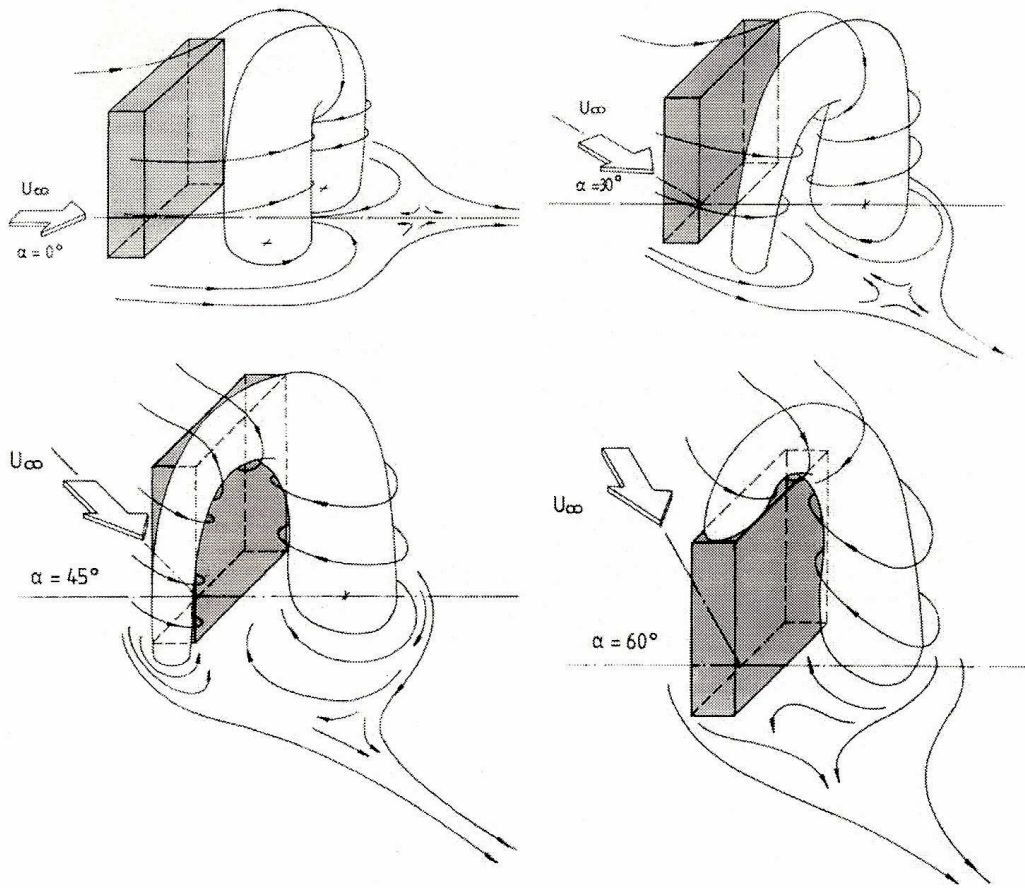


FIGURE 2.23 Standing vortex system at different angle of attacks [33]





# Chapter 3

## Aerofoil section and nonlinear gust response

In general, aerodynamic issues are very important for both manned and unmanned aircraft. Aerodynamics investigation and development for both unmanned and manned aircraft rely on stability and control. Most of the studies into low Reynolds number aerodynamics is a key feature for many, but not all, small size UAVs and use wind tunnels and simulation to conduct the aerodynamic studies. In this chapter, general details of basic research and studies related to an aerofoil in a wind tunnel test and nonlinear response due to gust generation will be discussed briefly.

### 3.1 Stall characteristic

For aeroplanes to have a capability to fly, the wings have to generate enough lift force induced by the wings themselves and a combination of wing lifting devices such as flaps and slats, etc. The lift force is a function of air density, the wing area, velocity and lift coefficient. Therefore, the maximum lift force that can be generated, if air density and velocity are kept constant, is solely dependent on wing surface area and the lift coefficient.

The maximum lift is defined as the greatest possible value of the lift force that can be produced by the wing so that when angle of attack is further increased it provides a negative or zero increase of lift. Hoerner and Borst [45] pointed out parameters that influence the value of maximum lift as:

1. Aerofoil section shape
2. Operating conditions such as Mach number and Reynolds number
3. Wing planform and twist

4. Supplementary devices such as flaps and slats, etc
5. Influence of fuselage and propulsion system
6. Types of application; that is, fixed wings, helicopter rotors, etc

Maximum lift is limited by stall behaviour which occurs when the boundary layer breaks away from the wing upper surface. Consequently, wing stall characteristics will be explained as part of the literature review in the next section.

## 3.2 Stall behaviour

Wing stall can happen when the aeroplane is hit by a gust or sideslip motion causing the flow to break down resulting in the wing losing lift. The stall characteristics produced by such conditions are dependent on the geometry of the wing section, thickness ratio and a range of Reynolds number that the aeroplane operates in. In this section, 3 different types of stall will be explained including some examples for each stall behaviour.

1. Leading edge stall

The leading edge stall always produces a sharp peak in the vicinity of  $C_{Lmax}$  with a rapid drop in  $C_L$  above the stall. In this particular stall, short bubble type appeared on the wing surface according to Polhamus [46] and Hoerner and Borst [45].

### Short separation bubble

As the angle of attack increases to a particular point, say  $6^\circ$ , a flow tends to separate close to the leading edge and reattaches to the surface and forms a small separation bubble on the wing surface. As the angle of attack increases, the lift continues to increase gradually and a turbulent separation moves forwards. When the angle of attack reaches a critical position where the air flow inside the bubble is too strained, the separation bubble from the near leading edge location bursts without any warning causing an abrupt loss of lift as show in Figure 3.1 and Figure 3.2. This type of stall is classified as an undesirable stall. Another form that causes the bubble to burst is a sufficient increase in angle of attack or decrease in Reynolds number which leads to the turbulent shear layer not attaching on the airfoil surface resulting in abrupt leading edge stall. After the short bubble bursts, the turbulent shear layer may attach as a long separation bubble or may not attach on the aerofoil surface depending on the local pressure gradient and Reynolds number. This

particular type of stall is generally found on a moderate to thick aerofoil sections,  $0.09 < t/c < 0.15$ . At high Reynolds numbers benefits increasing in leading edge radius due to flow separation. As leading edge radius increases, adverse pressure gradients decrease and reduce in turbulent boundary layer growth. This results in increases in  $C_{Lmax}$ .

## 2. Trailing edge stall

Trailing edge stall is a stall mechanism commonly found, in particular with a large aerofoil thickness ratio,  $t/c$ . This type of stall is normally associated with an aerofoil of high thickness ratio about 15% chord or more [47]. A point of separation is originated from the trailing edge of the aerofoil resulting in a progressive thickening of a turbulent boundary layer separation and a relatively gradual movement of the separation forwards to the leading edge as the angle of attack increases. Near the stall condition, the lift coefficient curve is progressively rounded near the maximum value of the lift coefficient. The maximum lift is obtained when the turbulent separation from the trailing edge is at a location of about half a chord length. An interesting point noted by Leishman [47] is that for a higher thickness ratio the maximum lift is reduced rapidly with the separation taking place at an extensively lower angle of attack.

## 3. Thin aerofoil stall

The stall in this classification is characterised by all sharp leading edge aerofoils and also encountered on a rounded leading edge with small thickness ratio, i.e.  $t/c < 9\%$  [48].

### **Long separation bubble**

A physical mechanism is that on the lower side of the aerofoil, a strong negative pressure gradient is generated between the leading edge and a stagnation point. The flow induced from these two points is assumed to be laminar flow causing the flow to separate suddenly from the leading edge as the angle of attack is above  $0^\circ$ . Subsequently, the reattachment point is further downstream leaving a long separation bubble on the wing surface. As the angle of attack increases, the reattachment moves aft and the stall gradually develops. When the reattachment point reaches the trailing edge the stall process completes. Another point which is unique for this type of stall is a discontinuity on the lift coefficient plot against angle of attack. The discontinuity point indicates a point where the reattachment is taking place.

### 3.3 Laminar separation bubble

A laminar separation bubble (see Figure 3.4) is an enclosed volume of separation and reattachment on the aerofoil surface. A separation bubble forms due to an adverse pressure gradient of sufficient magnitude to cause the flow to separate. The laminar separation bubble forms when a laminar boundary layer separates and is roughly divided into 2 different regions. The first region is contained in between a streamline  $ST'R$  and a solid surface, forming a bubble (see Figure 3.4). The second region is bounded in between the edge of the bubble and the outer edge of the boundary layer  $S''T''R''$  forming a viscous free shear layer which is highly unstable, and can undergo transition to turbulence; in this case the shear layer may reattach on the wing surface and will then form a turbulent boundary layer. The flow phenomenon is called a laminar separation bubble which grows larger and larger to degrade an overall performance of an aerofoil with decreasing Reynolds number.

Within the bubble, just downstream of the separation point denoting by "S" the velocity of the air inside the bubble is almost zero. Therefore, this region is called the "Dead-air region". Inside the bubble just upstream from the reattachment point, a circulation area of air is presented called a "reverse-flow vortex" region. The separation bubble is classified into 2 different sizes: short and long bubbles. For a short bubble, the length of the bubble is of the order  $10^2$  to  $10^3$  of a displacement thickness at the separation point or approximately 1% of the aerofoil chord, whereas, the long bubble length could be up to the order  $10^4$  of a displacement thickness at the separation point (Owen and Klanfer [49]). A remarkable distinction between the short and long bubbles is proposed by Tani [50] suggesting that the difference can be indicated by velocity and pressure distributions. The short bubble has a small effect on the external potential flow with the pressure distribution approximately as an inviscid distribution profile. In contrast, the long bubble influences the pressure distribution around an aerofoil such that the pressure distribution differs from the inviscid distribution and hence the velocity peak reduces. A comparison of the velocity distribution of the short and long bubble is shown in Figure 3.5. According to Alam and Sandham [51], thin aerofoils produce the short laminar separation bubble at moderate angle of attack and finally it bursts to form either a long bubble with reattachment far downstream or not reattach at all.

### 3.4 Lift Characteristics for low speed aerofoils

The purpose of this section is to describe some details regarding to aerofoil characteristics such as zero lift angle of attack and lift curve. The shape of aerofoils are

generated by specifying different mean camber line and thickness. These results in variation in aerodynamic properties.

1. **Angle of zero lift.**

Camber determines the angle of zero lift. According to Anderson [52], a symmetric aerofoil provides a zero-lift angle at  $\alpha_{L=0} = 0^\circ$  whereas when camber is added i.e. more highly cambered aerofoil, the absolute magnitude of zero-lift angle of attack is larger. In addition, camber is introduced to an aerofoil in order to generate more lift and its effect leads to a reduced angle where the aerofoil starts stalling. A disadvantage of adding too much camber is that air flow over the upper surface does not stay attached along the wing surface at moderate angle of attack. This influences the flow to separate at an early stage causing the wing to stall at a lower angle of attack than an uncambered section.

2. **Lift curve slope.**

For an aerofoil thickness ratio of about 6%–10% especially for NACA series, a value of the lift curve slope is close to the theoretical value of thin wing section which is  $2\pi$ . Abbott and von Doenhoff [53] summarise that in general as the viscous effect is negligible, the lift curve slope should increase with an increase of the aerofoil thickness ratio but does not exceed the theoretical value of  $2\pi$ .

### 3.5 Nonlinear gust response

A phenomenon of dynamic stall due to rapid incidence changes or unsteady aerofoil motions has long been known to be a key feature that limits helicopter performance. The problem of dynamic stall normally happens on the helicopter rotor at fast forward speed or sometimes during manoeuvres with high torsional loads or rotor vibration. Stall on helicopters is different to stall occurring on a fixed-wing aircraft because stall on a helicopter rotor occurs at relatively high airspeeds and close to a point where an air flow is able to remain attached to the rotor surface. Whereas for a fixed-wing aircraft, stall happens at relatively lower speed and angle of attack. By a definition given by McCrosky [54] dynamic stall occurs on an aerofoil or any lifting surface when it is subjected under motion which is time-dependent under pitching, plunging or even vertical unsteady motion where the effective angle of attack is greater than the static stall angle. Generally, dynamic stall is a delay of the flow separation at a higher angle of attack than occurring under static conditions. A characteristic of the dynamic stall is governed by the shedding of a vortex near the aerofoil's leading edge region. This vortex

disturbance creates an additional lift on the aerofoil.

A survey of literature, for example by Carr and Chandrasekhara [55] has found that a process of dynamic stall is dependent on an aerofoil's geometry, aerofoil's boundary layer condition, Mach number and unsteadiness pitch rate. A similar experiment was conducted by Lawrence et al [56] in 1977 to investigate effects of dynamic stall on an oscillating aerofoil in pitch. Their experiments included a wide range of parameters such as reduced frequencies and the effect of mean angle of attack at constant pitch rate. Simulated results of aerofoils oscillating at large angles of attack by Akbari and Price [57] also provide a clear understanding of the vortex system/wake created at the leading edge and shed downstream over the upper surface of the aerofoil during an oscillation motion. Another recent literature by Singh et al investigated the control of a helicopter blade stall using air-jet vortex generation. In this chapter some useful techniques based on literatures will be reproduced to observe dynamic stall due to an unsteady gust.

### 3.5.1 Flow patterns of dynamic stall

Behaviours of unsteady motion and dynamic flow separation have been mainly investigated in wind tunnel experiments of oscillating aerofoils. As angle of attack increased to a moderate angle, the flow over the upper surface still remains attached. With increasing angle of attack, a high adverse pressure gradient, which starts building up near the leading edge under dynamic conditions, results in the flow beginning to separate at that location. Not long after the vortex is formed, this disturbance begins to convect along the upper surface of the aerofoil. As the angle of attack increases more and more, the rotating vortex progresses towards the trailing edge. Meanwhile at this high angle of attack, the flow on the lower surface begins to roll up at the trailing edge and interact with the vortex on the upper surface as shown in Figure 3.6. The various stages of dynamic stall can be seen on the lift coefficient plots against angle of attack as shown in Figure 3.7. Step 1 represents an aerofoil exceeding static stall angle where the flow starts to separate. Initially, the aerofoil passes the static stall angle without any detectable change in the flow over the upper aerofoil surface. This stage also indicates a delay in the flow separation produced by the upward motion which Figure 3.6a.) and b.) represent. Figure 3.6c.) and d.) represent stage 2 in Figure 3.7. The circulating vortex on the upper surface convects over the length of the upper aerofoil, inducing additional lift. Stage 3 is a critical stage as the aerofoil reaches the highest angle of attack before the downstroke begins. At this stage, stall occurs at the same time as the leading edge vortex leaves the upper surface at the trailing edge and passes into the wake region, see Figure 3.6(f.). After the vortex convects downstream, the flow on the upper surface is fully separated causing a sudden loss of lift and a nose-down pitching moment.

Then stage 4 begins with the flow reattachment taking place on the upper surface once again. Full reattachment may not be obtained until the aerofoil is well below a static stall angle as seen in stage 5. These five stages are called the hysteresis loop.

### 3.5.2 Parametric studies on dynamic stall

Extensive studies of dynamic stall mostly use oscillating  $2 - D$  aerofoils in wind tunnels. This is to simulate a periodic motion of time-dependent angle of attack variations in pitch which are problems on helicopter rotors during forward flight. A few examples of variations in parameters such as oscillation amplitude, mean angle of attack and reduced frequency will be shown. By changing one parameter and keeping others constant helps to provide a better understanding in terms of the morphology of dynamic stall. The two examples below studied the effects of dynamic stall on a NACA 0012 aerofoil section oscillating in pitch. The results taken from Lawrence et al [56] are displayed in Figure 3.8 based on a NACA 0012 section with a 1.22 m chord oscillated in pitch by a crank. They found that dynamic stall behaviour is sensitive to a small change in parameters as follows:

#### Effect of Reduced frequency, $k = \frac{\omega c}{2U}$

The results from Lawrence et al [56] and Leishman [47] have shown that as reduced frequency increases, a development of the dynamic stall hysteresis delays separation and gives a higher dynamic stall angle. Lawrence et al described the sequence of these events in terms of reduced frequency as; at lower frequency,  $k = 0.02 - 0.05$ , a vortex formed and moved towards the trailing edge, and was shed into the wake region before the aerofoil reached a maximum incidence. As the frequency increased, a delay in stall inception leads to the vortex interactions at larger incidence leading to a development of flow separation at higher angles of attack. Leishman also described in the same content as Lawrence's. He stated that the reduced frequency is powerful on lift response due to unsteady motion. The vortex shedding is delayed with increasing reduced frequency until the vortex reaches the maximum angle of attack. Increasing reduced frequency alleviates the leading edge pressure gradients for a given value of lift and, hence, it delays the onset of flow separation at high angles of attack. Dynamic stall is more difficult to occur at low angles of attack at high values of reduced frequency as seen in Figure 3.9(c). Each case is plotted with the static lift coefficient to compare with the results under dynamic conditions.

#### Effect of oscillation amplitude

Based on experiments by Lawrence et al [56], they mentioned that an amplitude

of oscillation is another predominant parameter accounting for the effect of unsteady aerodynamic motion. Figure 3.10 is the results of a NACA 0012 aerofoil oscillating at a particular angle of attack by varying in oscillation amplitude at the same reduced frequency,  $k\check{c} = 0.15$ . It can be seen clearly that the stall behaviour is dependent on oscillation amplitude. A key feature involved in these results is timing and strength of dynamic stall vortex. At the smallest amplitude,  $\Delta\alpha_m = 6^\circ$  the vortex forming at the aerofoil leading edge is always shed and convected downstream at the largest angle of attack. This early vortex leads to a mild stall due to moderate vortex strength. On the other hand, when  $\Delta\alpha_m$  gets larger and larger the vortex seems to shed near the maximum angle of attack before stall occurs, delaying the flow separation and finally causing deep dynamic stall behaviour, in Figure 3.10(b.) and (c.)

### **Effect of mean angle variation**

Figure 3.11 shows the effect of increasing the mean angle of attack while keeping oscillation amplitude and reduced frequency constant. The results indicate flow patterns from nominally attached flow through light dynamic stall and finally deep dynamic stall for the highest mean angle of attack. At low mean angle of attack, some small flow separation on the aerofoil surface occurs. Most of the time during the oscillation, the flow is mainly attached and tends to separate with a delay in the onset of stall at a higher angle of attack. On the down stroke motion, the flow reattaches as the angle of attack is decreased, but the angle of attack where the flow reattachment happens is well below the static stall angle as seen in Figure 3.11(a.). At a higher angle of attack, which is high enough to manipulate a strong vortex near the leading edge of the aerofoil causing the light dynamic stall, the hysteresis loop gets larger and the nose-down pitching moment is more significant than in the small mean angle of attack, Figure 3.11(b.). At the highest mean angle of attack,  $10.3^\circ$ , the flow separates and stalls at a very high angle of attack causing a deep dynamic stall characteristic which is represented by a large hysteresis loop. A combination of the leading edge vortex shedding and flow separation at high angle of attack results in a very large counter-clockwise hysteresis loop. The flow reattachment is delayed to a relative low angle of attack during the down stroke motion. It requires a long period of time for the flow to return to its original condition which allows the flow to reattach on the aerofoil surface.

### **Effect of Reynolds number/Mach number**

Reynolds number has the least dramatic effect on the unsteady oscillating aerofoil because it seems to influence only the hysteresis loop in terms of a delay in reattachment angle. In Figure 3.12(a.), the plots represent the effect of Reynolds



number based on Lawrence's experiment [56]. It can be seen that stall overshoot is minimal for both Reynolds numbers and reattachment angle in the case of a Reynolds number of  $1.5 \times 10^6$  is slightly lower than in the higher Reynolds number case. At low Mach number, Reynolds number variations influence types of stall and maximum lift coefficient. Increasing Reynolds number leads to an increase of the inertial effects in the air flow, which will reduce boundary layer thickness and delay the onset of flow separation to a higher value of angle of attack and lift coefficient. When Mach number is over 0.3 which is above the incompressible range, the effect of Reynolds number on maximum lift and stall characteristics can be significant because the effect of Reynolds number is somewhat dependent on Mach number.

$$Ma = \left( \frac{\mu}{\rho a} \right) \frac{Re}{c} \quad (3.1)$$

where  $c$  is an aerofoil chord length.

Whereas the experiment referenced by Leishman [47] was focused on the effect of Mach number, he explained that the effect of Mach number is found in the dynamic stall region where the dynamic stall angle and amount of hysteresis increased with increasing Mach number, as seen in Figure 3.12. If Mach number is high enough to produce a shock wave which it involved in the dynamic stall onset, the shock wave will introduce a more complex behaviour during the separation and reattachment process.

### 3.6 Aerofoil shape on Dynamic stall

Experiments carried out by McCrosky et al [58] are concluded with results of three different aerofoil shapes; the NACA 0012, the HH-02 aerofoil which is used on the Apache and the SC1095 aerofoil, which is used on the Blackhawk helicopter. The latter two aerofoils are cambered with 9.5%  $t/c$  ratio. The experiments were conducted at a free-stream Mach number of 0.3. All three aerofoils demonstrate dramatic increases in lift over the static stall value although the stall occurs at approximately the same angle of attack. However, in the case of the HH-02 and the SC1095 aerofoils the flow attachment seems to maintain to a slightly higher angle than in the case of the NACA 0012 before it breaks down with a correspondingly larger value of  $C_N$ . Hysteresis loops for all three aerofoil shapes are similar with a secondary vortex shedding near the maximum angle of attack. Both the HH-02 and the NACA0012 aerofoils exhibit a gradual pitching moment break at the onset of dynamic stall (not shown here) in comparison to the SC1095, which has an

abrupt pitching moment break. McCrosky suggested that a gradual break in pitching moment happens due to some trailing edge flow separation occurring on the NACA 0012 and the HH-02 prior to the onset of leading edge separation and dynamic stall. However, the NACA 0012 has the least nose-down pitching moment compared to the HH-02 and the SC1095 aerofoils due to it having a smaller peak value of pitching moment.

### 3.7 Three-dimensional effect on dynamic stall

Experiments of unsteady lift are mostly carried out with 2-dimensional aerofoils in oscillation motion. Lorber [59], Pizialli [60] and Lorber et al [61] used a semi-span cantilevered wing oscillating through various angles of attack in and out of stall. The experimental results shown here are based on those of Lorber et al with a swept wing tested at a Mach number of 0.2. Miniature pressure transducers were placed at five locations along the span-wise direction towards the wing tip. It can be seen that for an angle of attack below the static stall angle, elliptical hysteresis loops are formed with no evidence of unusual behaviour such as loop crossing as particularly appears on a 2-D aerofoil case. The untwisted swept wing, stall initiates at the root section of the swept wing and moves outboard towards the wing tip causing a gradual reduction in lift and lift curve slope as seen in Figure 3.14. Dynamic stall characteristics for 3-dimensional wings are similar to the 2-dimensional case except the crossing hysteresis loop did not appear in the 3-dimensional case. It is interesting to note that when moving towards the wing tip the lift overshoot is reduced and a fluctuation of the hysteresis loop is vanished. Lorber believed this is a result from an element of a tip vortex creating a steady induced lift which eliminates the fluctuation during the oscillation period. He finally concluded the effect of the 3-dimensional wing as near the root of the wing the lift overshoot characteristic can still be seen but the results are less transient suggesting that leading edge vortex shedding does not influence it much. On the other hand, it appears that the tip vortex itself influences the flow field of the 3-dimensional wing. Furthermore, if the wing aspect ratio is relatively high then the oscillating finite wing can be considered as a 2-dimensional case.

### 3.8 Present study

In the past three decades up to now, various technical methods to produce an oscillating flow in a wind tunnel have been introduced, for example [55–57, 62–68]. Examples of these are to study the effect of aeroelastic models excited by gust loads, a nonlinear aeroelastic response to a wing model from a single and double

harmonic gust excitations, and nonlinear flutter and stall response of a helicopter blade. A purpose of the study was to investigate the behaviour of a three dimensional wing without vortex generators under static and dynamic conditions. From the literature review, the experiments available in the literature seem to test at Reynolds numbers of the order of  $10^6$ . Also from these example studies, the wings were oscillated in pitch by model drive mechanisms in a fixed wind direction.

In this study with a representation of a small UAV with a wing span of the order of a metre, the nature of the experiments restricted the investigation flow regimes to Reynolds numbers of the order of  $10^5$ . To differentiate from the literature, a three dimensional wing will be fixed at a given mean angle of attack relative to an oncoming flow. The oncoming flow will be sinusoidally oscillated in pitch by an array of oscillating flaps to produce a sinusoidal gust. The mean angle of attack, oscillating amplitude, and oscillation frequency will be varied to observe the wing behaviour.

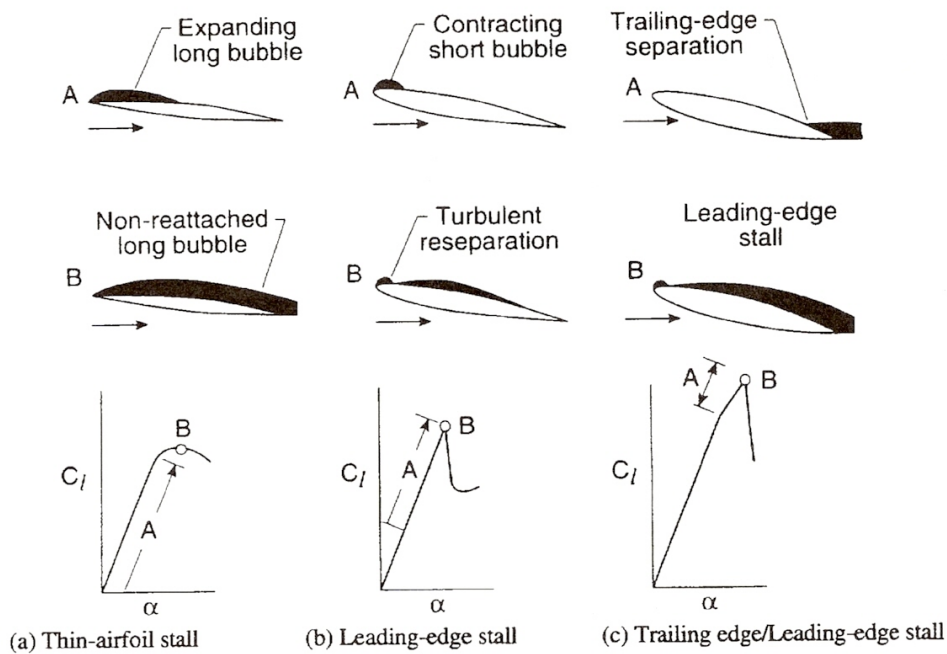


FIGURE 3.1 Types of stall [46].

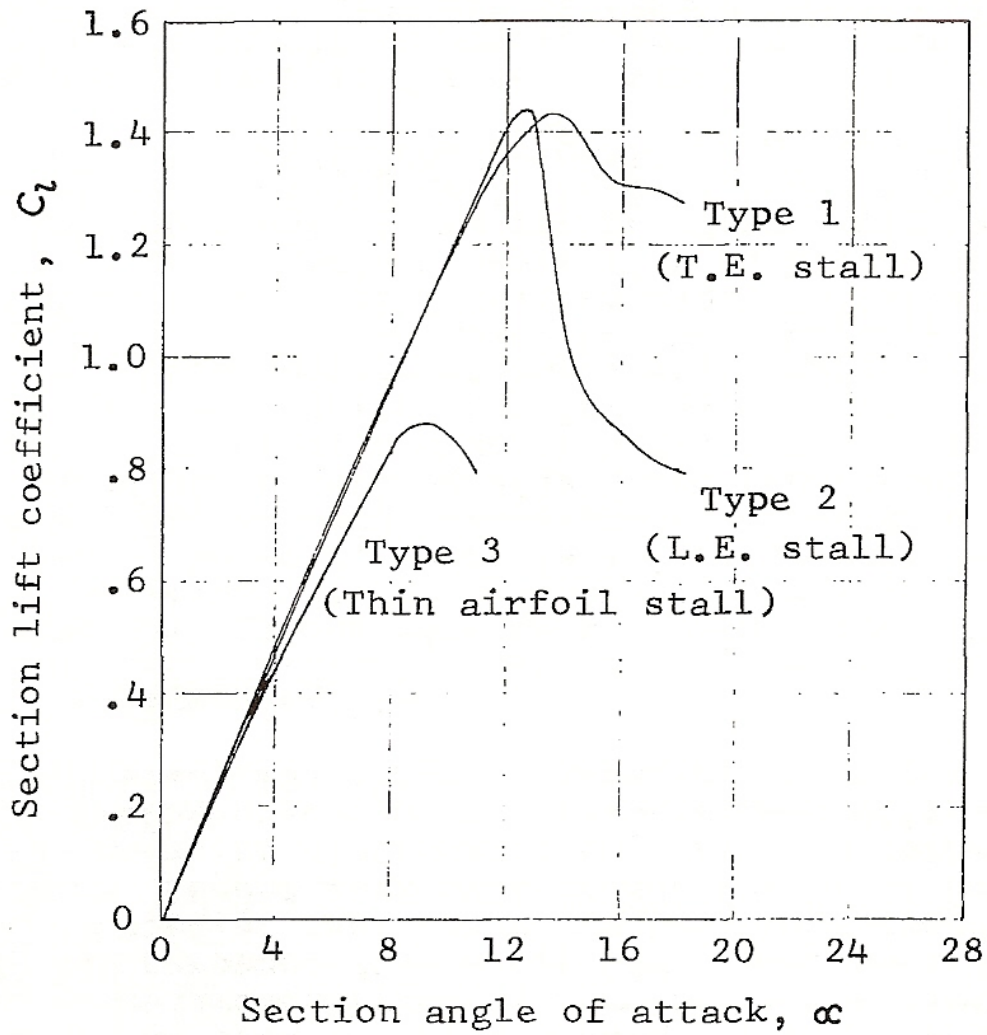
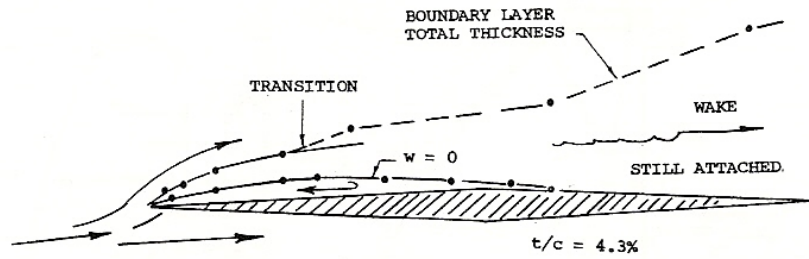
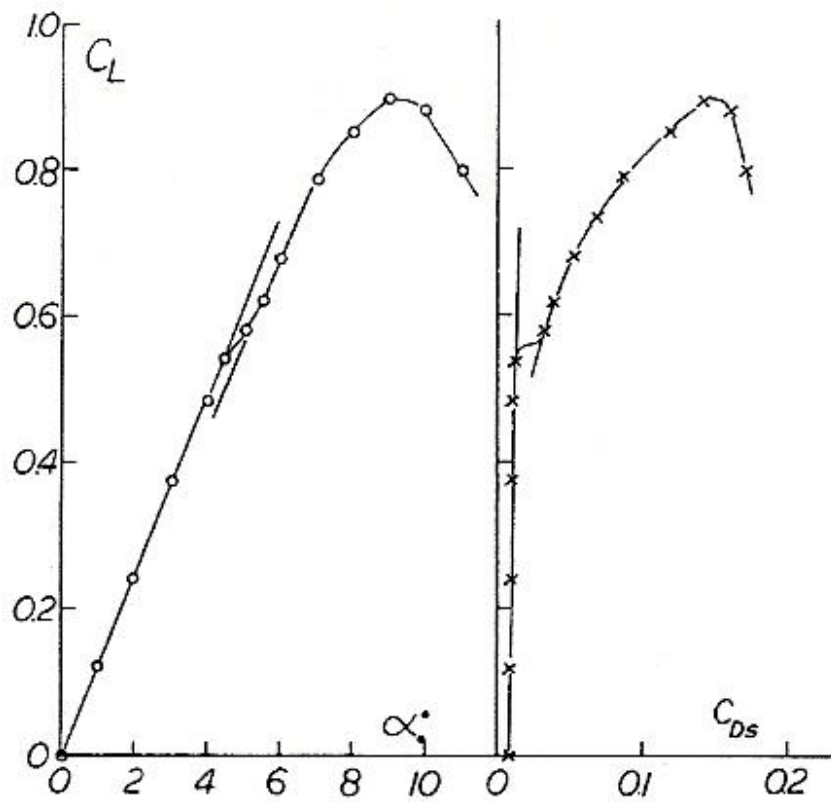


FIGURE 3.2 Types of stall comparison [48].



(a) Thin aerofoil stall mechanism



(b) Lift, drag and separation bubble characteristics

FIGURE 3.3 Thin aerofoil stall [45]

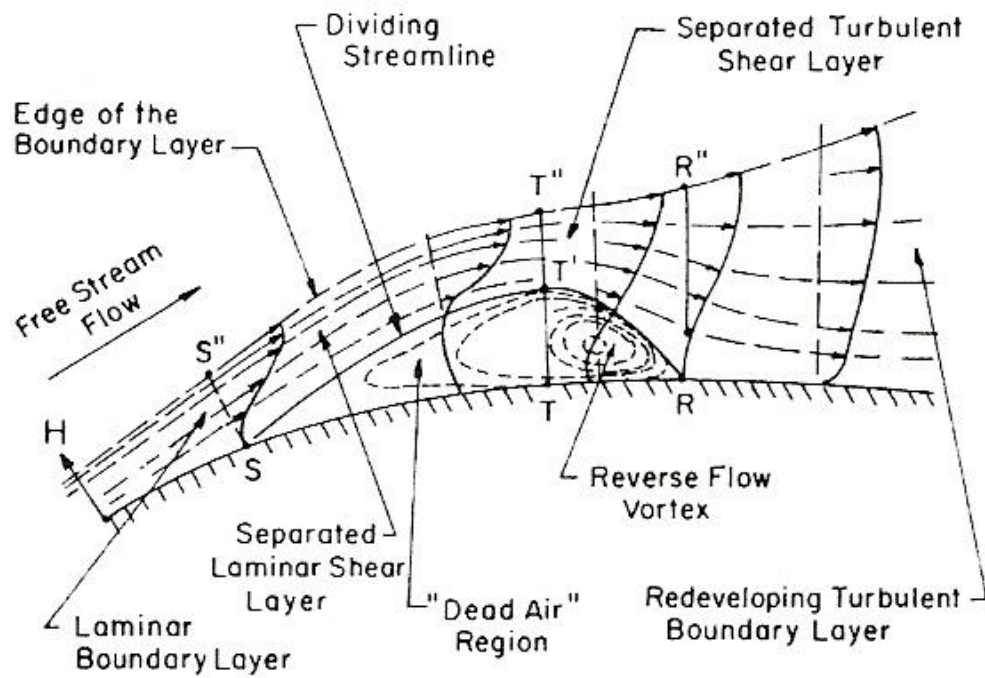
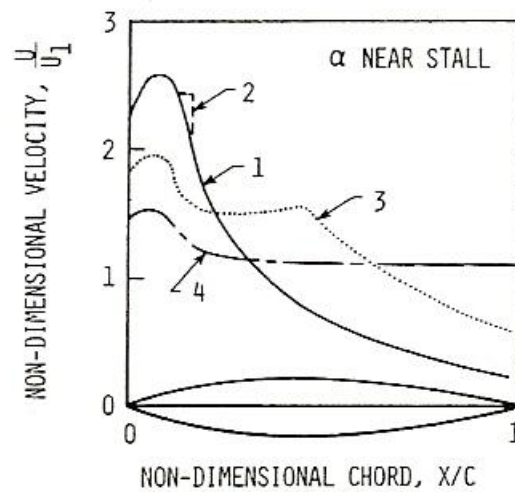


FIGURE 3.4 Laminar separation pattern [69, 70]



- 1 - HIGH  $R_c$ : NO SEPARATION, VELOCITY DISTRIBUTION APPROXIMATES INVISCID DISTRIBUTION
- 2 - MEDIUM  $R_c$ : SHORT SEPARATION BUBBLE, DISTRIBUTION APPROXIMATES INVISCID OUTSIDE BUBBLE REGION
- 3 - LOW  $R_c$ : LONG BUBBLE AFTER BURSTING, VELOCITY DISTRIBUTION SIGNIFICANTLY AFFECTED
- 4 - LOWER  $R_c$ : LONG BUBBLE WITH COMPLETE SEPARATION

FIGURE 3.5 Diagram of different flow conditions for short and long separation bubbles, where  $R_c$  is Reynolds number based on chord length [70]

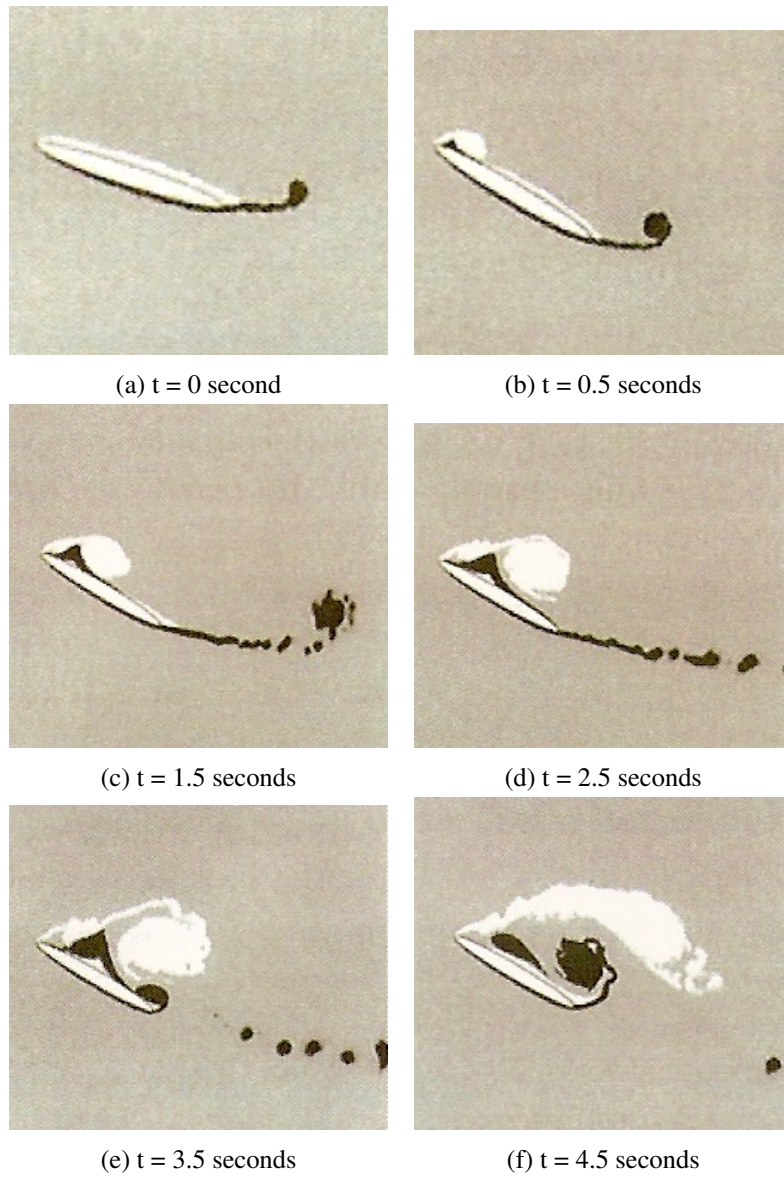


FIGURE 3.6 Simulated vortex shedding at different time [57]



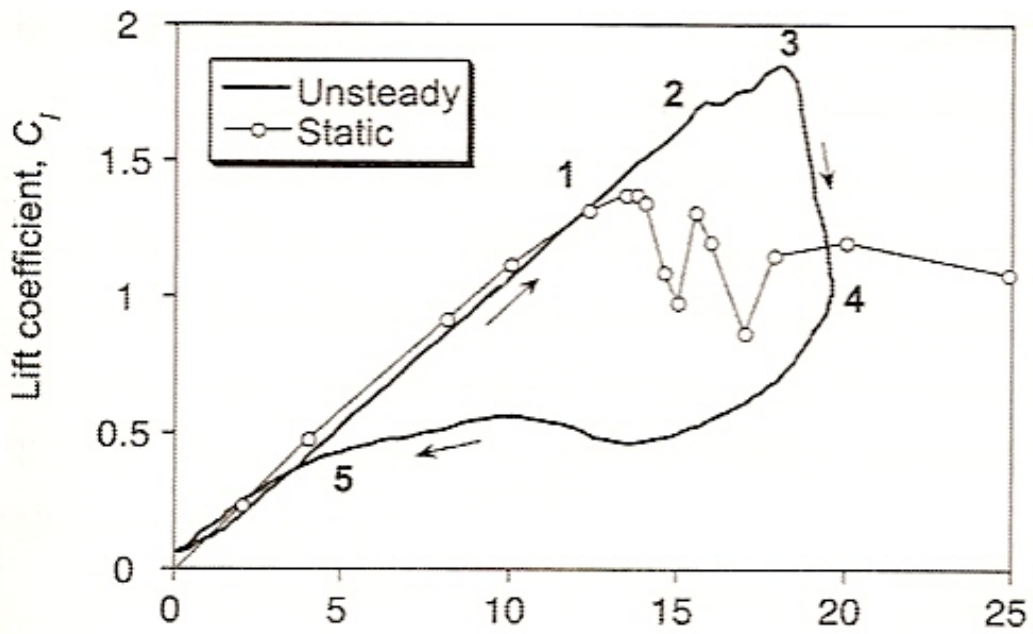


FIGURE 3.7 Schematic of the lift coefficient plot and flow morphology under dynamic motion [47]

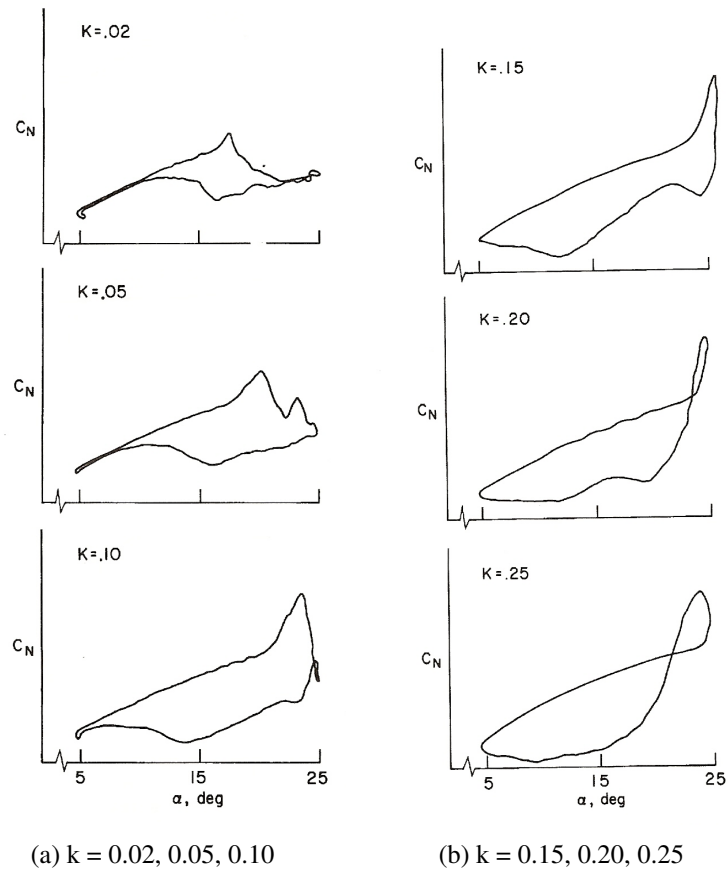
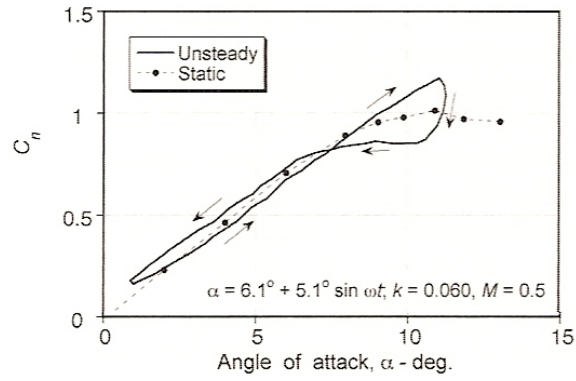
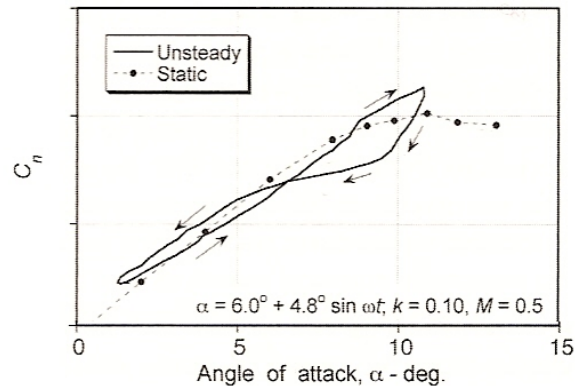


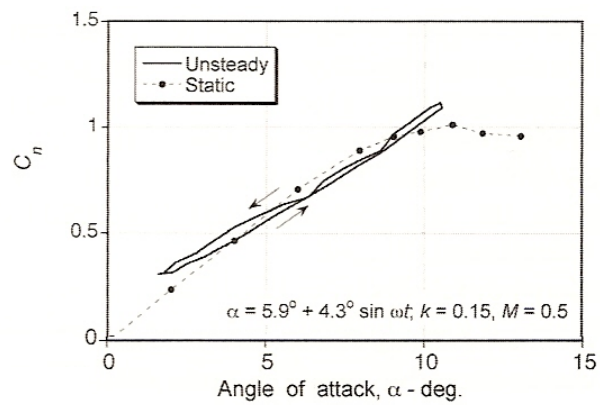
FIGURE 3.8 Normal force on NACA 0012 [56]



(a)  $k = 0.06$

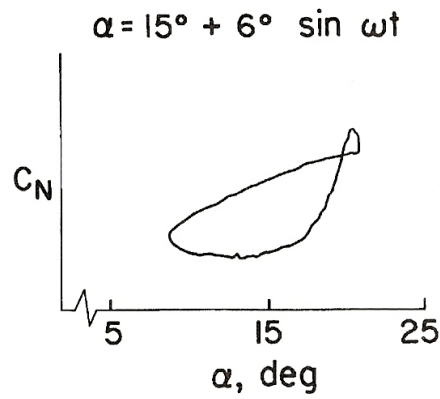


(b)  $k = 0.10$

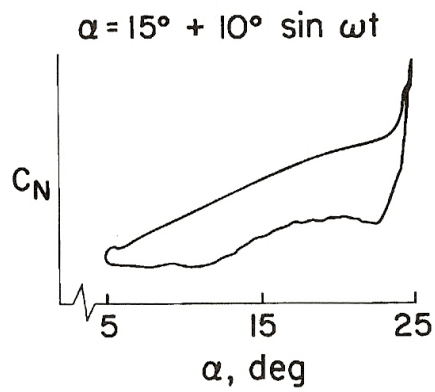


(c)  $k = 0.15$

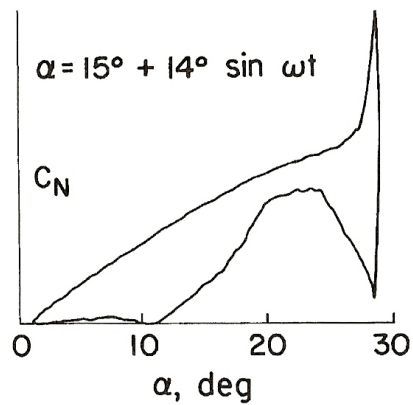
FIGURE 3.9 Effect of reduced frequency on unsteady lift of an oscillating NACA 0012 [47]



(a) Amplitude =  $\pm 6^\circ$

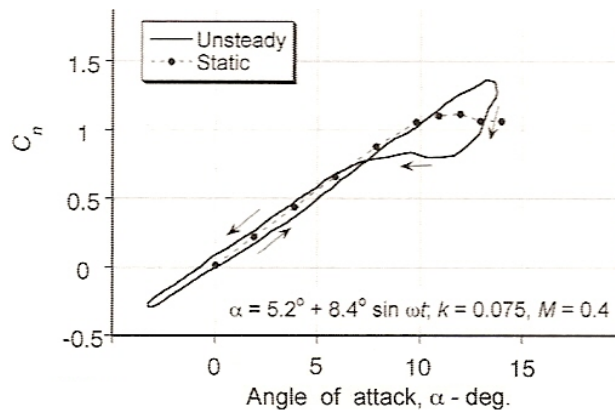


(b) Amplitude =  $\pm 10^\circ$

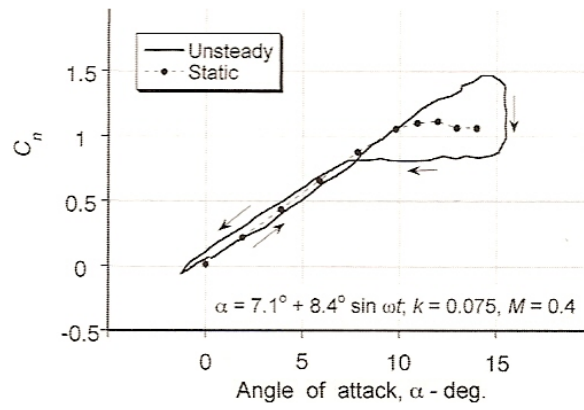


(c) Amplitude =  $\pm 14^\circ$

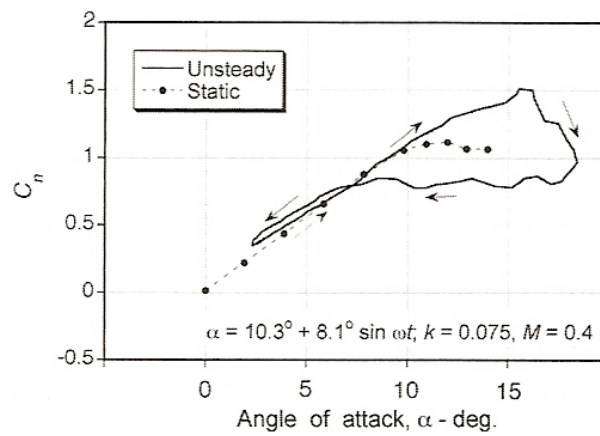
FIGURE 3.10 Effect of oscillation amplitude on NACA 0012 at constant mean angle of attack at  $15^\circ$  [56]



(a)  $\alpha = 5.2^\circ$



(b)  $\alpha = 7.1^\circ$



(c)  $\alpha = 10.3^\circ$

FIGURE 3.11 Effect of mean angle of attack on unsteady lift of an oscillating NACA 0012 at  $M = 0.4$  and  $k = 0.075$  [47]

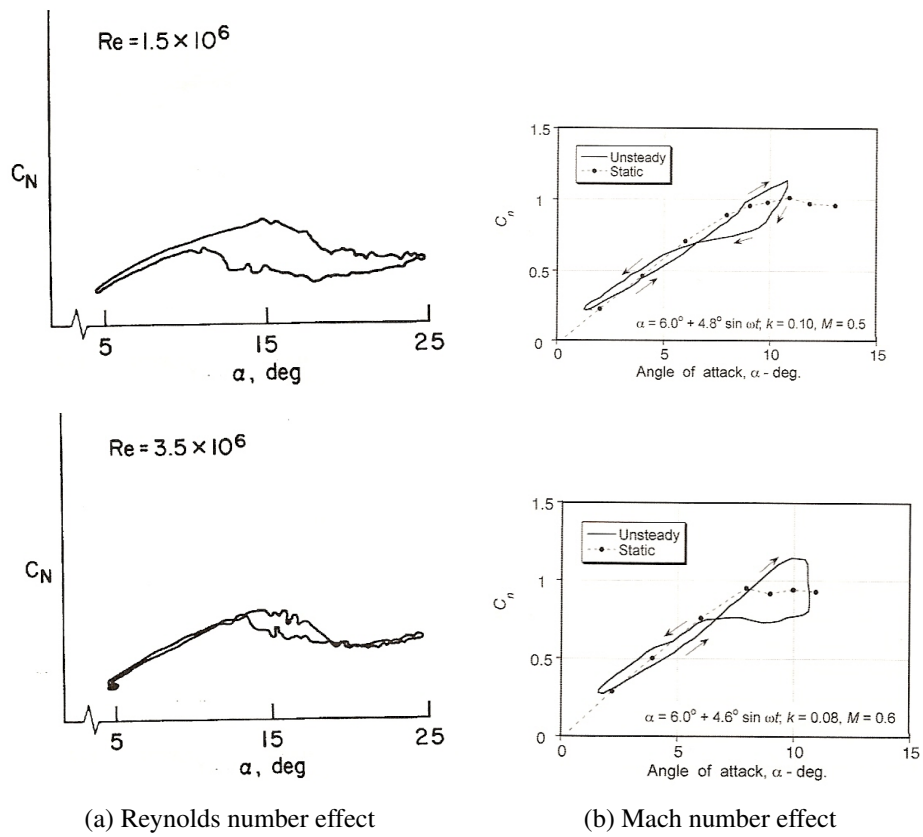
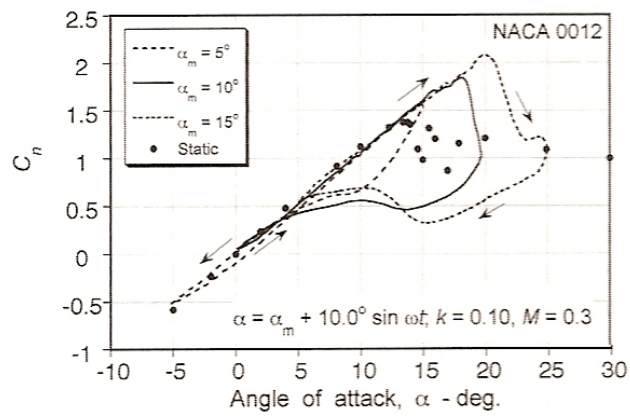
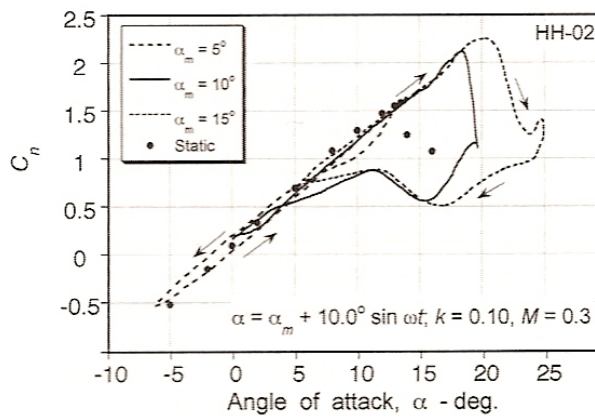


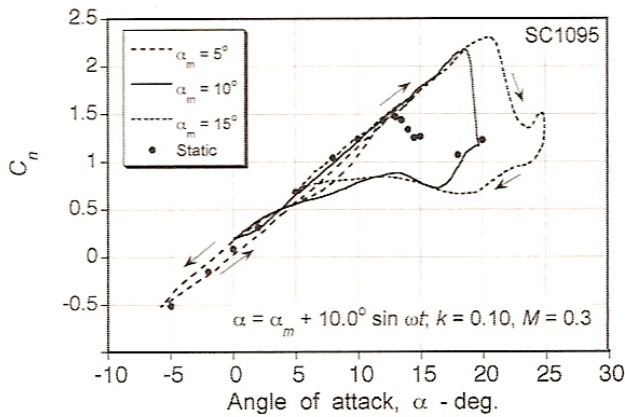
FIGURE 3.12 Effect of Reynolds number and Mach number on the unsteady lift of an oscillating NACA 0012 aerofoil [47,56]



(a) NACA0012 aerofoil

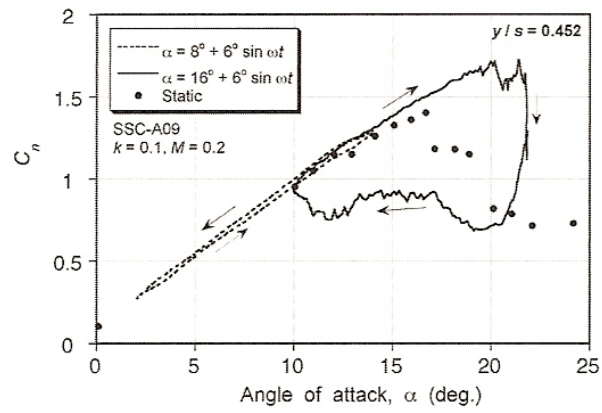


(b) HH-02 aerofoil

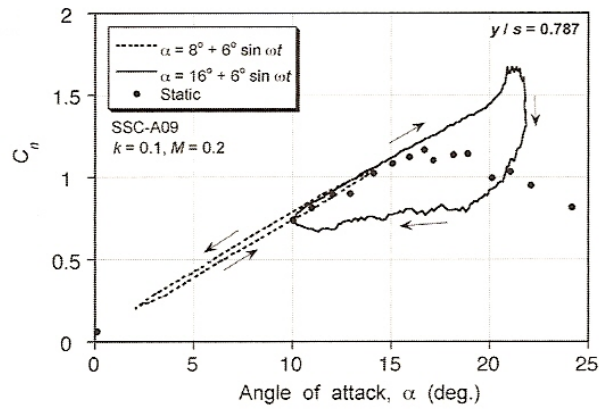


(c) SC1095 aerofoil

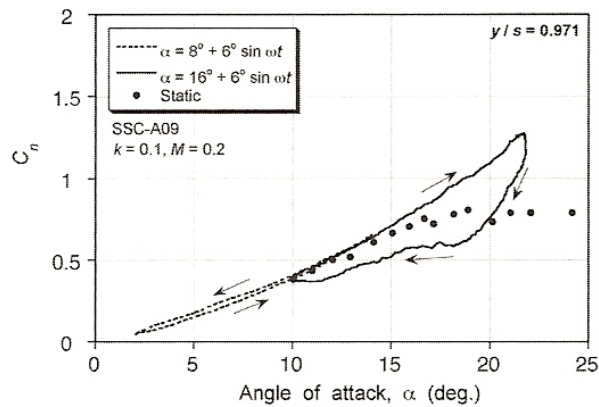
FIGURE 3.13 Effect of aerofoil shape on dynamic stall [58]



(a)  $y/s = 0.452$



(b)  $y/s = 0.787$



(c)  $y/s = 0.971$

FIGURE 3.14 Unsteady lift on a finite semi-span swept wing at  $Ma = 0.2$  [58]



# Chapter 4

## Boundary layer measurement

This chapter describes experimental procedures to investigate the boundary layer in a closed circuit wind tunnel at Cranfield University (Shrivenham campus). Three different sets of measurements were carried out in order to observe the difference in the boundary layer heights in an empty tunnel and with flow mixing devices installed in the tunnel. The principal measurements of the boundary layer height has been based on total pressure, static pressure, dynamic pressure, and static pressure across a screen in the tunnel which was used as a reference pressure. Experimental results of a boundary layer in the closed section wind tunnel are also discussed from two different tunnel set-ups. The objectives of the boundary layer measurements are to compare the thickness produced by different wind tunnel set-ups and a selection of a building geometry for the next set of experiments based on the boundary layer thickness.

### 4.1 Experimental apparatus and instrumentation

The experimental works were carried out using the closed circuit wind tunnel at Cranfield University as represented in Figure 4.1. The closed-section tunnel was constructed with two different working sections with both sections fitted with turntables. The larger working section is suitable for environmental aerodynamics with working section dimensions of 2.30 m  $\times$  1.96 m. The tunnel is powered by 50 KW motor, capable of delivering 3228 m<sup>3</sup>/min at 1250 rpm, giving a maximum wind speed in the small section at 40 m/s and 12.5 m/s in the large section.

In the preliminary tests, two different set-up configurations were tested. The aim of the tests was to measure the boundary layer height in both cases to scale the models for the following phases of work. It was necessary to measure the boundary layer height in the tunnel, consequently an empty tunnel was

considered to approximate the height of the boundary layer first. In order to satisfy the boundary layer height similitude, flow mixing devices such as sharks fins and egg boxes were introduced into the upstream location in front of the turntable to represent roughness elements of the site. To provide consistency of the boundary layer height, the detailed results from each configuration were repeatedly conducted and compared. There was an assumption to be made before the experiments were conducted saying that "the boundary layer in the tunnel is symmetrical in the spanwise direction". Consequently, the boundary layer height measurements were taken only half a turntable from the centre line outwards.

Total pressure and static pressure were measured using a pitot static rake which consisted of eight pitot tubes located at various heights from the floor. The pitot static rake was controlled by two scanivalves which are electronic pressure scanners and these pressures were transferred to micromanometers to convert the pressure input signals from the scanivalves to computer-compatible electronic signals. The electrical signals were converted into legible signals by computing programs kindly provided by Dr. Mark Finnis. Another parameter taken into account was dynamic pressure which is the difference between total pressure and static pressure.

$$P_{total} = P_{static} + \frac{1}{2}\rho V^2 \quad (4.1)$$

It is important to keep in mind that dynamic pressure derived from these equations is valid for incompressible flow only because these equations are originally derived from Bernoulli's equation. Nonetheless, dynamic pressure in the experimental case was measured by taking the difference between the total pressure and static pressure signals coming out of the scanivalves and plugged into a micromanometer Model FC014 to obtain electrical signal. The electrical signal was then transformed into comprehensible signal to provide consistency data as total and static pressures were evaluated. Meanwhile, the pressure drop across the tunnel screen and temperature in the tunnel were measured in order to justify the change of the flow and be used as the frame of reference values after a long period of running time. The boundary layer profiles were non-dimensionalised with the freestream dynamic pressure.

## 4.2 Instrumentation

Total pressure and static pressure at different height from the floor were taken directly from the pitot static rake mounted on a traverse being placed underneath of the turntable. The aim of situating the traverse beneath the turntable is to navigate the rake across in a spanwise direction in order that the rake is able to meas-

ure the pressures at different points in the direction of cross-flow motion (with the probe pointing towards the tunnel contraction). Small tubes connected to the rake distributed total pressure and static pressure to the scanivalves. The simultaneous resolutions of the pressures were transferred to the micromanometer in order that these pressures were transformed into electrical signals and changed into comprehensible signal by a computing program in a computer. With reference to Figure 4.2, the preliminary set-up for the boundary layer height measurement is achieved.

### 4.3 Experimental procedures

The first step of each experimental case was to measure the ambient pressure and temperature before running the tunnel. Regarding the initial set up of the rake, considerable care must be taken since the rake can be easily damaged. After the rake had been located at the centre line above the turntable, setting up of the alignment of the probes proceeded. A connection between the small tubes linking from the rake to the scanivalves had been inspected before the test began.

An experiment with the empty tunnel was the initial experiment to be considered. Regarding the experimental set up mentioned previously, the rake located at the centre line above the turntable was the first position to start with. Total pressure, static pressure and dynamic pressure were then measured directly from the rake mounted on the traverse located beneath the turntable. Wind speed in the tunnel was dependent on the fan rotation speed and calculated from dynamic pressure. Ambient pressure was taken from a pressure transducer placed outside the tunnel in an open area. However, thermocouples were used to determine the temperature increasing in the tunnel to calculate flow density during the experimental period. Likewise in the tunnel with flow mixing devices installed, all of these procedures were reiterated with care.

Bearing in mind, there are many manners that can cause experimental errors during the test period. In order to minimise these errors, the most important thing to do is to ensure that during the experiments a great deal of care and concentration must be taken in to account. The unexpected circumstances and possibilities regarding those errors likely to affect the experimental data are identified as follows:

- Probes alignment and distance from the surface.

The static pressure indication is sensitive to distance from solid boundaries. The probe and boundary form a Venturi passage, which accelerates the flow and decreases the static pressure on one side. Therefore static readings should not be taken closer than 5 tube diameters from a boundary for 1% accuracy

and 10 tube diameters is safer [71]. A minimum distance for measuring the boundary layer was 5 mm whereas the pressure tube diameter was 1 mm. Hence, the accuracy should be within 1%. Another factor believed to be an influence of the errors is yaw and pitch angle of the probes. If the flow is not parallel to the probes' head, errors in total and static pressure readings occur due to misalignment between the probes and the flow direction.

- Tubes are folded and leaking.  
Check tubes for leakage before the experiments were conducted.
- Instrumentation errors.
- Human error

The velocity profile is obtained from  $U/U_{ref}$ , i.e. dynamic pressure at various height divided by reference dynamic pressure and take a square root value.

## 4.4 Preliminary test

The preliminary experiments into boundary layer flow were carried out in two stages; empty wind tunnel and with flow mixing devices placed inside the tunnel far upstream from the test section to investigate the boundary layer thicknesses from the two different configurations. In each case, the wind tunnel motor speed was set constant at 1250 rpm which is equivalent to a flow speed of approximately 5 m/s. Please note that dynamic pressure readings from pitot static rake contained approximately  $\pm 1\%$  error due to the uncertainty from the micromanometer reading. Each set of boundary layer measurement was carried out once, so the repeatability of the experimental results is not available.

### 4.4.1 Empty wind tunnel

The investigation was initialised with a measurement of the boundary layer thickness in an empty wind tunnel at three different spanwise locations. Primarily, the motor speed was selected to run at 1250 rpm to provide the flow speed in the tunnel at approximately 5 m/s. The pitot static rake and all the instruments were set up as described in previous section with the rake aligned at the centreline 400 mm downstream from the centre of the turntable. The free stream velocity in the closed wind tunnel was measured by the pitot static rake; as a reference point  $z = 0$  at the surface of the turntable. Static pressure from a pitot static tube mounted on a side wall of the wind tunnel was used as a reference pressure to evaluate dynamic

pressure at a fixed point in the tunnel, which was used as a denominator to dynamic pressure at different vertical heights. A sampling frequency of 20 Hz and a sampling time of 102.4 seconds for each vertical altitude were used for these pressure measurements. Figure 4.4 and Figure 4.5 represent boundary layer profiles in the empty tunnel configuration. Figure 4.4 shows that with different sample rates, the boundary layer profiles show almost similar distributions above 100 mm while the sample time was kept constant at 102.4 seconds. Therefore, as the number of samples increased by 1000, the boundary layer profile did not have a great influence from increasing the sample rate. Theoretically, a boundary layer thickness is a point where its velocity is equivalent to 99% of a velocity at the outer edge of the boundary layer. In this experimental case, it can be summed up that the average boundary layer thickness is 100 mm but which varies between 95 mm to 105 mm across the spanwise direction.

#### **4.4.2 Wind tunnel with roughness elements and spires**

In the previous section, the average boundary layer thickness in the empty tunnel is 100 mm. In this section, the experimental data in the tunnel with roughness elements and flow mixing devices will be discussed. The measurements were made with four elliptical spires placing in front of the roughness elements where the roughness elements located 2 metres upstream from the test section. As mentioned earlier, the experiments in the empty tunnel were sampling at 20 Hz with a sampling time of 102.4 seconds. Therefore, the experiments with flow mixing devices would be measured by using the same sampling frequency and sampling time.

The experiments with roughness elements and spires were divided into two different tests. The first measurement included four elliptical wedges without roughness elements. The other measurement was carried out with four elliptical wedges and roughness elements. The objectives of the two separated tests are to compare the boundary layer thickness produced with/without roughness elements. The measurements were made at three spanwise locations: at centre of the test section, 175 mm and 350 mm from the centre of the test section in a spanwise direction. A result from the first configuration without surface roughness is presented in Figure 4.6.

The results obtained without surface roughness were all based on the four elliptical wedges placed across the whole width of the tunnel a distance of 580 mm apart from each other located approximately 5 metres upstream from the test section. In Figure 4.6 the boundary layer profiles for all three locations appear to be similar to the empty tunnel profiles. Interestingly, from Figure 4.7 where

surface roughness was introduced, at the height between 50 mm to 200 mm the boundary layer profile seems to be linearly proportional to height. It is believed that the surface roughness manipulates high velocity flow in the range between 50 mm and 200 mm from the tunnel floor. The test section of the closed wind tunnel used for the boundary layer experiment is not as long as wind tunnels used in many applications explained in the literatures, therefore, it might be a factor that influences a steady state of the boundary layer in a low altitude which in this case is the range between 50 mm and 200 mm from the tunnel floor. Another reason to support this behaviour was explained by Cermak [72]; as the introduction of mixing flow devices at the test section entrance leads significant loss of similarity with the atmospheric boundary layer unless the test section is sufficiently long enough for the flow structure to reach statistical equilibrium. However, an average boundary layer thickness defined in this experimental configuration with only the elliptical wedges introduced upstream of the test section is 175 mm across the spanwise direction.

A combination of the elliptical wedges and roughness elements was carried out to simulate another thickness of the boundary layer. The roughness elements used in this configuration to produce a turbulent flow were egg boxes representing surface roughness. The egg boxes, 1.60 metres long, were located across the tunnel width at 1.40 metres downstream of the wedges. Also the pitot static rake measuring total and static pressures was mounted on a traverse 2 metres downstream from the trailing edge of the egg boxes. Hence, total distance of measurement from leading edge of the roughness elements to the point of measurement was 3.60 metres. Figure 4.7 shows the boundary layer profiles obtained from this configuration at various spanwise locations. It can be seen that at low altitude below 50 mm and above 200 mm, the magnitudes of the normalised velocity,  $U/U_{ref}$  at three locations are eventually similar which is linearly proportional to vertical height. The average boundary layer thickness defined in this experimental configuration is 235 mm across the spanwise direction.

Maruyama et al [73] indicates that a relationship between a boundary layer thickness  $\delta$ , and a fetch  $x$ , can be expressed as

$$\delta \propto x^{0.56} \quad (4.2)$$

According to this expression, the experimental results in the closed wind tunnel with elliptical wedges and roughness elements provided a similar range of the exponential value. As mentioned earlier a measurement distance from the leading edge of the roughness elements to the point of measurement where the pitot static rake situated was 3.60 metres. This distance is the fetch length,  $x$ . The experi-

mental results verified that at centreline, 175 mm and 350 mm from the centreline the exponential values are 0.517, 0.540 and 0.545 respectively. Having said that, measurement of the boundary layer growth at the beginning from the leading edge of the roughness elements to the point of the pitot static rake was not performed. It was the only measurement point to obtain these exponential values which is in the centre of the test section. Thus, in the wind tunnel with elliptical wedges and roughness elements configuration a relationship between the boundary layer thickness  $\delta$ , and the fetch length  $x$ , can be expressed as

$$\delta \propto x^{0.52-0.55} \quad (4.3)$$

where unit of  $\delta$  and  $x$  is in centimetre.

Maruyama et al [73], additionally, also indicated that the boundary layer profile can still be divided into three different regions; wake region, log region and urban canopy depending on wind characteristics in a boundary layer. In the middle region where the mean thickness is approximately 40 – 50 percent of the boundary layer is called "log region". The middle region of the experimental results still agrees with Maruyama's results. The mean thickness of the results is 121 mm which is equivalent to 51 percent of the boundary layer thickness. The first and the last points of this region from the experiment are at 85 mm and 175 mm respectively where Maruyama suggested that the Reynolds stress in the middle region is approximately constant. Above 175 mm where it is called wake region is believed that turbulence intensity and Reynolds stress reduce with height and the velocity gradient becomes larger than the middle region. In the lowest region, an urban canopy region is generally affected by the roughness elements which mean velocity varies little with increasing height. In this particular region, turbulence intensity level is larger than 30% whereas in the log region turbulence intensity level is normally less than 30%. The graphs show mean velocity profiles at the test section without any models in position.

## 4.5 Boundary layer profile relating to scale

Building scale and geometry in wind tunnel modeling are selected by comparing the results from the simulated atmospheric boundary layer experiments and the appropriate ESDU methods to approximate the atmospheric boundary layer thickness. In the present work, it was decided to simulate boundary layer thickness from three different wind tunnel configurations to similitude the highest boundary layer thickness which will be used in the next set of experiments of flow field behind buildings. All the results will be discussed later in Chapter 6. To compare the boundary layer thickness from the experimental results and estimate the atmospheric boundary layer thickness, ESDU Data Item 82026 was used to calculate

mean wind speeds based on parameters such as changes in surface roughness, zero-plane displacement, roughness factors and height from the ground. All parameters involved in the calculation can be seen in ESDU Data Item 82026. All the parameters were selected carefully to ensure the same measurement conditions of boundary layer in the wind tunnel are met. The calculation of the wind profile cannot be shown in this section. However, the calculations of the wind profile are based on a copy of calculation sheet 1 of Table 11.1 and calculation sheet 2 of Table 11.2 of ESDU Data Item 82026. The wind speed plots are then compared with the experimental result of the simulated atmospheric boundary layer in the wind tunnel, represented in Figure 4.10. From the comparison it can be seen that the plots of the wind speed at a site downwind of a sudden change, two changes in surface roughness and the experimental result are similar except for an altitude over the roof-top level. This result denotes the change of the roughness surface does not have a significant effect of the flow field below a surface layer which is approximately 10% of the boundary layer thickness. On the other hand, above the surface roughness layer the experimental result and the estimating hourly-mean wind speed are different. This could be a result of short wind tunnel where the simulated boundary layer did not have time to grow and reach a stability condition.

Figure 4.11 shows an atmospheric boundary layer in an urban area which is also calculated from ESDU Data Item 82026. This boundary layer calculation is based on a small town with an average roof-top level about 10 – 15 metres with an open area and terrain roughness change located upwind from the urban region. It is found that the atmospheric boundary layer is approximately 372 metres in reality. In order to compare a scale of the simulated atmospheric boundary layer in the wind tunnel to the atmospheric boundary layer, the scale can be estimated as 1 : 1600. For most wind tunnel modeling of the atmospheric boundary layer, the scale ratio of the boundary layer thickness is often selected in the range of 100 – 1000 to generate the best similitude of the velocity profile and flow characteristics. For this the experiment, the scale of the boundary layer of 1 : 1600 is beyond the scale ratio to obtain the best solution for experimental measurement. However, as long as a building model is immersed in the boundary layer and the ratio of  $H/\delta$  is greater than 0.85 as described in Chapter 2, the flow characteristics around bluff body can be obtained.

## 4.6 Conclusion

To summarise, three different approaching flows were generated by three different set-ups. The boundary layer characteristics can be divided into three cases; thick, medium and thin layers. Firstly, the thin boundary layer ( $\delta = 95 - 105$  mm varies



across spanwise locations) was generated in the empty tunnel by only a screen across the tunnel located upstream of the test section. Reynolds number,  $Re_\delta$  based on the boundary layer thickness and free stream velocity measured in the centre of the test section was  $3.42 \times 10^4$ . Displacement thickness ( $\delta^*$ ) and momentum thickness ( $\theta$ ) were 11.26 mm and 6.49 mm respectively. Secondly, the medium boundary layer was obtained by four elliptical wedges without surface roughness. It provides average boundary layer thickness across spanwise direction of 175 mm. Reynolds number based on the boundary layer thickness and free stream velocity in the centre of the test section was  $5.98 \times 10^4$ . Displacement thickness ( $\delta^*$ ) and momentum thickness ( $\theta$ ) were 21.52 mm and 6.67 mm respectively. Finally, the thick boundary layer was obtained by four elliptical wedges and surface roughness. The average boundary layer thickness is maximum and equal to 235 mm. Reynolds number based on the boundary layer thickness and free stream velocity in the centre of the test section was  $8.04 \times 10^4$ . Displacement thickness ( $\delta^*$ ) and momentum thickness ( $\theta$ ) were 159.36 mm and 24.18 mm respectively. Furthermore, the shape factors,  $H \equiv \delta^*/\theta$  for the thick, medium and thin boundary layers case are 6.59, 3.22 and 1.73 respectively. This indicated that adverse pressure gradients easily happen in the case of the thick boundary layer with less possibility to occur in the thin boundary layer since adverse pressure gradients increase the value of the shape factor. On the other hand, favourable pressure gradients and suction reduce the value of the shape factor [74].

The appropriate ESDU methods were used to define the boundary layer profile as shown in Figure 4.10 and Figure 4.11. The atmospheric boundary layer in a small town is also estimated and compare to the simulated atmospheric boundary layer obtained from from the wind tunnel experiment. The scale ratio of the simulated layer to the full-scale is approximately 1 : 1600 which is quite small to obtain a fine resolution from flow around building. Nonetheless, a good result can be achieved if the building model is large,  $H/\delta > 0.80$ . Investigation of the flow structures in the boundary layer in the wind tunnel in Chapter 6 focuses on the flow field around building in the lower third of the boundary layer. As long as the building model is fully immersed in the boundary layer, the experimental data are satisfactorily obtained.

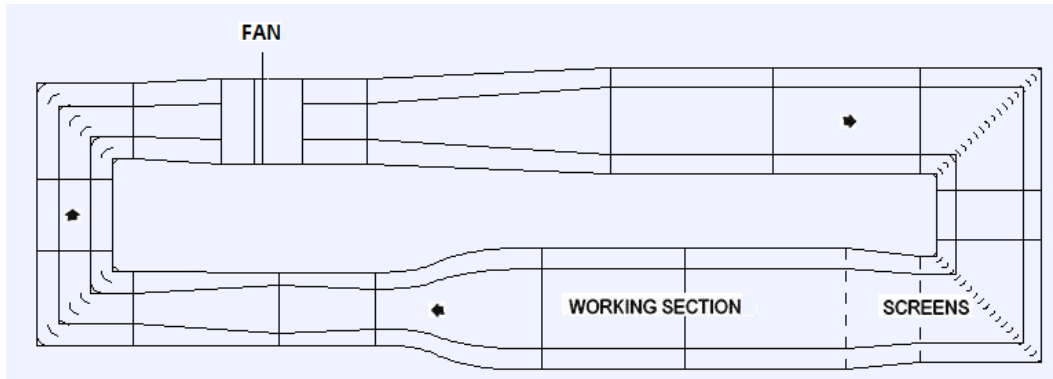


FIGURE 4.1 Schematic of a closed section wind tunnel used for experiments.

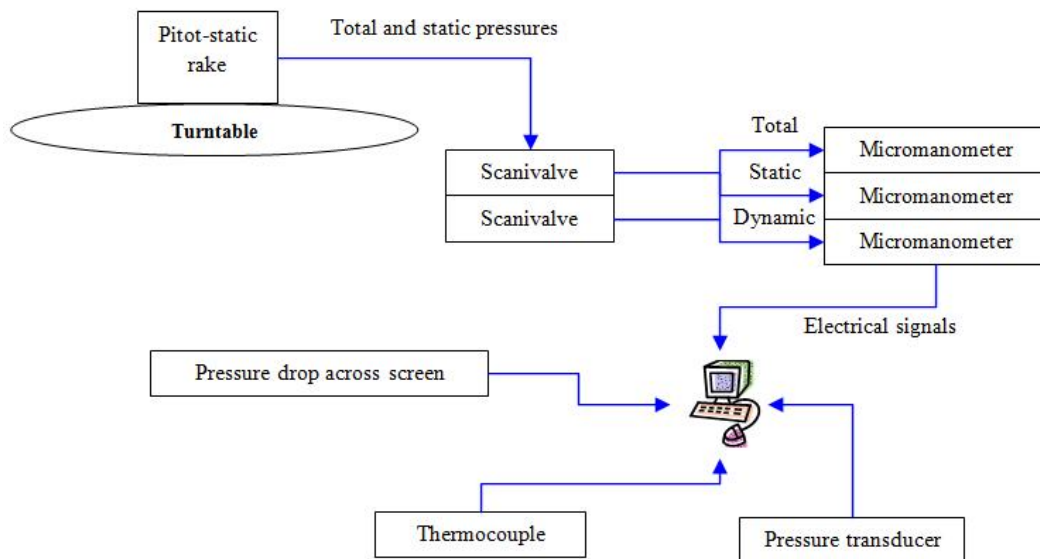
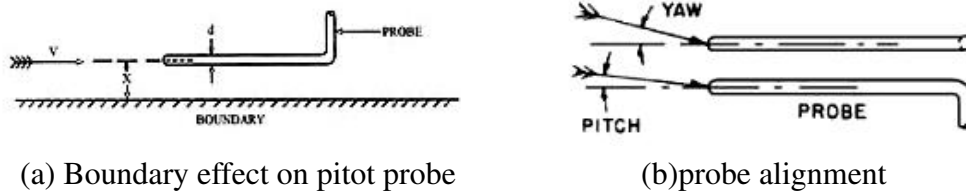


FIGURE 4.2 Instrumental set-up



(a) Boundary effect on pitot probe

(b) probe alignment

FIGURE 4.3 Probe alignment and distance to surface [71]

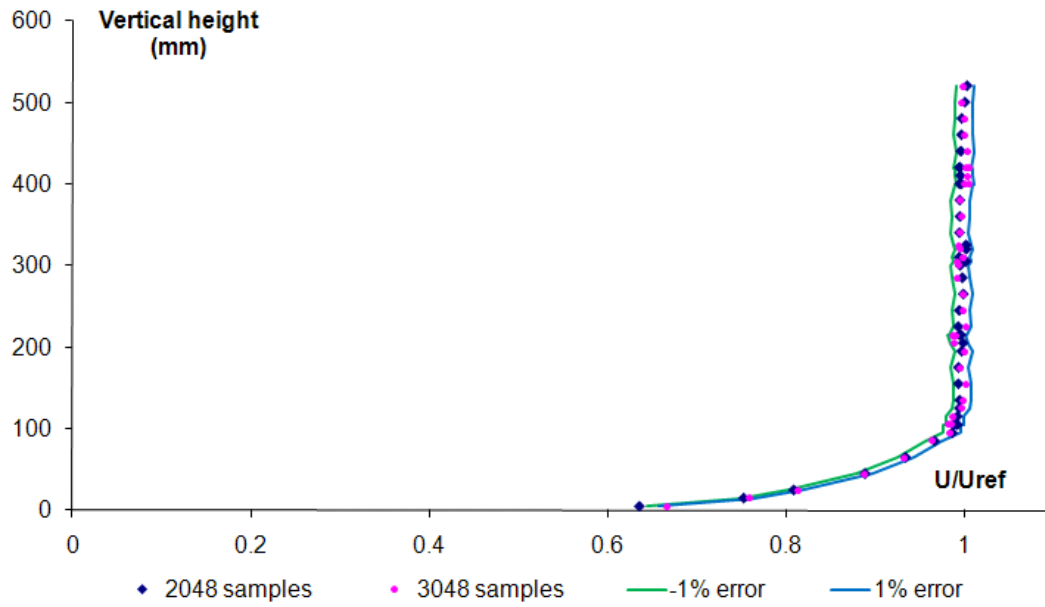


FIGURE 4.4 Centre line with different sample rates

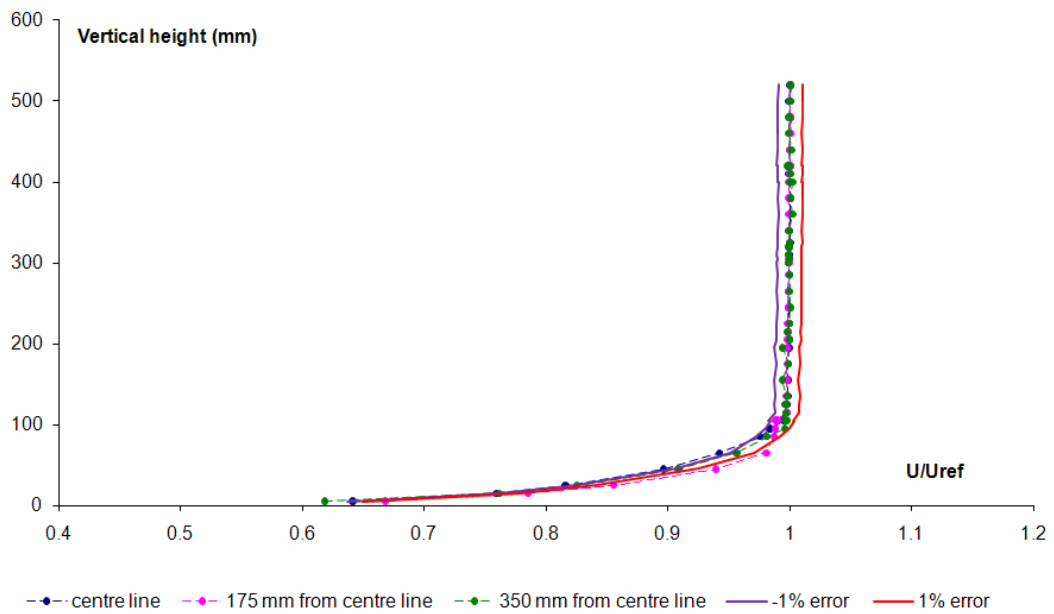


FIGURE 4.5 Empty wind tunnel in the spanwise locations at frequency 20 Hz

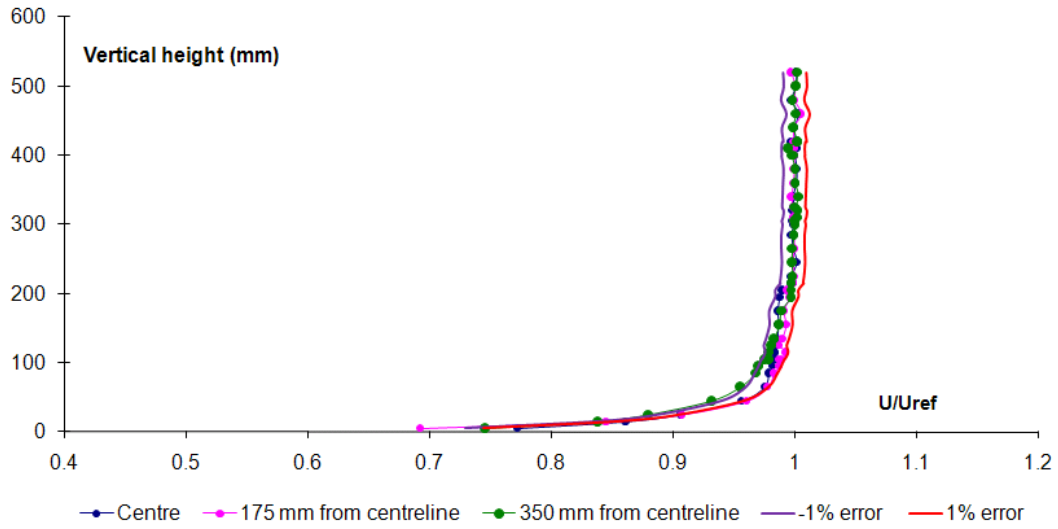


FIGURE 4.6 Boundary layer profiles with elliptical wedges but without surface roughness

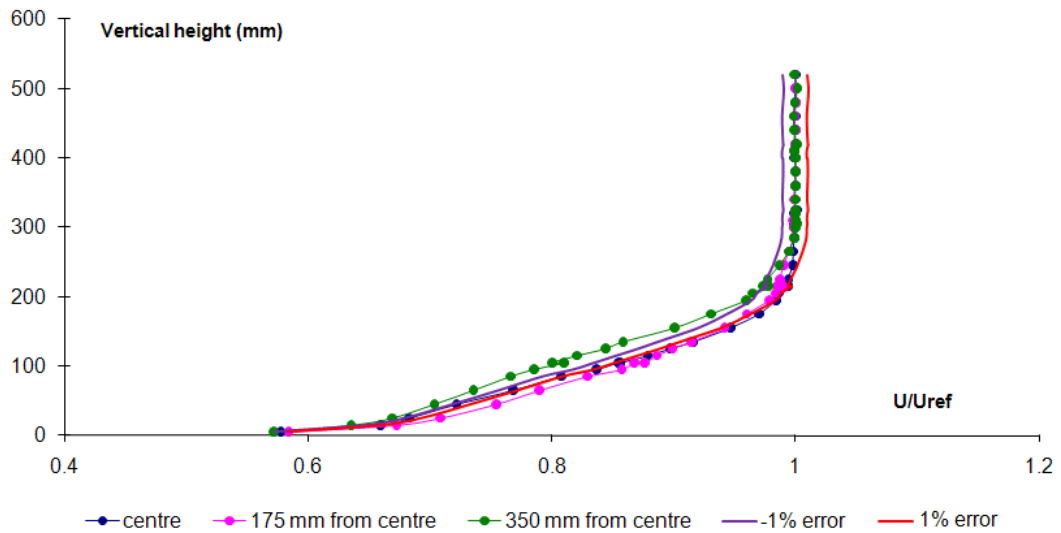


FIGURE 4.7 Boundary layer profiles with elliptical wedges and with surface roughness

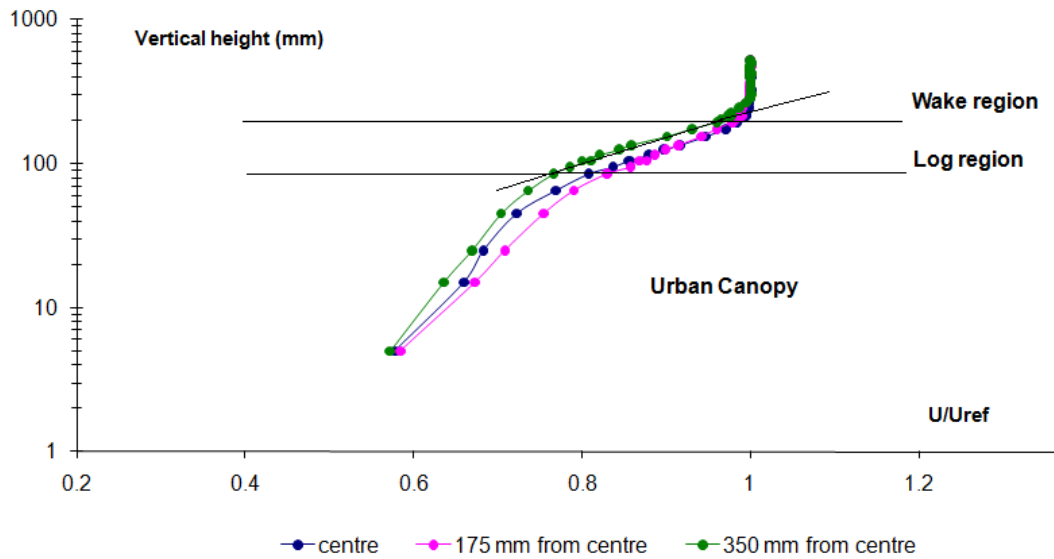


FIGURE 4.8 Profiles of mean velocity at various spanwise locations

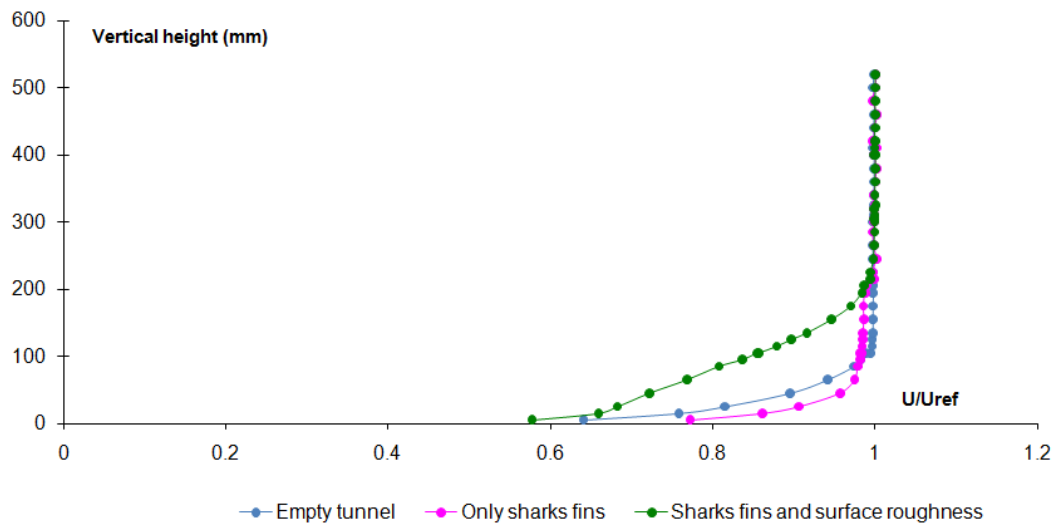


FIGURE 4.9 Comparison between three different set up methods

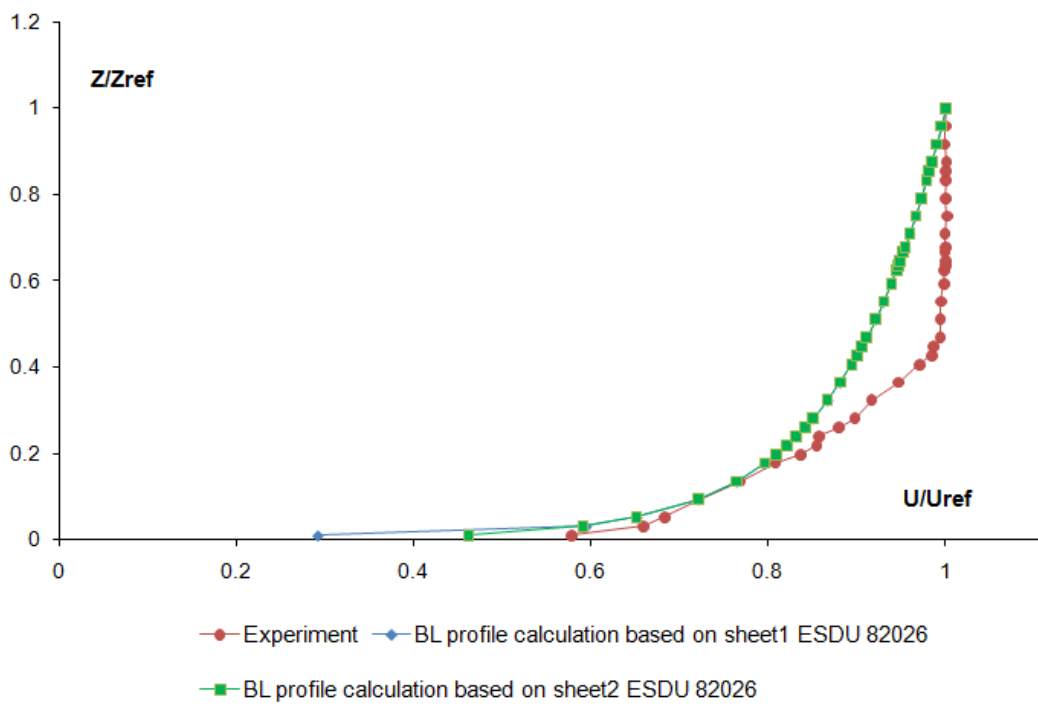


FIGURE 4.10 Experimental result compare with ESDU methods to define the profile characteristics

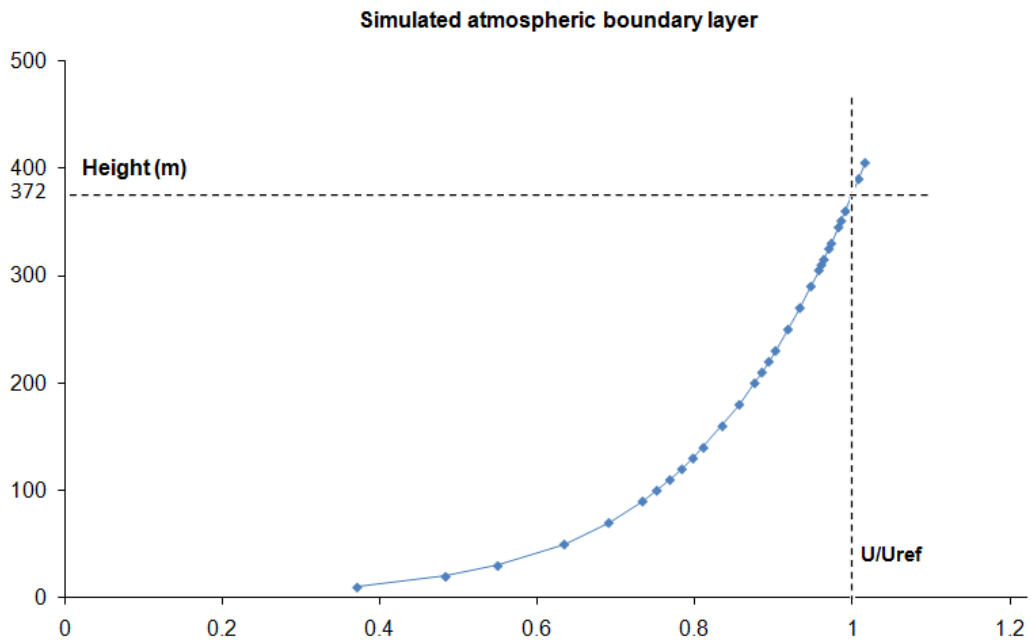


FIGURE 4.11 Simulated atmospheric boundary layer in an urban area





# Chapter 5

## Five-hole probe

### 5.1 Applications of Five-hole Probe and Calibration Process

In turbulent flow fields such as the wake region behind wing tips, in turbomachines and in turbulent shear layers, three-dimensional flow characteristics are usually detected. In such swirling flow fields as mentioned, measurements are very difficult to determine the flow characteristics. In order to investigate the three-dimensional flow, the experimental techniques such as Particle Image Velocimetry (PIV) and Laser Doppler Anemometry (LDA) methods should be implemented. The main features of these techniques are nonintrusive instrumentations and all three velocity-components can be measured instantaneously. On the other hand, time is an issue that has to be taken into account if they are used in measuring velocity components and turbulent properties. Multi-hole pressure probe is another experimental instrument conventionally employed to examine flow direction, magnitude of static pressure and flow velocity in three-dimensional flow fields [75]. Five-hole probe geometry consists of five pressure tubes aligned in two different planes perpendicular to each other. Meanwhile, the two-plane intersects at a central tube as shown in Figure 5.1. The central probe measures a form of stagnation pressure (total pressure) and the pressures in the other four probes are proportional to static pressure which is approximately 65% of  $P_{ave}/(P_5 - P_{ave})$  and below this when  $\theta = 35^\circ$ , also about 55% of  $P_{ave}/(P_5 - P_{ave})$  and below when  $\theta = 45^\circ$  at pitch and yaw angles at  $0^\circ$  [76, 77]. Typical calibration technique can be divided into two different techniques; nulling and non-nulling techniques. The nulling technique is required when the pressures in the outer four tubes are equal, i.e. ( $P_1 = P_2 = P_3 = P_4$ ). The central tube measures a form of total pressure. This nulling technique requires a long period of time to calibrate because the probe has to be yawed and pitched to a correct direction until the outer four probes read equal pressures. On the other

hand, the non-nulling technique requires the probe to be fixed relative to a point of reference. The probe is set at constant pitch and yaw angles, measuring the pressure directly from the probe at each location by traversing the probe into the flow field. When the pressures from the five-hole probe are measured, magnitudes of flow characteristics are determined [77]. This technique requires the calibration procedures by changing the probe at various pitch and yaw angles. Hence at each pitch and yaw angle at each location, the magnitude of pressures of the five-hole probe is recorded then flow direction and flow velocity are calculated.

## 5.2 Probe Geometries and Description

The five-hole probe was designed and manufactured at Cranfield University (Shrivenham Campus) with the assembled probe tip of 1.68 mm outer diameter. The effect of this diameter can be to flatten the peaks in areas of changing velocity gradients. Each of the five-hole tubes was made of stainless steel hypodermic tubing with inner diameter of 0.305 mm and outer diameter of 0.56 mm. The five-hole tubes were firstly bonded together by silver solder along the length of approximately 100 mm. The probe tip was chamfered at an appropriate angle of  $45^\circ$  relative to the end of the central tube and a longitudinal axis. The four-chamfered ends were shaped by machine grinder leaving the central tube square-ended. The five-hole tubes were then placed into a stainless steel housing with inner and outer diameters of 1.77 mm and 2.34 mm respectively to increase the probe strength and also protect the main tubes. The array of the five-hole tubes were inserted into another cover housing which were then placed into a  $90^\circ$  bending tube with 5.07 mm inner diameter and 6 mm outer diameter with a radius of 40 mm. Figure 5.2 shows the schematic diagram of the five-hole probe in two dimensions with 25 mm tip extension (approx. 15 tip diameters) beyond the cover housing. Similarly, the tip is approximately 180 mm from the main probe stem so that disturbance from the probe stem is minimised. As a method of Babu et al [78] explained a reason to minimise a stem influence effect that a ratio of a length from a probe tip to a stem-to-stem diameter should be more than 3. However, for the five-hole probe in this case, the ratio is approximately 30 which is 10 times more than the ratio specified by Babu. Therefore, the stem influence effect is initially negligible in this case. The probe does not measure instantaneous readings of pressure. The pressure readings from the transducers are the average reading over a number of samples and for a short period of time and so the time averaged values for the pressures in the tubes are recovered.

In general to design pressure probes for three dimensional flow measurements, there are a few design parameters to be considered in order to obtain correct data as dependent on sensitivity effect. Owing to these parameters, two main issues are determined; probe tip shape including a chamfer angle,  $\theta$  and the influence of

Reynolds number (based on tip diameter) on performance of the probe. The former design parameter indicates a direct sensitivity of the probe and minimising near-wall effect due to flow blockage. To elaborate the sensitivity effect, Bryer et al [79] suggested that the effect of sensitivity is dependent on apex angle of the probe, which is twice the chamfered angle. This means that the larger apex angle, the less sensitivity produced by the probe. At 45° inclination to the longitudinal, the probe axis is the most suitable for many pressure probes. Another issue is the shape of the probe tip which Ligrani et al [80] recommended that conical shape is preferable because the near-wall flow blockage effect is more severe for the prismatic shape than conical shape. Another design parameter specifying the sensitivity effect is Reynolds number based on the outer tip diameter if the value of Reynolds number of a square and sharp-edged tip below 1500, the sensitivity effect is likely to decrease. The performance of the five-hole probe in compressible flow resulting in changing of sensitivity due to Mach number is neglected in this case.

### 5.3 Calibration Procedures

A standard calibration procedure for non-nulling technique is simple and does not require much time compared with the nulling technique. As mentioned earlier, the nulling technique requires the four static pressures of the outer tubes to be equivalent, ( $P_1 = P_2 = P_3 = P_4$ ). This technique will require some time until the side tubes read equal pressure. However, an advantage of this method is that it provides the most accurate results compared with the non-nulling technique. An example of this method was performed by Bryer et al [79]. A simple way is to place the five-hole probe in a known flow direction. Following by changing pitch and yaw angles and the pressures from the probe are recorded individually for pitch and yaw angles. Calibration by this method is called non-nulling technique. There are a number of the advantage reasons for calibration the probe in non-nulling mode such as space limitations of probe rotation, time consuming for system response and difficulty of experimental set up, e.g. in turbomachines. The salient point of the calibration of the five-hole probe is that the pressure differences between two pressure ports are normalised to obtain pressure coefficients which are dependent on the flow angularity but independent of velocity. Meanwhile, total and static pressure coefficients can be determined in the same manner. Generally, the pressure difference or the normalised term is expressed by a fraction of difference between total pressure from the central tube and the average pressure from the outer four chamfered tubes. The non-dimensional parameters are then determined as follows:

$$C_{P\alpha} = \frac{P_3 - P_1}{P_5 - P_{ave}} \quad (5.1)$$

$$C_{P\beta} = \frac{P_2 - P_4}{P_5 - P_{ave}} \quad (5.2)$$

$$C_{Ptotal} = \frac{P_{total} - P_{ave}}{P_5 - P_{ave}} \quad (5.3)$$

$$C_{Pstatic} = \frac{P_{total} - P_{static}}{P_5 - P_{ave}} \quad (5.4)$$

or,

$$C_{Ptotal} = \frac{P_5 - P_{total}}{P_5 - P_{ave}} \quad (5.5)$$

$$C_{Pstatic} = \frac{P_{ave} - P_{static}}{P_5 - P_{ave}} \quad (5.6)$$

It is interesting to note that sometimes dynamic pressure coefficient is used instead of static pressure coefficient for example in a calibration process performed by Dominy and Hodson [81] as shown:

$$C_{Pdynamic} = \frac{P_{total} - P_{static}}{P_5 - P_{ave}} \quad (5.7)$$

where,

$P_1 - P_4$  are pressures from different pressure tubes (outer tubes)

$P_5$  is pressure from the central tube

$P_4 = (P_1 + P_2 + P_3 + P_4)/4$

$P_{total}$  is total pressure and  $P_{static}$  is static pressure.

Normalisation by  $P_5 - P_{ave}$  is widely used in the majority of the five-hole probe calibration process for many years especially G. Zilliac [82] explained a reason why this "normalised term" has been incorporated as a tested flow angle is up to 30° pressure coefficient collapses on a straight line within experimental uncertainty. Pressure coefficients in Eq. 5.3 and Eq. 5.4 are different from the pressure coefficient forms from Treaster and Yocum [83] and Lee and Wood [84]. Ligrani et al [80] provided a reason for not using the pressure coefficient forms in Eq. 5.5 and Eq. 5.6 that as pitch and yaw angles approach to zero,  $C_{Ptotal}$  and  $C_{Pstatic}$  also approach to zero. Consequently, in order to avoid being close to zero, the numerator terms used by Treaster and Yocum and Lee and Wood experiments, Ligrani replaced  $(P_5 - P_{total})$  and  $(P_{ave} - P_{static})$  by  $(P_{total} - P_{ave})$  and  $(P_{total} - P_{static})$  respectively as represented in Eq. 5.3 and Eq. 5.4. Hence a relationship between

velocity magnitude,  $V$  and static pressure coefficient is defined by Ligrani et al using Bernoulli's equation as:

$$\mathbf{P}_{total} = \mathbf{P}_{static} + \frac{1}{2}\rho\mathbf{V}^2 \quad (5.8)$$

$$\mathbf{P}_{total} - \mathbf{P}_{static} = \frac{1}{2}\rho\mathbf{V}^2 \quad (5.9)$$

From equation 5.4,

$$\mathbf{P}_{total} - \mathbf{P}_{static} = \mathbf{C}_{Pstatic}(\mathbf{P}_5 - \mathbf{P}_{ave}) = \frac{1}{2}\rho\mathbf{V}^2 \quad (5.10)$$

$$\mathbf{V}^2 = \left[ \frac{2}{\rho} (\mathbf{P}_5 - \mathbf{P}_{ave}) \mathbf{C}_{Pstatic} \right] \quad (5.11)$$

$$\mathbf{V} = \sqrt{\left[ \frac{2}{\rho} (\mathbf{P}_5 - \mathbf{P}_{ave}) \mathbf{C}_{Pstatic} \right]} \quad (5.12)$$

On the other hand, using the pressure coefficients forms from Treaser and Yocum [83] and Wood's experiments [84] from Eq. 5.5 and Eq. 5.6, the magnitude of the velocity will be expressed by using Bernoulli's equation as:

$$\mathbf{V}^2 = \left[ \frac{2}{\rho} (\mathbf{P}_{total} - \mathbf{P}_{static}) \right] \quad (5.13)$$

Rearranging Eq. 5.5 and Eq. 5.6:

$$(5.14)$$

$$\mathbf{P}_{total} = \mathbf{P}_5 - \mathbf{C}_{Ptotal} (\mathbf{P}_5 - \mathbf{P}_{ave}) \quad (5.15)$$

$$\mathbf{P}_{static} = \mathbf{P}_{ave} - \mathbf{C}_{Pstatic} (\mathbf{P}_5 - \mathbf{P}_{ave}) \quad (5.16)$$

Substituting equation 5.14 into 5.13 yields,

$$\mathbf{V}^2 = \left[ \frac{2}{\rho} [\mathbf{P}_5 - \mathbf{C}_{Ptotal} (\mathbf{P}_5 - \mathbf{P}_{ave})] - [\mathbf{P}_{ave} - \mathbf{C}_{Pstatic} (\mathbf{P}_5 - \mathbf{P}_{ave})] \right] \quad (5.17)$$

$$\mathbf{V}^2 = \left[ \frac{2}{\rho} [\mathbf{P}_5 - \mathbf{P}_{ave} - \mathbf{C}_{Ptotal} (\mathbf{P}_5 - \mathbf{P}_{ave}) + \mathbf{C}_{Pstatic} (\mathbf{P}_5 - \mathbf{P}_{ave})] \right] \quad (5.18)$$

$$\mathbf{V}^2 = \left[ \frac{2}{\rho} (\mathbf{P}_5 - \mathbf{P}_{ave}) (1 - \mathbf{C}_{Ptotal} + \mathbf{C}_{Pstatic}) \right] \quad (5.19)$$

$$\mathbf{V} = \left[ \frac{2}{\rho} (\mathbf{P}_5 - \mathbf{P}_{ave}) (1 - \mathbf{C}_{Ptotal} + \mathbf{C}_{Pstatic}) \right]^{\frac{1}{2}} \quad (5.20)$$

Moreover, the velocity components in Cartesian and Cylindrical polar coordinates are then evaluated as in Appendix B depending on which mode the probe is calibrated. If the probe is calibrated in "yaw-pitch mode", the three velocity components in Cartesian coordinates are defined as:

$$\mathbf{u} = \mathbf{V} \cos \beta \cos \alpha \quad (5.21)$$

$$\mathbf{w} = \mathbf{V} \cos \beta \sin \alpha \quad (5.22)$$

$$\mathbf{v} = \mathbf{V} \sin \beta \quad (5.23)$$

In contrast, if the probe is calibrated in "pitch-yaw mode", the three velocity components are defined as:

$$\mathbf{u} = \mathbf{V} \cos \alpha \cos \beta \quad (5.24)$$

$$\mathbf{w} = \mathbf{V} \sin \alpha \quad (5.25)$$

$$\mathbf{v} = \mathbf{V} \cos \alpha \sin \beta \quad (5.26)$$

The derivation of the two distinguished modes can be seen in Appendix B as the formulas are evaluated in the relationship between pitch angle  $\alpha$  and yaw angle  $\beta$  and velocity magnitude  $\mathbf{V}$  respect to axis of rotation. The five-hole probe for this project was calibrated in "pitch-yaw mode". Therefore, the relationship of the three velocity components will be used is in the latter forms, e.g. Eq. 5.24.

## 5.4 Calibration Results

The forward facing pyramid five-hole probe was calibrated in a boundary layer wind tunnel at Cranfield University Shrivenham campus with nominal free stream velocity at 3 m/s, 5 m/s and 7 m/s, corresponding to Reynolds numbers of 340, 565 and 790 based on 1.68 mm tip diameter. Consequently, the flow was considered as incompressible. The position of the probe tip was located at a centre of 50 mm downstream from the nozzle exit plane in order that boundary layer and wall vicinity effects were neglected and to ensure the tip would be in line with the oncoming

flow direction. The probe was set on a quadrant arc to allow the sensing holes to record pressures at different pitch and yaw angles with an increment of  $5^\circ$  in which pressure coefficients at each calibration point in pitch and yaw planes were calculated. Bryer and Pankhurst [79] had shown that a direct calibration at one Reynolds number can be applied to applications at a wide range of Reynolds numbers.

Pressures from the five-hole probe were measured separately using five differential pressure transducers by mean values from each individual sensing hole in the ranges of  $-30^\circ < \beta < 30^\circ$  and  $-20^\circ < \alpha < 30^\circ$  for each pitch and yaw motions. Dynamic pressures of the flows were measured by a use of pitot-static tube locating at a fixed point from the nozzle exit plane. However, owing to its small size probe tip diameter, an individual sensing hole calibration is required to indicate the salient features such as probe sensitivity, effect of Reynolds number and viscous effect.

#### 5.4.1 Reynolds number effect

Figure 5.4, Figure 5.6 and Figure 5.8 represent typical pitch and yaw pressure coefficients plots in non-nulling calibration of the pyramid-type five-hole probe at three different Reynolds numbers. A reasonable clarification from Bryer and Pankhurst [76] can be able to explain this particular equivocal measurement. Separation over one or more sensing holes is an important issue which should be taken into account. G. Zilliac [82] and C. Tropea [85] agree that the flow separation involves at an oncoming flow angle approximately  $30^\circ$  leading to separation for most of pressure probes. Brayer and Prankhurst [76] also indicated that to give an accuracy in the measurement, pitch and yaw angles are limited to  $\pm 25^\circ$ . Similarly, Melda [75] supported Brayer and Prankhurst that the use of five-hole probe with an accuracy of  $\pm 2\%$ , pitch and yaw angles should be limited in the range of  $\pm 20^\circ$  to  $\pm 25^\circ$ . Consequently, an examination of the individual sensing hole-based coefficients would identify the flow phenomena which might prove that they are sensitive to pitch and yaw motions. Three-dimensional surface curves for pitch, yaw and static pressure coefficients at different  $\alpha$  and  $\beta$  are displayed in Appendix D. From the typical calibration plots for the pressure coefficients at all three Reynolds numbers provide that at moderate pitch and yaw angles, say  $|\alpha|$  and  $|\beta|$  are approximately at  $20^\circ$  the pressure coefficient in pitch is a linear function. Similarly, the pressure coefficient in yaw also alters linearly. In contrast, when the angle is larger than  $20^\circ$  the pressure coefficient is non-linear. Minimum static pressure was measured when pitch and yaw angles approach  $0^\circ$  and increases when pitch and yaw angles increase. This minimum value was calculated by Eq. 5.4 where the denominator depends on pressure from the centre hole and the average pressure from the outer four holes.

Another form of pitch and yaw angle calibration is shown in Figure 5.4 to Figure 5.15. Pressure coefficient with yaw angle increases with increasing yaw angle.

Unlikely, it decreases as the pitch increases in Figure 5.11, Figure 5.13 and Figure 5.15. Now that behaviour of the pressure coefficients in both pitch and yaw is linearly proportional to the angles of  $-20^\circ < \alpha, \beta < 20^\circ$ . The probe asymmetry is observed about zero pitch and yaw angles, which is due to an imperfection during a manufacturing process. It is also displayed in Figure C.11 and Figure C.12 in terms of static pressure coefficient as at zero pitch and zero yaw angle the static pressure coefficients are not in the centre of the plots. In Figure 5.20 presents the centre pressure sensing hole response which indicates the true probe alignment to the air flow. It can be easily seen that the in the calibration process the probe axis was aligned at  $0^\circ$  to pitch and yaw angles to the flow.

### 5.4.2 Probe sensitivity

Due to small tip diameter, the probe is expected to be sensitive to flow direction. Sensitivity is a parameter to determine a performance of the probe in measuring pressure difference in order to determine an ability of the probe which reflects the magnitude change of flow velocity and direction. Hence to investigate an individual sensing hole at variation in pitch and yaw should provide an optical suggestion of the probe sensitivity to the flow direction. The individual sensing-hole coefficient is in the form of:

$$\text{Pressure coefficient (i)} = \frac{\mathbf{P}_i - \mathbf{P}_{dynamic}}{\mathbf{P}_{total} - \mathbf{P}_{static}} \quad (5.27)$$

where i represent the sensing-hole from 1 to 4

The corresponding data from pitch holes (hole no.1 and hole no.3) and yaw hole (hole no.2 and hole no.4) at Reynolds number of 565 and 790 are presented in Figure C.13 to Figure C.16 in Appendix C. The pressure distribution in hole no.1 increases as the angle increases in pitch plane from Figure 5.16. In contrast, the pressure distribution from hole no.3 decreases as pitch angle increases from Figure 5.18. Likewise, the pressure distributions in the yaw hole in the yaw plane also behave the same way as in the pitch plane. The curvature of contour arcs from the pressure distributions increases as the pressure decreases since the flow more directly gets into the pressure sensing holes.

Figure 5.16 to Figure 5.20 show all five pressure sensing holes respond to flow angles in pitch and yaw. There are only four out of five pressure taps which were perfectly manufactured. The pressure reading from hole 3 is believed to contain some error due to manufacturing imperfections caused by the grinding process. The calibration plot of the probe for this hole can be seen in Figure 5.18 as the pressure distribution between  $-30^\circ < \beta < -20^\circ$  is slightly lower than the pressure distribution from  $20^\circ < \beta < 30^\circ$  at the same pitch angle. The contour of pressure distribution generated from an average pressure coefficient in Figure C.10 in



Appendix C replicates the effect of the probe asymmetric response very well. The contour does not generate a symmetrical pattern but missing a quarter section on the left hand side of the plot. This is a result of  $P_3$  being asymmetric. However, the characteristics of the probe response such as  $CP_{pitch}$  and  $CP_{yaw}$  are acceptable.

In the study of G. Zilliac [82] it was indicated that the spacing between pressure coefficients specifies the probe sensitivity. A larger gap of pressure coefficient shows the higher region of the probe sensitivity. In his case study, he tested a cone-type seven-hole probe across a Reynolds number range between  $1.8 \times 10^4$  and  $5.9 \times 10^4$ . According to Zilliac's method and the calibration results, the five-hole probe sensitivity depends on the flow angle and the sensitivity to the flow direction increases due to an increase in space between pressure coefficients.

### 5.4.3 Uncertainty analysis

Although the measurements are carefully tested, they are subject to contain some errors. The sources of any uncertainty can be classified into two groups, those associated with the instruments used to acquire the experimental data and those associated with the data reduction process. This analysis section is one of the significant parts of any experiment to reduce errors to a certain level in order that the experimental results are acceptable. The uncertainty analysis in this section is based on a study of uncertainties in physical measurements by John Taylor [86].

The analysis introduces a discrepancy of two measurement quantities then using the discrepancy called a "fractional uncertainty" in a percentage defined as:

$$uncertainty = \frac{\delta \mathbf{x}}{|\mathbf{x}_{best}|} \times 100\% \quad (5.28)$$

where  $(\delta x)$  is the uncertainty (discrepancy) in any measurement value,

$$measured\ value\ \mathbf{x} = \mathbf{x}_{best} + \delta \mathbf{x} \quad (5.29)$$

Suppose that a quantity "q" is a measured value which contains the independent quantities x, y, z, u, v and w in products and quotient terms as shown

$$\mathbf{q} = \frac{\mathbf{x} \times \mathbf{y} \times \mathbf{z}}{\mathbf{u} \times \mathbf{v} \times \mathbf{w}} \quad (5.30)$$

Thus the uncertainty can be evaluated as;

$$\frac{\delta \mathbf{q}}{\mathbf{q}} = \sqrt{\left(\frac{\delta x}{x}\right)^2 + \left(\frac{\delta y}{y}\right)^2 + \left(\frac{\delta z}{z}\right)^2 + \left(\frac{\delta u}{u}\right)^2 + \left(\frac{\delta v}{v}\right)^2 + \left(\frac{\delta w}{w}\right)^2} \quad (5.31)$$

Notice that the pressure coefficients in pitch and yaw motions are defined in equation 5.32 and equation 5.33

$$C_{P\alpha} = \frac{P_3 - P_1}{P_5 - P_{ave}} \quad (5.32)$$

$$C_{P\beta} = \frac{P_2 - P_4}{P_5 - P_{ave}} \quad (5.33)$$

Subsequently, the uncertainties for the pressure coefficients in both pitch and yaw motions can be defined by "the uncertainty in quotients" from Eq. 5.34

$$\frac{\delta C_{p\alpha}}{C_{P\alpha}} = \sqrt{\left[\frac{\delta(P_3 - P_1)}{P_3 - P_1}\right]^2 + \left[\frac{\delta(P_5 - P_{ave})}{P_5 - P_{ave}}\right]^2} \quad (5.34)$$

However, the uncertainty of the pressure difference can be expressed similarly to the uncertainty in products and quotients and is called "an uncertainty in difference";

$$\delta(P_3 - P_1) = \sqrt{\delta(P_3)^2 + \delta(P_1)^2} \quad (5.35)$$

$$\delta(P_5 - P_{ave}) = \sqrt{\delta(P_5)^2 + \delta(P_{ave})^2} \quad (5.36)$$

Five cases of typical values for the pitch and yaw pressure coefficients will be investigated. The five regions of interest are when the flow is close to zero pitch and yaw, at large pitch angles, at large yaw angles, moderate pitch and yaw angles and when both pitch and yaw angles are large;

- at small pitch-yaw angle, pitch 0° degree yaw 0° degree
- at small pitch angle large yaw angle, pitch 0° degree yaw 30° degrees
- at small yaw angle large pitch, pitch 30° degrees yaw 0° degree
- at moderate pitch and yaw angles, pitch 15° degrees yaw 20° degree
- at large pitch-yaw angle, pitch 30° degrees yaw 30° degrees and pitch 30° degrees yaw -30°.

The estimated uncertainties and the calculated quantities compared with measured quantities are shown in Table 5.1 to Table 5.3. These are typical values for the errors involved with taking the pressure measurements and entering them through the data reduction scheme. Typical values of the angles found in the 5-hole probe calibration are between  $-15^\circ$  and  $+15^\circ$  in pitch and  $-20^\circ$  and  $+20^\circ$  in yaw.

$\alpha$	$\beta$	$C_{P\alpha}$	$C_{P\beta}$	$C_{P\alpha}$ new	$C_{P\beta}$ new	$\delta\alpha$	$\delta\beta$
$0^\circ$	$0^\circ$	0.0705	-0.0894	0.0411	-0.0522	$0.12^\circ$	$0.03^\circ$
$30^\circ$	$0^\circ$	-2.6619	0.1031	-2.1903	0.0851	$1.09^\circ$	$0.06^\circ$
$0^\circ$	$30^\circ$	0.1424	2.0894	0.1569	2.2994	$0.19^\circ$	$1.25^\circ$
$15^\circ$	$20^\circ$	-1.5684	2.0355	-1.2863	1.7709	$0.34^\circ$	$0.32^\circ$
$30^\circ$	$30^\circ$	-26.2943	19.5206	-21.1170	15.6770	$1.02^\circ$	$1.01^\circ$
$30^\circ$	$-30^\circ$	-24.2572	-27.8936	-19.6241	-22.5659	$1.08^\circ$	$-1.09^\circ$

TABLE 5.1 The uncertainties for  $Re = 340$ 

$\alpha$	$\beta$	$C_{P\alpha}$	$C_{P\beta}$	$C_{P\alpha}$ new	$C_{P\beta}$ new	$\delta\alpha$	$\delta\beta$
$0^\circ$	$0^\circ$	-0.0387	-0.0416	-0.0127	-0.0131	$0.70^\circ$	$0.48^\circ$
$30^\circ$	$0^\circ$	-3.4268	0.2231	-2.9002	0.2573	$1.03^\circ$	$0.21^\circ$
$0^\circ$	$30^\circ$	0.0403	3.7648	0.0494	2.9148	$0.09^\circ$	$1.05^\circ$
$15^\circ$	$20^\circ$	-1.8563	2.5997	-1.5106	2.2356	$0.51^\circ$	$0.67^\circ$
$30^\circ$	$30^\circ$	-21.6835	21.5199	-18.8864	18.7438	$1.17^\circ$	$1.26^\circ$
$30^\circ$	$-30^\circ$	-24.4437	-24.7298	-22.8548	-22.8009	$1.08^\circ$	$-1.25^\circ$

TABLE 5.2 The uncertainties for  $Re = 565$ 

$\alpha$	$\beta$	$C_{P\alpha}$	$C_{P\beta}$	$C_{P\alpha}$ new	$C_{P\beta}$ new	$\delta\alpha$	$\delta\beta$
$0^\circ$	$0^\circ$	-0.0592	-0.0214	-0.0523	-0.0189	$0.12^\circ$	$0.03^\circ$
$30^\circ$	$0^\circ$	-4.4726	0.3130	-3.7570	0.3630	$2.07^\circ$	$0.28^\circ$
$0^\circ$	$30^\circ$	-0.0277	4.4416	-0.0321	3.7446	$0.03^\circ$	$2.09^\circ$
$15^\circ$	$20^\circ$	-2.1605	3.1198	-1.7285	2.6518	$0.42^\circ$	$0.51^\circ$
$30^\circ$	$30^\circ$	-21.5381	19.7493	-18.3720	15.9969	$2.03^\circ$	$1.85^\circ$
$30^\circ$	$-30^\circ$	-19.0249	-22.0459	-15.7906	-18.2981	$1.97^\circ$	$-2.05^\circ$

TABLE 5.3 The uncertainties for  $Re = 790$

## 5.5 Concluding remarks

The five-hole probe in this study is a "forward facing pyramid" type. It was manufactured by soldering five stainless steel hypodermic tubes with outer diameter of 0.56 mm together providing the probe tip diameter of 1.68 mm. Each of the outer tube was chamfered at 45° with respect to a horizontal axis. The probe tip is 180 mm from the stem in order to minimise the stem influence effect.

Calibration procedures were tested in a boundary layer wind tunnel at three different flow speeds at 3 m/s, 5 m/s and 7 m/s providing Reynolds number based on the probe tip of 340, 565 and 790 respectively so as to investigate Reynolds number effect. Within this range of flow speed, the flow is considered to be incompressible flow. The probe was calibrated in a non-nulling mode with the probe tip located at a centre plane of 50 mm downstream from the nozzle exit plane to avoid the boundary layer and wall vicinity effects to influence the pressure reading. It has been demonstrated that as Reynolds number increases, the grids elongation in the diagonal direction contract providing a reduction in the pitch and yaw pressure coefficients when  $\alpha$  and  $\beta$  were large. When  $\alpha$  and  $\beta$  were less than 20°, each grid shape is nearly rectangular which represents an accuracy of the pitch and yaw angles in determination of flow angle and velocity magnitude as in Figure 5.5, Figure 5.7 and Figure 5.9. There is an important point to note that at large pitch and yaw angles,  $\alpha = 35^\circ$  and  $\beta = \pm 35^\circ$  the pressure coefficient values in both pitch and yaw planes at all three Reynolds numbers became interchangeable, i.e. values change sign from positive to negative or negative to positive. This result was thought to be due to viscous effects and flow separation at the probe tip when the probe was tested at pitch and yaw angles of more than 30°. Hence, the calibration process for pitch and yaw angles over 30° were neglected. All the results represented here are corresponding to maximum of  $\pm 30^\circ$  in yaw and  $-20^\circ \leq \alpha \leq 30^\circ$  in pitch. From the individual hole-based coefficient plots allow the probe sensitivity to be inspected. It has been indicated from Figure C.13 to Figure C.16 in Appendix C that the probe sensitivity increases as the pitch and yaw increase. The final analysis considers in the errors of the pressure reading at five different areas. The results of uncertainty were interpolated in Table 5.1, Table 5.2 and Table 5.3 that the errors in the flow angles in both pitch and yaw are found to be more than 1° at large pitch and yaw angles. The angle variations get smaller and smaller at the small angles for both pitch and yaw motions. Therefore, it is reasonable to pronounce that the typical values of the angles used by the 5-hole probe measurement are between  $\pm 15^\circ$  in pitch and  $\pm 20^\circ$  in yaw.

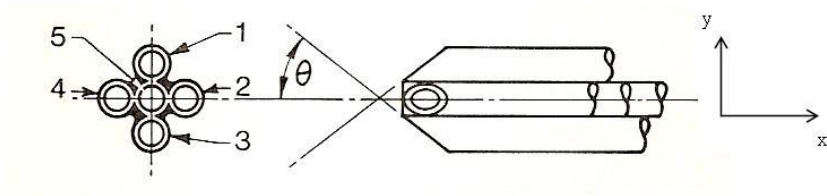


FIGURE 5.1 Schematic diagram of forward facing Pyramid five-hole pressure probe [76]

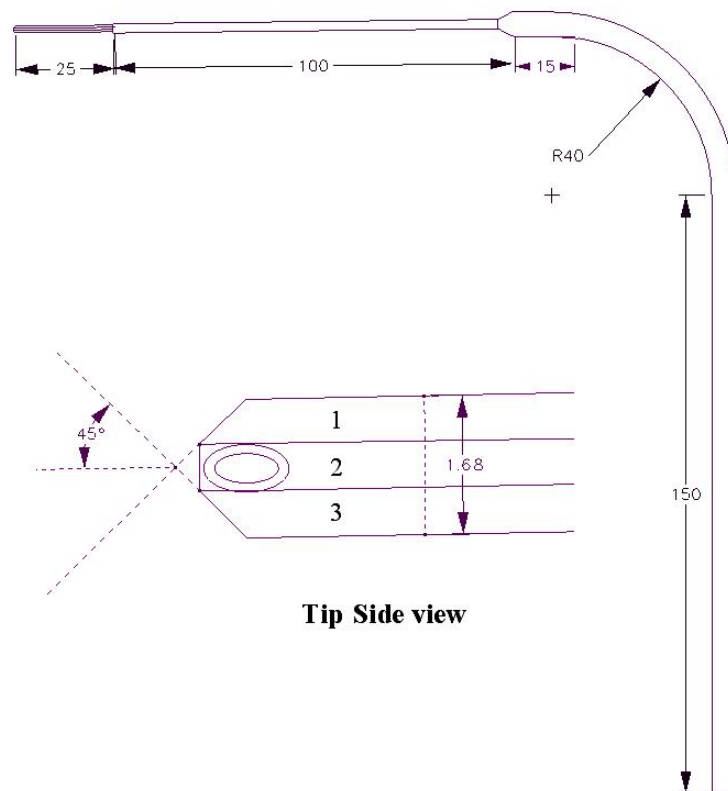


FIGURE 5.2 Schematic diagram of five-hole probe in 2 dimensions (Unit in mm)

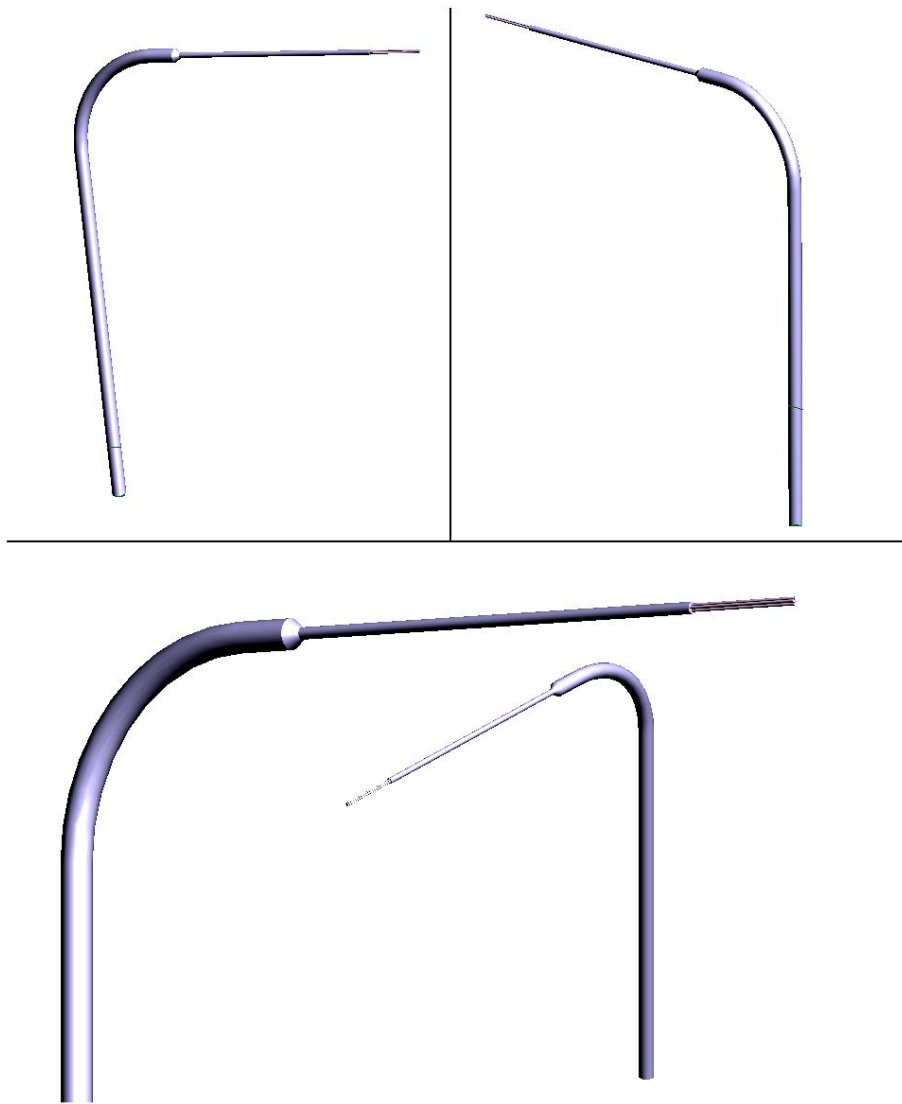


FIGURE 5.3 Schematic diagram of five-hole probe in 3 dimensions

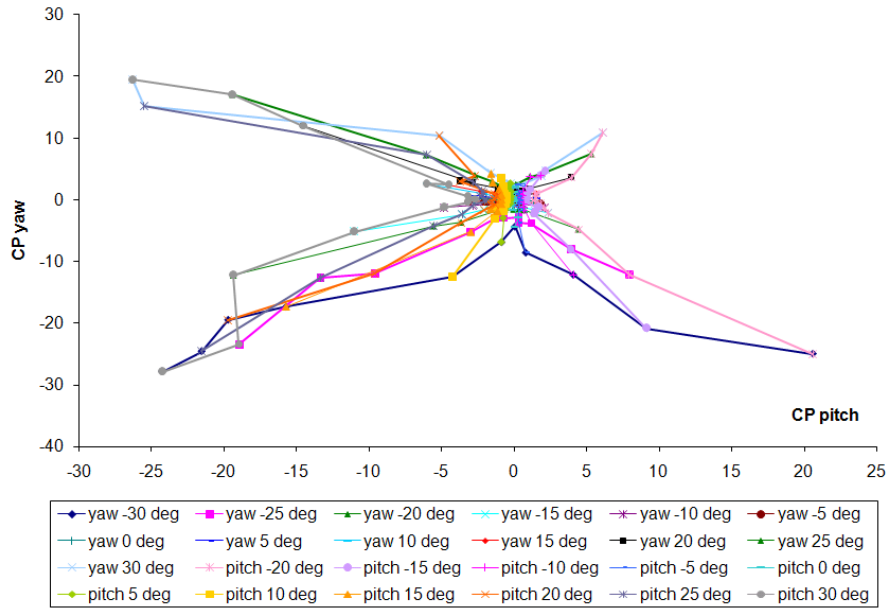


FIGURE 5.4 Pitch and yaw angles pressure coefficient at  $Re = 340$

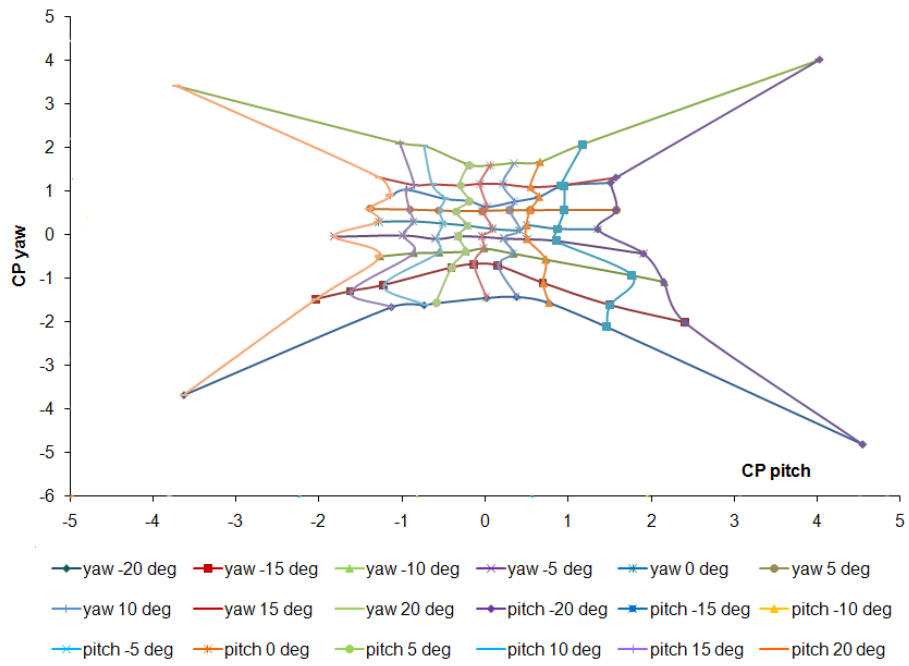


FIGURE 5.5 Pitch and yaw angles pressure coefficient at  $Re = 340$  at  $\alpha = \pm 20^\circ$  and  $\beta = \pm 20^\circ$

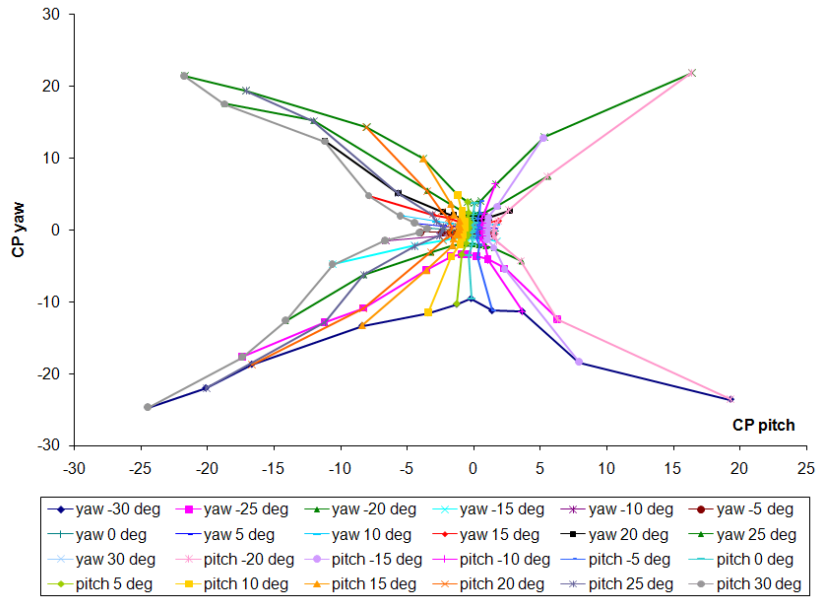


FIGURE 5.6 Pitch and yaw angles pressure coefficient at  $Re = 565$

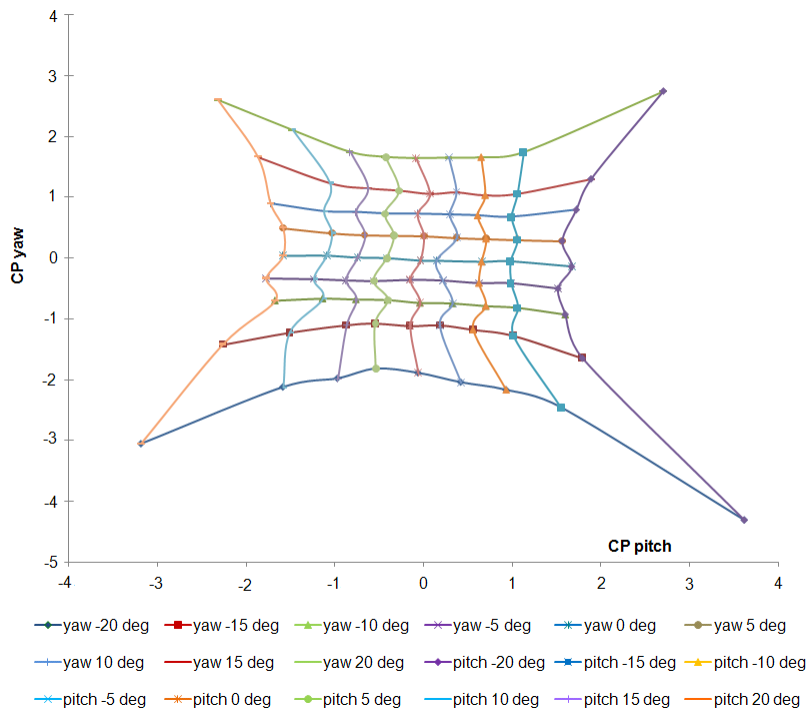


FIGURE 5.7 Pitch and yaw angles pressure coefficient at  $Re = 565$  at  $\alpha = \pm 20^\circ$  and  $\beta = \pm 20^\circ$



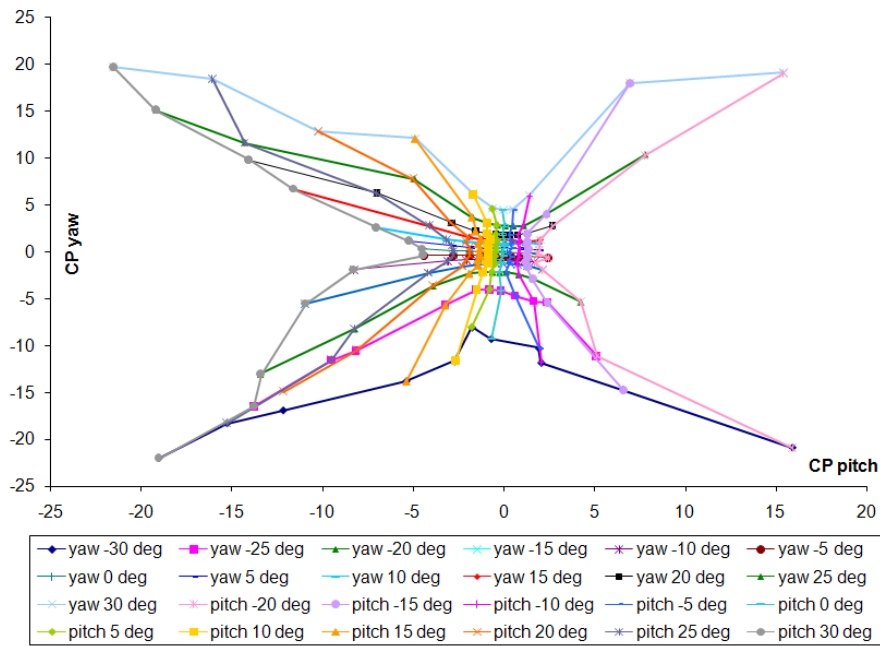


FIGURE 5.8 Pitch and yaw angles pressure coefficient at  $Re = 790$

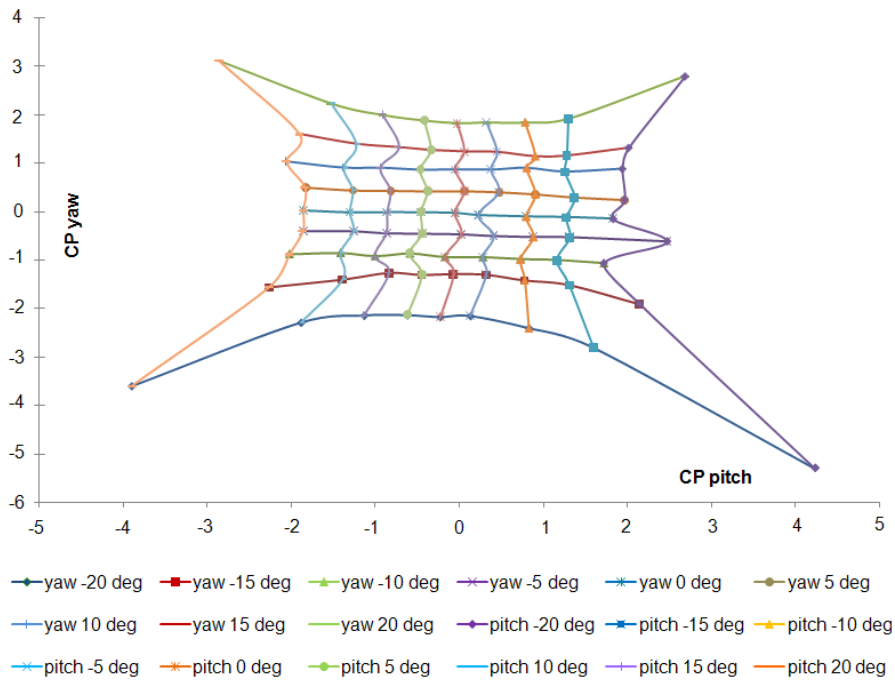


FIGURE 5.9 Pitch and yaw angles pressure coefficient at  $Re = 790$  at  $\alpha = \pm 20^\circ$  and  $\beta = \pm 20^\circ$

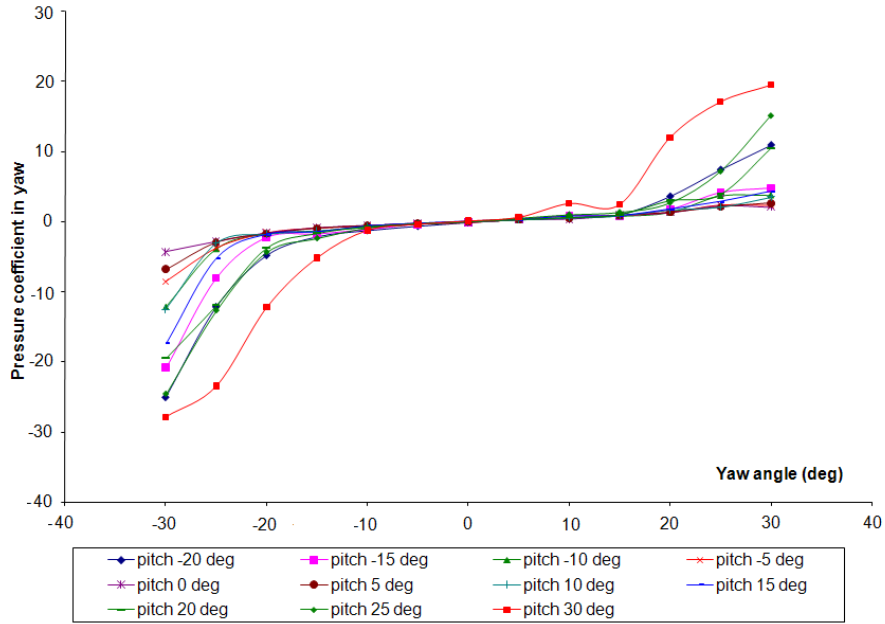


FIGURE 5.10 Yaw angle calibration at  $Re = 340$

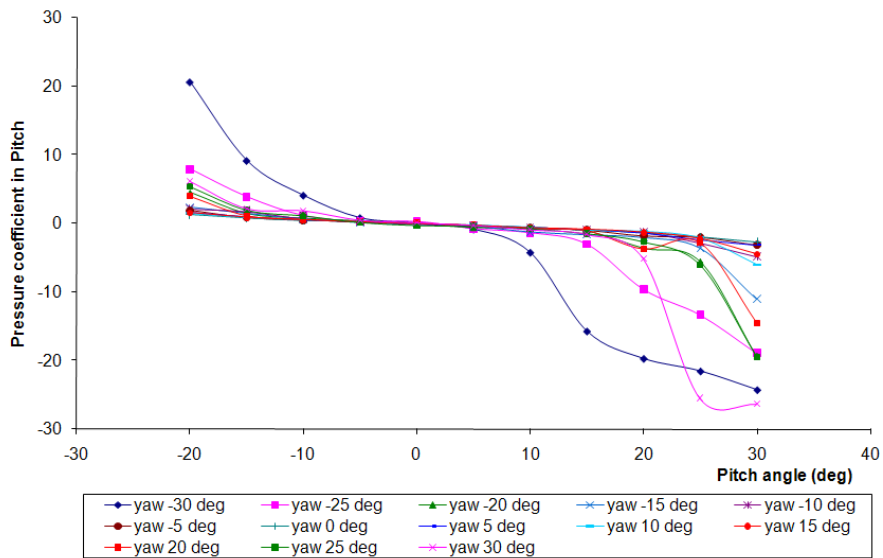


FIGURE 5.11 Pitch angle calibration at  $Re = 340$

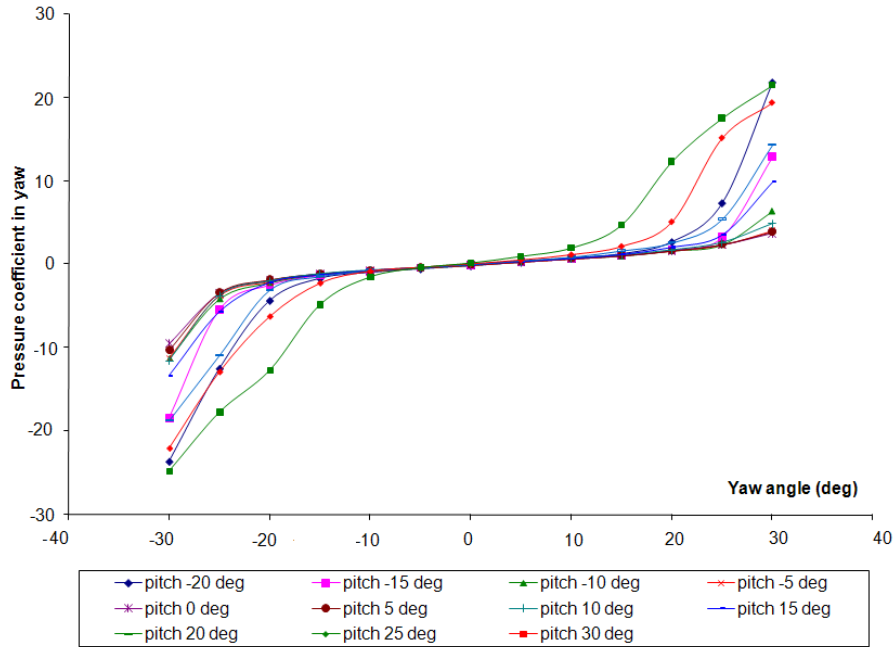


FIGURE 5.12 Yaw angle calibration at  $Re = 565$

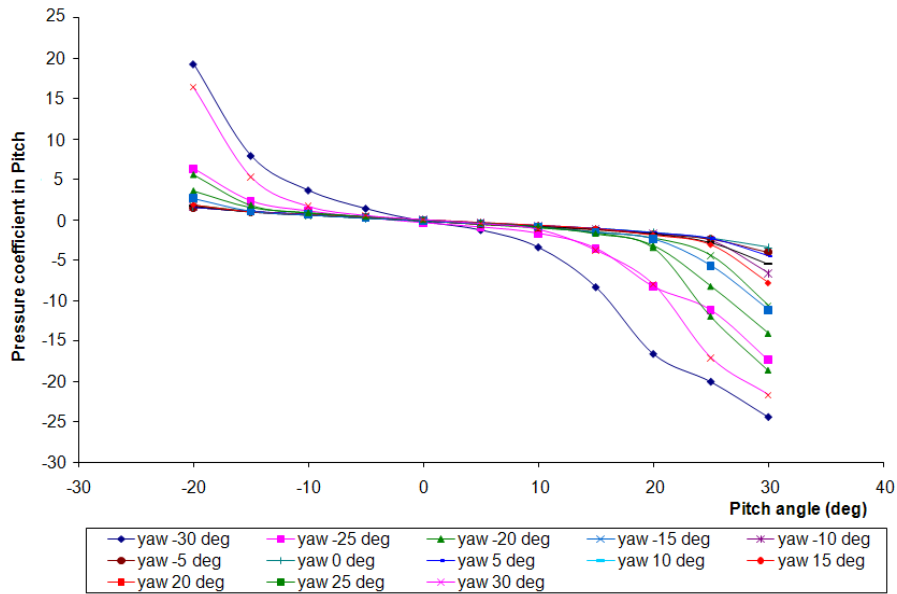


FIGURE 5.13 Pitch angle calibration at  $Re = 565$

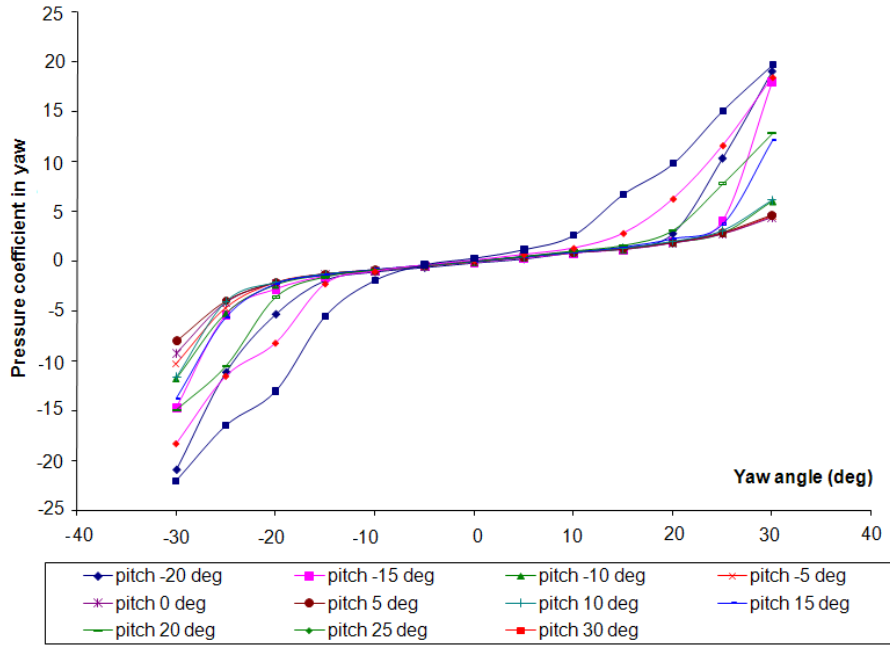


FIGURE 5.14 Yaw angle calibration at Re = 790

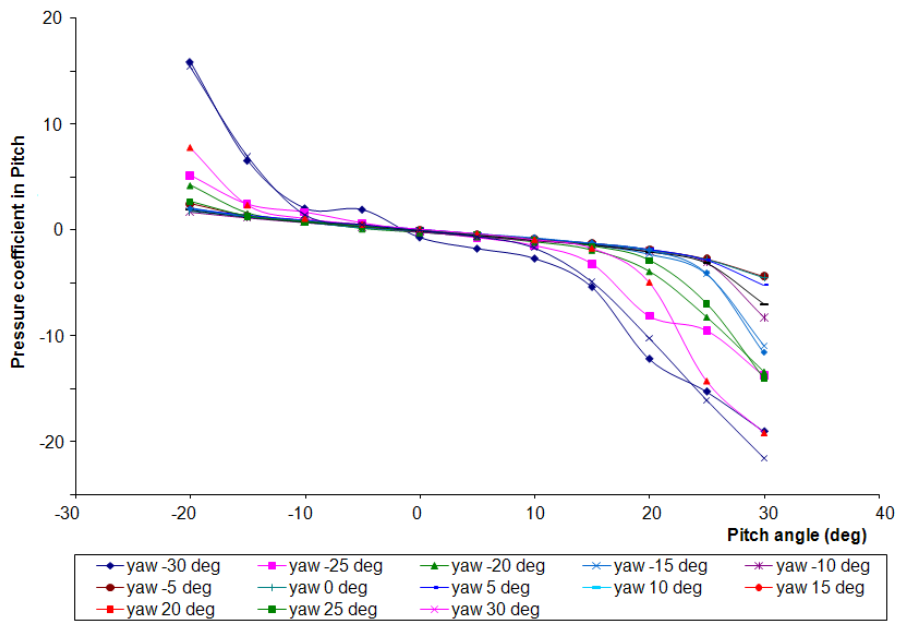


FIGURE 5.15 Pitch angle calibration at Re = 790

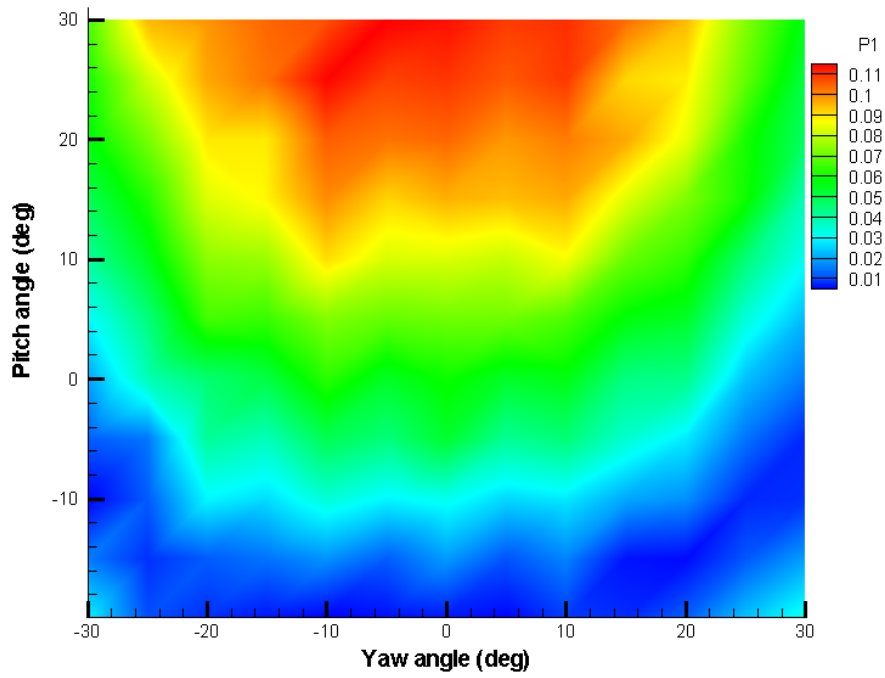


FIGURE 5.16 Pressure port no. 1 response to pitch and yaw motions

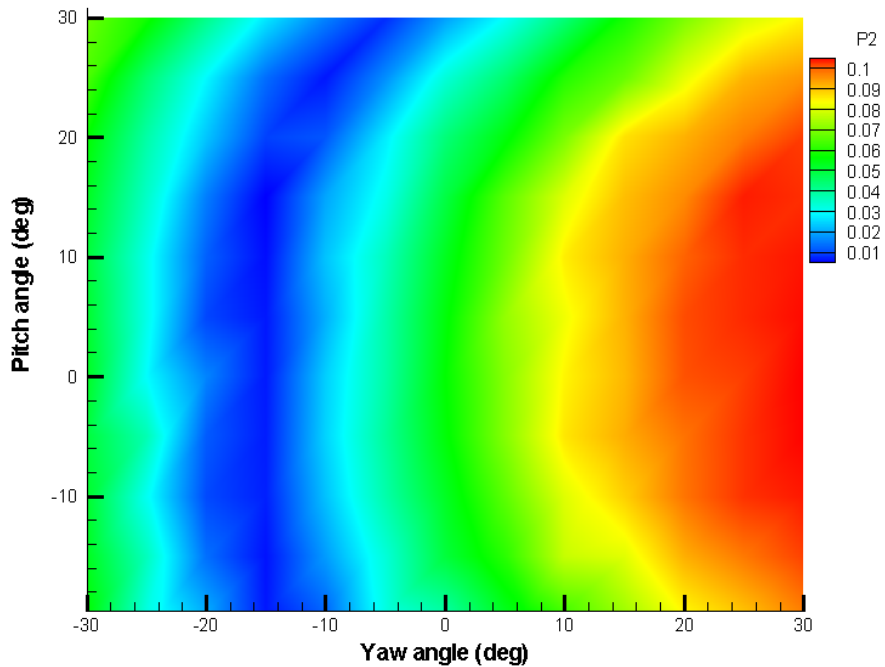


FIGURE 5.17 Pressure port no. 2 response to pitch and yaw motions

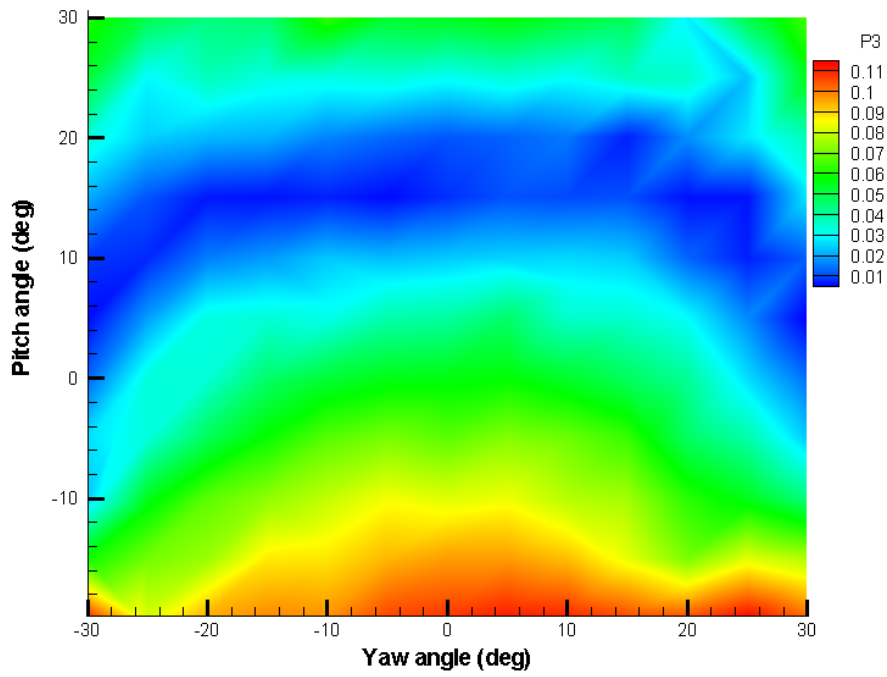


FIGURE 5.18 Pressure port no. 3 response to pitch and yaw motions

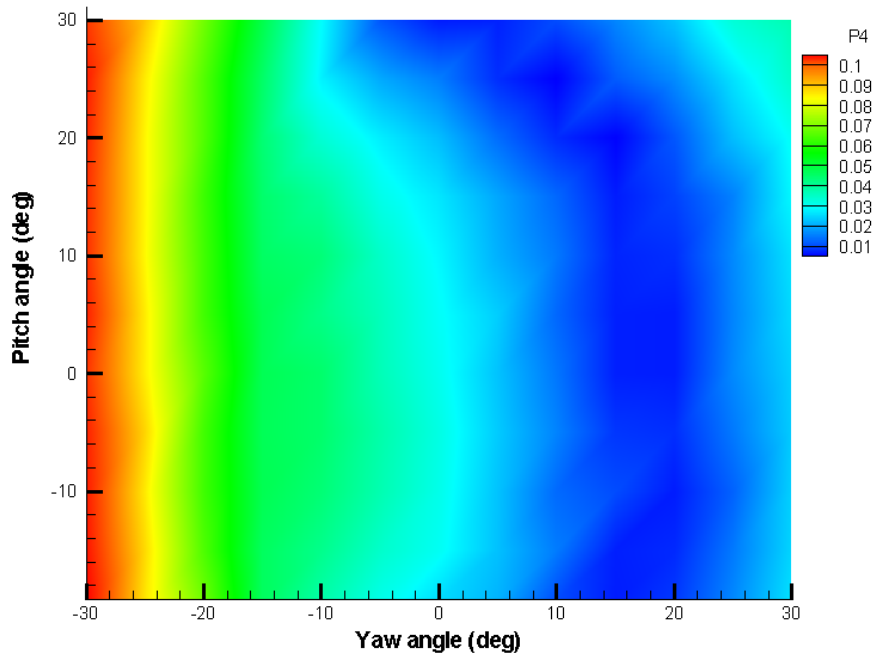


FIGURE 5.19 Pressure port no. 4 response to pitch and yaw motions

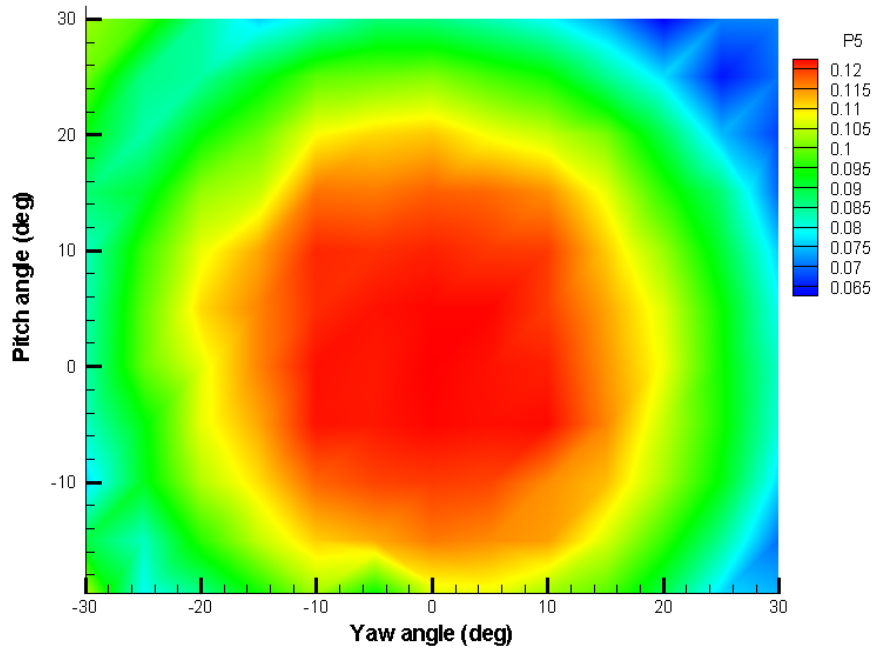


FIGURE 5.20 Pressure port no. 5 response to pitch and yaw motions





# Chapter 6

## Flow behind surface mounted bluff bodies

### 6.1 Introduction

In general, wind tunnel experiments are focused on measurement of the forces, such as lift, drag, pitching moment and pressure fields which represent the free-air condition in the full-scale application. A study of a flow field around surface-mounted obstacles is a fundamental study to evaluate how airflow behaves and understands the flow mechanisms of complex three dimensional flow. Over two decades, there have been a number of research projects into the physics of the airflow around surface-mounted bluff bodies to predict the effect of wind loading on buildings, wake flow behind buildings and air pollution dispersion, etc. The aim of this study is to analyse velocity flow fields and angularity in 2– dimensions at different locations downstream from the back of a single- and twin-building configurations by the use of the five-hole probe. The building models were mounted in the wind tunnel with roughness elements and wake generators located far upstream from the buildings to simulate a three dimensional flow representing urban flow conditions. The analysis concentrates on major characteristics of the flow influenced by the model geometry. Finally, gust frequencies produced by two building configurations will be approximated for simulation of the unsteady and nonlinear forces on UAVs encountering gusts around buildings.

## 6.2 Experimental apparatus and measurement technique

### 6.2.1 Building geometry and boundary layer thickness

Experiments of the flow behind the 3– dimensional surface-mounted obstacles were conducted in the closed wind tunnel, (see Figure 4.1 in Chapter 4). The experiments were conducted with a combination of roughness elements and wake generators shown in Figure 6.1 which allowed the simulation of a boundary layer thickness,  $\delta$  of 235 mm. A configuration of the boundary layer thickness agrees with a power law of the mean velocity with an exponent between  $0.143 < n < 0.17$ . Additionally, due to the calculation based on ESDU Data sheet 82026 the atmospheric boundary layer is approximately 372 metres which provides the scale ratio of the simulated boundary layer to the atmospheric boundary layer as 1 : 1600.

A single building model and twin-building model with a passage gap of 120 mm,  $W/H = 0.6$ , were tested separately in the closed wind tunnel with free stream velocity of approximately 5 m/s. Pressure and velocity fields were measured at three different downstream locations at specified distance  $X/H$  ratios of 0.75, 1.00 and 1.50 as in Figure 6.3. The locations downstream from the back of the building were estimated by Figure 6.2 where the tufts were the most interrupted. From the photographs, the location can be estimated in between  $X/H = 0.5$  and  $X/H = 1.5$ . The location downstream from  $X/H = 1.5$ , the tufts were not interrupted as much as the area between  $0.5 < X/H < 1.5$ .

The building models were made of ureol (polyurethane) with dimensions of 200 mm wide, 200 mm high and 100 mm long, mounted on a turntable in the middle of the test section of the wind tunnel facing normal to the freestream direction. The building(s) geometry of 200 mm wide, 200 mm high and 100 mm long were chosen based on wind environment around a single building of rectangular shape (Figure 2.17 in Chapter 2). Wind flow around a tall building configuration as shown in the first column of Figure 2.17 is not predominant and has the worst effect compared with all three configurations because the majority of the air flow around the tall slender building is mainly transported alongside of the building and reverse air flows behind the building may or may not occur. A long building configuration in the third column of Figure 2.17 was also taken into account. For a long building case, the majority of the flow is mainly transported over the building rather than passing along sides. Hence, this configuration is not suitable for the air flow investigation either. High building of the transitional type in the second column of Figure 2.17 was selected because the air flow on the windward face of

## §6.2 EXPERIMENTAL APPARATUS AND MEASUREMENT TECHNIQUE

a building is greatly transported downwards and the interaction of the vortex from the windward and the shear separations from the side-edges generate large areas of reverse flow. Another reason to consider is the boundary layer thickness at the test section. This reason determines the height of building models. As boundary layer thicknesses with different experimental set up were measured, the maximum thickness of 235 mm was obtained by the combination of wake generators and surface roughness. In order to investigate the air flow behaviour in as much detail as possible, the model height should not be too small and/or larger than the boundary layer thickness. Therefore, the models height of 200 mm high seems to be sensible compared with the boundary layer thickness. The models with the frontal width of 200 mm wide and thickness of 100 mm were chosen because of a decision of height-to-width ratio of 1. A reason to choose the models thickness of 100 mm is because when rotating a model to different orientation, the model is still considered as the high building of the transitional type. The estimated atmospheric boundary layer thickness in an urban environment is 372 metres above the ground and the simulated boundary layer in the test section is 235 mm. The test boundary layer scale to actual boundary layer scale is 1 : 1600 scale. Hence, the models of 200 mm high in the test section are 320 metres high in real world which is too large compared with UAVs of wingspan in an order of a metre. However, as long as the models immerse in the boundary layer thickness, it is acceptable to investigate the flow around rectangular buildings.

The blockage ratio is based on the frontal area of the building(s) to the total area of the wind tunnel facing freestream direction. This blockage describes in percentage of the oncoming freestream felt by the building(s). These model dimensions resulted in a blockage ratio of the wind tunnel of  $< 1.00\%$ . According to ESDU [87], typically the blockage effect which results in an increase in velocity in the flow around a bluff body is considered in terms of solid-blockage ratio up to approximately 10% to 15%. Hence, the blockage effect is neglected in this case. Reynolds number of the experiment is  $6.8 \times 10^4$  based on the model height (H) and freestream velocity of 5 m/s. The passage width between the twin-building model of 120 mm, ( $w/H = 0.6$ ) allowed an interaction flow between the building model to be investigated. Schofield and Logan [34] described a development of the flow downstream of a surface-mounted obstacle dependent on a parameter called "relative obstacle height" which is the ratio of height of a building model to a boundary layer thickness,  $H/\delta$ . The explanation from Schofield and Logan indicated that the length of separation and reattachment of the flow field behind a building model increases with an increase in the relative obstacle height. The relative obstacle height for this experiment,  $H/\delta \approx 0.85$  specifies that the building is large relative to the boundary layer thickness. It means the flow should separate closer to the front of the building with high average momentum from the upstream flow.

## 6.2.2 Measurement technique

Pressure and velocity fields measured by the five-hole probe were described in Chapter 5. To complement the pressure and velocity fields, the five-hole probe was connected to five Setra Systems differential pressure transducers, model 267, to measure the mean pressure from an individual hole referenced to static pressure of the tunnel. These transducers sense differential pressure and convert this pressure to a proportional high level analog output for both unidirectional and bidirectional pressure ranges. An accuracy of the pressure transducers is within  $\pm 1\%$  error in normal ambient temperature environments, with less than  $\pm 0.06\%$  thermal error over temperature range of  $5^\circ\text{C}$  to  $65^\circ\text{C}$ . Therefore, the velocity distribution and flow angularity measurements contain  $\pm 1\%$  error of the pressure readings from the transducers, but thermal error is neglected.

Measurements of spontaneous pressure response from the five-hole probe were collected. The pressure measurements were sampling at 1000 Hz with a sample time of 8.124 seconds per measurement point. The probe was located in the centre of the tunnel and was traversed horizontally to measure the pressure field at different locations in a spanwise direction with a resolution of  $4 \times 4 \text{ mm}^2$  on three  $yz$  planes as seen in Figure 6.3. For the twin buildings configuration, only half of the plane in a spanwise direction was considered with an assumption of a symmetrical flow condition. The measurement of the individual plane covered an area of  $1.25Y/H$  by  $1.425Z/H$ . On the other hand, the flow field measurements behind the single model arrangement were measured the whole plane in  $YZ$  direction. The measurements covered an area of  $1.35Y/H$  by  $1.425Z/H$  with the same resolution of  $4 \times 4 \text{ mm}^2$  ( $0.02Y/H \times 0.02Z/H$ ).

## 6.3 Experimental results and discussion

This section presents and discusses detailed information of wind flow fields behind three dimensional buildings in 2 different configurations at various downstream locations. Please note that each experiment takes a long period of time up to 2 weeks to conduct, therefore, the repeatability of the experimental results is not available.

### 6.3.1 Single Building Configuration

A rectangular building model was located in a turbulent shear flow produced by roughness elements and turbulence generators placed far upstream from the test section to initially simulate a turbulent urban atmospheric boundary layer. The Reynolds number based on freestream velocity and the building model height is  $6.8 \times 10^4$ .

Figure 6.5, Figure 6.6 and Figure 6.7 show the experimental results of total velocity distribution behind a single building at downstream locations  $X/H = 0.75$ ,  $= 1.0$  and  $= 1.5$  respectively.  $X/H = 0.75$  in Figure 6.5, large wake area of low velocity appears at the plane very close to the back of the building model where further downstream location this wake reduces in size and diffuses as the wake is convected downstream. The area of the low velocity wake may result from the interaction of the shear flow deflected from the front face of the building model and the separation shear layer which separates from the sharp-edge corners causing the wake flow on the back of the building model. Please note that the areas with white shades are the areas where the five-hole probe is believed to encounter the reverse air flow and/or the flow angularity is beyond the probe limits. Hence, all the data encountered in these areas are removed. The air flow from the front of the building model is partly deflected above and aside causing the flow to divide into different velocity layers indicating by different contours. On the second plane  $X/H = 1.0$ , there are more white areas where the flow is beyond the probe limits, i.e. more than  $\pm 15^\circ$  in pitch and  $\pm 20^\circ$  in yaw, and/or is believed the reversal air flow occurred see Figure 6.6. At  $X/H = 1.5$ , the large area of the reversed flow is detected. At this location, it is believed that the shear layer from the roof-top level interferes with the flow circulation from the sharp-edged corner forming the reversal flow which the probe could not measure. At  $X/H = 0.75$  and  $X/H = 1.0$ , the flow is decelerated around the building model, illustrated by the contour velocity less than freestream velocity. The deceleration of the velocity is due to a formation of the separated shear layer around the building model and interference with the recirculation flow from the sharp-edged corners. As the distance from the back of the building increases, the interference of the separated shear flow and the flow circulation from the building corners occur more. It results in a development of the highly complex three dimensional turbulence structure. The results of total velocity distribution at three locations downstream show a small variation of the total velocity outside the building geometry plane because the low velocity shear layer can still be observed, and it reduces in size at the distance  $X/H = 1.5$  from the back of the building model.

2– dimensional velocity vectors in  $y$ - $z$  plane at three different locations downstream from the building model are shown in Figure 6.8, Figure 6.9 and Figure 6.10. At  $X/H = 0.75$ , the majority of the air flow in 2–D is deflected upwards, illustrated by the upward vectors and positive velocity. The vectors over the roof-top level also point upwards indicating the majority of the air flow deflects upwards. Also the flow angularity at  $-0.75 < Z/H < -0.6$  indicates the air flow from the front of the building model is partly deflected aside since the total velocity vectors are very small. Downstream of the building model the wake in  $y$ - $z$  plane is visible because the vectors just above the roof-top level and near the centre point to any random dir-

ections. Further downstream at  $X/H = 1.0$ , the wake region is confirmed to reduce in size. It is clearly seen that the vectors in random direction disappear as it is convected downstream, and at the roof-top level a small wake region is still visible to be seen. At  $X/H = 1.5$ , the wake region completely disappears. Instead, the highly complex three dimensional flow becomes the main flow pattern at this location as one third of the flow field near the sharp-edged corner is removed. The majority of the air flow is still deflected upwards but less in velocity magnitude compared with the air flow at  $X/H = 0.75$ . Near the base on the back of the building model, the total velocity in 2-D and vector length are very small. This may indicate that this location is a stagnation point behind the building model.

The velocity gradients in lateral and vertical directions at  $X/H = 0.75$ , 1.0 and 1.5 are displayed in Appendix D in Figure D.10, Figure D.11 and Figure D.12 respectively. The velocity gradients have the influence to generate in excessive moments during a UAV operation which might cause a difficulty in control. The highest vertical gradients at  $X/H = 0.75$  and  $X/H = 1.5$  are over the roof-top level. Whereas at  $X/H = 1.0$ , the highest velocity gradients are over the roof-top level and near the vertical sharp-edged side. For these locations, it denotes that high velocity gradients seem to happen near the separated shear layer and a location where flow circulation occurs. For the lateral gradients, the location of the highest gradients at  $X/H = 0.75$  and  $X/H = 1.0$  occurs near the vertical sharp-edged side where the separated shear flow and the flow circulation interferes. Whereas at  $X/H = 1.5$ , the velocity gradients are highest above the roof-top and in the centre of the plane. The magnitude of the highest lateral and vertical velocity gradients for the three locations are approximately,  $dU/d(Z/H)$  and  $dU/d(Y/H) \approx 140$ . It means for a 20 metres tall building in an urban environment, the velocity gradients of up to 7 m/s per metre both lateral and vertical directions may be expected.

### 6.3.2 Twin Building Configuration

Wind flow between parallel buildings normally induces problems in passages. The air flow pattern along a channel created by two or more buildings is called "channeling effect" which sometimes generates unpleasant environmental conditions. The model buildings used in this configuration are two rectangular blocks of the same dimensions placed side by side perpendicular to the freestream direction. Wind speed in the passage between the buildings provides a maximum value at a certain separation gap distance depending on the building dimensions. According to Ishizaki and Sung [36], building models with dimensions of  $H \times L \times W = 200 \times 200 \times 100$  (mm) induce a maximum wind speed in the centre of the passage relative to freestream velocity when a separation gap between the building models equals to  $w/H = 0.6$ . Further downstream from the passage gap, wind speed reduces due to increase of flow section and interaction with complex 3-dimensional flow. Please bear in mind

that, the measurement was taken only half of the plane from centre of the gap to one end of the building model. It is assumed that the flow is symmetrical about the centre line between the building models.

Figure 6.11 to Figure 6.13 show the total velocity distributions achieved from the two parallel buildings with a relative separation distance,  $w/H$  of 0.6 to produce a maximum wind speed in the passage. At  $X/H = 0.75$  and  $X/H = 1.0$ , the velocity magnitudes between the buildings are less than the freestream velocity at a location below two-thirds of the building height. The results seem to agree reasonably with numerical simulations from Tutar and Oguz [88] where the velocity distributions obtained in the passage gap between buildings are less than freestream velocity from a distance  $X/H > 0.65$  downstream from the passage exit. The maximum peak value of the velocity in the passage of the first and second planes of the present measurement begins at height of approximately two-thirds of the building height upwards. At  $X/H = 0.75$ , the separated shear layer originating from the passage exit corners can be seen in Figure 6.11 and the measurement points where the five-hole probe was beyond its calibration limits has been removed. The separated shear flow and reversed air flow in Figure 6.12 and Figure 6.13 have also been removed. These shear layers interact with the flow induced by the passage exit, merge together into a single stream and dissipate downstream with decrease in velocity represented by blue contour in Figure 6.13. It is difficult to identify by the total velocity distribution plot whether or not the wake occurs behind the back of the twin buildings compared with a single building case. However, there are some regions where low velocity appears on the back of the twin buildings. The separated shear flow deflected upwards coming from the front of the buildings still visible at  $X/H = 0.75$  and  $X/H = 1.0$  represented by an arc-shaped velocity contour. Further downstream, the separated shear flow begins to disappear due to viscous mixing. Instead, large areas of highly complex flow due to flow interaction are predominant at  $X/H = 1.5$ . The area of an acceleration of the air flow between the buildings disappears. However, the air flow speed in the gap is still higher than the surrounding areas in the same plane of measurement.

Figure 6.14 to Figure 6.16 show the time averaged velocity vector fields obtained from two parallel buildings having the same height at different downstream locations. Please note that the flow was assumed to be symmetrical about the centre of the gap between the buildings. At  $X/H = 0.75$  where the location is closest to the back of the buildings, the wake in 2-dimensions, i.e. in  $y$ - $z$  plane, can be identified as the vectors point to a random direction although recirculation area cannot be presented in 2-dimensional plane. Compare the experimental result at  $X/H = 0.75$  with Tutar and Oguz experiment [88] in  $x$ - $z$  plane at the same ratio  $w/H = 0.6$  in Figure 6.17, it can be seen that in the middle of the gap between the buildings the flow is accelerated and the velocity vectors in  $x$ - $z$  plane are convected downstream due to channeling flow effect and the maximum flow velocity happens clearly in the

centre of the gap between the buildings. In addition in  $y$ - $z$  plane, the maximum of the velocity magnitude occurs at about two-thirds of the building height, see Figure 6.14. In  $x$ - $z$  plane from Tutar's simulation, downstream from the passage exit the flow is still accelerated but less in magnitude than the magnitude in between the gap. At  $X/H = 1.0$  in  $y$ - $z$  plane, the measurement points where the five-hole probe was beyond its calibration limits have been removed near the vertical sharp-edged side and in the gap between the buildings are believed to be the results of flow recirculation areas simulated by Tutar and Oguz in Figure 6.17. The area of the wake behind the back of the buildings in  $y$ - $z$  plane is smaller than the wake area at  $X/H = 0.75$  because the wake diffuses in space as it is convected downstream. The majority of the air flow in  $y$ - $z$  plane still moves upwards with the maximum velocity in the gap between the buildings occurs at approximately two-thirds of the building height. At  $X/H = 1.5$  in  $y$ - $z$  plane compared with Tutar simulation results in Figure 6.17 in  $x$ - $y$  plane, this location is approximately at the centre of the recirculation areas where the reversed flow is generated. It is then confirmed why the velocity vectors in  $y$ - $z$  plane have been removed. It is the location where the five-hole probe could not measure the air flow due to reversed air flow and flow circulation. The magnitude of velocity vectors in the gap between the buildings are also less than the magnitudes at  $X/H = 0.75$  and  $X/H = 1.0$ . The wake area behind the back of the building at this location almost disappears although only small portions of the wake areas can still be seen.

A concise investigation of velocity gradients in vertical and lateral directions are shown in Figure D.13 and Figure D.14 in Appendix D. At  $X/H = 0.75$ , vertical velocity gradients  $dU/d(Y/H)$ , change dramatically over the roof-top level. Whereas at  $X/H = 1.0$  and  $X/H = 1.5$ , the maximum gradients are closer to the gap between the buildings. The magnitude of lateral velocity gradients  $dU/d(Z/H)$  is smaller than vertical velocity gradients. The change in lateral velocity gradients is mainly in the gap between the buildings. The magnitude of the highest  $dU/d(Y/H)$  and  $dU/d(Z/H)$  are approximately 180 and 120 respectively. It means for a 20 metres tall building in an urban environment, the velocity gradients of up to 9 m/s per metre in vertical direction and 6 m/s in lateral direction may be expected.

## 6.4 Summary and conclusions

The study of wind flow fields behind rectangular building models has found the results which can be concluded as follows:

The contour of the total velocity behind a single building has shown large wake area of low velocity the adjacent to the back of the building. This wake area diffuses in space further downstream. The separated shear flow and recirculation area have been removed representing on the plots as white-shaded areas. These areas are the



area where the measurement of five-hole probe was beyond its calibration limits. Further from the leeward side, the white-shaded areas appear more and more. It indicates that as the distance downstream increases the interference of the shear layer and the recirculation area occurs more. In 2-dimensional vector fields in y-z plane at the location adjacent to the building, the majority of the flow moves upwards with low velocity and the random flow vector locates near the roof-top level. Further downstream at  $X/H = 1.0$ , the random velocity vector area is still visible but its location is near the base of the building. Whereas at  $X/H = 1.5$ , the area of high velocity is beyond the building roof-top and the random vector field disappears.

The wind flow pattern between the parallel buildings forms a significantly strong velocity flow in the passage. Large amount of an upstream flow can penetrate through the passage because when the ratio of  $w/H = 60\%$ , it provides the maximum amount of air flow through the passage between the buildings. On the other hand, if a distance of the gap is very small, then large amount of the flow will go around and above the buildings rather than through the gap because the buildings act as if they are only one building. The maximum velocity is observed in the gap between buildings at location approximately  $Z/H = 2/3$ . Further downstream from the passage exit the high velocity flow is reduced due to "free open area" and a viscous mixing flow from a recirculation. The velocity distributions for all three planes of measurement are high near the passage corners due to channeling flow effect. The time-averaged velocity vectors in y-z plane show the high velocity magnitude due to the channeling flow and low velocity magnitude near the inner corners due to separation shear layer. This results from the separated shear layer from the far corners turn towards the back side of the buildings interrelate with the reverse flow. At  $X/H = 1.5$ , the total flow velocity in the passage plane is less than the velocity near the buildings because the accelerated flow from the gap between the buildings decelerates and the channeling flow is less dominant.

The flow fields measured around buildings at model scale can be applied directly to full-scale because aerodynamic investigation of bluff bodies with sharp edges are independent of Reynolds number. According to experiments of Gunter [89], Hoxey et al [90] and Larose [91] suggested the flow around bluff and sharp-edged bodies is independent of Reynolds number. Hoxey et al indicated that the tests on small-scale models in simulated atmospheric boundary layers are acceptable and can be applied directly to full-scale. Hence, the measurements of total velocity distribution, flow angularity/vectors and velocity gradients at model-scale of the flow behind surface-mounted bluff bodies in this Chapter can be applied to full-scale buildings immersed under atmospheric boundary layer.

The results of a change of flow angularity in U-V velocity components behind a single building are presented in Appendix D from Figure D.15 to Figure D.17. The shear separated flow and the wake interaction create the change in flow angularity

in pitch direction. At  $X/H = 0.75$ , the change in flow angularity near the building model is of considerable interest in changing in pitch angle between  $\pm 4^\circ$ . Whereas a location further downstream at  $X/H = 1.0$ , the change in flow angularity tends to increase to approximately  $\pm 8^\circ$  with maximum change in pitch angle location near the sharp-edged left hand corner due to interaction between shear flow and recirculation flow. Moving further downstream at  $X/H = 1.5$ , the maximum change in pitch angle is still visible at the sharp-edged corners. Most of the area behind the building is covered by the highly unsteady complex flow with the flow angularity varies from  $\pm 8^\circ$ . The results of the change in angularity of the flow fields behind twin buildings can be seen from Figure D.18 to Figure D.23 in Appendix D. At the location closest to the buildings plane, most of the flow angularity induced by the channeling flow and flow interaction has a small change in pitch angle which varies in between  $\pm 4^\circ$  which the maximum angle change happens near the sharp-edged side. At  $X/H = 1.0$ , the angularity change in pitch becomes larger varies between  $\pm 9^\circ$  and some small change in pitch can still be seen behind the buildings. The large areas of maximum change in flow angularity are visible at  $X/H = 1.5$  from the back of the buildings. The highest change of the angularity happens in the gap at approximately half of the building height, near the sharp-edged side and near the roof of the building with pitch angle varies from  $\pm 9^\circ$ . To put the change of flow angularity into context, this indicates the difficulty of UAV flying into a sudden change of flow oscillation. It results in a behaviour of UAV to respond to such conditions at different pitch angles. In addition to study the response of UAV in the unsteady motion of a profile oscillation with respect to the change in pitch angle, the experiments of the lift force investigation due to a sinusoidal gust will be explained and discussed in the next Chapter, Chapter 7. The experiments investigate both static and dynamic conditions for a three dimensional wing by varying gust angle ( $\pm 4^\circ$  and  $\pm 8^\circ$ ), oscillation amplitude and frequency to observe UAV behaviour when it flies into a sudden change in flow angularity obtained from the experiments of flow fields behind buildings from this Chapter.

The separated shear layer and wake region behind the buildings generate velocity gradients in lateral and vertical directions. In the single building case, lateral velocity gradient,  $dU/d(Z/H)$  and velocity gradients in the vertical direction,  $dU/d(Y/H)$  reduce when the wake diffuses downstream. The highest velocity gradients in vertical and lateral directions are approximately 140. This implies that for a 20 metre tall building, velocity gradient of up to 7 m/s per metre can be happened. Likewise in the twin building case, velocity gradients in the passage both in lateral and vertical directions reduce as the distance increases downstream from the back of the buildings. The magnitude of velocity gradient in the vertical direction for the twin building case is slightly higher than the single building configuration. With the same actual building height of 20 metres, velocity gradient of 9 m/s per metre can be expected. A similar effect is observed in the twin buildings for velocity

gradient in the lateral direction, but is less in magnitude compared with velocity gradient in the vertical direction, (Figure D.13 and Figure D.14 in Appendix D). Velocity gradient in lateral direction implies approximately up to 6 m/s per metre of the actual building size of 20 metres high.

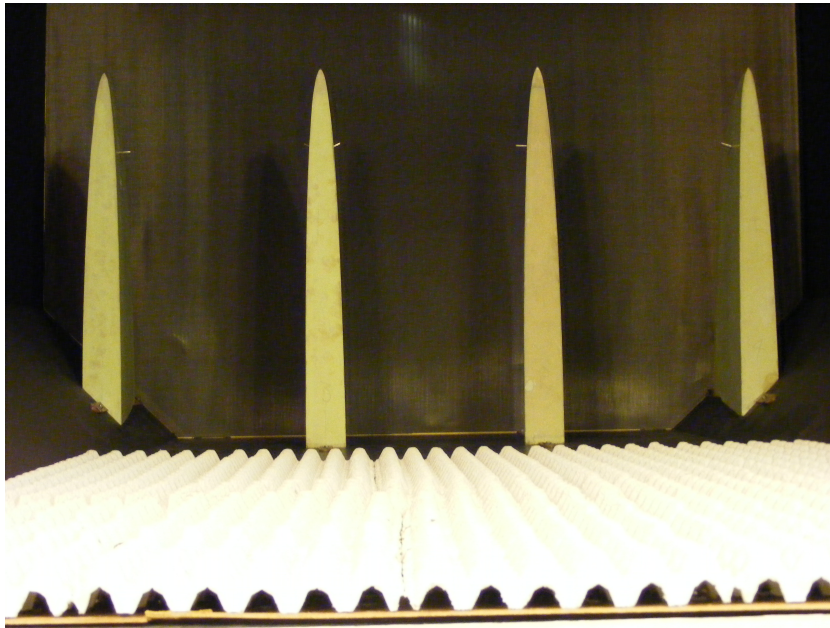
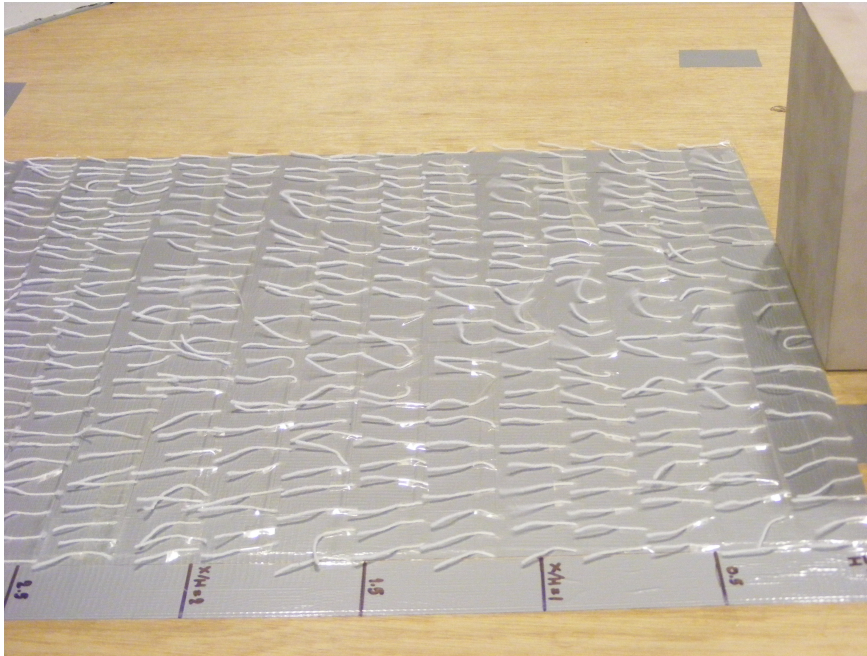


FIGURE 6.1 Wake generators and roughness elements

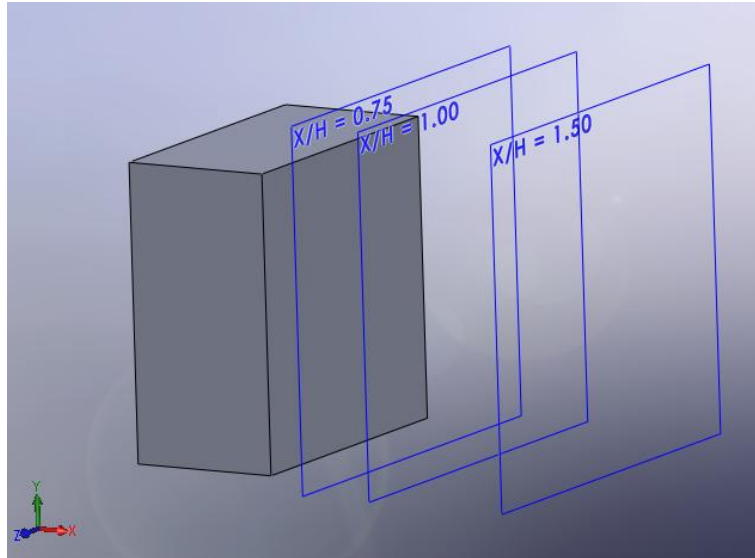


(a) Flow behind a single building

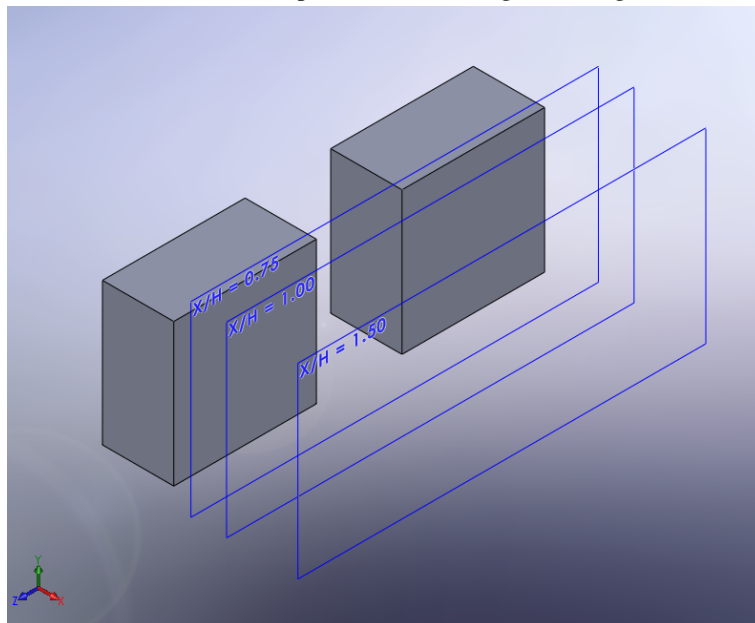


(b) Flow behind twin buildings

FIGURE 6.2 Estimated measurement locations based on tuft flow



(a) 3 different planes behind a single building



(b) 3 different plane behind twin buildings

FIGURE 6.3 Measurements at different longitudinal locations behind building models

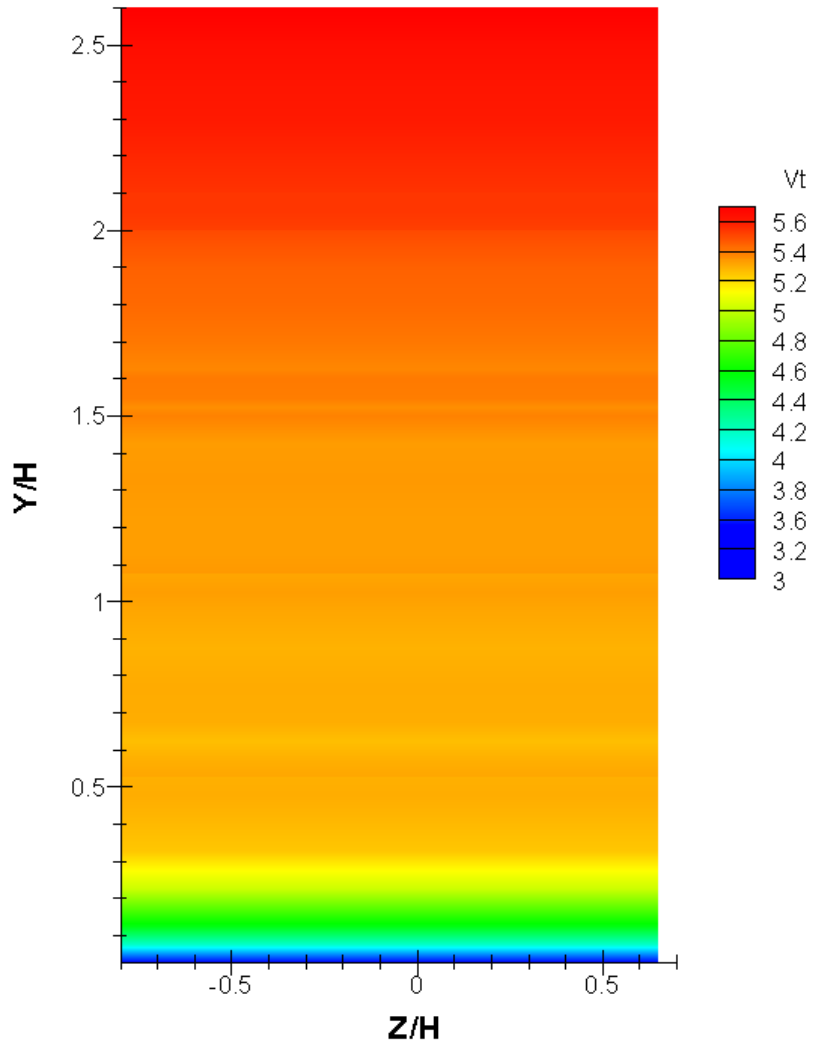


FIGURE 6.4 Velocity field without buildings at test section

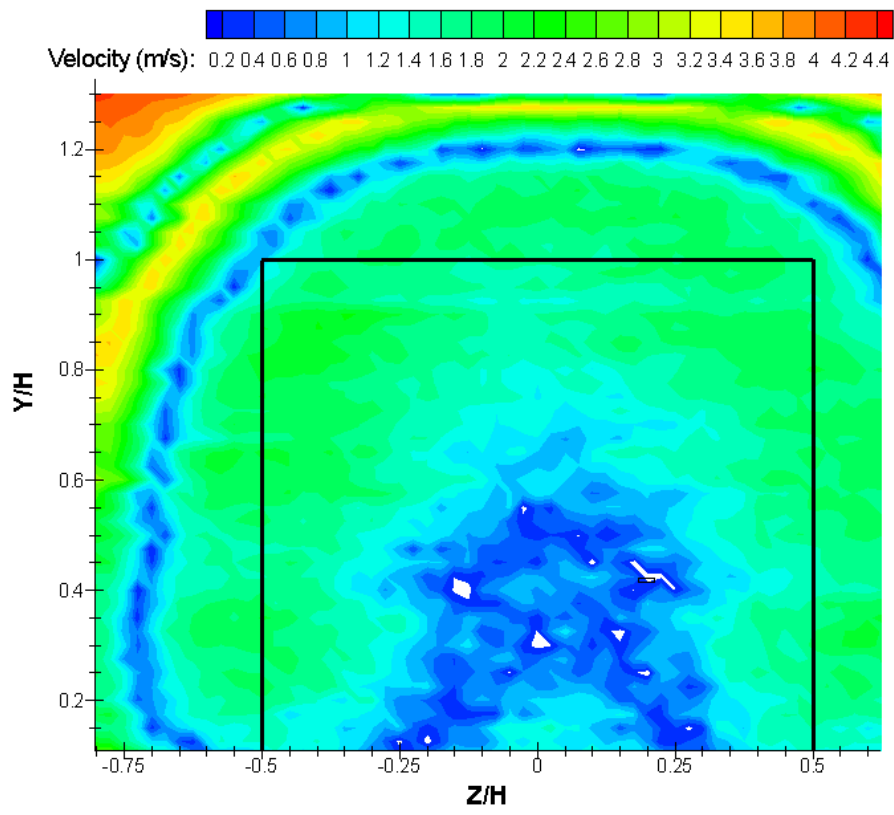


FIGURE 6.5 Velocity field behind a single building at  $X/H = 0.75$



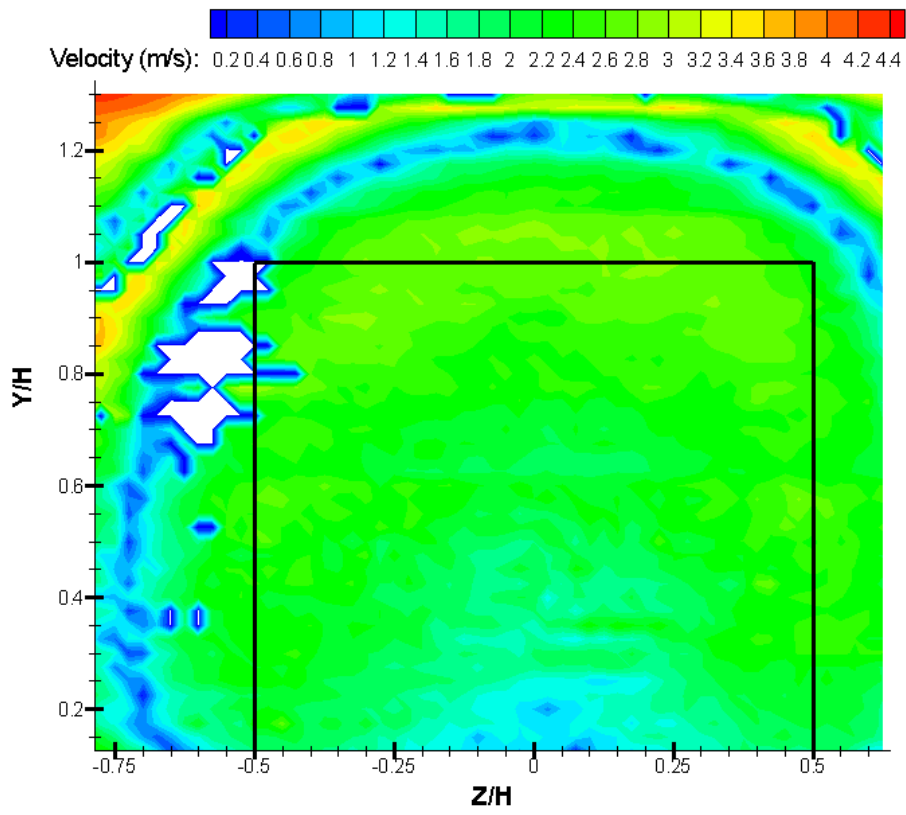


FIGURE 6.6 Velocity field behind a single building at  $X/H = 1.0$



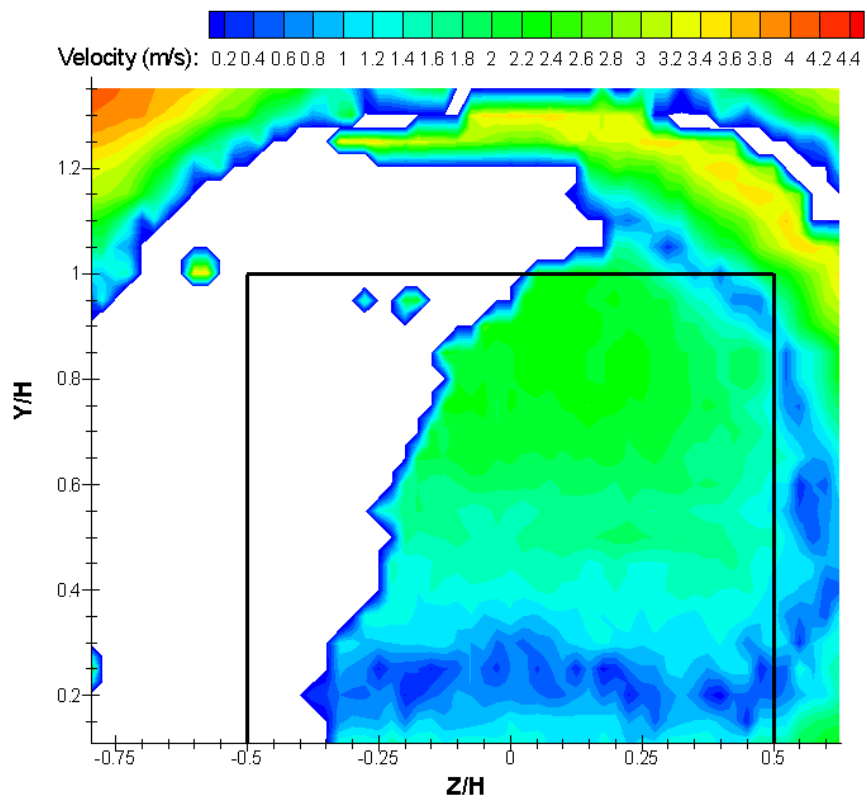


FIGURE 6.7 Velocity field behind a single building at  $X/H = 1.5$

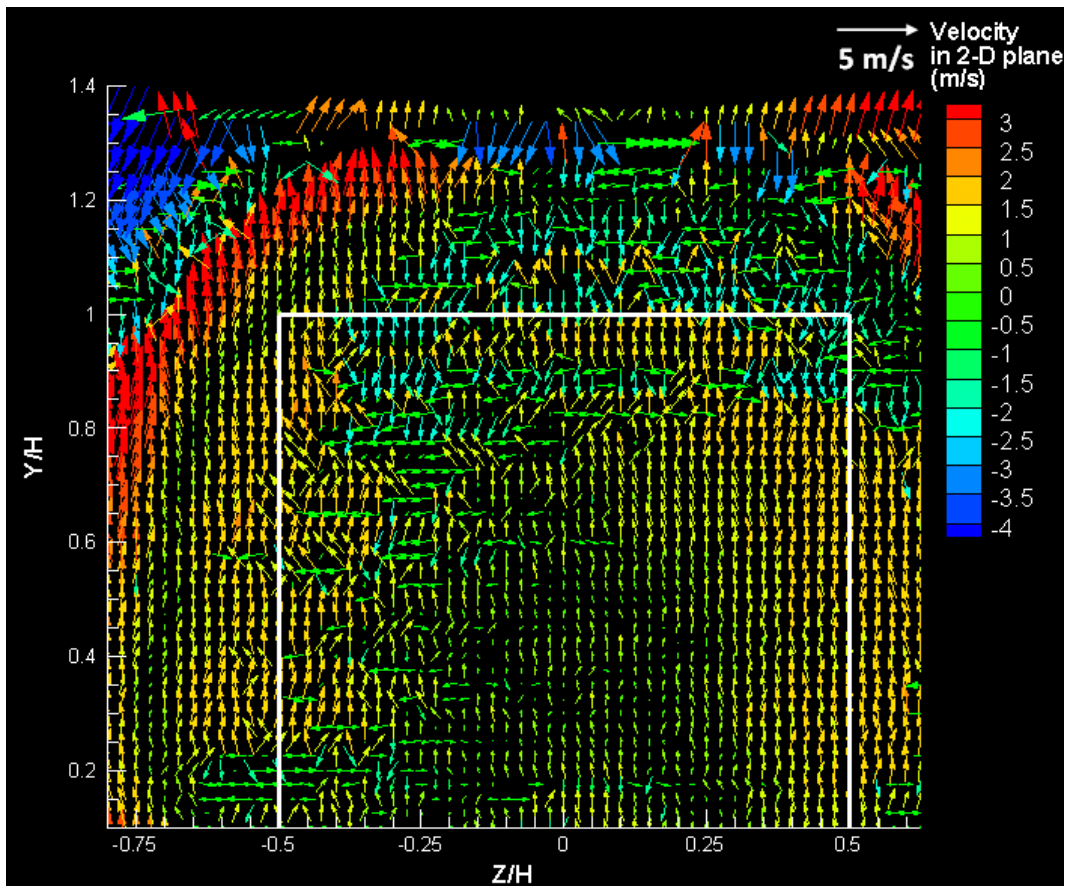


FIGURE 6.8 Vector plot in Y-Z plane behind a single building at  $X/H = 0.75$ . Positive velocity indicates upward velocity. Negative velocity indicates downward velocity.

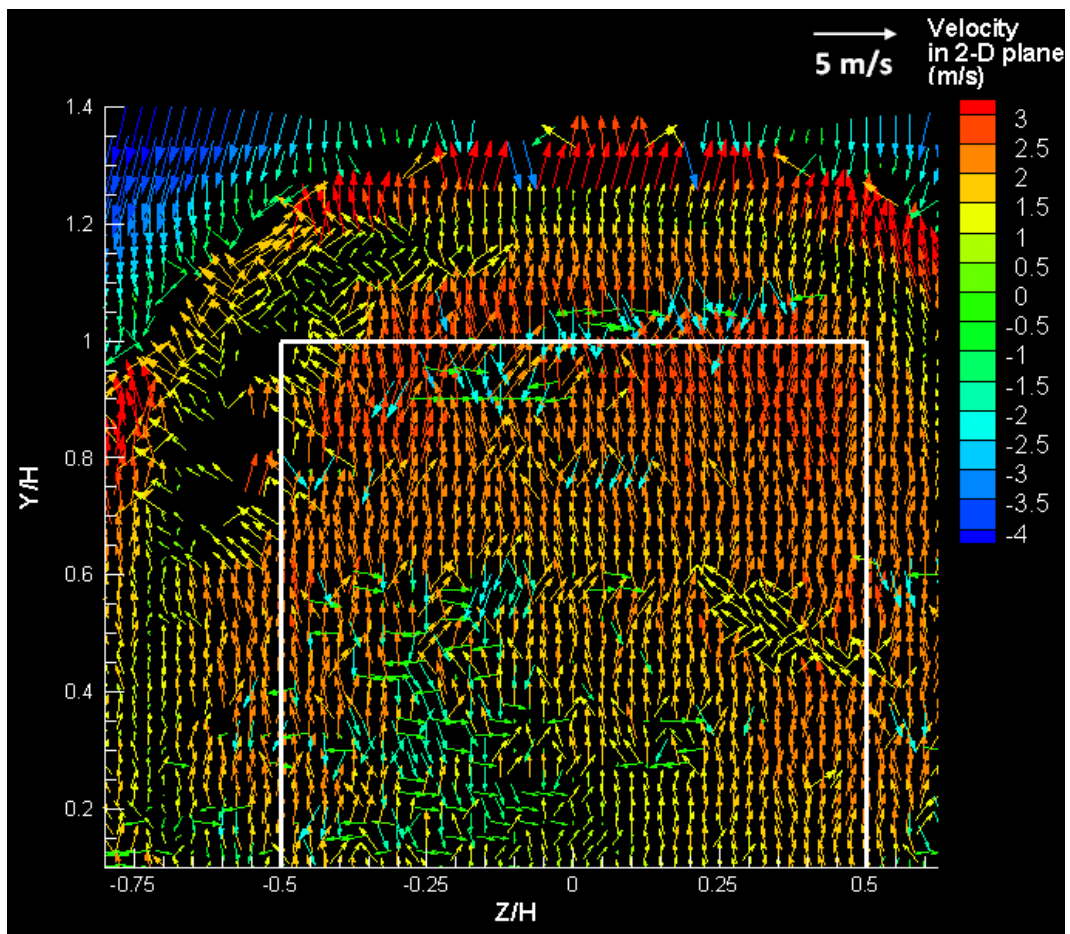


FIGURE 6.9 Vector plot in Y-Z plane behind a single building at  $X/H = 1.0$ . Positive velocity indicates upward velocity. Negative velocity indicates downward velocity.

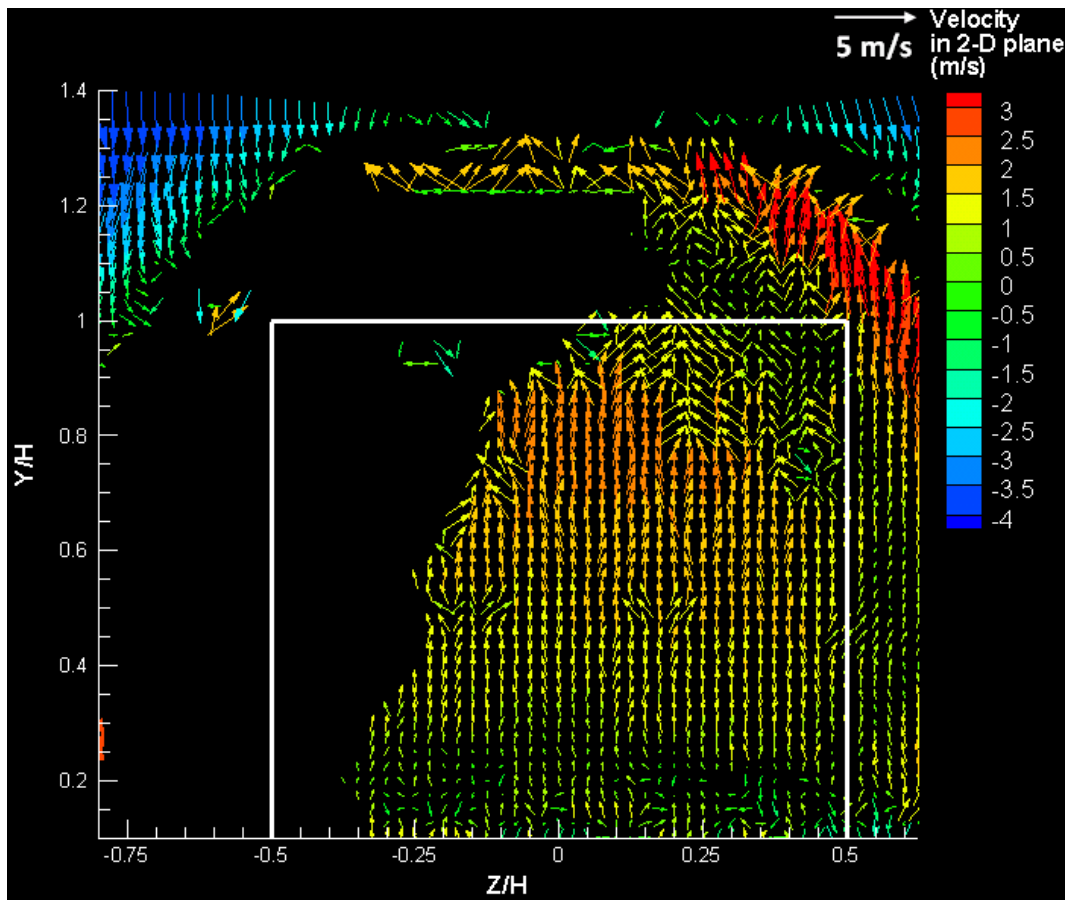


FIGURE 6.10 Vector plot in Y-Z plane behind a single building at  $X/H = 1.5$ . Positive velocity indicates upward velocity. Negative velocity indicates downward velocity.

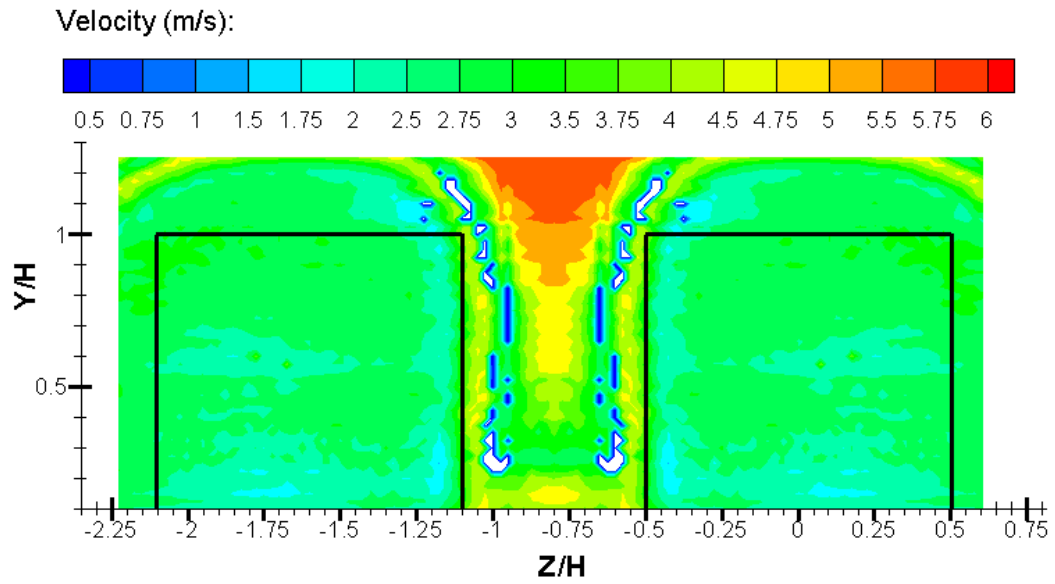


FIGURE 6.11 Velocity field behind twin buildings at  $X/H = 0.75$

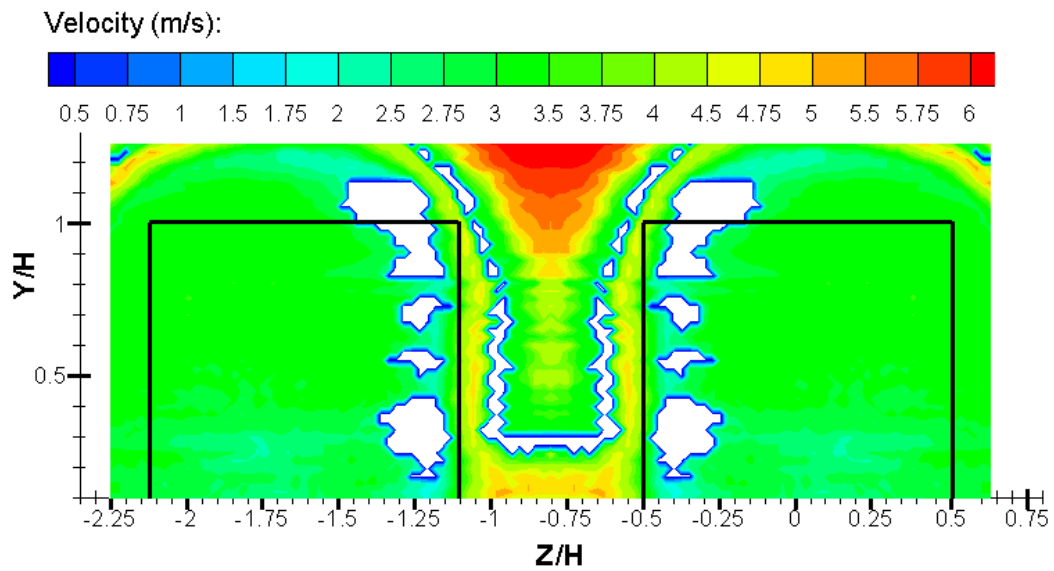


FIGURE 6.12 Velocity field behind twin buildings at  $X/H = 1.0$

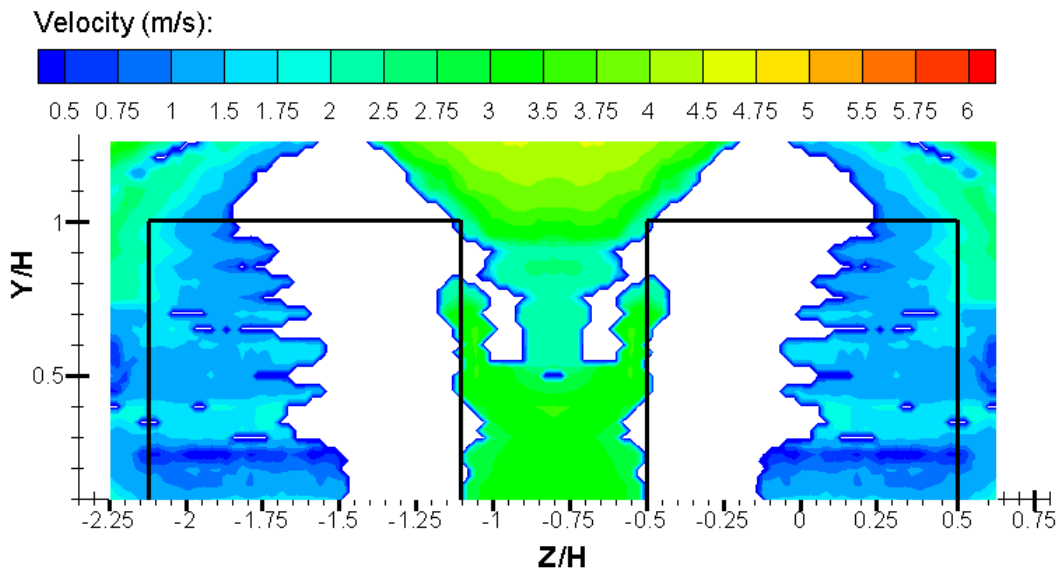


FIGURE 6.13 Velocity field behind twin buildings at  $X/H = 1.5$

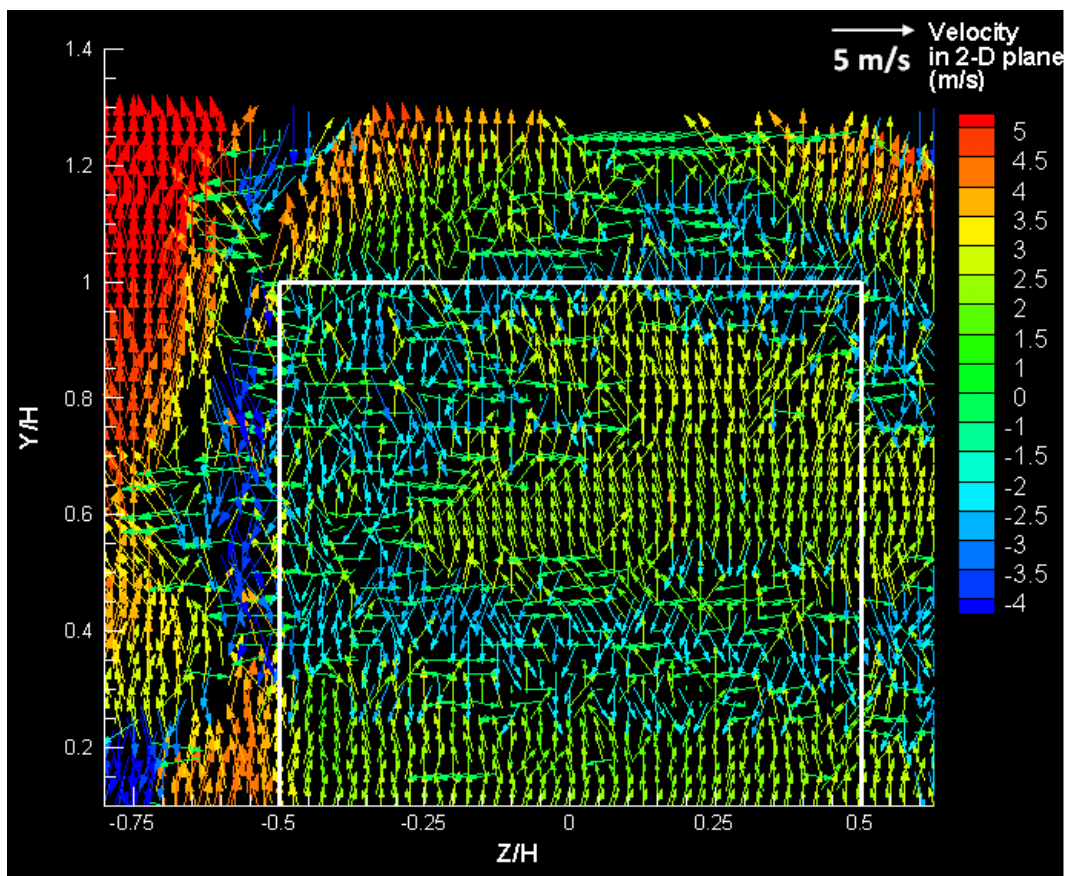


FIGURE 6.14 Time averaged velocity vector behind twin buildings at  $X/H = 0.75$ . Only one building on the right is shown here.

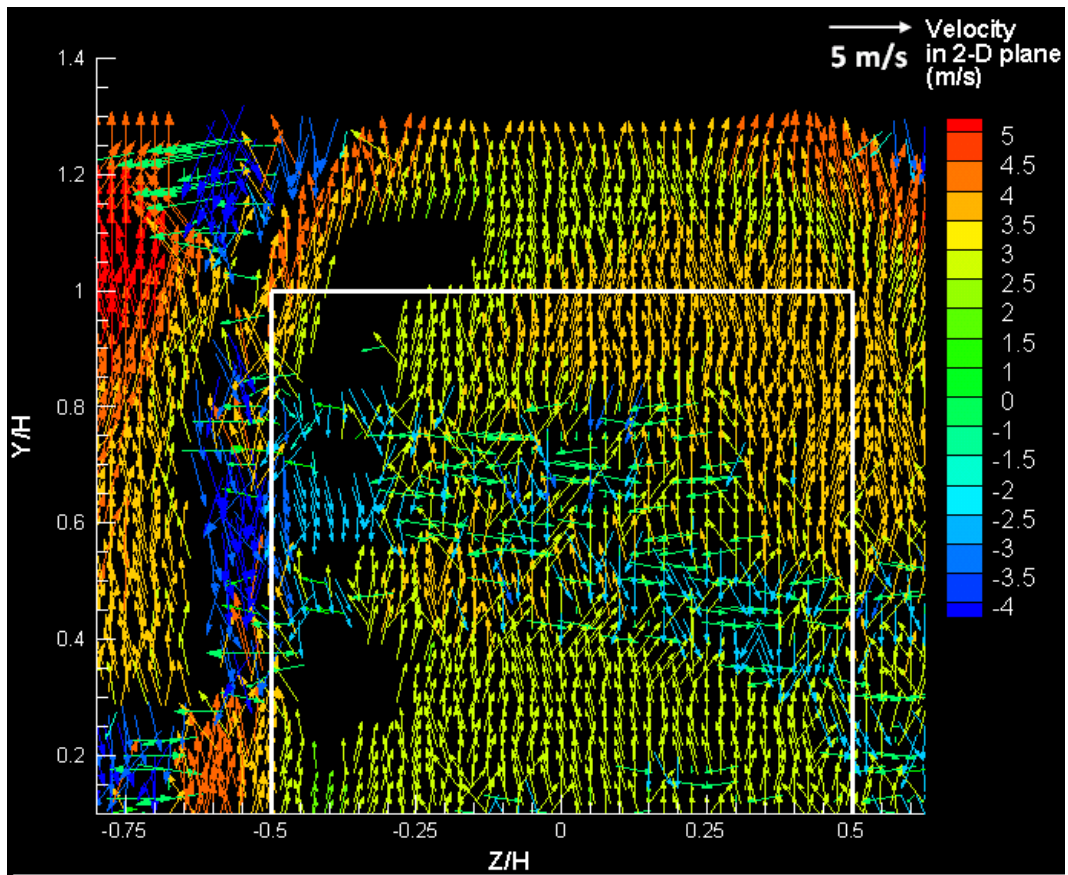


FIGURE 6.15 Time averaged velocity vector behind twin buildings at  $X/H = 1.0$ . Only one building on the right is shown here.



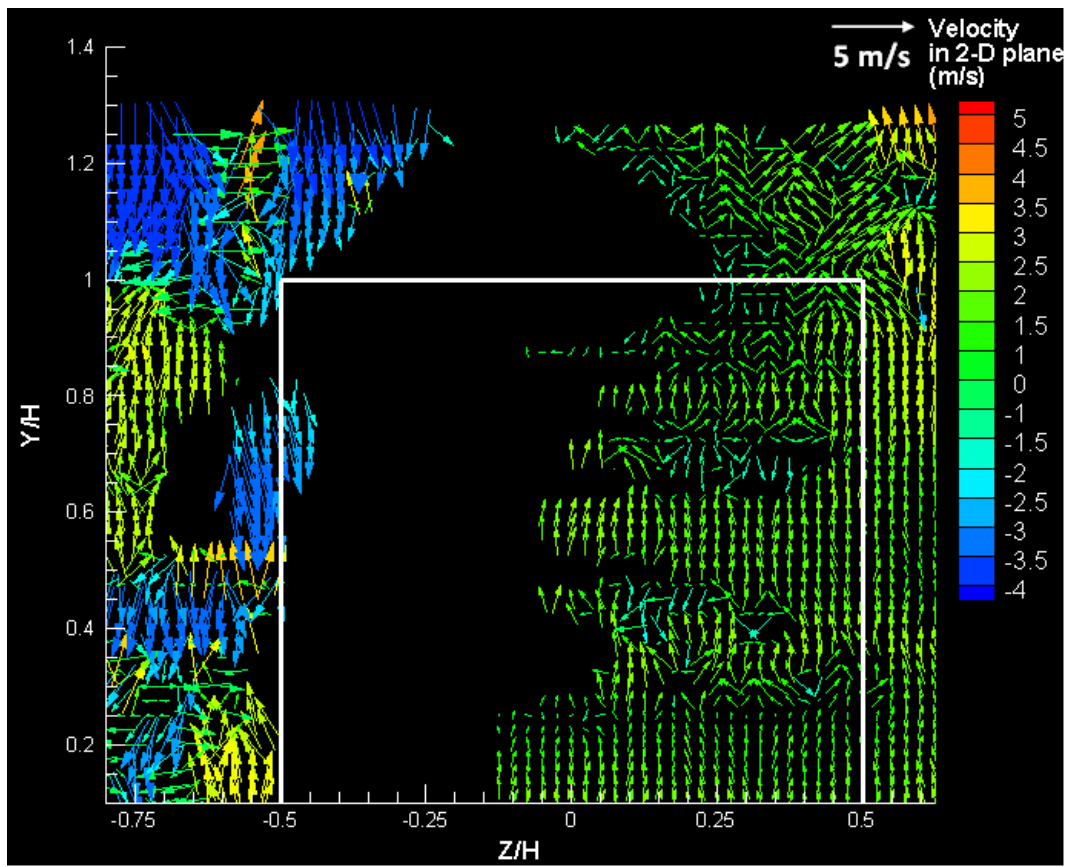


FIGURE 6.16 Time averaged velocity vector behind twin buildings at  $X/H = 1.5$ . Only one building on the right is shown here.

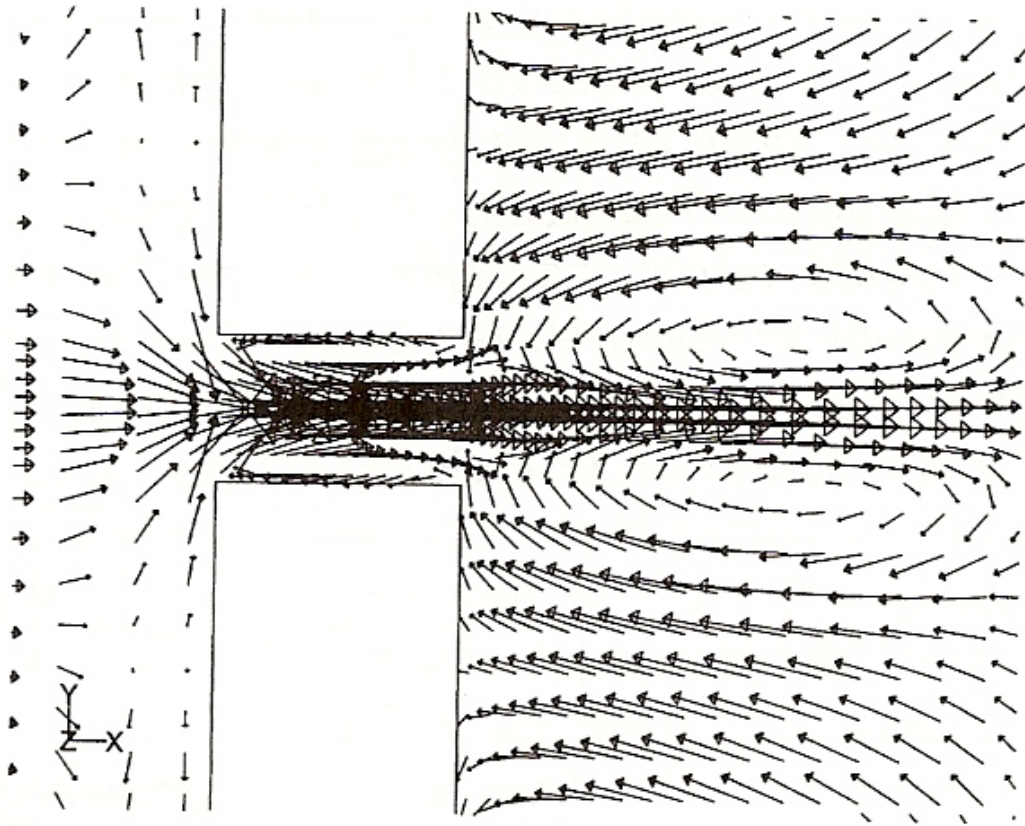


FIGURE 6.17 Time averaged velocity vector from Tutar and Ogus [88] in  $x$ - $z$  plane with  $w/H = 0.6$ .

# Chapter 7

## The lift of a wing due to a sinusoidal gust

### 7.1 Introduction

A series of wind tunnel tests under static and dynamic motions by using pitching vanes to produce flow oscillation were conducted in an open jet wind tunnel at Cranfield University, Shrivenham campus. The experimental investigations were carried out to examine the effects of several parameters encountered by an unsteady sinusoidal gust. A NACA 23012 wing with a wingspan of 0.75 metres was used to perform the investigations. Time-dependent data were collected during each set of experiments at a given mean angle of attack. The wing rotation axis was located approximately at a quarter chord location to examine the sinusoidal gust response in a wide range of gust frequencies, freestream velocities and oscillation amplitude. The effects of unsteady motion on unsteady airfoil behaviour and dynamic stall are only studied by an investigation of lift produced by the wing at a given mean angle of attack in the wind tunnel without flow visualisation over the wing surface. Flow morphology of dynamic stall will be determined based on available literatures.

All of the experimental results in this chapter were obtained and analysed from the experimental data performed by two visiting research students; Romain Bossard and Alice Tourteau, as part of their three-month project at Cranfield university, Shrivenham campus to investigate the response of a 3–dimensional wing due to unsteady sinusoidal gust. The author would like to thank them and very much appreciates their friendliness and kindness to allow the author to be involved in their experiments and use the experimental data as part of the author’s work.

## 7.2 Experimental Description

### 7.2.1 Apparatus

The experiments on a NACA 23012 wing responding to the unsteady sinusoidal gust were performed in an open section, closed circuit wind tunnel at Cranfield university, Shrivenham campus. The wind tunnel has an elliptic nozzle with dimension of  $5' \times 4'$  (height  $\times$  width for these experiments). The sinusoidal gust was generated by a gust generator which consists of a single array of six oscillating vanes placed in the horizontal direction at the nozzle exit approximately 1.5 – 2 metres upstream of the working section. The distance between each vane is 10 inches (254 mm). An oscillatory movement of the gust generator was controlled by an external motor providing a single harmonic excitation with a maximum frequency of 2 Hz. The gust angle of attack was also controlled by a crank arm attached to the external motor providing the angle of attack from  $\pm 1^\circ$  to  $\pm 15^\circ$ . The wing chord length of  $c = 0.167$  m and span,  $b = 0.76$  m were selected and its rotation axis was set at the quarter chord point. Aerodynamic forces, lift and drag, and pitching moment were measured directly from a 3–component mechanical balance positioned above the working section where the schematic of the balance is displayed in Figure 7.1. The balance is of the null-reading type which consists of three essential frames, earth frame, forces frame and pitching-moment linkage are suspended from a rigid frame and each individual frame is connected to a load cell to measure a nominal load.

The lift force applied on the wing was measured and transmitted through the two vertical support struts to the forces frame then conveyed through the vertical links to the levers on the cross shafts attached to the load cell. Similarly, drag measurement in the wind direction was also measured in a similar manner to the lift measurement. The pitching moment acting on the wing was measured about the rotation axis which was approximately at a quarter chord point supported by the two vertical struts, and resulted from a change in load on the tail strut. The associated change in load acts on the moment weighbeam rotating from its original position where no force acts on the wing.

### 7.2.2 Experimental measurements

The experiments were investigated at Reynolds numbers of  $1.11 \times 10^5$  and  $3.34 \times 10^5$  based on the wing chord and freestream velocity of 10 and 30 m/s respectively. Maximum Mach number for the experiment is less than 0.1. Hence, the compressible flow condition was neglected. An investigation of the wing when no gust involved was considered to determine the type of static stall that occurs, with angles

of attack varied from  $-6^\circ \leq \alpha \leq 21^\circ$  by  $3^\circ$  increment. The other experiment with a single harmonic gust excitation produced by the gust generator was to observe the unsteady nature of the forces at different gust angles of attack, oscillation frequencies and amplitudes. The force measurements to be investigated were defined in terms of reduced frequency,  $k$  of sinusoidal motion with angles of attack from  $-6^\circ \leq \alpha \leq 18^\circ$  by  $3^\circ$  increment with the oscillatory frequencies of 0.5 Hz 1 Hz and 2 Hz. Three different gust angles of attack of  $\pm 4^\circ$ ,  $\pm 8^\circ$  and  $0^\circ$  to  $4^\circ$  were selected to compare and contrast the effect of oscillation amplitude and the response due to sinusoidal gust. The accuracies of lift coefficient,  $C_L$  and drag coefficient,  $C_D$  are within the range of  $\pm 0.0125$  and  $\pm 0.0017$  respectively. The accuracy is a combination of tare offset measurements and  $\pm 1\%$  uncertainty of dynamic pressure reading from the micromanometer. The repeatability of the experimental results is not available because the experiments were carried out once.

## 7.3 Experimental results and discussion

### 7.3.1 No gust excitation (static condition)

#### 1. Reynolds number of $3.34 \times 10^5$

The initial experiment was on the steady state aerodynamic forces for the fixed wing at varying angles of attack. Lift, drag and pitching moment were experimentally measured but only lift force is considered in this case. The experimental condition is considered to be incompressible, due to very low Mach number, and viscous conditions because boundary layer seems to have a significant effect on upper surface of the wing.

Let us consider how the lift coefficient varies with angle of attack during static condition. At  $0^\circ$  angle of attack, there is already a lift force produced by the wing. This characteristic is a property of cambered airfoils/wings which lift at  $\alpha = 0^\circ$  is finite and zero-lift angle of attack is normally in between  $-1^\circ$  to  $-3^\circ$ . Whereas a flat plate or symmetrical wing, zero-lift angle of attack is at  $0^\circ$ . The theoretical slope shown in Figure 7.2 was calculated based on a thin, symmetrical airfoil with inviscid flow to compare the lift curve slope of NACA 23012 wing to a symmetrical wing. The values of the lift curve slope,  $dC_L/d\alpha$  for both experimental and theoretical results are  $4.71 \text{ rad}^{-1}$  and approximately  $4.42 \text{ rad}^{-1}$  respectively. Up to  $15^\circ$  under static condition, the plots in Figure 7.2 and Figure 7.3 are practically linearly proportional to angle of attack indicating that the lift increases steadily as angle of attack increases and the flow still remains attached on the upper surface up to this

point. It can also be seen on the plots that the the wing stalls roughly at angle of attack about  $18^\circ$  whereas from Jacobs and Pinkerton experiment [92], their wing stalls at around  $17^\circ$ . Stall type can be identified as a leading edge stall because the lift suddenly drops due to abrupt change in the airflow from the airfoil leading edge at stall angle and generally the leading edge stall can be estimated by the wing sections with thickness ratio between  $0.09 < t/c < 0.15$ . The lift force measurement under static condition agrees reasonably well with the results of Jacobs and Pinkerton. The maximum lift coefficient which occurs at the stall is denoted by  $C_{Lmax}$  and for the NACA 23012 wing under static condition, it is approximately 1.20 at Reynolds number of  $3.34 \times 10^5$ . The maximum lift coefficient obtained by Jacobs and Pinkerton is 1.68 at a test Reynolds number of  $3 \times 10^6$ . It makes sense that the value of the maximum lift coefficient is dependent on Reynolds number which governs the strength of inertia forces relative to viscous forces. The average lift force generated during dynamic motion at different frequencies are compared with the static lift force in the same plots from Figure 7.2 to Figure 7.4. Interestingly, the lift curve slopes,  $dC_L/d\alpha$  for all the experimental results both under static and dynamic motions are practically the same at  $4.71 \text{ rad}^{-1}$ .

Minimum drag was calculated dependent on lift curve slope  $a$ , lift coefficient  $C_L$ , wing aspect ratio,  $AR$ , profile drag  $C_{D0}$  and induced drag  $C_{Di}$ .

$$C_D = C_{D0} + \frac{C_L^2}{\pi AR}(1 + \delta) \quad (7.1)$$

where  $\delta$  is induced drag factor.

The minimum drag coefficient obtained from the experiment and is approximately 0.00709 (a calculation is not included in this section). The experimental drag value is slightly lower than the value obtained by Jacobs and Pinkerton which is equivalent to 0.0072. Consider NACA 23012 airfoil profile, the mean camber line for this airfoil is given by Anderson [52] and is defined as follows:

$$\frac{z}{c} = 2.6595 \left[ \left(\frac{x}{c}\right)^3 - 0.6075 \left(\frac{x}{c}\right)^2 + 0.1147 \left(\frac{x}{c}\right) \right] \text{ for } 0 \leq \frac{x}{c} \leq 0.2025$$

$$\text{and } \frac{z}{c} = 0.02208 \left(1 - \frac{x}{c}\right) \text{ for } 0.2025 \leq \frac{x}{c} \leq 1.0.$$

From the given shape of the mean camber line, the calculation from example 4.2 in section §4.7 by Anderson provides angle of attack at zero lift of

$\alpha_{L=0} = -1.09^\circ$ . The experimental value of  $\alpha_{L=0}$  lies in between  $-1.0^\circ$  and  $-1.50^\circ$ . Whereas  $\alpha_{L=0}$  from Jacobs and Pinkerton was obtained at  $-1.10^\circ$  which agrees well with the calculation from Anderson.

## 2. Reynolds number of $1.11 \times 10^5$

Similarly to the results of  $Re = 3.34 \times 10^5$ , lift coefficient is also determined and plotted against angle of attack at a Reynolds number of  $1.11 \times 10^5$ . The results are displayed in Figure 7.5. It can be seen clearly that the static lift coefficients are slightly higher than the averaged lift produced by the sinusoidal gust. At low speed test, the wing stalls at the angle around  $13^\circ$  which is lower than the stall angle from higher velocity case. The lower stall angle is believed to be an influence of Reynolds number dependent since below test Reynolds number of  $2.50 \times 10^5$ , transition to turbulence generally occurs. Therefore, at Reynolds number of  $1.11 \times 10^5$ , the majority of the flow passing over and under the airfoil is laminar flow and its tendency to separate is very easy as the angle of attack increases. Thus, the stall angle at low test Reynolds number is lower than the stall angle at higher Reynolds number owing to flow separation condition. The maximum lift coefficient,  $C_{Lmax}$  obtained at this test Reynolds number is approximately 0.96 and minimum drag is about 0.00388 which a calculation is not included either. A comparison of experimental results, Jacobs' result and calculation results is shown in Table 7.1.

Stall type of test Reynolds numbers of  $1.11 \times 10^5$  and  $3.34 \times 10^5$  are considered as "thin airfoil stall" and "leading edge stall" respectively. As Reynolds number increases, the improvement in wing performance and transition of stall type occur. In this experiment, the transition of the stall is seen. Transition of stall type is governed by adverse pressure gradient and turbulent flow condition. Increasing in Reynolds number leads to increase adverse pressure gradient and increase turbulent flow. As the flow turns into turbulence due to increasing in Reynolds number, turbulent flow has a tendency to retard the flow to separate. Because the energy of the fluid elements extracting close to the wing surface is larger in case of turbulent flow than in laminar flow, the turbulent flow does not separate easily. This indicates that larger Reynolds number induce higher maximum lift coefficient. This results in transition of stall type occurred in the experiments. The size of separation bubble is the main characteristic to influence the leading edge stall and the flow tends to be more turbulent to entrain high momentum fluid from outside to retard the flow to separate. The influence of Reynolds number on the

maximum static lift coefficient is displayed in Figure 7.6. Reynolds number has a moderate effect on the maximum lift coefficient and stall characteristic.

The pressure distributions along the upper and lower surfaces of the wing were not measured during the experiments. However with a useful software, "xfoil" [93], the pressure distributions in 2–dimensions are numerically calculated based on the experimental conditions. The software applies a basic panel method to generate pressure coefficients. Figure 7.8 to Figure 7.11 show the numerical pressure distributions for NACA23012 airfoil at two different test Reynolds numbers at different angles of attack. It can be seen from the pressure distributions at  $3^\circ$  that a separation bubble dominates the performance of the airfoil. The separation bubble changes the pressure distribution as a reduction in pressure peak and followed by a pressure plateau. The location of the point where the actual and inviscid pressures are equal indicates a reattachment location where a rapid pressure recovery is found. A region of rapid pressure recovery is shown by a steep slope immediately following by the plateau pressure distribution. Figure 7.10 and Figure 7.11 represent the laminar separation bubble at  $\alpha = 3^\circ$  at Reynolds number of  $1.11 \times 10^5$  and  $3.34 \times 10^5$  respectively. From the static lift coefficient plot in Figure 7.6, the separation bubble can be estimated to occur at around  $3^\circ$ . The location where the separation bubble occurs is where the slope deviates from its original slope. It is clearly seen that at larger Reynolds number, the separation bubble is smaller than at lower Reynolds number. At Reynolds number of  $1.11 \times 10^5$  with the xfoil simulation, the laminar separation occurs at 20%  $x/c$  and reattaches on the surface at 45%  $x/c$ . Similarly, the separation occurs at 17%  $x/c$  and reattachment at 32%  $x/c$  at  $Re = 3.34 \times 10^5$ . Hence, Reynolds number affects the size of the separation bubble.

### 7.3.2 Single harmonic excitation

In the previous section are the discussion of the NACA 23012 wing tested under static condition to observe general characteristics at the test Reynolds numbers of  $1.11 \times 10^5$  and  $3.34 \times 10^5$  based on freestream velocity and wing chord. In this section, a single harmonic sinusoidal gust excitation was introduced at different frequencies to investigate behaviour of the wing. Three different gust/vane oscillation limits,  $\pm 4^\circ$ ,  $\pm 8^\circ$  and  $0^\circ$  to  $4^\circ$  were set with freestream velocity,  $U = 10$  and  $30$  m/s.

For reduced frequency  $k = \omega c/2U$ , varies between  $8.74 \times 10^{-3} \leq k \leq 0.105$  with three different vane oscillation amplitudes, dynamic lift force was then collected experimentally over a period of time. With eliminating an additional



resonance frequency induced by support struts, the average lift coefficients from the sinusoidal motion can be seen from Figure 7.2 to Figure 7.5. The average of lift due to the sinusoidal gust at different oscillation amplitudes at Reynolds number of  $3.34 \times 10^5$  nearly coincide with the lift under static condition. It indicates that reduced frequency and oscillation amplitude do not have much influence on the average lift over a period of time. However, stall angle of the average lift from dynamic condition is much less than stall angle under static condition. At the same test Reynolds number with the vane oscillation from  $0^\circ$  to  $4^\circ$  providing a mean oscillatory pitch cycle of  $2^\circ$ , the average lift coefficient is shifted away from the  $0^\circ$  mean oscillation amplitude upwards by 0.143. The time-averaged lift coefficient for 4 oscillation cycles at mean angle of attack  $12^\circ$  is shown in Figure 7.7. At Reynolds number of  $1.11 \times 10^5$  with a combination of sinusoidal gust, the wing did not seem to stall and the lift still increased beyond the static stall angle of attack.

As shown by the plots from Figure 7.2 to Figure 7.6, it can be summarised as

- Frequency and oscillation amplitude do not have much effect on the mean value of lift produced by the sinusoidal gust
- Dynamic stall angle is lower than in static condition
- The mean of the vane oscillatory pitch cycle has an effect on the average lift coefficients. As the mean of the vane oscillation is  $0^\circ$ , the average lift coefficients more or less overlapped with the static lift coefficients. Nonetheless, as the mean of the vane oscillatory cycle is shifted positively upwards, the lift coefficients are shifted upwards by an arbitrary value.
- Reynolds number has a moderate effect on the maximum lift coefficient and stall characteristic which provided higher maximum lift coefficient and more sudden stall as Reynolds number increases.

Oscillatory characteristics for the NACA 23012 wing section were obtained at various gust reduced frequencies for Reynolds numbers of  $1.11 \times 10^5$  and  $3.34 \times 10^5$  which corresponds to Mach number of 0.03 and 0.087 respectively. The measurements of the dynamic characteristic were recorded during each vane oscillation pitch cycle to investigate the wing performance under oscillatory pitch conditions. The harmonic motion profile of variation of the angle of attack for the sinusoidal oscillatory pitch cycle is defined as

$$\alpha(t) = \alpha_m + \alpha_a \sin(\omega t + \phi) \quad (7.2)$$

In all cases, the tests were carried out over four continuous cycles and the data were then subsequently averaged. The summary of the effects of forcing conditions

on dynamic stall based on different parameters are concluded. To this end, the summary of the physics of dynamic stall by varying one parameter and keeping the others constant is shown.

### 1. Effect of mean angle of attack

The effect on the lift encountered by the sinusoidal gust at a constant oscillation amplitude of  $\pm 8^\circ$  and reduced frequency of 0.02 at the given mean angles of attack,  $12^\circ$ ,  $15^\circ$  and  $16^\circ$  is considered. The result in Figure 7.12 represents the wing oscillating in and out of stall under dynamic conditions compared with the static lift coefficient indicated by dash lines. The harmonic motion profile for the mean angle of attack used to evaluate the hysteresis loop is defined as  $\alpha(t) = \alpha_m + 8^\circ(\sin \omega t - \pi/2)$ . At  $12^\circ$  mean angle of attack, the up-stroke and down-stroke hysteresis loop follow the static lift coefficient curve which indicates that the majority of flow over the wing surface still remains attached because the mean of the oscillation is within the static stall limit, see Figure 7.12a. Note that the hysteresis loop is in a clock-wise direction. The lift coefficient induced by the vane oscillatory pitch cycle exceeds the static stall only by a small margin and no sign of dynamic stall at this moment. At higher mean angle of attack at  $15^\circ$ , light dynamic stall starts to develop with further increase in lift which is believed to be high enough to create a strong vortex near the leading edge. Singh et al [68] describes the increment in lift beyond the static stall angle that the pitching wing can resist a large region of a reverse flow on a wing surface before a boundary layer separation occurs. This tolerance permits a wing to additionally increase the lift beyond the static stall angle of attack. At  $16^\circ$  where the angle is well beyond the static stall angle, the lift cannot be further produced. At this stage the flow is fully separated causing deep dynamic stall represented by a large hysteresis loop. The maximum lift coefficient is found at approximately  $23^\circ$  for the mean angles of attack of  $15^\circ$  and  $16^\circ$ , see Figure 7.12b - c. In the oscillation phase corresponding to a decrease in angle of attack from its maximum angle during downstroke motion, the value of lift coefficient turns out to be smaller than the static lift at the same angle of attack before the flow returns to its original condition. The separated flow around the wing restores to an unseparated flow state during the downstroke motion. After deep dynamic stall, the flow reattachment is delayed to a low angle of attack but does not take time for the flow to recover and attach on the wing surface. The time history of the lift coefficients for all three mean angles of attack is shown in Figure 7.13a for four cycles during the measurement after the additional resonance frequency has been eliminated. The plot shows that at the mean angles of  $12^\circ$  and  $15^\circ$ , the lift behaviour still follows the sinusoidal oscil-

lation pattern with the maximum lift increases as the mean angle of attack increases. Interestingly at  $16^\circ$ , the flow breaks down rapidly represented by a sudden drop in lift, then gradually recovers and continues in a sinusoidal pattern. The maximum lift at  $16^\circ$  equals to the maximum value at  $15^\circ$ . This represents dynamic stall begins to occurs at  $15^\circ$ .

## 2. Effect of oscillation amplitude

The effect on the lift coefficients caused by variation in the vane oscillation amplitude at constant mean angle of attack at  $18^\circ$  and reduced frequency,  $k = 0.02$  is shown in Figure 7.14. The harmonic motion profile for the mean angle of attack used to evaluate the hysteresis loop is defined as  $\alpha(t) = 18^\circ + \alpha_m(\sin \omega t - \pi/2)$ . It is clear that the dynamic stall is dependent on the oscillation amplitude. At the lowest amplitude of  $2^\circ$ , the wing already stalls and a small hysteresis loop appears to be seen. At higher oscillation amplitude, the stall angle under dynamic motion re-appears with the hysteresis loop becoming larger. The time history of the lift coefficients at the mean angle of attack of  $18^\circ$  is plotted, see Figure 7.13b. The lift is still produced further beyond static stall angle under the unsteady flow condition at oscillation amplitude of  $4^\circ$  and  $8^\circ$ . The experiments conducted by Romain and Alice, the time-averaged of lift and drag, and pitching moment of the NACA 23013 wing under static and dynamic conditions were measured without investigation of flow behaviour on the upper surface. Price and Akbari [57] provides a simulation of the flow over an airfoil oscillation at large angle of attack. This information gives more understanding how the flow behaves under dynamic condition. According to Price and Akbari, a vortex starts to form at the leading edge as the oscillation angle of attack increases during the up-stroke motion leading to a formation of a counter-rotating vortex from the leading edge. In the down-stroke cycle, the vortex is released and shed downstream. Then the formation of this vortex starts again at the beginning of the up-stroke cycle. This small formation and release of the vortex results in a small effect in lift due to sinusoidal gust. At small amplitude, the vortex is shed downstream at the maximum angle of attack. On the other hand, when the oscillation amplitude increases the vortex created near the leading edge is stronger and larger than the small amplitude case. This strong vortex is then shed/convected beyond maximum angle of attack causing the delay of the flow separation and dynamic stall.

## 3. Effect of reduced frequency

Figure 7.15 shows the effect of reduced frequency increasing from 0.009 to 0.035 at constant mean angle of attack of  $16^\circ$ , constant oscillation amplitude of  $8^\circ$  at Reynolds number of  $3.34 \times 10^5$ . For all three reduced frequencies,

the dynamic stall characteristic is clearly seen. In terms of flow mechanism described by Akbari and Price [57], the vortex formation starts from the leading edge of the wing during the up-stroke cycle of oscillation. The vortex continues shedding and convecting downstream from the upper surface at the maximum angle of attack as the up-stroke cycle continues. At a lower reduced frequency, the leading edge vortex is shed into the wake before the wing reaches the maximum angle of attack. Price [57] explains that due to a shorter period of oscillation at high frequency, the leading edge vortex does not have sufficient time to convect far over the upper surface before the next leading edge vortex is formed causing the number of leading edge vortices increases with time and they are left over the upper surface. At the same time, the trailing edge maintains shedding the vortices from leading edge and trailing edge away but not fast enough to push the leading edge vortices downstream. This results in the leading edge vortices separates from the upper surface rather than at the trailing edge. This is to delay the lift generation at higher reduced frequency compared with lower reduced frequency case, see the time history in Figure 7.13c. Meanwhile, Lawrence et al [56] also explains the effect of reduced frequency as the flow reversal is delayed by increasing reduced frequency. At lower reduced frequency, a vortex is formed and shed away into the wake region before the airfoil reaches a maximum angle of attack. From the experimental results, it can be concluded that when reduced frequency increases, the vortex interaction occurs at a higher angle of attack resulting in a delay to the onset of flow separation, and dynamic stall is less likely to happen at low angle of attack. As the reduced frequency becomes larger, the hysteresis loop has more time to recover. The lift coefficient during down-stroke motion becomes less and less when the reduced frequency increases, and the maximum lift coefficient only increases by a small portion.

#### 4. Effect of Reynolds number

The effect of Reynolds number on the lift coefficient at constant oscillation amplitude and oscillation frequency of 1 Hz is shown in Figure 7.16. It seems that the effect of Reynolds number is likely to influence the maximum lift coefficient and size of the hysteresis loop. The hysteresis loop at Reynolds number of  $1.11 \times 10^5$  is wider than the loop at Reynolds number of  $3.34 \times 10^5$ . At low Reynolds number, the flow breakdown at large angle of attack is gradual progression while at higher Reynolds number the flow breakdown seems to be instantaneous. During the down-stroke cycle at large mean angle of attack of  $15^\circ$  and Reynolds number at  $1.11 \times 10^5$ , the hysteresis loop is likely to be attributable to a delayed reattachment because lift coefficient is much lower than the high Reynolds number case. Interestingly at Reynolds

number of  $1.11 \times 10^5$ , the crossing hysteresis loop occurs at large mean angle of attack. This characteristic is a characteristic of 2-dimensional airfoil. It might be influenced by a combination of high angle of attack near stall and low flow speed where wing tip vortex does not have a strong impact on the wing.

## 7.4 Conclusions

The experiments were conducted to examine the stall characteristics of the NACA 23012 wing under the static and dynamic conditions. Based on the static experimental results, static stall is thought to be the mechanism of abrupt leading edge separation due to separation bubble bursting. Maximum lift coefficient is another parameter influenced by Reynolds number effect. It was found that Reynolds number increases a value of maximum lift coefficient. Also the static stall abruptness increases with increasing in Reynolds number. The tests in pitching vanes oscillations were carried out to verify the effects of several parameters according to oscillation profile  $\alpha = \alpha_m + \alpha_a(\sin \omega t - \pi/2)$ . These parameters includes the mean of angle of attack of the stationary wing, oscillation amplitude, reduced frequency and Reynolds number. Summary of the observed parameters are as follows:

1. Mean angle of attack.

At low mean angle of attack, the flow is fully attached to wing surface with hysteresis loop appearance. At around  $12^\circ$ , the stall characteristic due to dynamic condition appears to be an overshooting in lift coefficient above the maximum lift coefficient under static condition. As the mean angle of attack increases, dynamic stall severity changes from light stall to fully deep stall. This indicates the flow starts to breakdown and strong vortex near the leading edge becomes higher as the angle of attack increases.

2. Oscillation amplitude.

The pitching cycle oscillation amplitude is significant on dynamic stall. At small oscillation amplitude, the stall characteristic under dynamic condition is similar to static stall. At large oscillation amplitudes, the stall characteristic under dynamic conditions reappears with a wider hysteresis loop as the oscillation amplitude increases. This indicates that the large amplitude of oscillation is sufficient to cause the flow to separate at the large angle of attack and reattachment has sufficient time to return to its original condition at low angle of attack.

3. Reduced frequency.

From the experimental results obtained, the reduced frequency appears to in-

fluence the lift force characteristic. When reduced frequency increases, the vortex interaction occurs at a higher angle of attack resulting in delaying the onset of flow separation and dynamic stall is less likely to happen at low angles of attack. As the reduced frequency becomes larger, the hysteresis loop has more time to recover. The lift coefficient during down-stroke motion becomes less and less when the reduced frequency increases, and the maximum lift coefficient only increases by a small portion.

#### 4. Reynolds number.

For all the parameters investigated in the experiment, Reynolds number seems to have the least dramatic effect on dynamic stall. Hysteresis loop is attributable to a delay in reattachment causing the more gradual progression in flow breakdown before stall. At a low Reynolds number with low flow speed, the crossing hysteresis loop which is a general characteristic for 2-dimensional airfoil appears to be seen. Also the width of hysteresis loop at low Reynolds number is wider than the loop at high Reynolds number.

The viscous, incompressible flow over a three-dimensional NACA 23012 wing subjected to pitching oscillation of the freestream flow was investigated at different oscillation frequencies and amplitudes. Experimental results were obtained from the oscillatory flow past the fixed wing at given angles of attack. Time-dependent histories of lift with four oscillations were recorded. The lift under static condition was also investigated to compare with the dynamic lift due to a sinusoidal gust. The phenomenon of dynamic stall has been shown to be a significant parameter for a small UAV with a wingspan of the order of a metre. It has been summarised that dynamic stall is characterised by a delay of flow separation to higher angles of attack. This includes a phenomenon of leading edge vortex shedding which explained by Akbari and Price [57]. As long as the vortex stays on the upper surface of the wing, it enhances the additional lift to be created. The brief summary of the experiments and the response of a UAV to the full scale flow field into the static and dynamic lift responses to sinusoidal gusts can be discussed. During a stable condition at low Reynolds number of  $1.11 \times 10^5$ , the flow passing over the wing is laminar flow which has a tendency to separate easily. If a UAV operates in this range of Reynolds number, the wing stall angle is approximately  $13^\circ$  and it may experience thin airfoil stall type with low value of lift coefficient. If it operates at a higher Reynolds number at  $3.34 \times 10^5$ , it will experience leading edge stall type with sudden lost of lift due to separation bubble burst. The stall angle is around  $18^\circ$  for this range of Reynolds number. Effects of unsteady motion on unsteady wing motion are discussed in this Chapter mainly through experiments of a simulation of a sinusoidal gust on a 3-dimensional wing. For an increasing in angle of attack

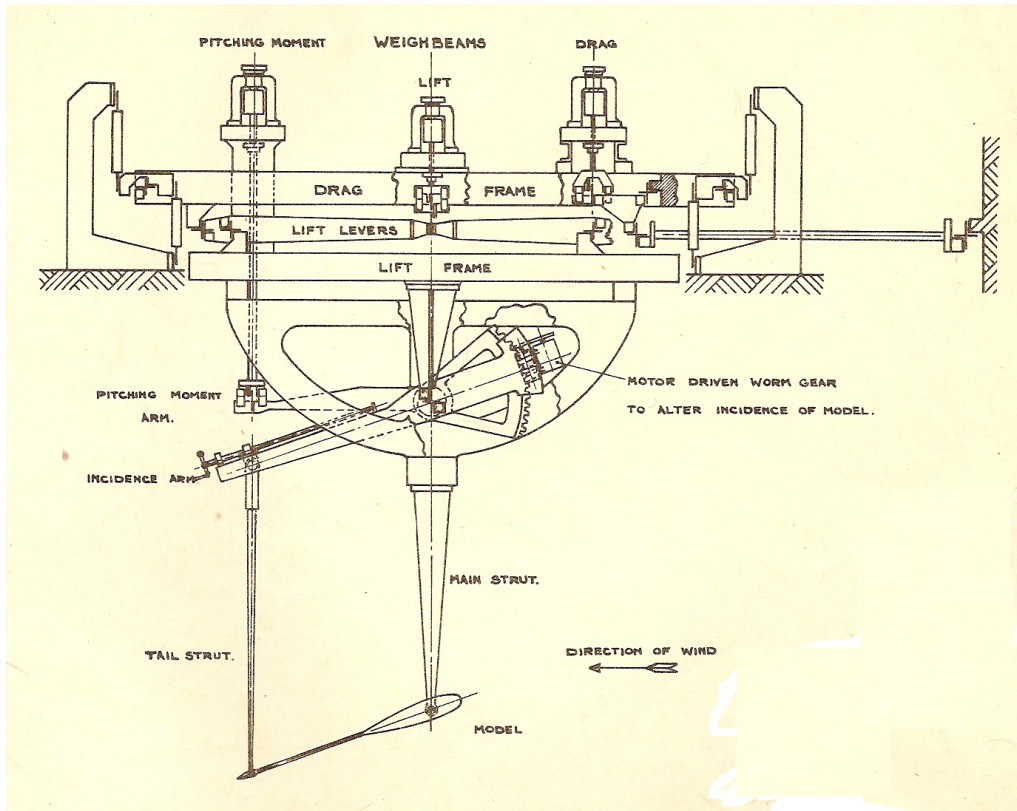
under dynamic condition, it has been seen that the flow remains attached to the upper surface of the wing to an angle much higher than stall angle under static condition. The effects of forcing conditions on dynamic stall which the UAV may experience during forward flight can be discussed. By varying parameters such as reduced frequency, mean angle of attack and oscillation amplitude, the various dynamic stall phenomenons like delay on separation, leading edge vortex shedding, and reattachment recovery happen around the cycle at different angles of attack. With variations in one parameter while keeping the other parameters constant would help to understand the dynamic stall mechanism. The response of the UAV to the full scale flow field due to the effect of mean angle of attack shows the wing experiences a change of flow condition as the air flow progresses from attached conditions at moderate angle of attack, through light dynamic stall and deep dynamic stall at the maximum angle of attack. If the UAV flies into an area of high flow amplitude with high angle of attack, it may encounter the effect of deep dynamic stall. It causes the aircraft to experience not only significant increase of lift but large nose-down pitching moment also. However, if the aircraft operates at moderate angle of attack, say at  $12^\circ$ , the aircraft does not experience dynamic stall condition. It experiences only a change in pitching motion with with the air flow remains attached on the upper wing surface. The effect of oscillation amplitude causes the aircraft to respond to nose-down pitching moment. If the aircraft involves in a small gust oscillation amplitude, the aircraft response is similar to the response under static condition with only small portion of extra lift has been produced and hysteresis loop is not important. However, when the amplitude becomes larger, dynamic stall behaviour with an overshoot in lift will be discovered. The larger the oscillation amplitude, the larger the flow hysteresis loop and the more nose-down pitching moment the aircraft experiences. The effect of reduced frequency on the aircraft response is mainly on lift and pitching moment responses. At a relatively low frequency of 0.009, the aircraft encounters light dynamic stall compared with higher frequencies. With increasing reduced frequency, the vortex shedding is delayed and shed away at the maximum angle of attack, so it delays the flow separation to a higher angle of attack than low reduced frequency case. The effect of Reynolds number on the response of the UAV seems to influence on value of lift generated. High Reynolds number case, the amount of lift created increases much quicker than low Reynolds number case. This indicates that when the UAV encounters an unsteady motion at high Reynolds number, the extra lift generated is much faster than at low Reynolds number range. Also it might be deduced that Reynolds number does not influence the aircraft response as much as the other parameters. Results of 3-dimensional dynamic stall from Lorber et al [59] has shown that the measurement of unsteady lift and pitching moment of the 3-dimensions near the mid-span is similar to the 2-dimensional aerofoil measurement. However, near the tip of the wing the unsteady lift and

pitching moment show different characteristics with more non-linear behaviour which Lorber indicated is the influence of the wing tip vortex.

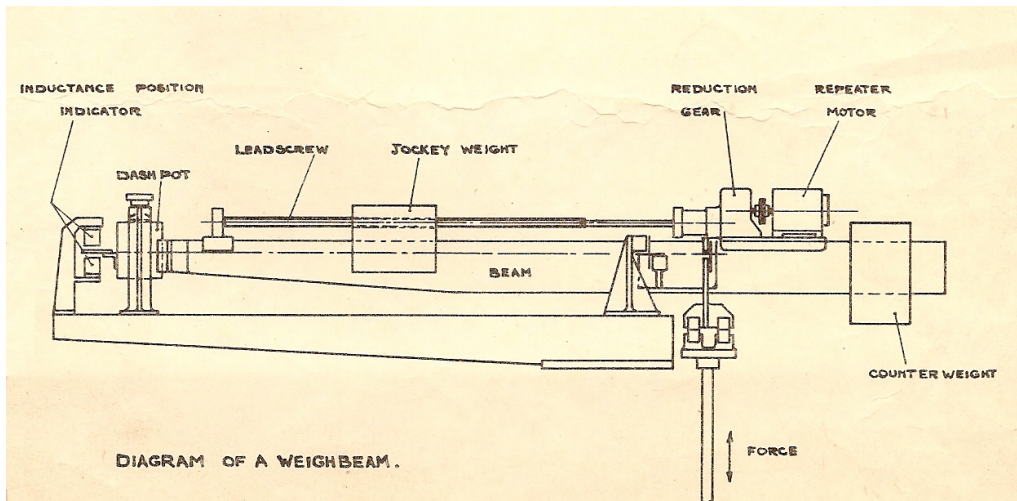
	$\text{Re} = 3.34 \times 10^5$	$\text{Re} = 1.11 \times 10^5$	Jacobs' result [92]	Calculated
$\alpha_{L=0}$	$-1.0^\circ - -1.50^\circ$	$-2.0^\circ - -2.50^\circ$	$-1.1^\circ$	$-1.09^\circ$
$\alpha_{stall}$	$18^\circ$	$14^\circ$	$17^\circ$	–
$dC_L/d\alpha$	$4.71 \text{ rad}^{-1}$	$4.48 \text{ rad}^{-1}$	$5.65 \text{ rad}^{-1}$	$4.42 \text{ rad}^{-1}$
$C_{D0}$	0.00709	0.00803	0.0072	0.0073

TABLE 7.1 Comparison of experimental results and calculated result





(a) Main mechanical balance



(b) Diagram of weighbeam

FIGURE 7.1 Schematic of the 3-component mechanical balance

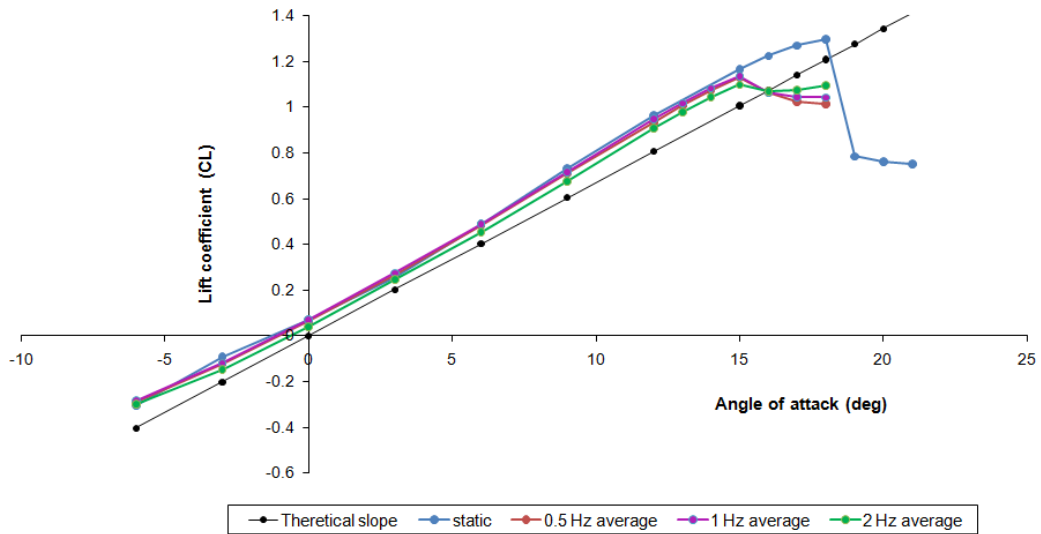


FIGURE 7.2 Average lift coefficients against angle of attack at freestream velocity of 30 m/s and theoretical inviscid static lift calculated based on thin aerofoil theory with the angles of attack from  $-6^\circ \leq \alpha \leq 21^\circ$  at  $Re = 3.34 \times 10^5$  and vane oscillation amplitude  $\pm 8^\circ$ .

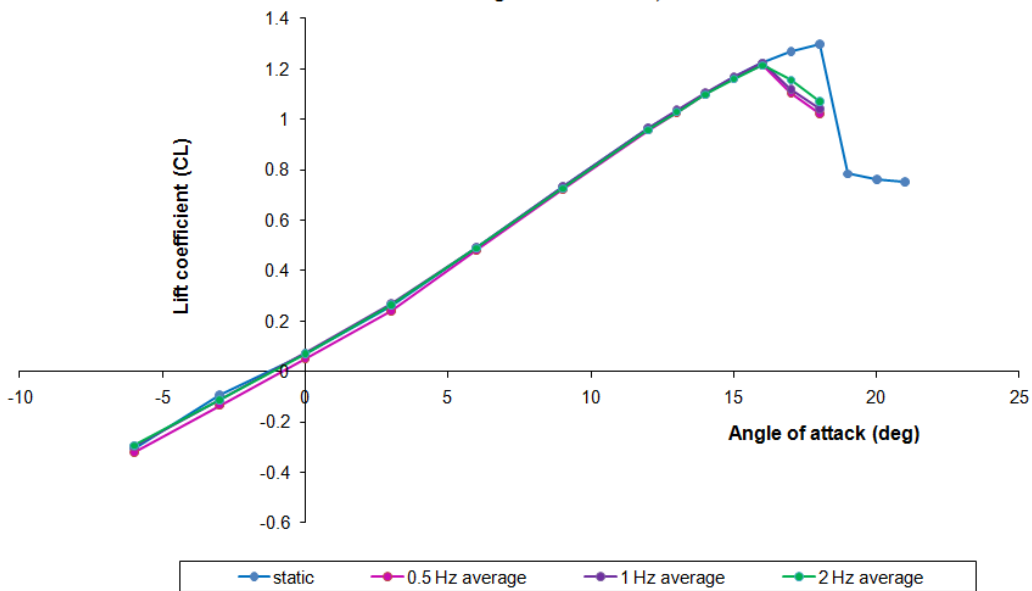


FIGURE 7.3 Average lift coefficients against angle of attack at freestream velocity of 30 m/s and theoretical inviscid static lift calculated based on thin aerofoil theory with the angles of attack from  $-6^\circ \leq \alpha \leq 21^\circ$  at  $Re = 3.34 \times 10^5$  and vane oscillation amplitude  $\pm 4^\circ$ .

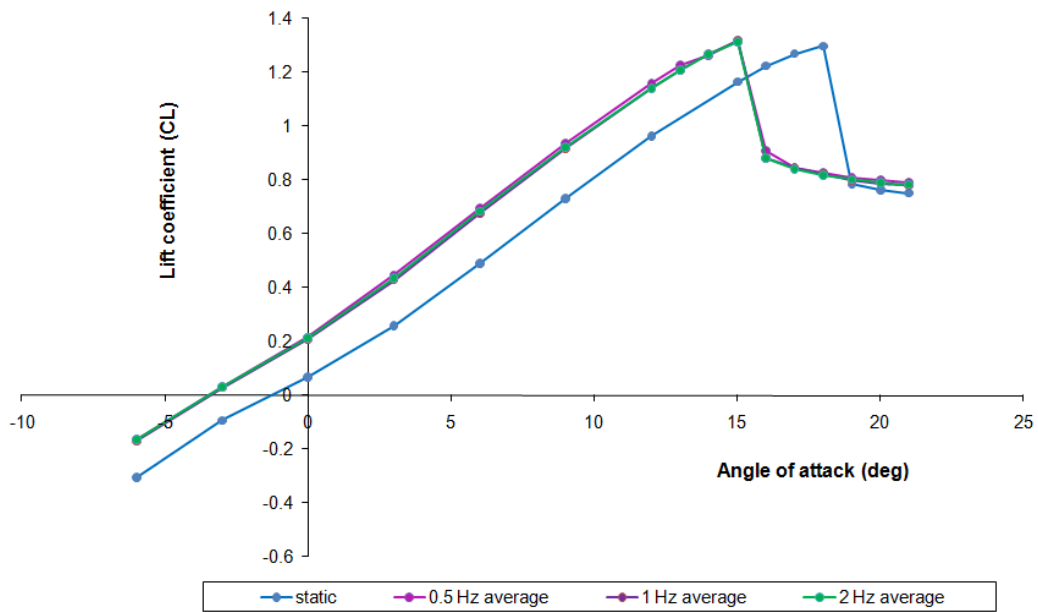


FIGURE 7.4 Average lift coefficients against angle of attack at freestream velocity of 30 m/s and theoretical inviscid static lift calculated based on thin aerofoil theory with the angles of attack from  $-6^\circ \leq \alpha \leq 21^\circ$  at  $Re = 3.34 \times 10^5$  and vane oscillation limit  $0^\circ - 4^\circ$ .

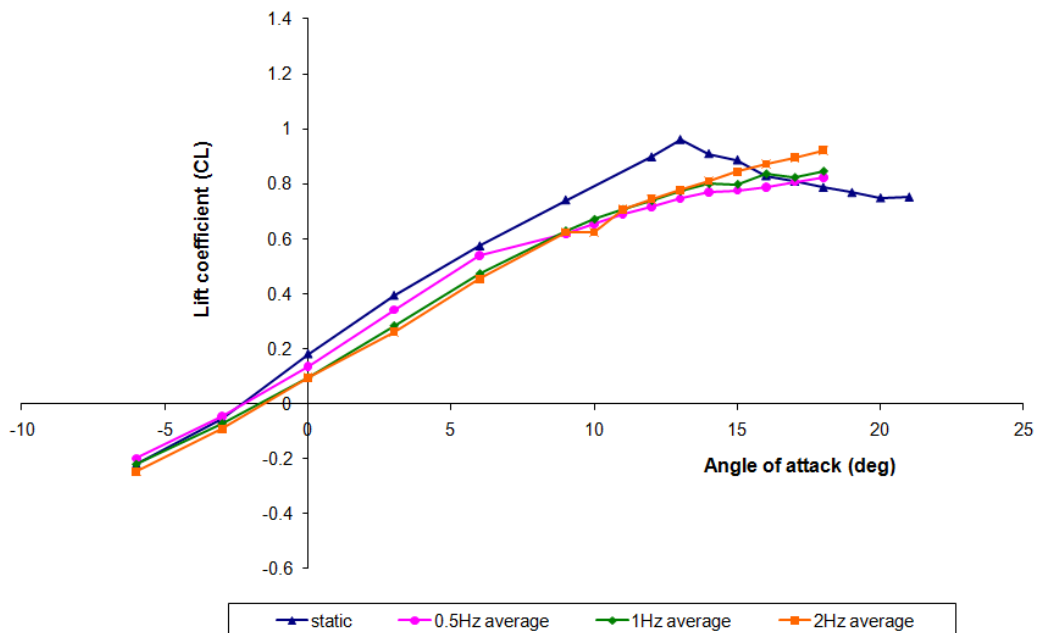


FIGURE 7.5 Average lift coefficients against angles of attack at  $Re = 1.11 \times 10^5$  and Vane oscillation amplitude  $\pm 8^\circ$ .

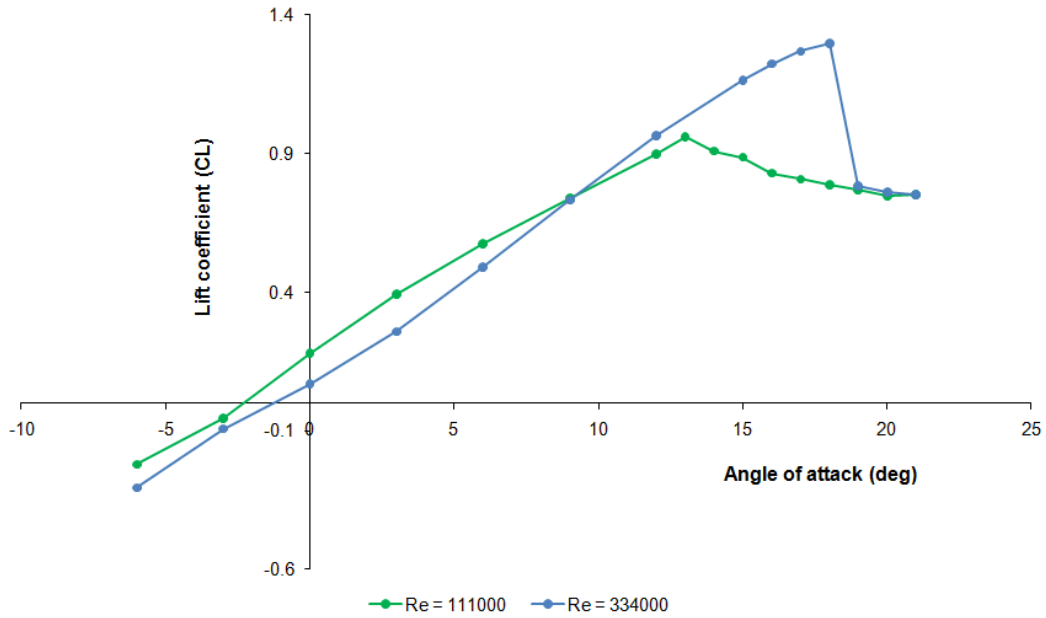


FIGURE 7.6 Static lift coefficients at different Reynolds numbers.

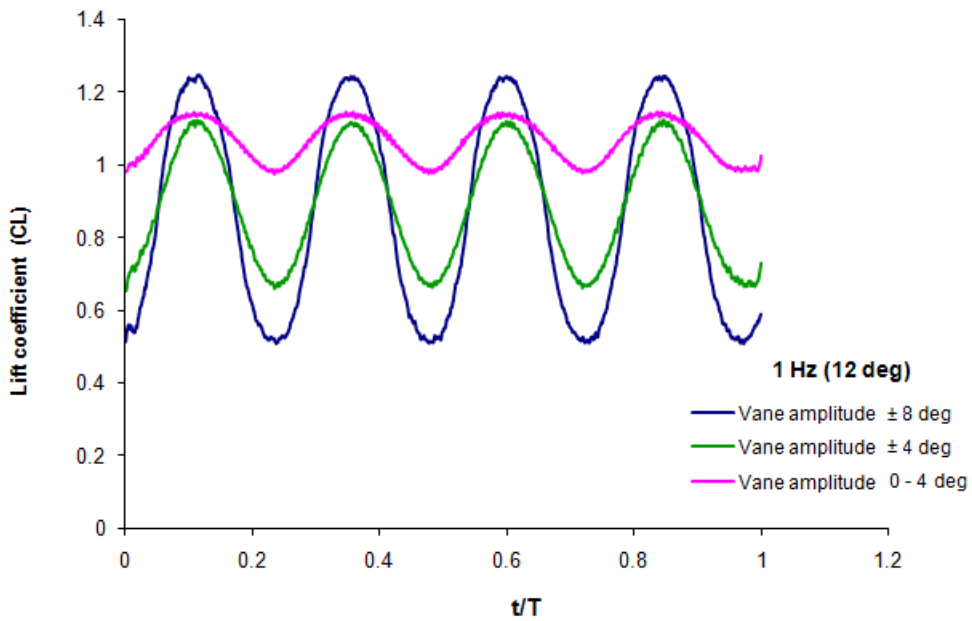


FIGURE 7.7 Lift coefficients at 12° at  $Re = 1.11 \times 10^5$ .

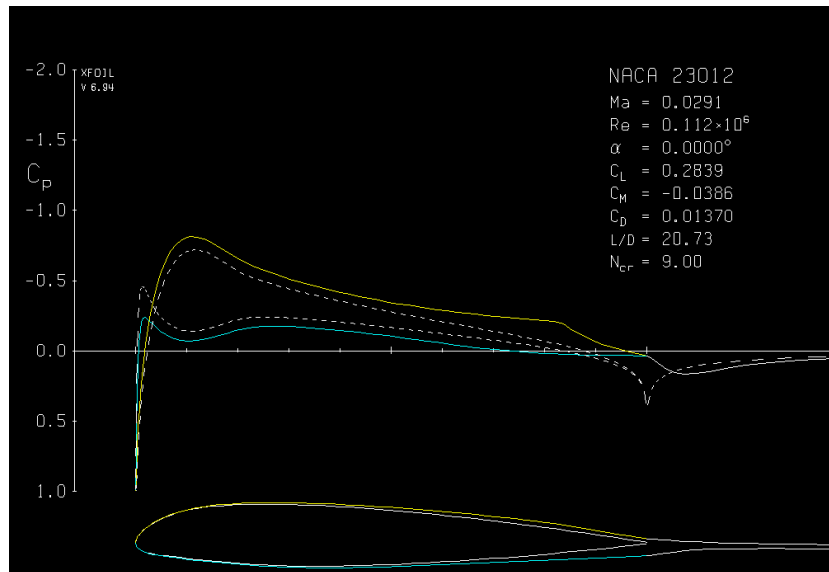


FIGURE 7.8 Static pressure distribution for NACA23012  $Re = 1.11 \times 10^5$ ,  $\alpha = 0^\circ$  where solid lines represent results included viscosity and dash lines represent results without viscosity.

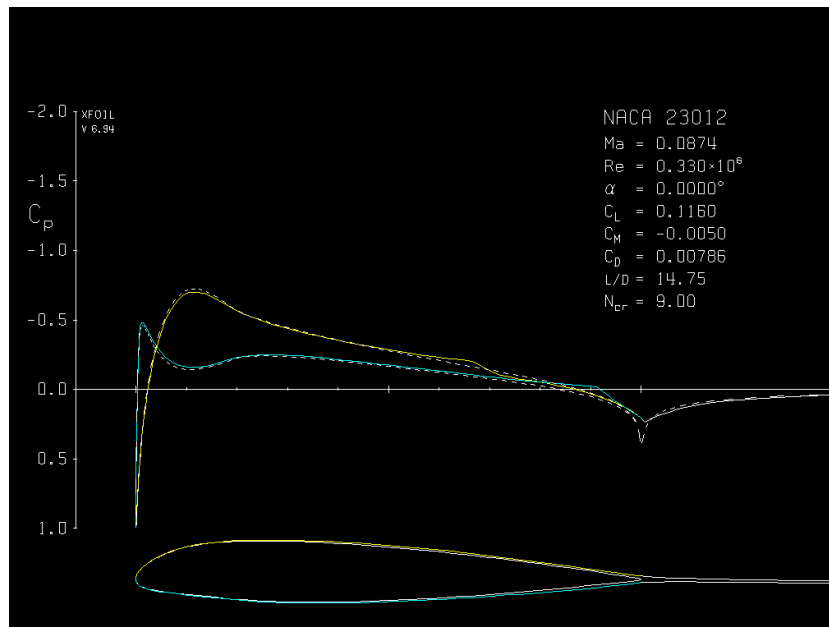


FIGURE 7.9 Static pressure distribution for NACA23012  $Re = 3.34 \times 10^5$ ,  $\alpha = 0^\circ$  where solid lines represent results included viscosity and dash lines represent results without viscosity.

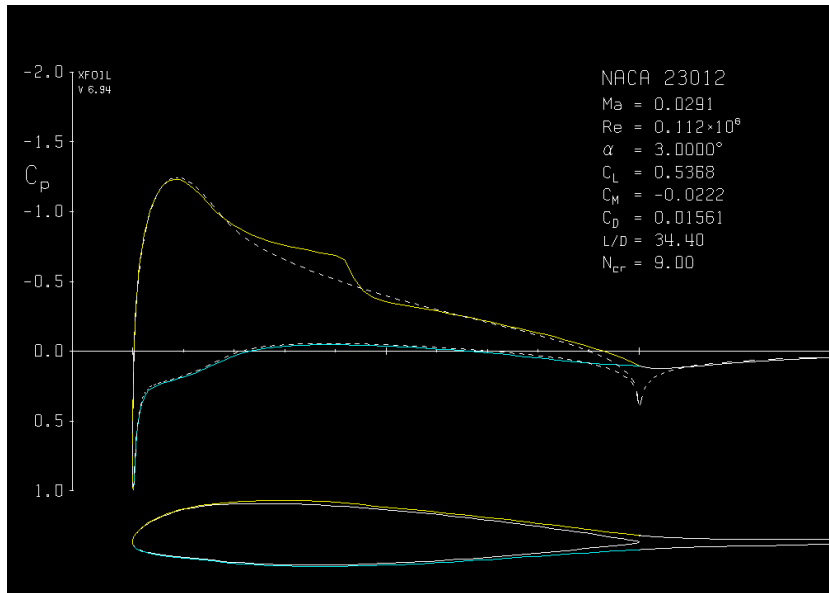


FIGURE 7.10 Static pressure distribution for NACA23012  $Re = 1.11 \times 10^5$ ,  $\alpha = 3^\circ$  where solid lines represent results included viscosity and dash lines represent results without viscosity.

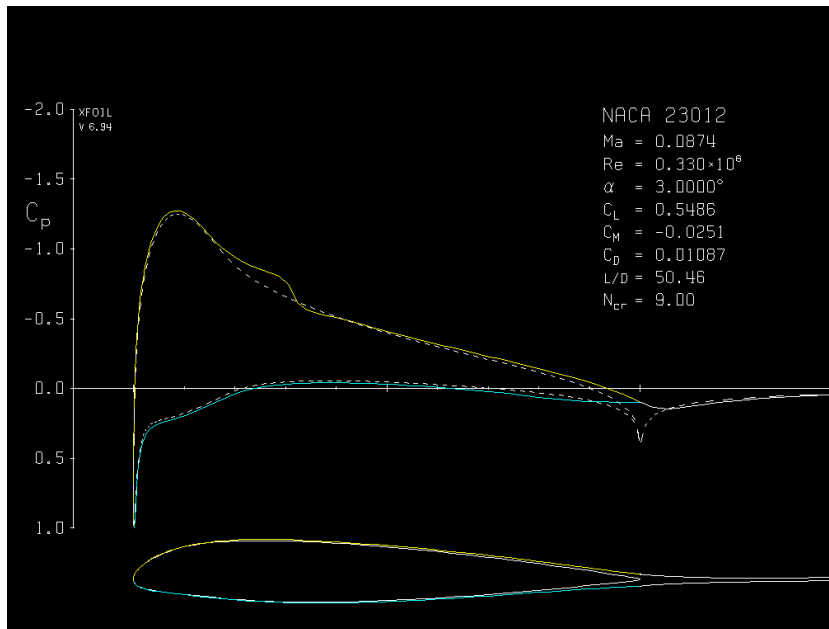
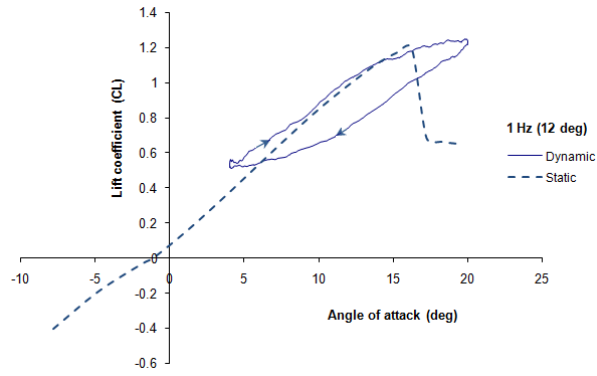
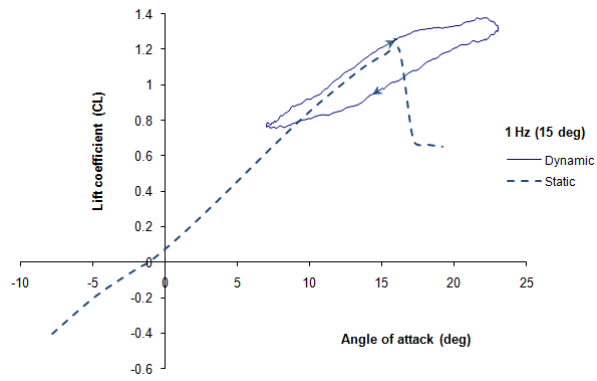


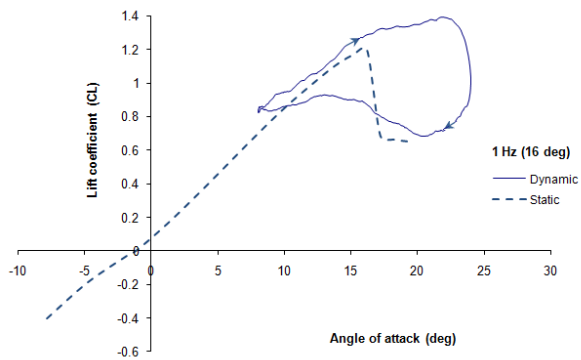
FIGURE 7.11 Static pressure distribution for NACA23012  $Re = 3.34 \times 10^5$ ,  $\alpha = 3^\circ$  where solid lines represent results included viscosity and dash lines represent results without viscosity.



(a)

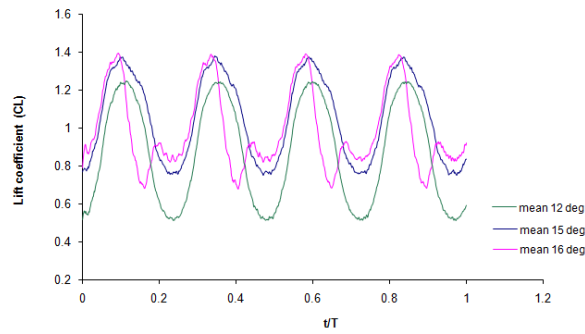


(b)

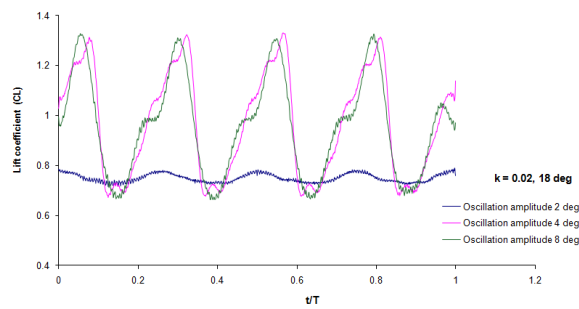


(c)

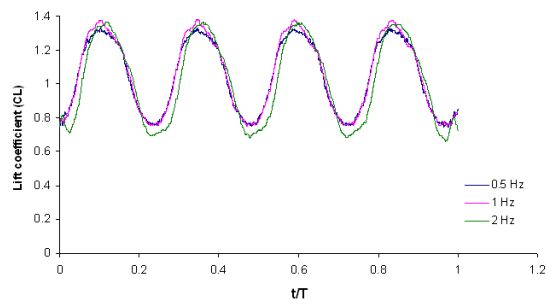
FIGURE 7.12 Effects of mean angle variation at a constant oscillation amplitude of  $\pm 8^\circ$  and reduced frequency of 0.02



(a) Lift coefficients at different mean angles of attack and  $Re = 3.34 \times 10^5$



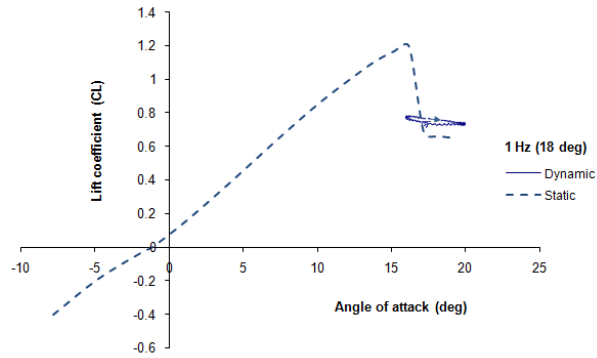
(b) Lift coefficients at different oscillation amplitudes and  $Re = 3.34 \times 10^5$



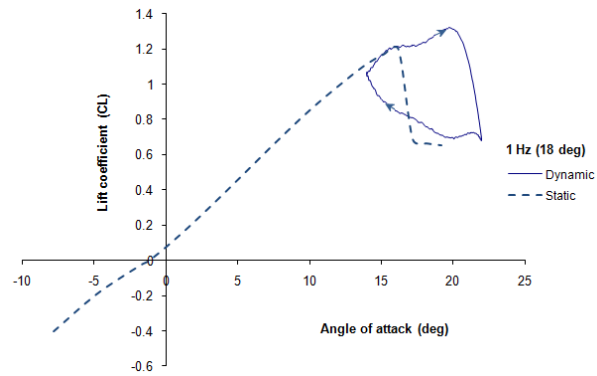
(c) Lift coefficients at different reduced frequencies and  $Re = 3.34 \times 10^5$

FIGURE 7.13 Time history of lift coefficients for the NACA 23012

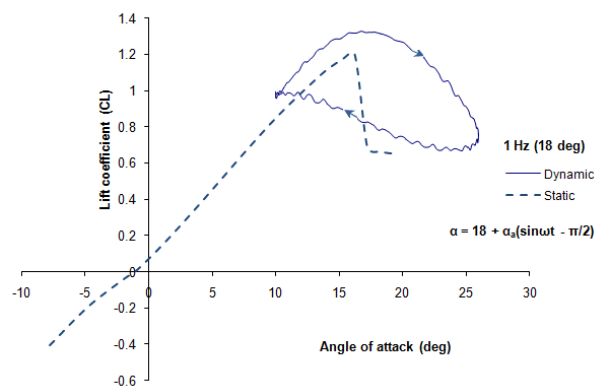




(a) Amplitude of oscillation = 2°

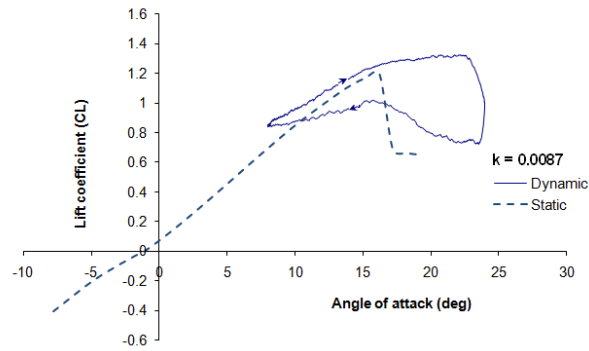


(b) Amplitude of oscillation = 4°

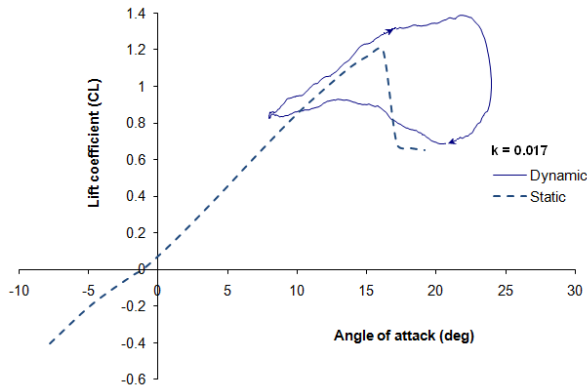


(c) Amplitude of oscillation = 8°

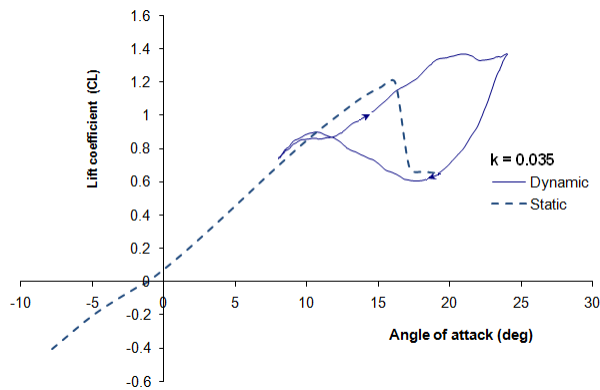
FIGURE 7.14 Effects of the lift coefficients at a constant mean angle of attack and reduced frequency of 0.02 with variation in oscillation amplitude



(a) Reduced frequency = 0.009

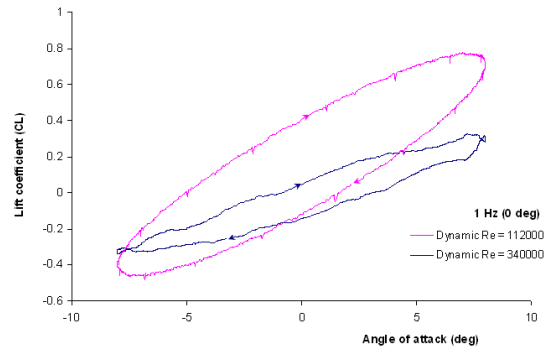


(b) Reduced frequency = 0.02

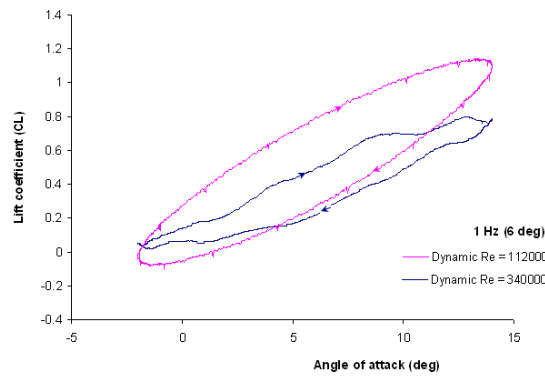


(c) Reduced frequency = 0.035

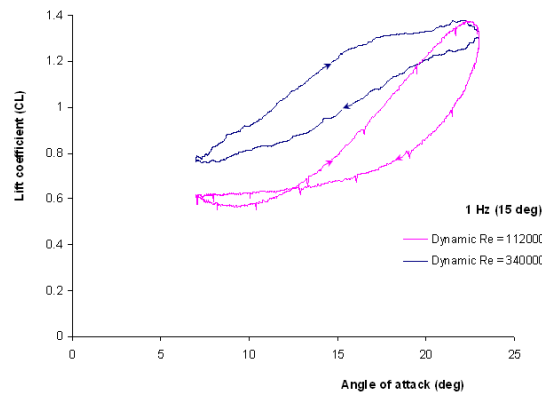
FIGURE 7.15 Effects of reduced frequency on the lift coefficients at constant mean angle of attack and oscillation amplitude of  $8^\circ$



(a) Constant oscillation amplitude at  $8^\circ$  and mean angle of attack =  $0^\circ$



(b) Constant oscillation amplitude at  $8^\circ$  and mean angle of attack =  $6^\circ$



(c) Constant oscillation amplitude at  $8^\circ$  and mean angle of attack =  $15^\circ$

FIGURE 7.16 Effects of Reynolds numbers on the lift coefficients at constant reduced frequency and constant oscillation amplitude of  $8^\circ$



# Chapter 8

## Conclusions and recommendations

### 8.1 Conclusions

The project into the aerodynamic problems of UAV operations in a lower part of an urban environment has been divided into three different experiments; boundary layer measurement, flow field behind bluff bodies and gust response due to sinusoidal gust.

The boundary layer experiment aim was to identify the mean velocity profile of a simulated turbulent boundary layer in a closed wind tunnel and estimate a boundary layer thickness in order to select a building geometry to fit in the simulated boundary layer. This led to a model simulation of a flow field at low altitude in an urban environment. Please note that the boundary layer measurements were tested only once. Therefore, the repeatability in the experimental results are not available. In the neutral boundary layer most of turbulence happens in a region close to the ground and it is diffused to a region away from the ground. The experimental results obtained in Chapter 4 are based on the freestream velocity of 5 m/s. The boundary layer thickness of the closed wind tunnel can be classified into three different cases; thick boundary layer, medium boundary layer and thin boundary layer with the average boundary layer thickness of 235 mm, 175 mm, and 100 mm according to three different upstream configurations. Thick boundary layer height is approximately 2.5 times higher than the thin boundary layer height indicating that the appearance of the upstream turbulence generators create more turbulent flow. The distance from the wind tunnel contraction to the test section is approximately 5 m, the boundary layer thickness measured at the test section possibly did not reach an equilibrium state. This means that the boundary layer thickness might grow further downstream from the test section. Consequently, measuring a boundary layer growth rate from the entrance to the test section

would be recommended in the future experiment. It is well-known that in stable conditions, the thickness boundary layer is reduced. However, if the turbulence condition was more unstable by increasing roughness elements and/or simulating a long stretch terrain upstream so that turbulence and the vertical shear in the test section could develop naturally, the boundary layer would be thicker.

The preliminary discussions of the simulated boundary layers in Chapter 4 lead to the conclusion of a selection of the building geometry and the relevant scale of atmospheric boundary layer in an urban environment. Two different models representing single and twin buildings were tested in the wind tunnel to investigate the flow fields around buildings immersed in the boundary layer. One objective is to determine the total velocity distribution at three different locations downstream from the leeward face. Another approach is to analyse the flow angularity behind the models in 2–dimensions in  $y$ - $z$  plane. The approach of simulating air flows around buildings are common in air pollution dispersion and wind loading on buildings. The results of the total velocity distributions and vector flows in the single and twin buildings are concluded separately. Flow field behind the single building is mainly induced by the flow separation from the roof and the separated shear flows from the sharp-edged sides. These flows interact with each other causing the highly unstable and reversed flow areas near the sharp-edged sides. The wake region adjacent to the building and its size are dependent on the boundary layer thickness and the building orientation [7]. The wake is reduced in size and diffused in space further downstream from the building. The vector plots of the velocity fields in  $y$ - $z$  plane are composed of lateral velocity and vertical velocity obtained from the measurement of five-hole probe. The majority of the flow behind the building tends to move upwards. A downwash of the flow originating from the flow deflected from the roof-top level is indicated by negative velocities. The magnitude of the highest lateral and vertical velocity gradients for the three locations are approximately,  $dU/d(Z/H)$  and  $dU/d(Y/H) \approx 140$ . It means for a 20 metres tall building in an urban environment, velocity gradients of up to 7 m/s per metre both lateral and vertical directions are expected. In case of twin-building configuration, the channeling flow is predominant. In the twin-building case, the flow interaction is classified into three different groups depending on a relative separation distance,  $w/H$ . If the buildings are too close together, the flow cannot penetrate into the gap between them because the buildings act as if they are one single building. On the other hand, if the gap between them is too large, there is not any flow interaction between them because the buildings act as if two individual buildings. The current experiments had the buildings set between these two extremes, at  $w/H = 0.6$  which provides the maximum flow interaction between them. The flow in the gap between the building accelerates leading to the maximum flow velocity at  $Z/H \approx 2/3$  near the exit plane. The flow separation

and flow recirculation at the side edges also cause the flow to accelerate but less magnitude than the velocity in the gap. The velocity vector fields in  $y$ - $z$  plane indicate more interaction between the shear flow and flow recirculation as moving away downstream from the buildings. Moreover, the air flow behind the building plane seems to slow down at  $X/H = 1.5$ . In the gap between the buildings, the velocity is still high with the majority of the air flow is deflected downwards. The author recommends further studies, using flow visualisation and PIV images, of the flow fields in an urban environment to aid, confirm and allow comparisons between the experiments by five-hole pressure probe. The magnitude of lateral velocity gradients  $dU/d(Z/H)$  is smaller than vertical velocity gradients. The change in lateral velocity gradients is mainly in the gap between the buildings. The magnitude of the highest  $dU/d(Y/H)$  and  $dU/d(Z/H)$  are approximately 180 and 120 respectively. It means for a 20 metre tall building in an urban environment, velocity gradients of up to 9 m/s per metre in vertical direction and 6 m/s in lateral direction can be expected. Another turbulence structure that may be involved in a difficulty of UAV stability and control is an influence of eddy scale or turbulence length scale. Simon and Viro [94] estimated the eddy scale in the atmospheric boundary layer can range from half a metre to approximately 15 metres long. Additionally from ESDU Data sheet 71016 [95] at low density built-up areas or small towns with mean hourly wind speed of 4.5 – 5.5 m/s, the turbulence length scale at altitude below 1000 metres can be up to 100 metres long. It is the author's belief that results from PIV would provide more details, fine resolutions and understanding of the instantaneous flow behaviours behind the buildings.

## 8.2 Recommendations

Recommendations for the future experiments relating to dynamic stall due to vane oscillation should include flow visualisation such as smoke flow to visualise the formation and mechanism of the leading edge vortex associated with dynamic stall with variation in parameters. Increase the oscillation amplitude up to  $\pm 15^\circ$  and reduced frequency up to 0.5, if possible, to further investigate the effects of oscillation amplitude and reduced frequency since these two parameters appear to have the most influence on the lift characteristic under dynamic condition. Also increase the angle of attack to approximately  $25^\circ - 27^\circ$  to observe the dynamic stall angle of incidence whether beyond this angle the lift is still further created.





# References

- [1] J.E. Cermak. Laboratory simulation of the atmospheric boundary layer. *AIAA Journal*, 9(9):1746–1754, 1971.
- [2] F.J. Maher T.A. Reinhold, H.W. Tieleman. Simulation of the urban neutral boundary layer for the model study of wind loads on tall buildings. Technical Report VPI-E-77-12, Virginia Polytechnic Institute and State University, 1978.
- [3] C. J. Baker. The laminar horseshoe vortex. *Journal of Fluids Mechanic*, 8:374, 1979.
- [4] N. Nigro, G. Filippini, G. Franck, M. Storti, and J. D’Elia. Flow around a sharp-edged surface-mounted cube by large eddy simulation. *Mecanica Computacional*, 24, November, 2005.
- [5] R. Martinuzzi and C. Tropea. The flow around surface-mounted, prismatic-obstacles placed in a fully developed channel flow. *ASME: Journal of Fluids Engineering*, 115:85–92.
- [6] T. V. Lawson. *Wind effects on Buildings*. Applied Science Publishers.LtD, Great Yarmouth, Great Britain, 1980.
- [7] E. R. Meinders and K. Hanjalic. Vortex structure and heat transfer in turbulent flow over a wall-mounted matrix of cubes. *International Journal of Heat and Fluid Flow*, 20:255–267, 1999.
- [8] S. Krajnovic and L. Davidson. Flow around a three-dimensional bluff body. *9<sup>th</sup> International Symposium on Flow Visualisation, Heriot-Watt University, Edinburgh*, 2000.
- [9] F. Ricciardelli and S. Polimeno. Some characteristics of the wind flow in the lower urban boundary layer. *Journal of Wind Engineering and Industrial Aerodynamics*, 94:815–832, 2006.

## REFERENCES

- [10] C. H. Chang and R. N. Meroney. Concentration and flow distributions in urban street canyons: wind tunnel and computational data. *Journal of Wind engineering and Industrial aerodynamics*, 91:1141–1154, 2003.
- [11] M. Farhadi and K. Sedighi. Flow over two tandem wall-mounted cubes using large eddy simulation. *JMES Proc. IMechE Part. C*, 222:1465–1475.
- [12] J. F. Sini et al. Pollutant dispersion and thermal effects in urban street canyons. *Atmospheric Environment*, 30:2659–2677, 1996.
- [13] R. J. Martinuzzi and Brian Havel. Turbulent flow around two interfering surface-mounted cubic obstacles in tandem arrangement. *ASME Journal of Fluids Engineering*, 122:24–31, 2000.
- [14] Jong-Jin Baik and Jae jin Kim. A numerical study of flow and pollutant dispersion characteristics in urban street canyons. *Journal of Applied Meteorology*, 38:1567–1589, 1998.
- [15] A. Kova-Panskus et al. Influence of geometry on the mean flow within urban street canyons - a comparison of wind tunnel experiments and numerical simulations. *Water, Air and Soil pollution: Focus. 2*, pages 356–380, 2000.
- [16] T. R. Oke. Street design and urban canopy layer climate. *Energy and Buildings*, 11:103–113, 1988.
- [17] I. D. Watson L. T. Hunter and G. T. Johnson. Modelling air flow regimes in urban canyons. *Energy and Buildings*, 15–16:315–324, 1990–1991.
- [18] Jan Carmeliet Bert Blocken and Ted Stathopoulos. Cfd evaluation of wind speed conditions in passages between parallel buildings-effect of wall-function roughness modifications for the atmospheric boundary layer flow. *Journal of Wind engineering and Industrial aerodynamics*, 95:941–962, 2007.
- [19] H. Sakamoto and H. Haniu. Aerodynamic forces acting on two square prisms placed vertically in a turbulent boundary layer. *Journal of Wind engineering and Industrial aerodynamics*, 31:41–66, 1988.
- [20] T. Statthopoulos and R. Storms. Wind environmental conditions in passages between buildings. *Journal of Wind engineering and Industrial aerodynamics*, 24:19–31, 1986.
- [21] H. Kawai. Local peak pressure and conical vortex on building. *Journal of Wind engineering and Industrial aerodynamics*, 90:251–263, 2002.

## REFERENCES

- [22] H.Kawai. Structure of conical vortices related with suction fluctuation on a flat roof in oblique smooth and turbulent flows. *Journal of Wind engineering and Industrial aerodynamics*, 69-70:579–588, 1997.
- [23] R. Marwood and C.J. Wood. Conical vortex movement and its effect on roof pressures. *Journal of Wind engineering and Industrial aerodynamics*, 69-71:589–595, 1997.
- [24] Taniguchi Tetsuro Taniike Yoshihito and Morozumi Tatsuro. Switching phenomenon of conical vortex on various flat roofs. *Proceedings of National Symposium on Wind Engineering*, 15:305–310, 1998.
- [25] T. Tamura Y. Ono and H. Kataoka. Les analysis of unsteady characteristics of conical vortex on a flat roof. *Journal of Wind engineering and Industrial aerodynamics*, 96:2007–2018, 2008.
- [26] Y. Okuda and Y. Taniike. Conical vortices over side face of three-dimensional square prism. *Journal of Wind engineering and Industrial aerodynamics*, 50:163–172, 1993.
- [27] V. G. Quincey M. E. Davies and S. J. Tindall. *The near wake of a tall block in uniform and turbulent flows, in Wind Engineering (Edited by J.E.Cermak)*, page 289. Pergamon Press, New York, 1980.
- [28] I. P. Castro and A. G. Robin. The flow around a surface mounted cube in a uniform and turbulent streams. *Journal of Fluid Mechanics*, 79:307–336, 1977.
- [29] J. A. Peterka H. G. C. Woo and J. E. Cermak. Wind tunnel measurements in the wakes of structures. Technical Report NASA–CR–2806, N77–19716, NASA, 1977.
- [30] W. H. Melbourne. Comparison of pressure measurements made on a large isolated building in a full and model scale. Number 253, Tokyo, Japan, 1971. Proceedings of the 3<sup>th</sup> International Conference on Wind Effects on Buildings and Structures.
- [31] J. Katsura Y. Okuda and S. Kawamura. Local severe suction on the side of a prism model on a field. *Journal of Wind engineering and Industrial aerodynamics*, 72:23–32, 1997.
- [32] W. H. Melbourne and P. N. Joubert. Problems of wind flow at the base of tall buildings. Number I.11-1 - I.11-10, Tokyo, Japan, 1971. Proceedings of the 3<sup>th</sup> International Conference on Wind Effects on Buildings and Structures.

## REFERENCES

- [33] H. Leinhart S. Becker and F. Durst. Flow around three-dimensional obstacles in boundary layer. *Journal of Wind engineering and Industrial aerodynamics*, 90:265–279, 2002.
- [34] W. H. Schofield and E. Logan. Turbulent shear flow over surface mounted obstacles. *Journal of Fluids Engineering*, 112:376–385, 1990.
- [35] W. J. Benarek. Wind environment around single buildings of rectangular shape. *Heron*, 29, 1984.
- [36] H. Ishizaki and I. W. Sung. Influence of adjacent buildings to wind effects. pages 145–152, Tokyo, Japan, 1971. Proceedings of the 3<sup>RD</sup> International Conference on Wind Effects on Buildings and Structures.
- [37] Berend Feddersen. Wind tunnel modelling of turbulence and dispersion above tall and highly urban roughness. *Dissertation submitted to Swiss Federal Institute of technology Zurich*, 2005.
- [38] Masaaki Ohba. Experimental study of effects of separation distance between twin high-rise tower models on gaseous diffusion behind the downwind tower model. *Journal of Wind engineering and Industrial aerodynamics*, 77 and 78:555–566, 1998.
- [39] B. Blocken and J. Carmeliet. Pedestrians wind environment around buildings: Literature review and practical examples. *Journal of Thermal Env and Bldg. Sci.*, 28, 2004.
- [40] Sigrid Reiter Geoffrey Van Moeseke, Elisabeth Gratia and Andre De Herde. Wind pressure distribution influence on natural ventilation for different incidences and environment densities. *Energy and Buildings*, 37:878–889, 2005.
- [41] I. D. Watson L. T. Hunter and G. T. Johnson. Modelling air flow regimes in urban canyons. *Energy and Buildings*, 15/16:315–324, 1990/1991.
- [42] W. J. Benarek. Wind environment around building configurations. *Heron*, 29, 1984.
- [43] J.E Allen. *Aerodynamics A Space-Age Survey*. Hutchinson and CO. Ltd, London, 1963.
- [44] D. Banks, R.N. Meroney, P.P. Sarkar, Z. Zhao, and F. Wu. Flow visualization of conical vortices on flat roofs with simultaneous surface pressure measurement. *Journal of Wind engineering and Industrial aerodynamics*, 84:65–85, 2000.

## REFERENCES

- [45] Hoerner and Borst. *Practical information on aerodynamic and hydrodynamic lift*. Mrs. Liselotte A. Hoerner, 1985.
- [46] Edward C. Polhamus. A survey of reynolds number and wing geometry effects on lift characteristics in the low speed stall region. Technical Report NASA Contractor Report 4745, NASA, Langley Research Centre, 1996.
- [47] J. G. Leishman. *Principles of helicopter aerodynamics*. Cambridge University Press, 2006.
- [48] M. A. McVeigh and E. Kisielowski. A design summary of stall characteristics of straight wing aircraft. Technical Report NASA Contractor Report 1646, NASA, Washington D. C., 1971.
- [49] P. Owen and L. Klanfer. On the laminar boundary layer separation from the leading edge of a thin aerofoil. Technical Report RAE Rep. Aero 2508, 1953.
- [50] I. Tani. Low speed flow involving bubble separations. *Progress in Aeronautical Science, Pergamon Press*, pages 70–103, 1964.
- [51] M. Alam and N. D. Sandham. Direct numerical simulation of ‘short’ laminar separation bubbles with turbulent reattachment. *Journal of Fluid Mechanics*, 410:1–28, 2000.
- [52] Jr J. D. Anderson. *Fundamentals of Aerodynamics*, chapter 2<sup>th</sup> Edition. McGraw-Hill Book Company, 1991.
- [53] Ira H. Abbott and Albert. E. von Doenhoff. *Theory of wing section*. Dover Publications, Inc, 1958.
- [54] W.J. McCrosky and P.M. Goorjian. Interactions of airfoils with vertical gusts and concentrated vortices in unsteady transonic flow. *AIAA paper 83-1691*, 1983.
- [55] L. H. Carr and M. S. Chandrasekhara. Compressibility effects on dynamic stall. *Progress in Aerospace Sciences*, 32:523–573, 1996.
- [56] K. W. McAlister W. C. Lawrence and W. J. McCrosky. Analysis of the development of dynamic stall based on oscillating airfoil experiments. Technical Report NASA Technical Note D-8382, NASA, Washington D. C., 1977.
- [57] M. H. Akbari and S. J. Price. Simulation of the flow over elliptic airfoil oscillating at large angles of attack. *Journal of Fluids and Structures*, 14:757–777, 2000.

## REFERENCES

- [58] L. W. Carr K. W. McAlister, W. J. McCrosky and S. L. Pucci. An experimental study of dynamic stall on advanced airfoil sections. Technical Report NASA TM 84245, NASA, Washington D. C., 1982.
- [59] P. F. Lober. Compressibility effects on dynamic stall of a three-dimensional wing. *AIAA paper 92-0191*, 1992.
- [60] R. A. Piziali. 2-d and 3-d oscillating wing aerodynamics for a range of angles of attack including stall. Technical Report Technical Report 94-A-011, NASA, Washington D. C., 1994.
- [61] Lober P. F., Covino A. F., and Carta F. O. Dynamic stall experiments on a swept three-dimensional wing in compressible flow. *AIAA paper 91-1795*, 1991.
- [62] Paul G. A. Cizmas D. M. Tang and E. H. Dowell. Experiments and analysis for a gust generator in a wind tunnel. *Journal of Aircraft*, 33(1):139–148, 1996.
- [63] J. K. Henry D. M. Tang and E. H. Dowell. Effects of steady angle of attack on nonlinear gust response of a delta wing model. *Journal of Fluids and Structures*, 16(8):1093–1110, 2002.
- [64] D. M. Tang and E. H. Dowell. Experimental and theoretical study of gust response for high-aspect-ratio wing. *AIAA Journal*, 40(3):419–429, 2002.
- [65] P. W. Hanson L. T. Redd and E. C. Wynne. Evaluation of a wind-tunnel gust response technique including correlations with analytical and flight test results. Technical Report NASA Technical Paper 1501, NASA, Langley, 1979.
- [66] J. Bicknell and A. G. Parker. A wind-tunnel stream oscillation apparatus. *Journal of Aircraft*, 9(6):446–447, 1972.
- [67] T. Theodorsen. General theory of aerodynamics instability and mechanism of flutter. Technical Report N.A.C.A. 496, NASA, Langley, 1949.
- [68] D. J. Peake C. Singh and A. Kokkalis. Control of rotorcraft retreating blade stall using air-jet vortex generator. *Journal of Aircraft*, 43:1169–1176, 2006.
- [69] M. M. O’Meara and T. J. Mueller. Laminar separation bubble characteristics on an airfoil at low reynolds numbers. *AIAA Journal*, 25(8):1033–1041, 1987.
- [70] W. B. Roberts. Calculation of laminar separation bubbles and their effect on airfoil performance. *AIAA Journal*, 18(1):25–31, 1980.

## REFERENCES

- [71] <http://www.unitedsensorcorp.com/pitot.html>.
- [72] J. E. Cermak. *Physical modelling of the atmospheric boundary layer in long boundary-layer wind tunnel*, *Wind Tunnel Modelling for Civil Engineering Applications*, pages 97–125. Cambridge University Press, 1982.
- [73] T. Maruyama and H. Ishizaki. A wind tunnel test on the boundary layer characteristics above an urban area. *Journal of Wind Engineering and Industrial Aerodynamics*, 28:139–148, 1988.
- [74] Joseph A. Schetz. *Boundary layer analysis*. Prentice-Hall, Englewood Cliffs, New Jersey, 1993.
- [75] M. Y. Gundogdu and M. O. Carpinlioglu. A multi-hole pressure probe calibration method for measurements of mean flow parameters in swirling flows. *Flow Measurement and Instrumentation*, 9:243–248, 1998.
- [76] D. W. Bryer and R. C. Pankhurst. *Pressure-probe methods for determining wind speed and flow direction*. National Physical Laboratory, HMSO, 1971.
- [77] M. T. Schobeiri G. L. Morrison and K. R. Pappu. Five-hole pressure probe analysis technique. *Flow Measurement and Instrumentation*, 9:153–158, 1998.
- [78] M. Govardhan C. V. Babu and N. Sitaram. A method of calibration of a seven-hole pressure probe for measuring highly three-dimensional flows. *Meas. Sci. Technol*, 9:468–476, 1998.
- [79] D. E. Walshe D. W. Bryer and H. C. Garner. Pressure probes selected for three-dimensional flow measurement. *Rep. Memor. Aero. Res. Coun. Lond.*, No.3037, 1958.
- [80] B. A. Singer P. M. Ligrani and L. R. Baun. Miniature five-hole pressure probe for measurement of three mean velocity components in low-speed flow. *J. Phys. E: Sci. Instrum*, 22:868–876, 1989.
- [81] R. G. Dominy and H. P. Hodson. An investigation of factors influencing the calibration of five-hole probes for three-dimensional flow measurements. *Journal of Turbomachinery*, 115:513–519, 1993.
- [82] Gregory G. Zilliac. Calibration of seven-hole pressure probes for use in fluid flows in large angularity. Technical Report NASA Tech. Mem. 102200, NASA, 1989.

## REFERENCES

- [83] A. L. Treaster and A. M. Yocum. The calibration and application of five-hole probes. *ISA Trans*, 18:1–51.
- [84] C. S Lee and N. J. Wood. Calibration and data reduction for a five-hole probe. Technical Report JIAA TR-73, Joint Institute for Aeronautics and Acoustics Stanford University, 1986.
- [85] A. L. Yarin C. Tropea and J. F. Foss. *Springer Handbook of Experimental fluid mechanics*, chapter 5. Springer, 2007.
- [86] John R. Taylor. *An introduction to error analysis*. University Science Books, 1982.
- [87] Blockage corrections for bluff bodies in confined flow. *ESDU Item No. 80024, Engineering Science data Unit*, 1998.
- [88] M. Tutar and G. Oguz. Large eddy simulation of wind flow around parallel buildings with varying configurations. *Fluid Dynamics Research*, 31:289–315, 2002.
- [89] G. Schewe and A. Larsen. Reynolds number effects in the flow around a bluff bridge deck cross section. *Journal of Wind Engineering and Industrial Aerodynamics*, 74-76:829–838, 1996.
- [90] R. P. Hoxey, A. M. Reynolds, G. M. Richardson, A. P. Robertson, and J. L. Short. Observations of reynolds number sensitivity in the separated flow region on a bluff body. *Journal of Wind Engineering and Industrial Aerodynamics*, 73:231–249, 1998.
- [91] G. L. Larose and A. D’Auteuil. On the reynolds number sensitivity of the aerodynamics of bluff bodies with sharp edges. *Journal of Wind Engineering and Industrial Aerodynamics*, 94:365–376, 2006.
- [92] E. N. Jacobs and R. M. Pinkerton. Tests of n.a.c.a. airfoils in the variable-density wind tunnel. series 230. Technical Report NASA Technical Paper 567, NASA, Langley, 1936.
- [93] <http://web.mit.edu/drela/Public/web/xfoil/>.
- [94] S. Watkins and G. V. V. The turbulence wind environment of birds, insects and mavs. *15<sup>th</sup> Australian Fluid Mechanics Conference*, 2004.
- [95] Fluid forces, pressures and moments on rectangular block. *ESDU Item No. 71016, Engineering Science data Unit*, 1978.



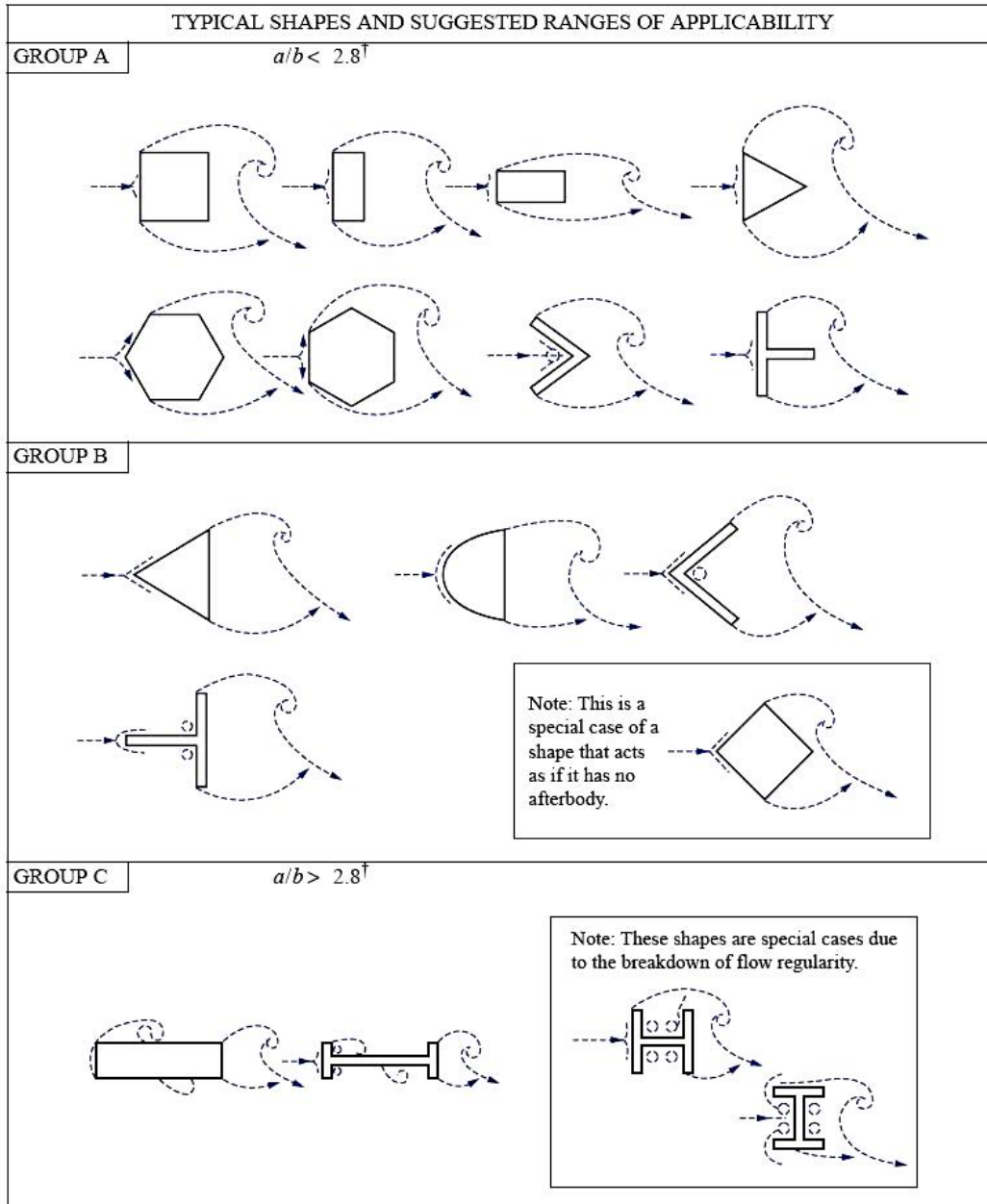
## REFERENCES

- [96] Structure of non-circular cross section: Dynamic response due to vortex shedding. *ESDU Item No. 90036, Engineering Science data Unit*, 2006.
- [97] L. Rosenhead. The airfoil in a wind tunnel of elliptic section. *Proceedings of the Royal Society of London. Series A*, 140(842):579–604, 1933.
- [98] JR J. B. Barlow, W. H. Rae and A. Pope. *Low-speed wind tunnel testing*. John Wiley and Sons. Inc, 1999.



# **Appendix A**

## **Classification of Structural Shapes**



\* Vortex spacing is not drawn to scale

† These values assume low turbulence intensity. High values of turbulence can lead to flow reattachment, and section shapes can move from Group A to Group C.

FIGURE A.1 Vortex shedding from different bluff body shapes [96]

# Appendix B

## Vector Resolution for Five-hole Probe Calibration Modes

In this appendix, there are two different calibration modes presented referenced by Treaster and Yocum [83]. Consider velocity vector  $\mathbf{V}$  in an original coordinate consists of another three velocity components  $V_1, V_2$  and  $V_3$ . Also the prime velocity components  $V'_1, V'_2$  and  $V'_3$  are the velocity in a rotated plane. The velocity in the rotated plane can be derived from

$$\mathbf{V}'_1 = \sum \mathbf{a}_{ij} \mathbf{V}_j \quad (\text{B.1})$$

Meanwhile the  $a_{ij}$  terms are a direction of cosine derived from

$$\mathbf{a}_{ij} = \cos(X'_i, X_j) \quad (\text{B.2})$$

The meaning of  $(X'_i, X_j)$  is an angle between  $X'_i$  and  $X_j$  in a positive direction.

### B.1 For "yaw-pitch mode" for probe calibration

The first mode to be looking at is "yaw-pitch mode" where the rotation is about the  $X_1$  axis. The velocity vector  $\mathbf{V}$  is in the  $X_3$  direction of the original axes with yawing angle of magnitude  $\beta$  as shown in FigureB.1. Hence,  $V_1 = V_2 = 0$  and  $V_3 = V$

Considering the yaw motion, the direction of cosine  $a_{ij} = \cos(X'_i, X_j)$  can be expressed in all three directions as follows:

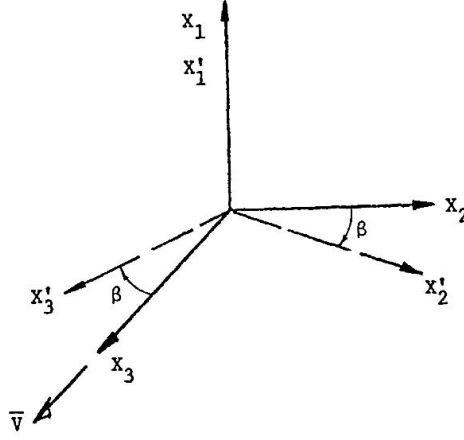


FIGURE B.1

$$\begin{aligned}
 \mathbf{a}_{11} &= \cos(\mathbf{X}'_1, \mathbf{X}_1) = \cos(0^\circ) = 1.0 \\
 \mathbf{a}_{12} &= \cos(\mathbf{X}'_1, \mathbf{X}_2) = \cos(90^\circ) = 0 \\
 \mathbf{a}_{13} &= \cos(\mathbf{X}'_1, \mathbf{X}_3) = \cos(90^\circ) = 0 \\
 \mathbf{a}_{21} &= \cos(\mathbf{X}'_2, \mathbf{X}_1) = \cos(90^\circ) = 0 \\
 \mathbf{a}_{22} &= \cos(\mathbf{X}'_2, \mathbf{X}_2) = \cos(\beta) \\
 \mathbf{a}_{23} &= \cos(\mathbf{X}'_2, \mathbf{X}_3) = \cos(90^\circ - \beta) = \sin(\beta) \\
 \mathbf{a}_{31} &= \cos(\mathbf{X}'_3, \mathbf{X}_1) = \cos(90^\circ) = 0 \\
 \mathbf{a}_{32} &= \cos(\mathbf{X}'_3, \mathbf{X}_2) = \cos(90^\circ + \beta) = -\sin(\beta) \\
 \mathbf{a}_{33} &= \cos(\mathbf{X}'_3, \mathbf{X}_3) = \cos(\beta)
 \end{aligned} \tag{B.3}$$

Therefore from Eq.B.1 velocity components in the three rotated axes system are

$$\mathbf{V}'_1 = \mathbf{a}_{11}\mathbf{V}_1 + \mathbf{a}_{12}\mathbf{V}_2 + \mathbf{a}_{13}\mathbf{V}_3 = 0 \tag{B.4}$$

$$\mathbf{V}'_2 = \mathbf{a}_{21}\mathbf{V}_1 + \mathbf{a}_{22}\mathbf{V}_2 + \mathbf{a}_{23}\mathbf{V}_3 = \mathbf{V} \sin(\beta) \tag{B.5}$$

$$\mathbf{V}'_3 = \mathbf{a}_{31}\mathbf{V}_1 + \mathbf{a}_{32}\mathbf{V}_2 + \mathbf{a}_{33}\mathbf{V}_3 = \mathbf{V} \cos(\beta) \tag{B.6}$$

next rotation is to consider the pitch direction rotating about the  $X'_2$  axis with pitch angle of  $\alpha$  as displayed in Figure B.2.

## B VECTOR RESOLUTION FOR FIVE-HOLE PROBE CALIBRATION MODES

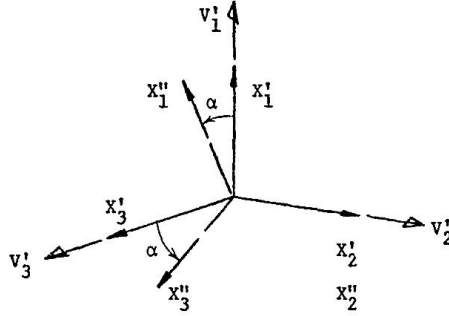


FIGURE B.2

$$\begin{aligned}
 \mathbf{a}_{11} &= \cos(\mathbf{X}''_1, \mathbf{X}'_1) = \cos(\alpha) \\
 \mathbf{a}_{12} &= \cos(\mathbf{X}''_1, \mathbf{X}'_2) = \cos(90^\circ) = 0 \\
 \mathbf{a}_{13} &= \cos(\mathbf{X}''_1, \mathbf{X}'_3) = \cos(90^\circ - \alpha) = \sin(\alpha) \\
 \mathbf{a}_{21} &= \cos(\mathbf{X}''_2, \mathbf{X}'_1) = \cos(90^\circ) = 0 \\
 \mathbf{a}_{22} &= \cos(\mathbf{X}''_2, \mathbf{X}'_2) = \cos(0^\circ) = 1.0 \\
 \mathbf{a}_{23} &= \cos(\mathbf{X}''_2, \mathbf{X}'_3) = \cos(90^\circ) = 0 \\
 \mathbf{a}_{31} &= \cos(\mathbf{X}''_3, \mathbf{X}'_1) = \cos(90^\circ + \alpha) = -\sin(\alpha) \\
 \mathbf{a}_{32} &= \cos(\mathbf{X}''_3, \mathbf{X}'_2) = \cos(90^\circ) = 0 \\
 \mathbf{a}_{33} &= \cos(\mathbf{X}''_3, \mathbf{X}'_3) = \cos(\alpha)
 \end{aligned} \tag{B.7}$$

Therefore, combining the velocity components of the pitch motion in equation B.7 through equation B.1 giving:

$$\mathbf{V}''_1 = \mathbf{a}_{11}\mathbf{V}'_1 + \mathbf{a}_{12}\mathbf{V}'_2 + \mathbf{a}_{13}\mathbf{V}'_3 = 0 + 0 + \mathbf{V} \cos(\beta) \sin(\alpha) = \mathbf{V} \cos(\beta) \sin(\alpha) \tag{B.8}$$

$$\mathbf{V}''_2 = \mathbf{a}_{21}\mathbf{V}'_1 + \mathbf{a}_{22}\mathbf{V}'_2 + \mathbf{a}_{23}\mathbf{V}'_3 = 0 + \mathbf{V} \sin(\beta) + 0 = \mathbf{V} \sin(\beta) \tag{B.9}$$

$$\mathbf{V}''_3 = \mathbf{a}_{31}\mathbf{V}'_1 + \mathbf{a}_{32}\mathbf{V}'_2 + \mathbf{a}_{33}\mathbf{V}'_3 = 0 + 0 + \mathbf{V} \cos(\beta) \cos(\alpha) = \mathbf{V} \cos(\beta) \cos(\alpha) \tag{B.10}$$

Therefore, three velocity components in cylindrical polar coordinates are defined as in Cartesian Coordinates as

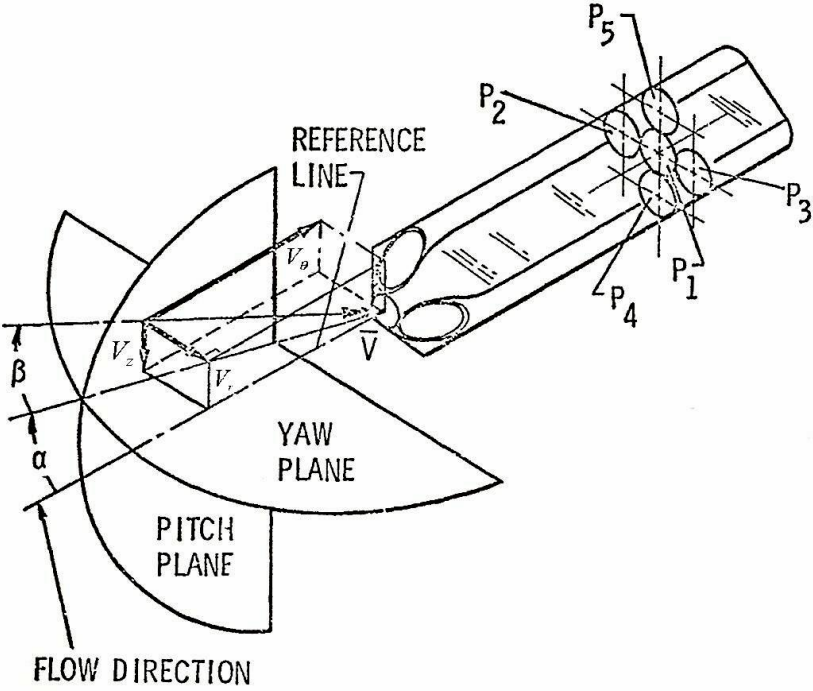


FIGURE B.3



## B VECTOR RESOLUTION FOR FIVE-HOLE PROBE CALIBRATION MODES

Cylindrical Polar Coordinates	Cartesian Coordinates
$V_z = V_1'' = V \cos(\beta) \sin(\alpha)$	$w = V \cos(\beta) \sin(\alpha)$
$V_r = V_2'' = V \sin(\beta)$	$v = V \sin(\beta)$
$V_\theta = V_3'' = V \cos(\beta) \cos(\alpha)$	$u = V \cos(\beta) \cos(\alpha)$

TABLE B.1 yaw-pitch mode

### B.2 For "pitch-yaw mode" for probe calibration

The other mode is only the change of rotation. A pitching motion is first to be rotated about  $X_2$  axis with pitch angle of magnitude  $\alpha$ . Once again, the reference velocity,  $V$  is still kept constant as in the "yaw-pitch mode" where  $V_1 = V_2 = 0$  and  $V_3 = V$ . The illustration of the geometry is displayed in

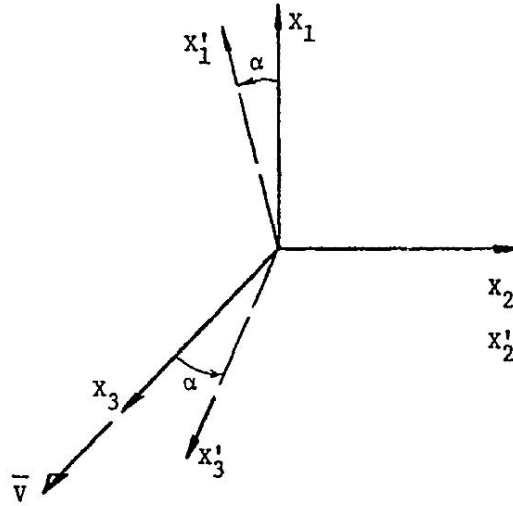


FIGURE B.4

$$\begin{aligned}
 \mathbf{a}_{11} &= \cos(\mathbf{X}'_1, \mathbf{X}_1) = \cos(\alpha) \\
 \mathbf{a}_{12} &= \cos(\mathbf{X}'_1, \mathbf{X}_2) = \cos(90^\circ) = 0 \\
 \mathbf{a}_{13} &= \cos(\mathbf{X}'_1, \mathbf{X}_3) = \cos(90^\circ - \alpha) = \sin(\alpha) \\
 \mathbf{a}_{21} &= \cos(\mathbf{X}'_2, \mathbf{X}_1) = \cos(90^\circ) = 0 \\
 \mathbf{a}_{22} &= \cos(\mathbf{X}'_2, \mathbf{X}_2) = \cos(0^\circ) = 1.0 \\
 \mathbf{a}_{23} &= \cos(\mathbf{X}'_2, \mathbf{X}_3) = \cos(90^\circ) = 0 \\
 \mathbf{a}_{31} &= \cos(\mathbf{X}'_3, \mathbf{X}_1) = \cos(90^\circ) = 0 \\
 \mathbf{a}_{32} &= \cos(\mathbf{X}'_3, \mathbf{X}_2) = \cos(90^\circ - \beta) = \sin(\alpha) \\
 \mathbf{a}_{33} &= \cos(\mathbf{X}'_3, \mathbf{X}_3) = \cos(\alpha)
 \end{aligned} \tag{B.11}$$

VECTOR RESOLUTION FOR FIVE-HOLE PROBE CALIBRATION MODES B

Due to  $V_1 = V_2 = 0$

$$\mathbf{V}'_1 = \mathbf{a}_{11}\mathbf{V}_1 + \mathbf{a}_{12}\mathbf{V}_2 + \mathbf{a}_{13}\mathbf{V}_3 = V \sin(\alpha) \quad (\text{B.12})$$

$$\mathbf{V}'_2 = \mathbf{a}_{21}\mathbf{V}_1 + \mathbf{a}_{22}\mathbf{V}_2 + \mathbf{a}_{23}\mathbf{V}_3 = 0 \quad (\text{B.13})$$

$$\mathbf{V}'_3 = \mathbf{a}_{31}\mathbf{V}_1 + \mathbf{a}_{32}\mathbf{V}_2 + \mathbf{a}_{33}\mathbf{V}_3 = V \cos(\alpha) \quad (\text{B.14})$$

The next rotation is yaw motion with rotation about  $X_1$  axis with yaw angle of magnitude  $\beta$

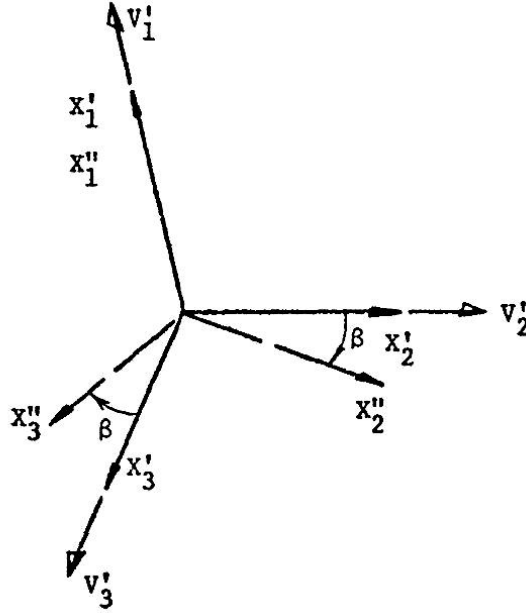


FIGURE B.5

$$\begin{aligned}
 \mathbf{a}_{11} &= \cos(\mathbf{X}_1'', \mathbf{X}_1') = \cos(0^\circ) = 1.0 \\
 \mathbf{a}_{12} &= \cos(\mathbf{X}_1'', \mathbf{X}_2') = \cos(90^\circ) = 0 \\
 \mathbf{a}_{13} &= \cos(\mathbf{X}_1'', \mathbf{X}_3') = \cos(90^\circ) = 0 \\
 \mathbf{a}_{21} &= \cos(\mathbf{X}_2'', \mathbf{X}_1') = \cos(90^\circ) = 0 \\
 \mathbf{a}_{22} &= \cos(\mathbf{X}_2'', \mathbf{X}_2') = \cos(\beta) \\
 \mathbf{a}_{23} &= \cos(\mathbf{X}_2'', \mathbf{X}_3') = \cos(90^\circ - \beta) = \sin(\beta) \\
 \mathbf{a}_{31} &= \cos(\mathbf{X}_3'', \mathbf{X}_1') = \cos(90^\circ) = 0 \\
 \mathbf{a}_{32} &= \cos(\mathbf{X}_3'', \mathbf{X}_2') = \cos(90^\circ + \beta) = -\sin(\beta) \\
 \mathbf{a}_{33} &= \cos(\mathbf{X}_3'', \mathbf{X}_3') = \cos(\beta)
 \end{aligned} \quad (\text{B.15})$$

## B VECTOR RESOLUTION FOR FIVE-HOLE PROBE CALIBRATION MODES

Therefore, the velocity components relative to the final rotation are:

$$\mathbf{V}_1'' = \mathbf{a}_{11}\mathbf{V}_1' + \mathbf{a}_{12}\mathbf{V}_2' + \mathbf{a}_{13}\mathbf{V}_3' = V \sin(\alpha) + 0 + 0 = V \sin(\alpha) \quad (\text{B.16})$$

$$\mathbf{V}_2'' = \mathbf{a}_{21}\mathbf{V}_1' + \mathbf{a}_{22}\mathbf{V}_2' + \mathbf{a}_{23}\mathbf{V}_3' = V \cos(\alpha) \sin(\beta) + 0 + 0 = V \cos(\alpha) \sin(\beta) \quad (\text{B.17})$$

$$\mathbf{V}_3'' = \mathbf{a}_{31}\mathbf{V}_1' + \mathbf{a}_{32}\mathbf{V}_2' + \mathbf{a}_{33}\mathbf{V}_3' = V \cos(\alpha) \cos(\beta) = V \cos(\alpha) \cos(\beta) \quad (\text{B.18})$$

This, it has been illustrated that the velocity components in three directions reference to Figure B.3

Cylindrical Polar Coordinates	Cartesian Coordinates
$V_z = V_1'' = V \sin(\alpha)$	$w = V \sin(\alpha)$
$V_r = V_2'' = V \cos(\alpha) \sin(\beta)$	$v = V \cos(\alpha) \sin(\beta)$
$V_\theta = V_3'' = V \cos(\alpha) \cos(\beta)$	$u = V \cos(\alpha) \cos(\beta)$

TABLE B.2 Pitch-yaw mode



# Appendix C

## Pressure Coefficient plots in 3-dimensions

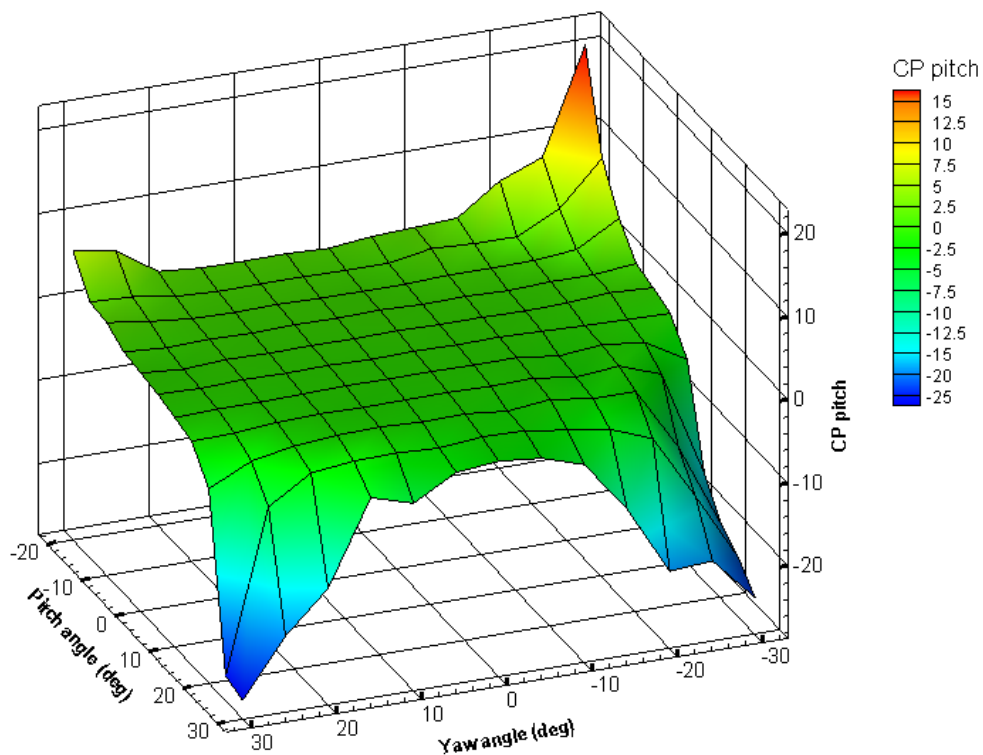
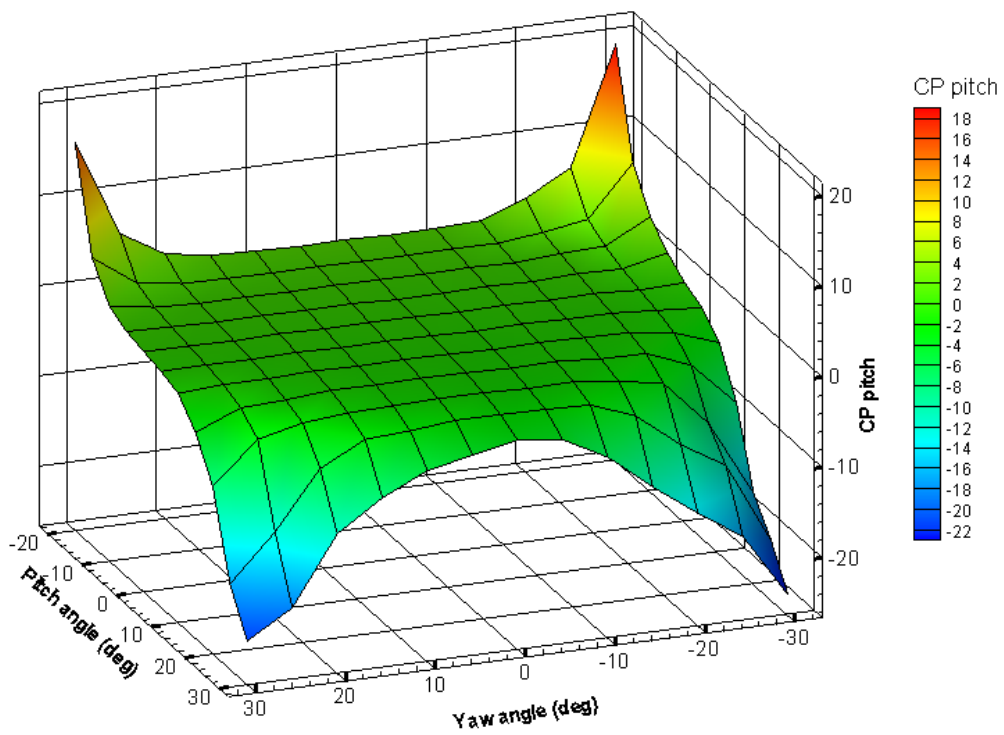


FIGURE C.1 Typical calibration plot for pressure coefficient in pitch motion at  $Re = 340$

FIGURE C.2 Typical calibration plot for pressure coefficient in pitch motion at  $Re = 565$

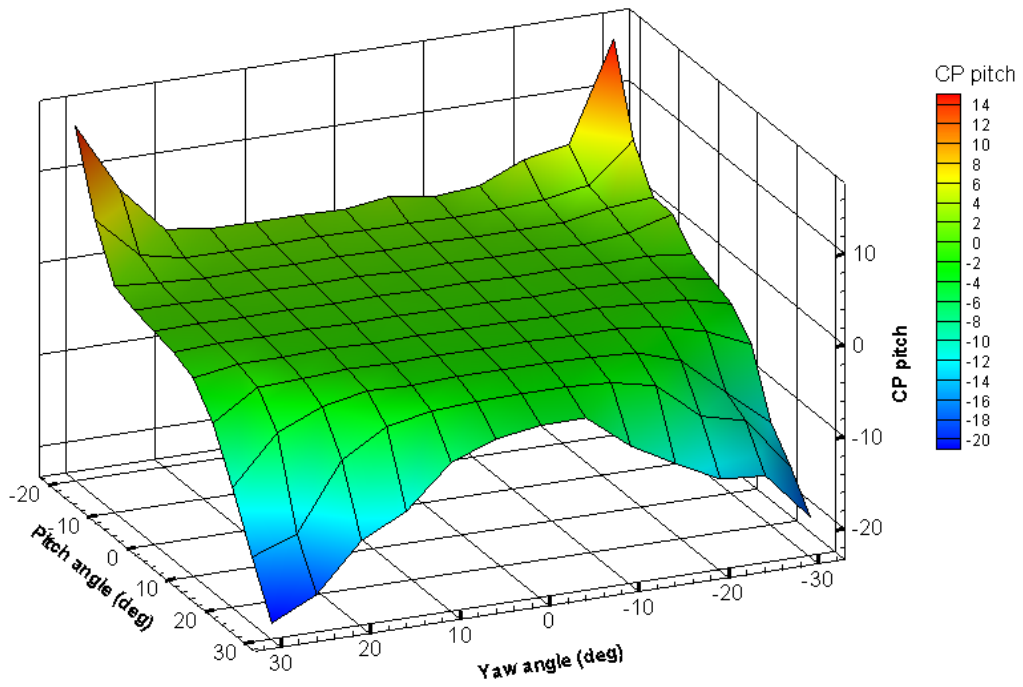
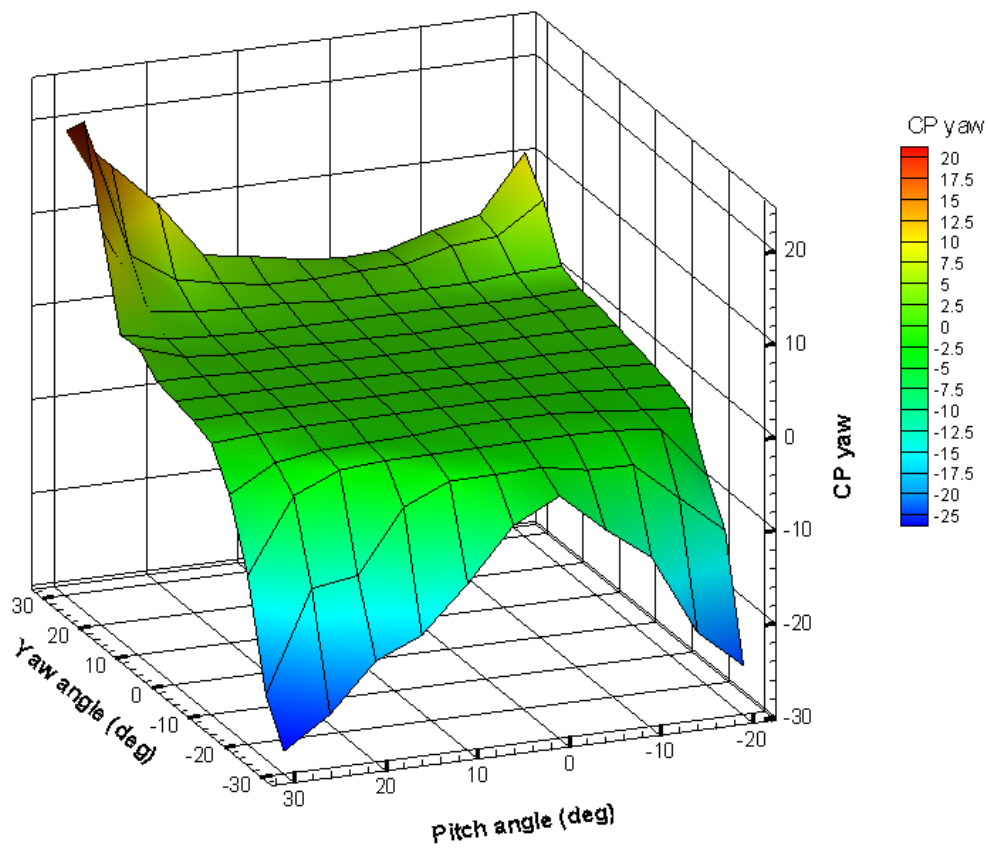


FIGURE C.3 Typical calibration plot for pressure coefficient in pitch motion at  $Re = 790$

FIGURE C.4 Typical calibration plot for pressure coefficient in yaw motion at  $Re = 340$



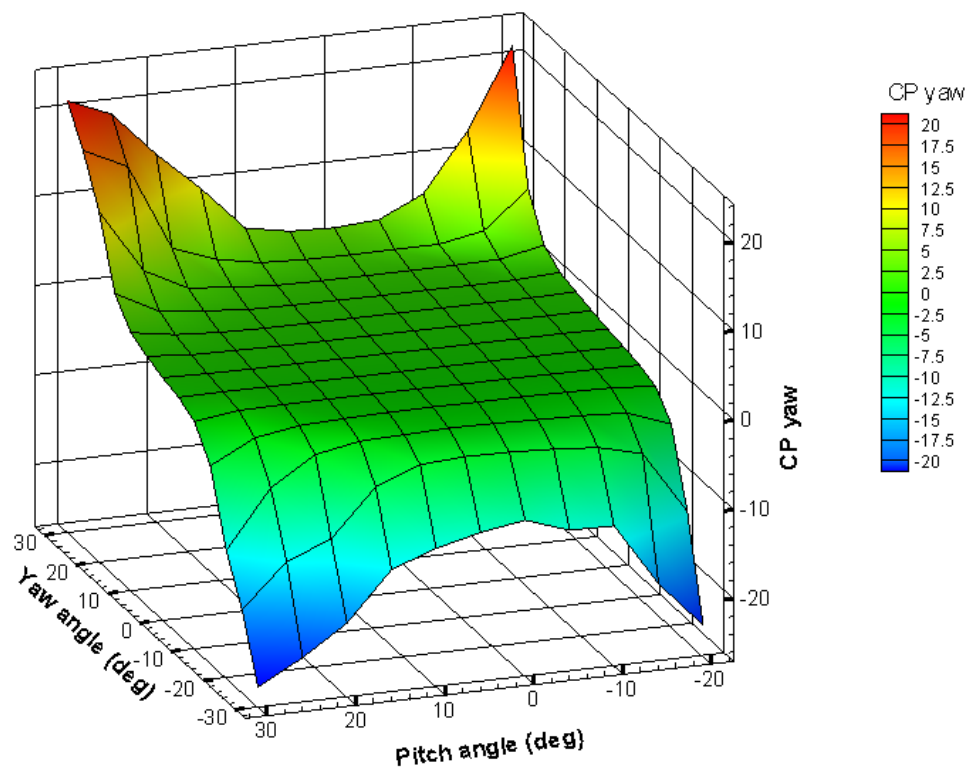


FIGURE C.5 Typical calibration plot for pressure coefficient in yaw motion at  $Re = 565$

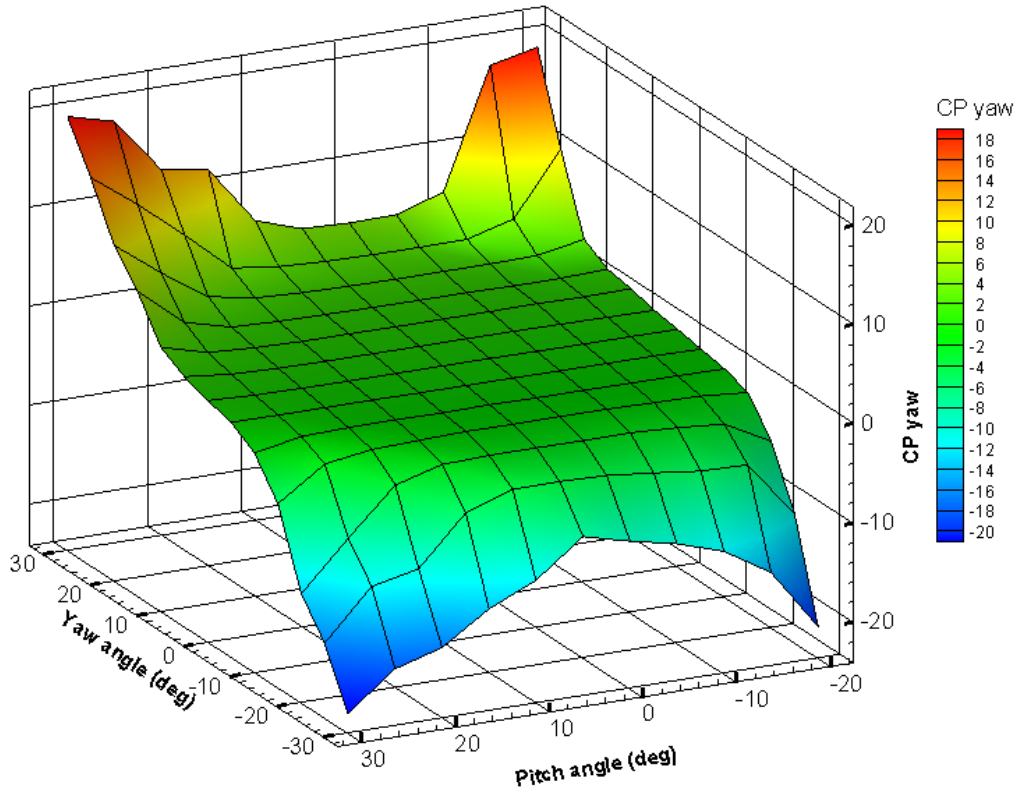


FIGURE C.6 Typical calibration plot for pressure coefficient in yaw motion at  $Re = 790$

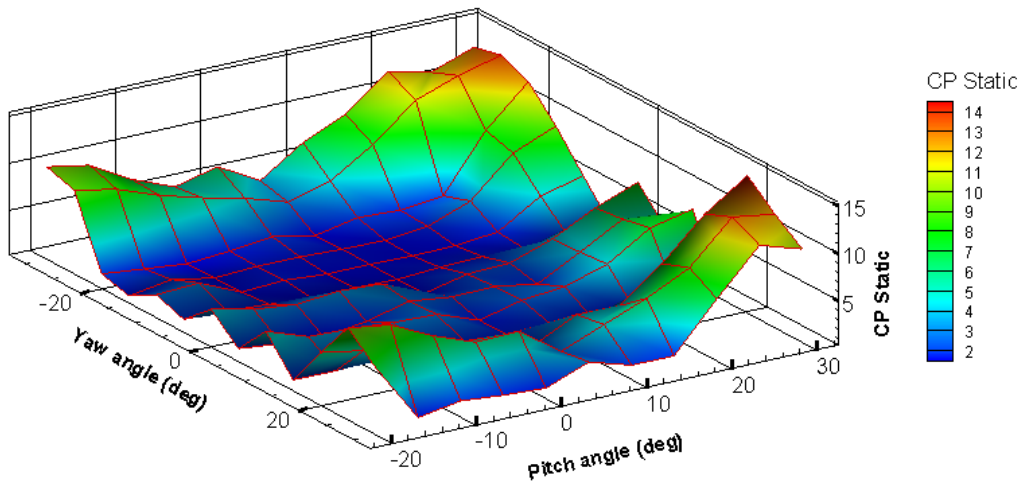


FIGURE C.7 Typical calibration plot for static pressure coefficient at  $Re = 340$

C

PRESSURE COEFFICIENT PLOTS IN 3-DIMENSIONS

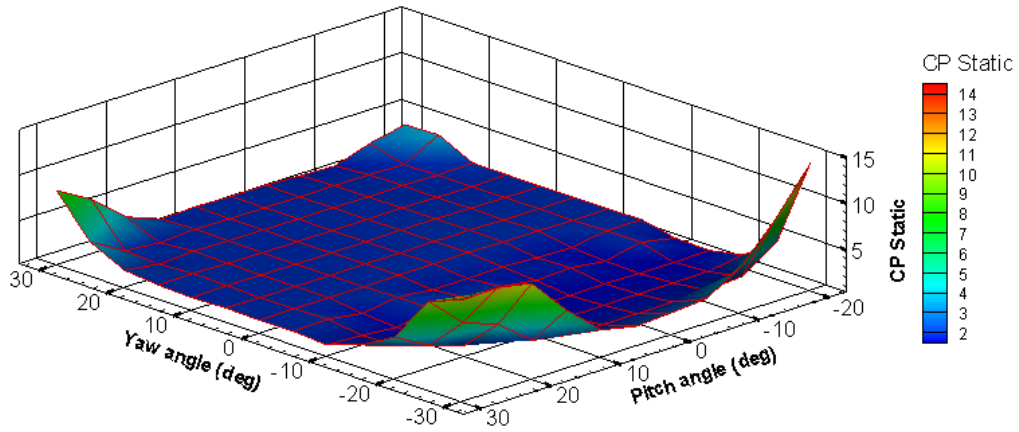


FIGURE C.8 Typical calibration plot for static pressure coefficient at  $Re = 565$

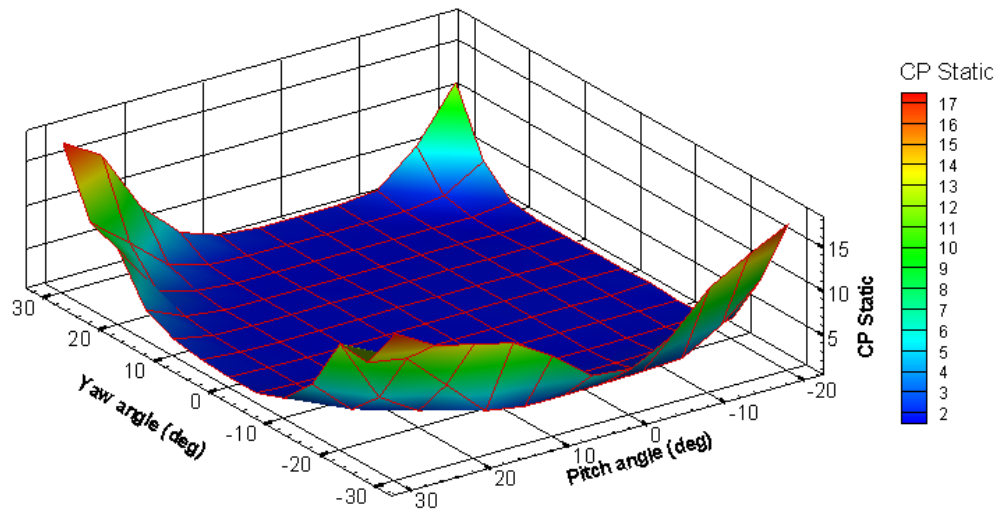


FIGURE C.9 Typical calibration plot for static pressure coefficient at  $Re = 790$

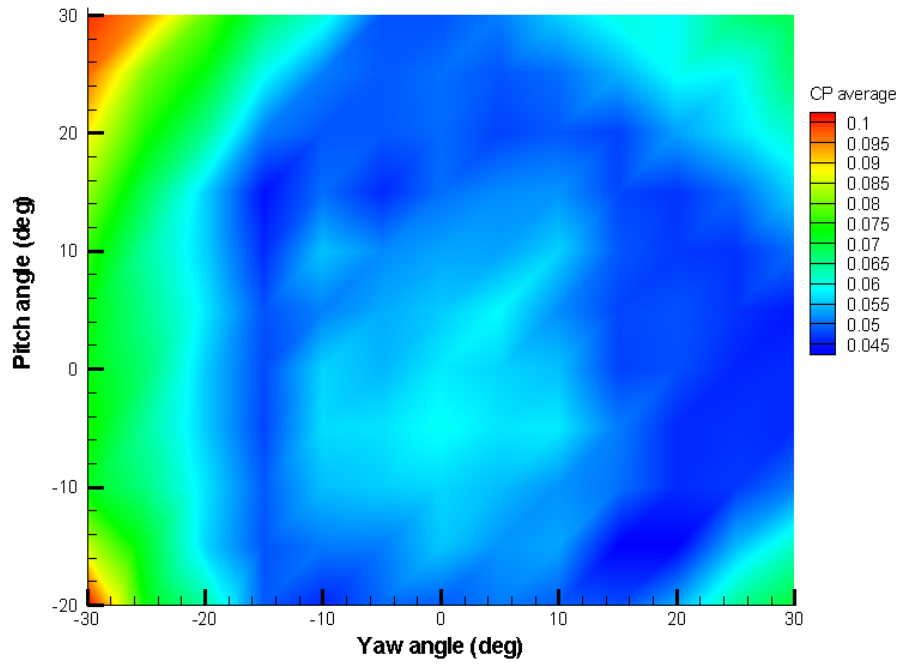


FIGURE C.10 Average pressure coefficient contour dependent upon  $\alpha$  and  $\beta$

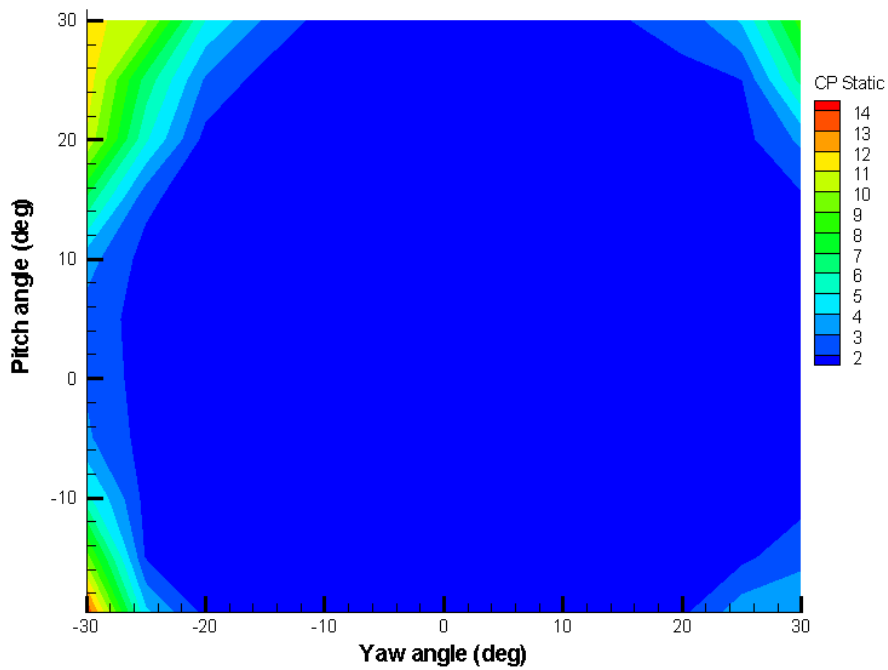


FIGURE C.11 Static pressure coefficient at  $Re = 565$

C

PRESSURE COEFFICIENT PLOTS IN 3-DIMENSIONS

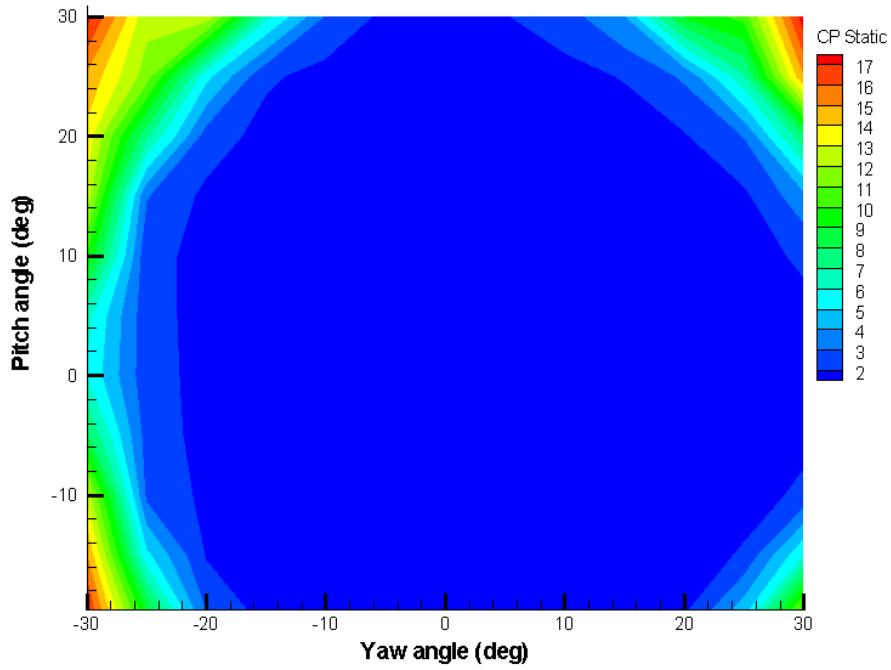


FIGURE C.12 Static pressure coefficient at  $Re = 790$

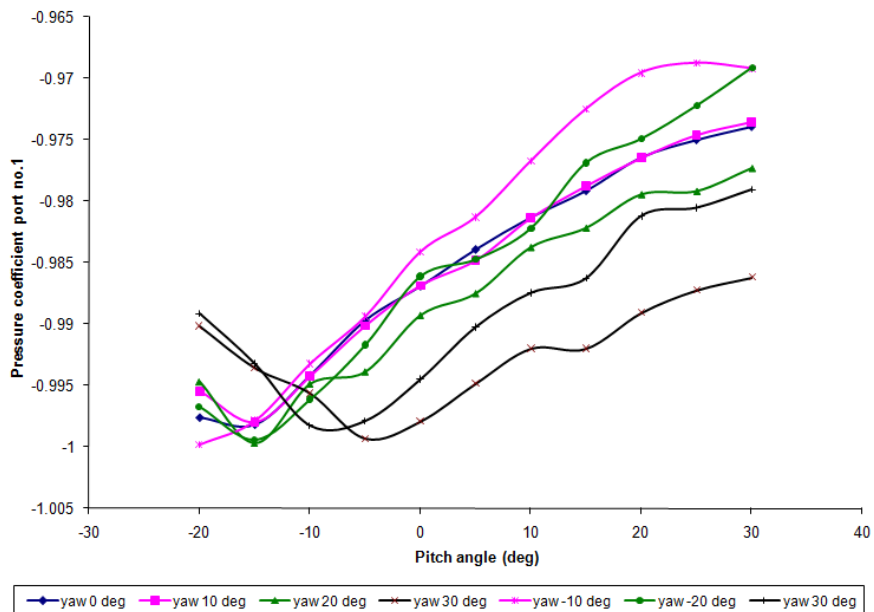


FIGURE C.13 Effect of probe sensitivity from port no.1 at  $Re = 565$

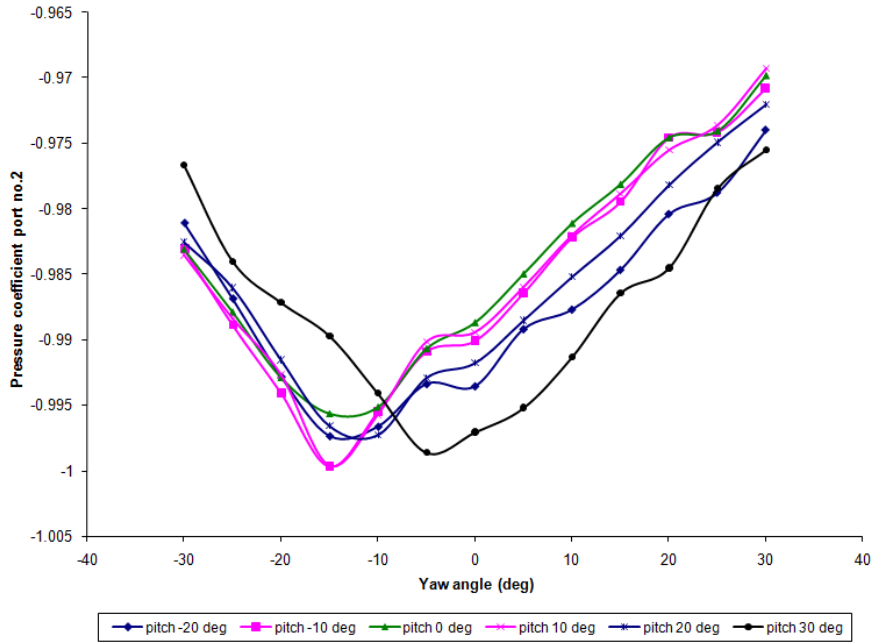


FIGURE C.14 Effect of probe sensitivity from port no.2 at  $Re = 565$

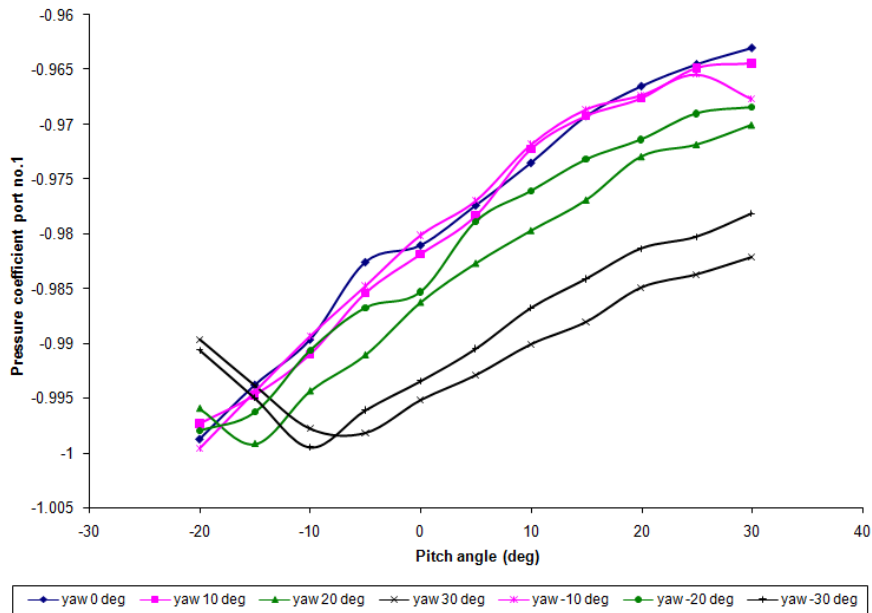


FIGURE C.15 Effect of probe sensitivity from port no.1 at  $Re = 790$

C

PRESSURE COEFFICIENT PLOTS IN 3-DIMENSIONS

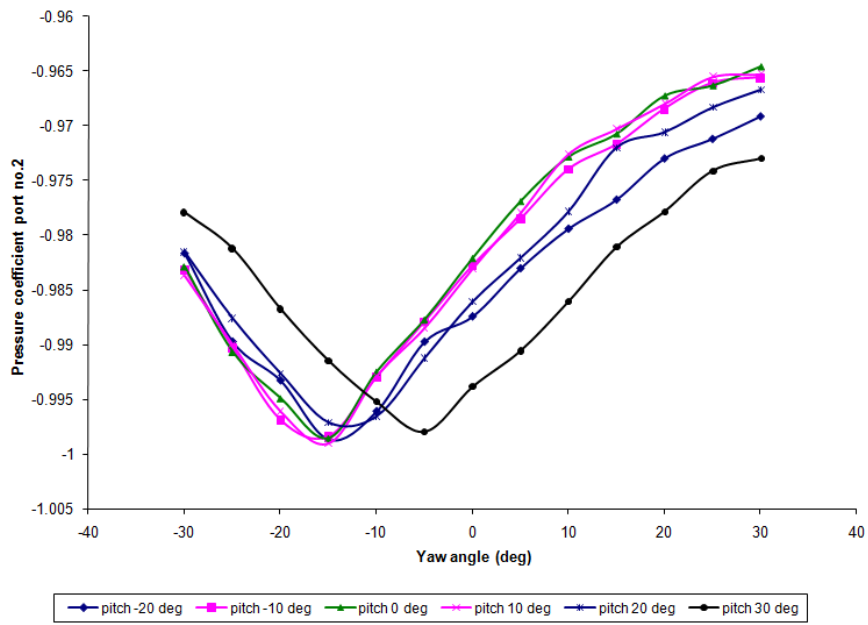


FIGURE C.16 Effect of probe sensitivity from port no.2 at  $Re = 790$





# Appendix D

## Flow fields around buildings of rectangular shape

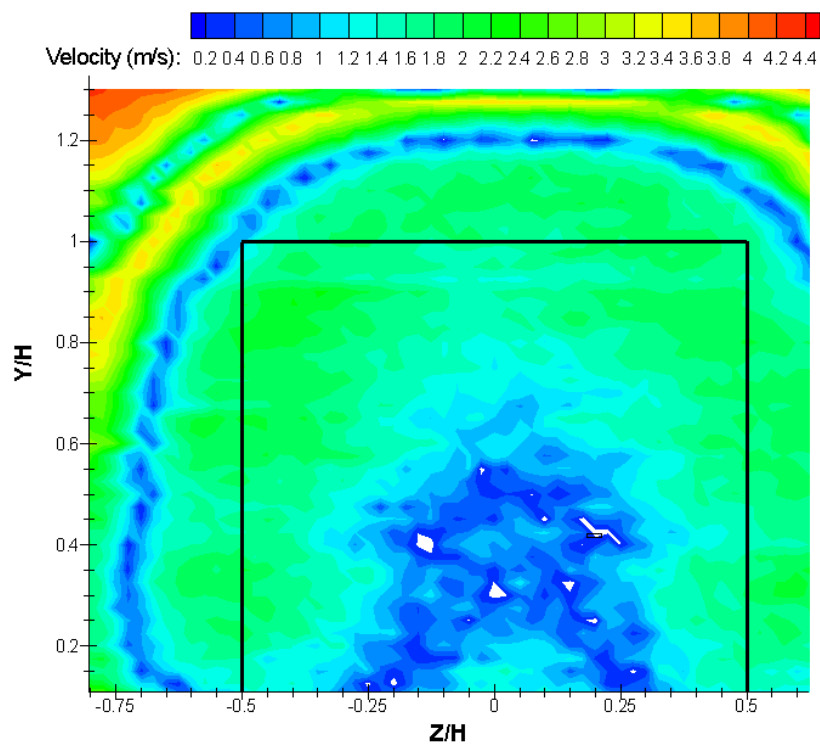


FIGURE D.1 Velocity field behind a single building at  $X/H = 0.75$

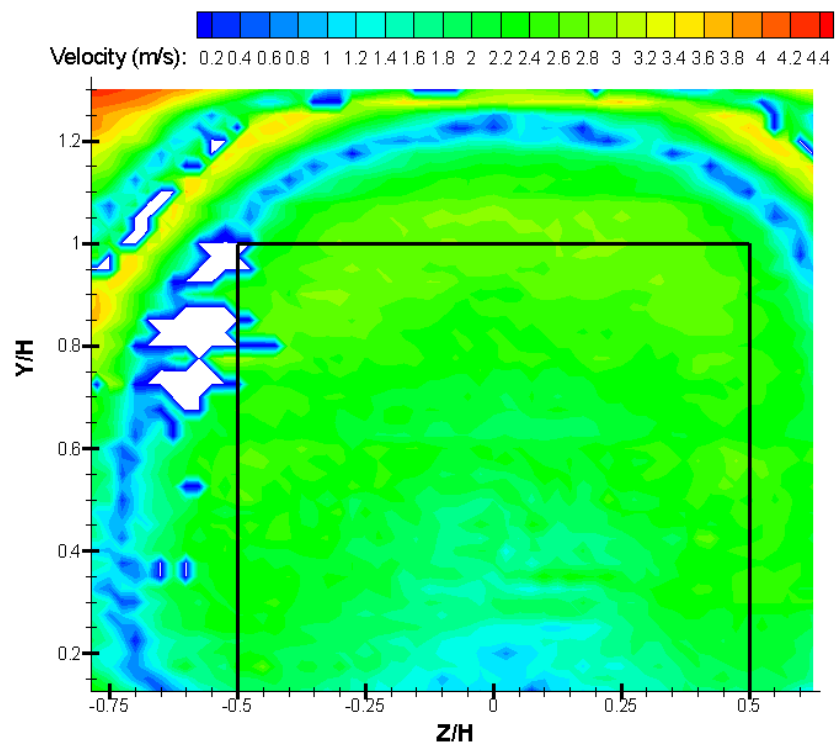


FIGURE D.2 Velocity field behind a single building at  $X/H = 1.0$

D FLOW FIELDS AROUND BUILDINGS OF RECTANGULAR SHAPE

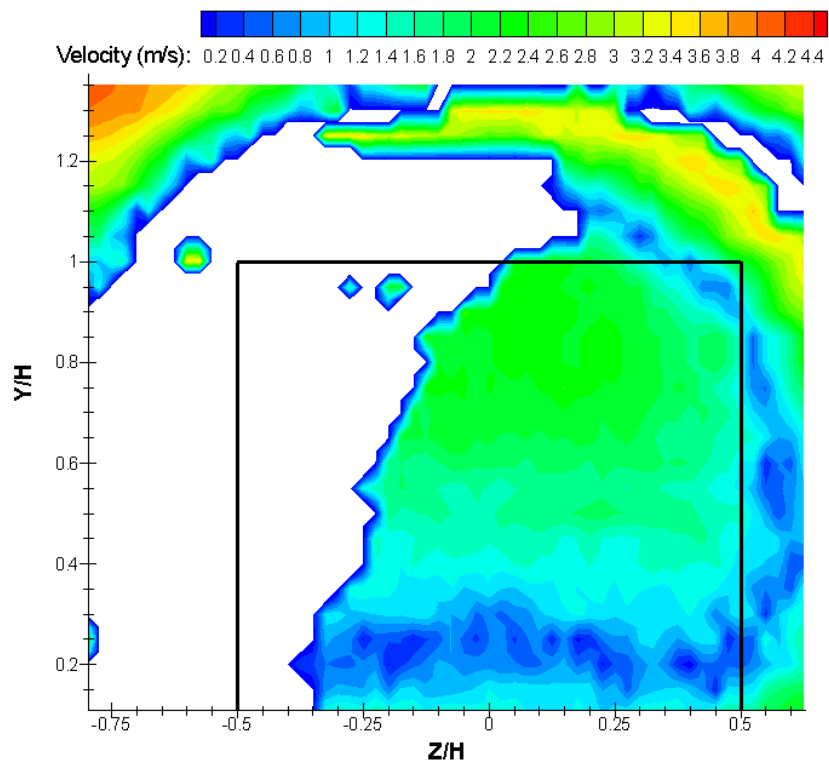


FIGURE D.3 Velocity field behind a single building at  $X/H = 1.5$

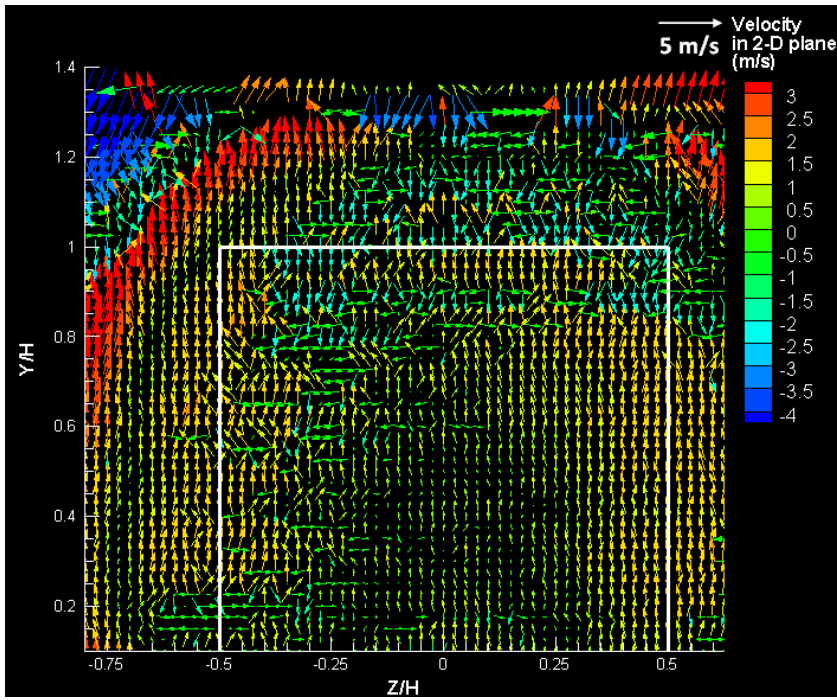


FIGURE D.4 Vector plot in Y-Z plane behind a single building at  $X/H = 0.75$

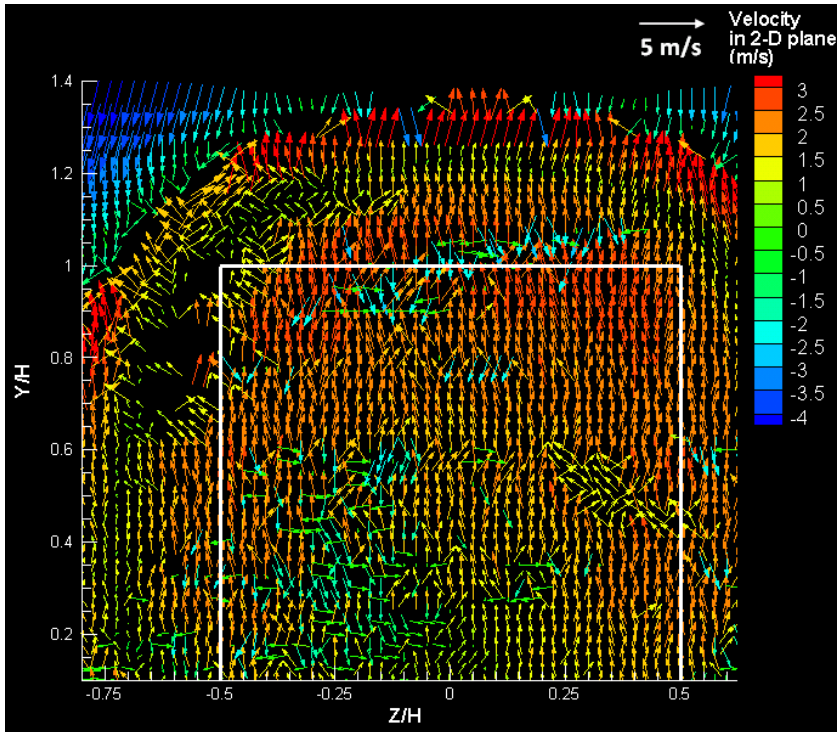


FIGURE D.5 Vector plot in Y-Z plane behind a single building at  $X/H = 1.0$

D FLOW FIELDS AROUND BUILDINGS OF RECTANGULAR SHAPE

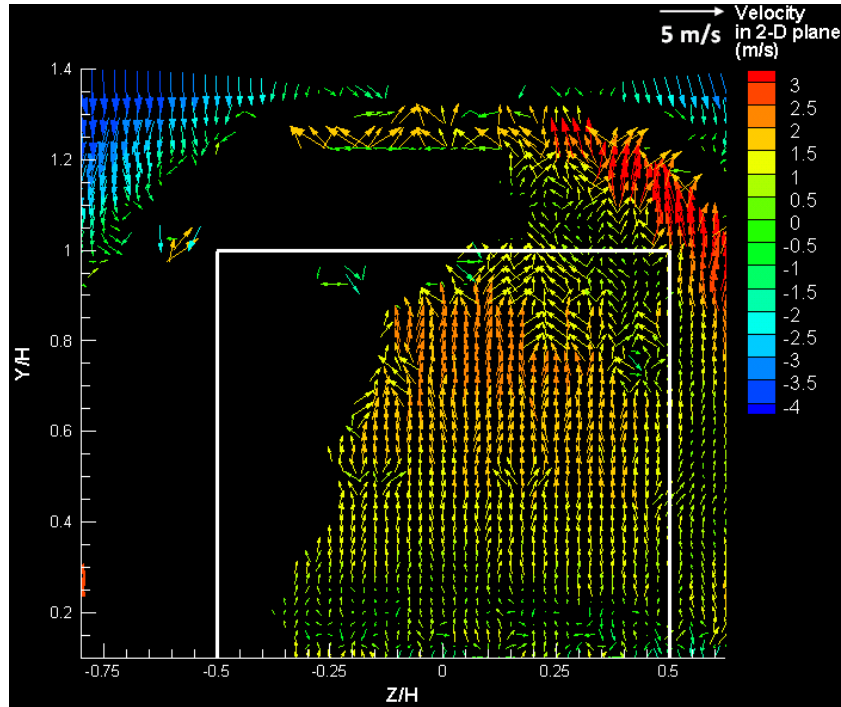


FIGURE D.6 Vector plot in Y-Z plane behind a single building at  $X/H = 1.5$

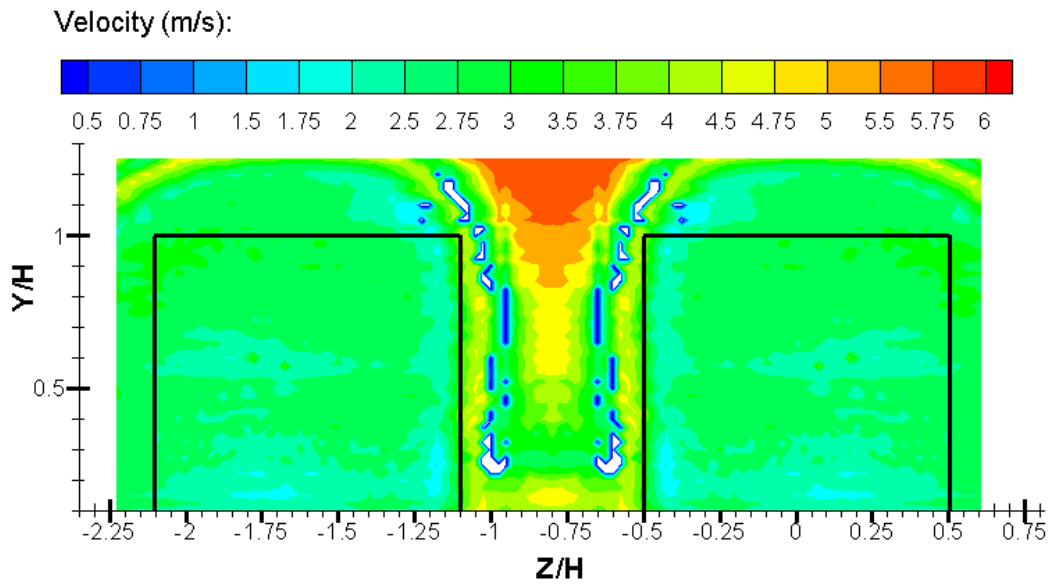


FIGURE D.7 Velocity field behind twin buildings at  $X/H = 0.75$

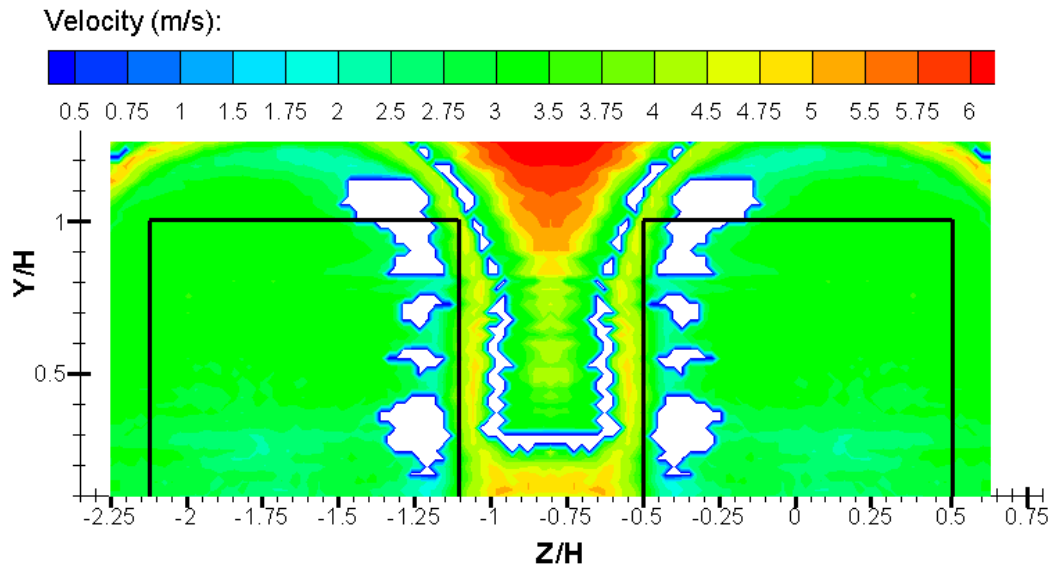


FIGURE D.8 Velocity field behind twin buildings at  $X/H = 1.0$

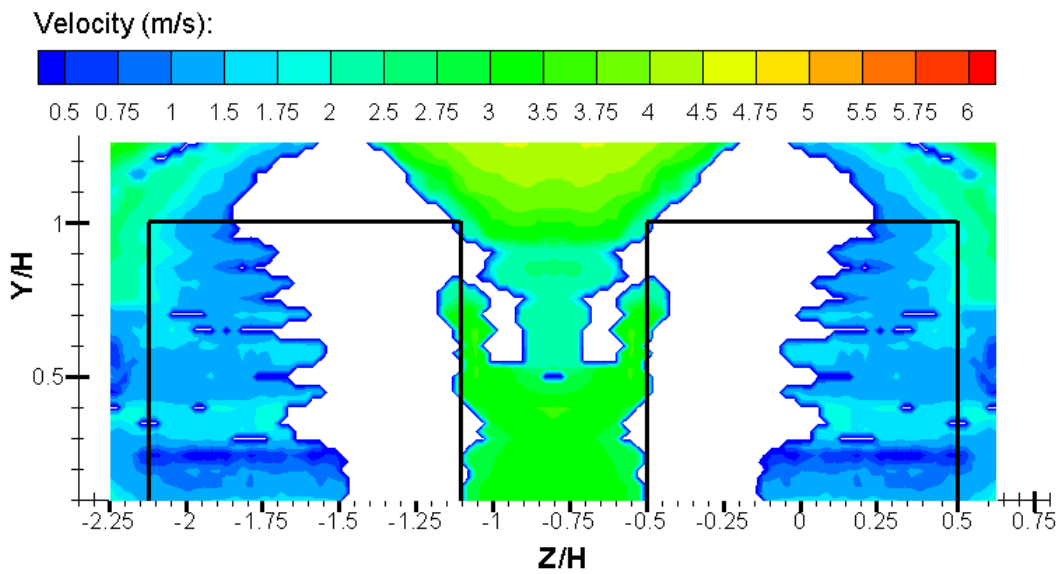
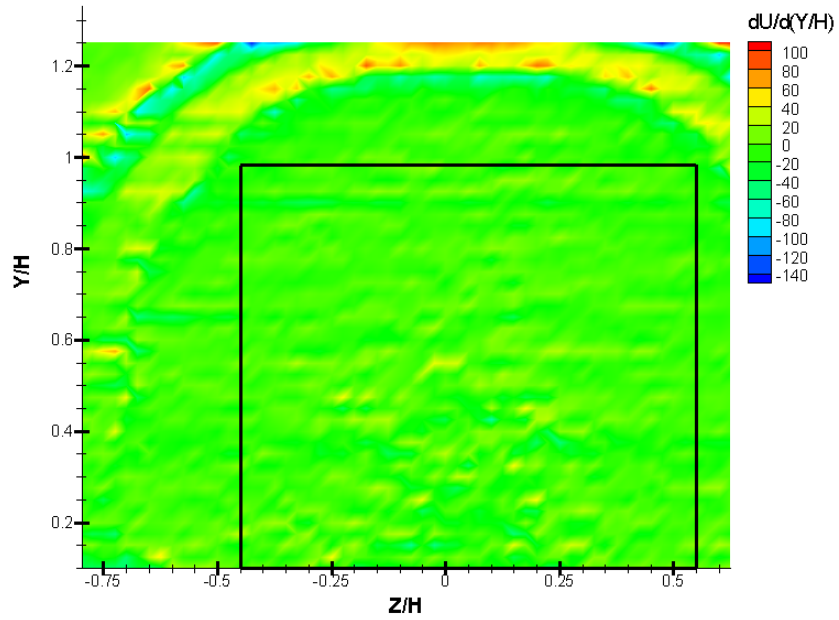
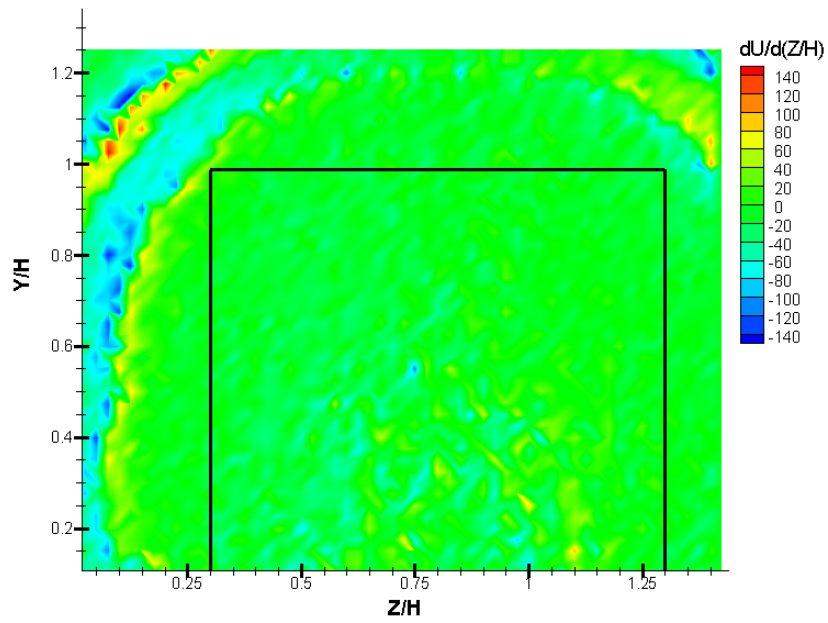


FIGURE D.9 Velocity field behind twin buildings at  $X/H = 1.5$

D FLOW FIELDS AROUND BUILDINGS OF RECTANGULAR SHAPE

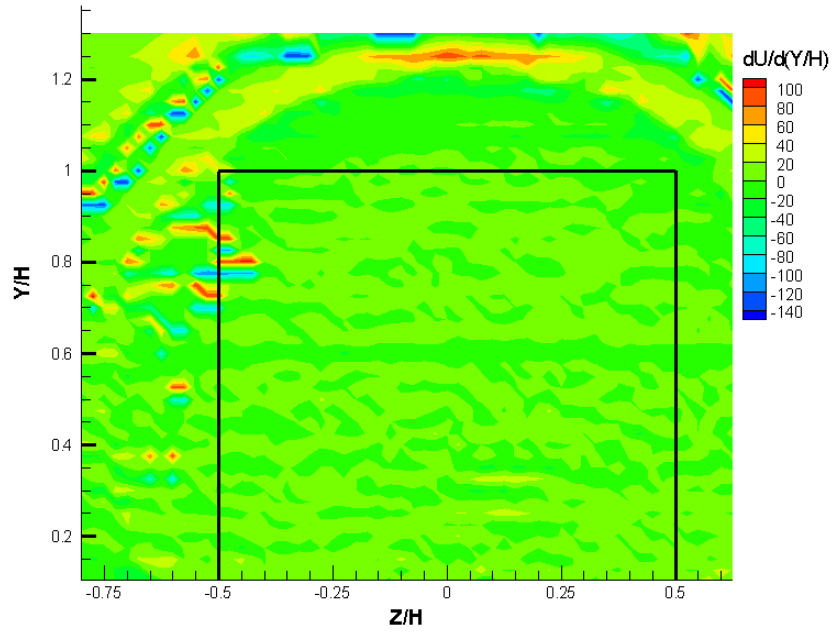


(a)

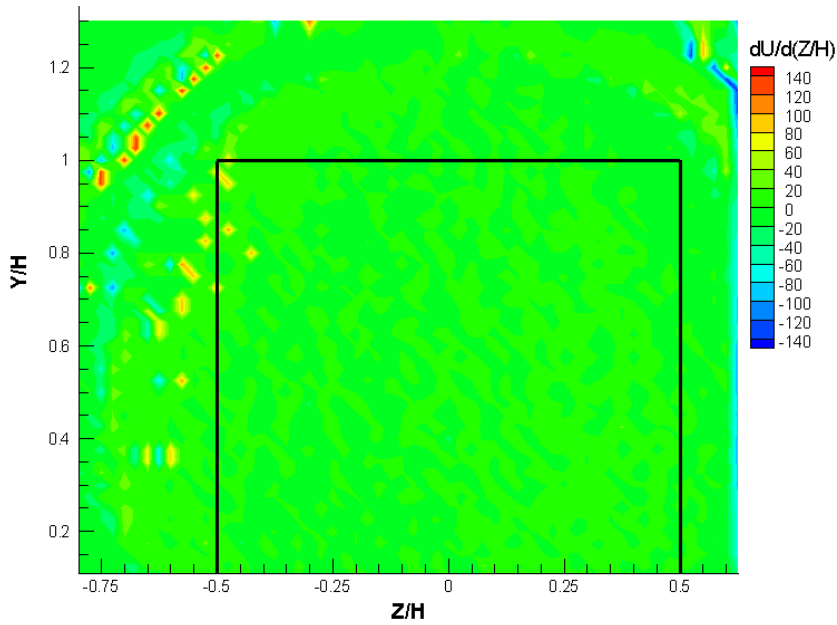


(b)

FIGURE D.10 Vertical and lateral velocity gradients at  $X/H = 0.75$  downstream behind a single building configuration



(a)  $X/H = 1.0$

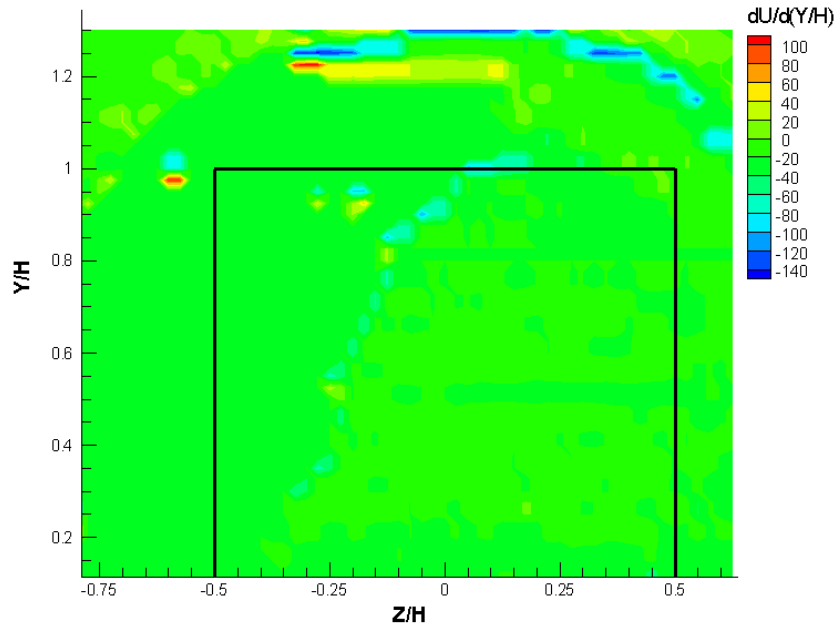


(b)  $X/H = 1.0$

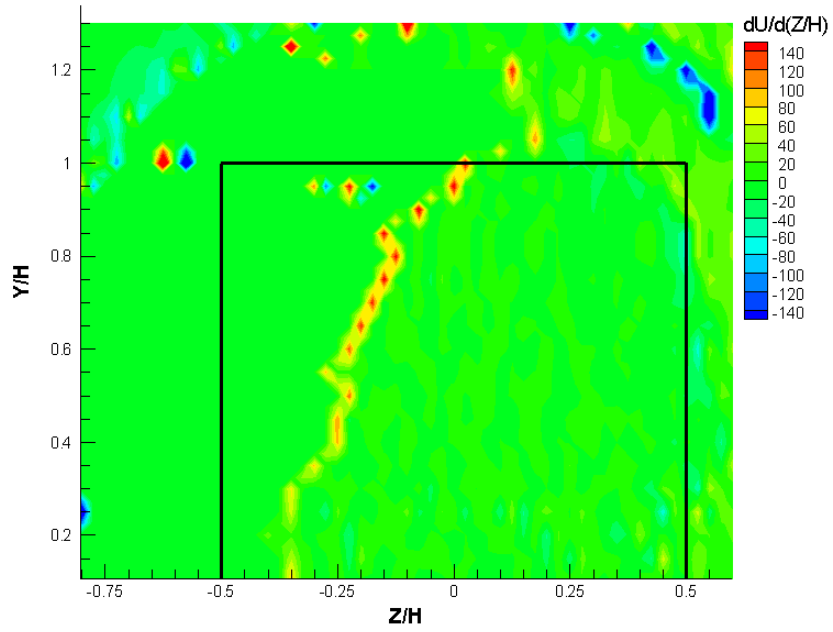
FIGURE D.11 Vertical and lateral velocity gradients at  $X/H = 1.0$  downstream behind a single building configuration



D FLOW FIELDS AROUND BUILDINGS OF RECTANGULAR SHAPE

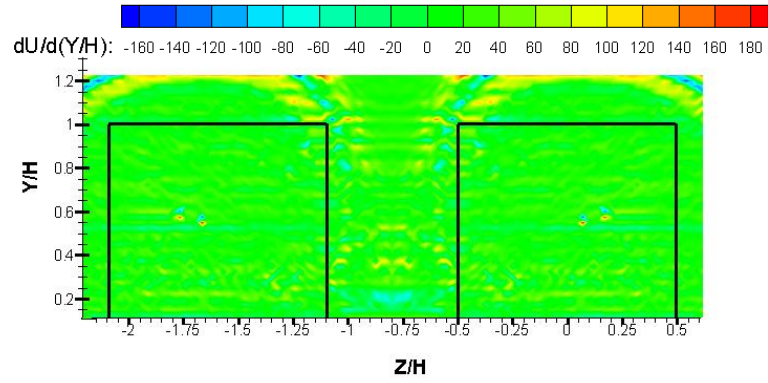


(a)

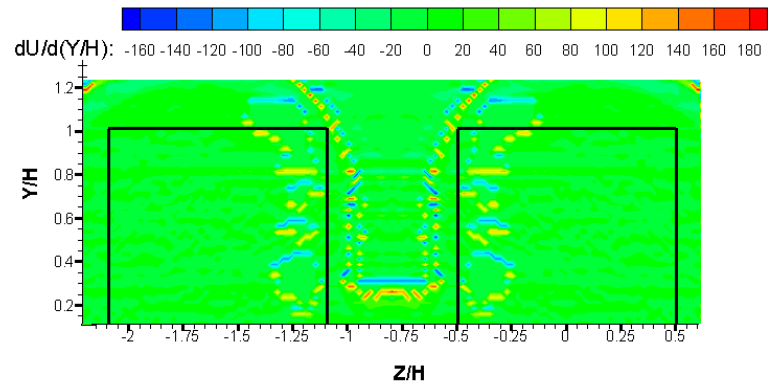


(b)

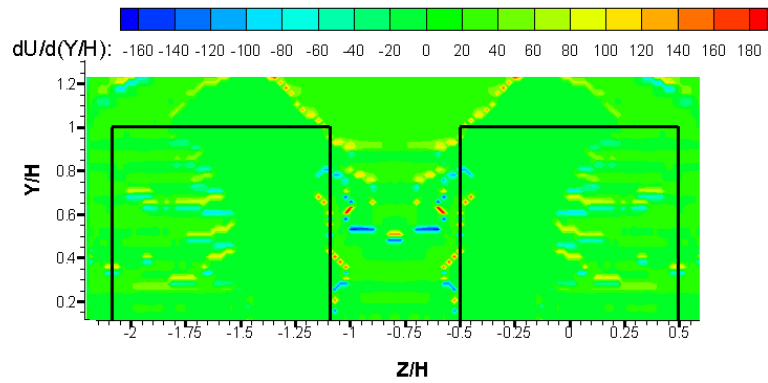
FIGURE D.12 Vertical and lateral velocity gradients at  $X/H = 1.5$  downstream behind a single building configuration



(a)  $X/H = 0.75$



(b)  $X/H = 1.0$



(c)  $X/H = 1.5$

FIGURE D.13 Vertical velocity gradient plots at three locations downstream behind twin buildings configuration

D FLOW FIELDS AROUND BUILDINGS OF RECTANGULAR SHAPE

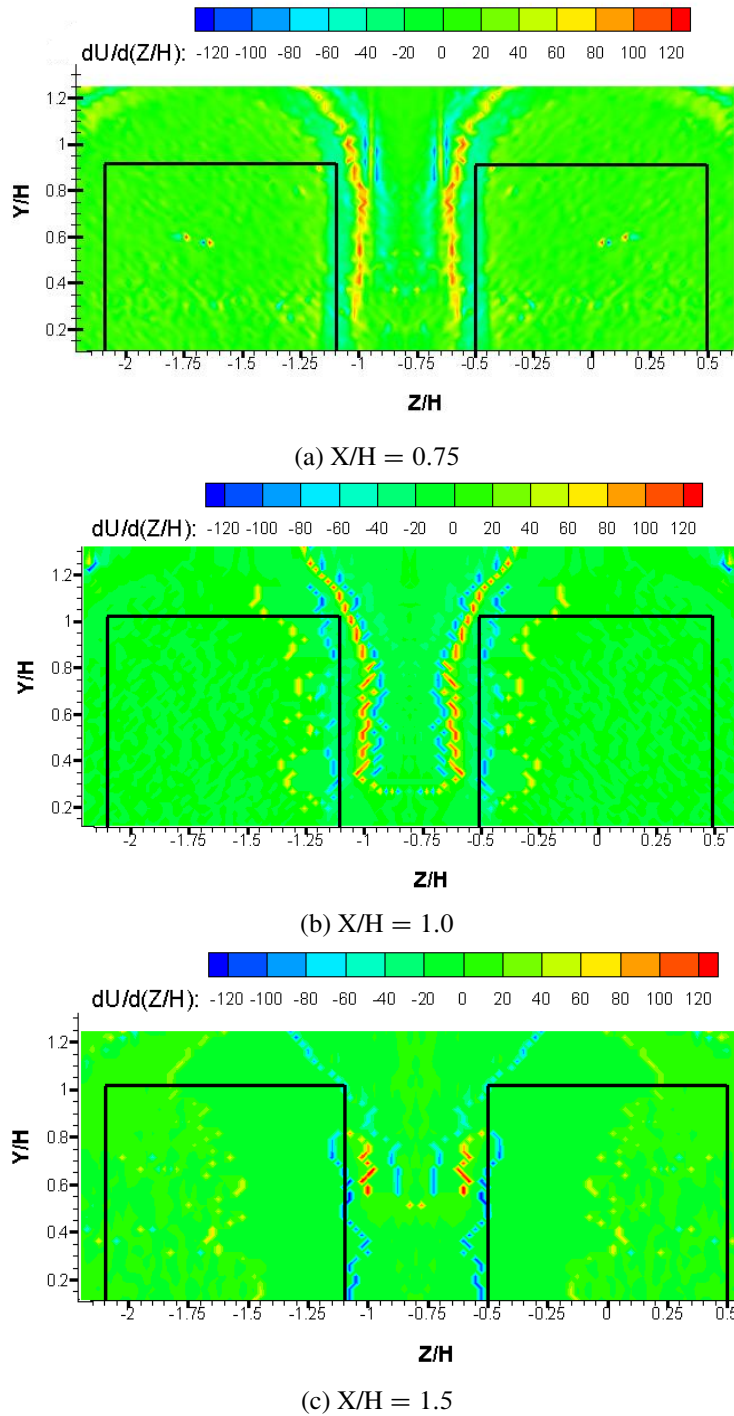


FIGURE D.14 Lateral velocity gradient plots at three locations downstream behind twin buildings configuration

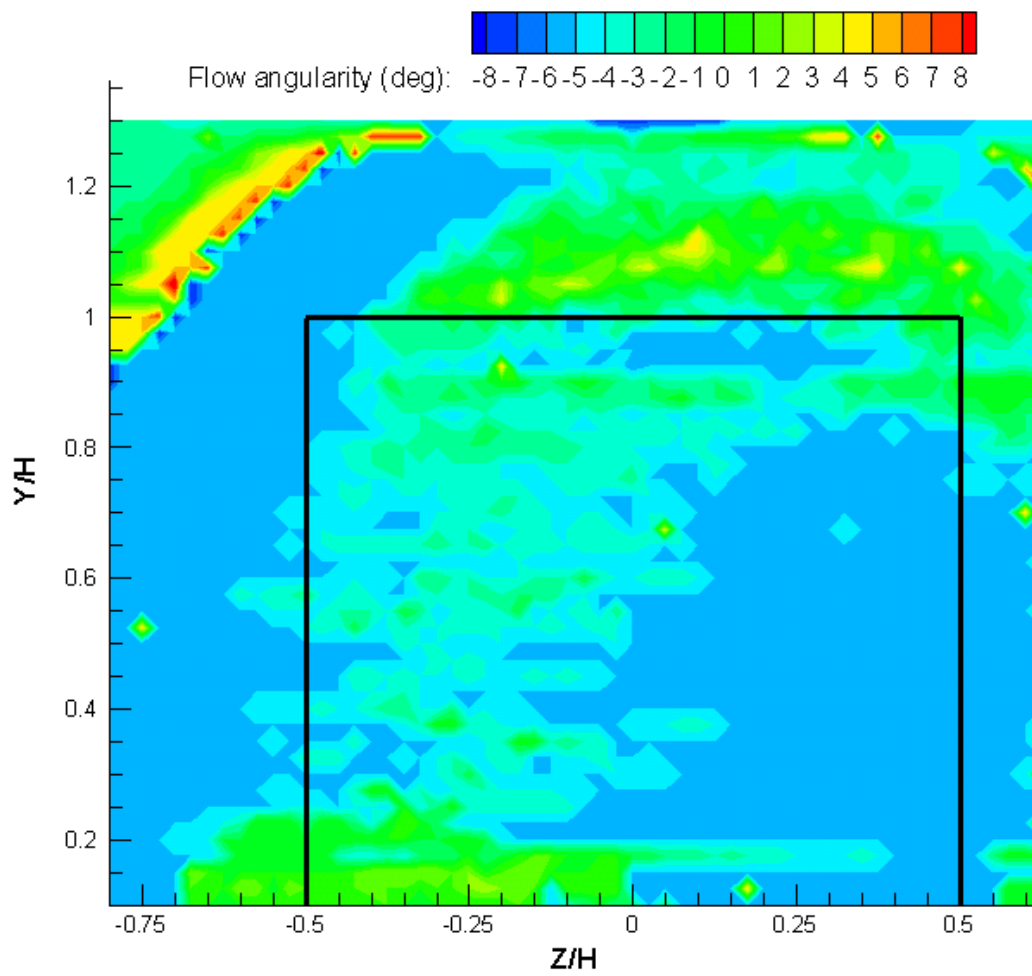


FIGURE D.15 Change in flow angularity in U-V velocity components at  $X/H = 0.75$

D FLOW FIELDS AROUND BUILDINGS OF RECTANGULAR SHAPE

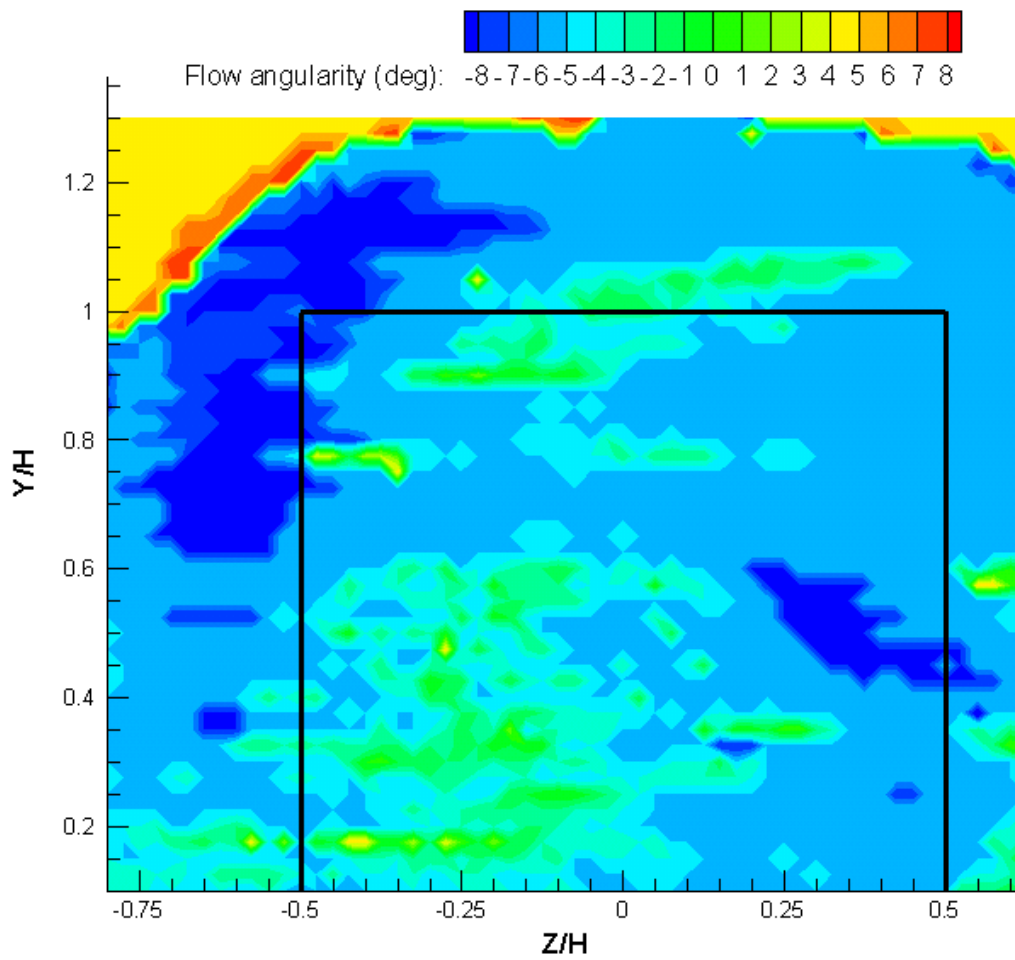


FIGURE D.16 Change in flow angularity in U-V velocity components at  $X/H = 1.0$

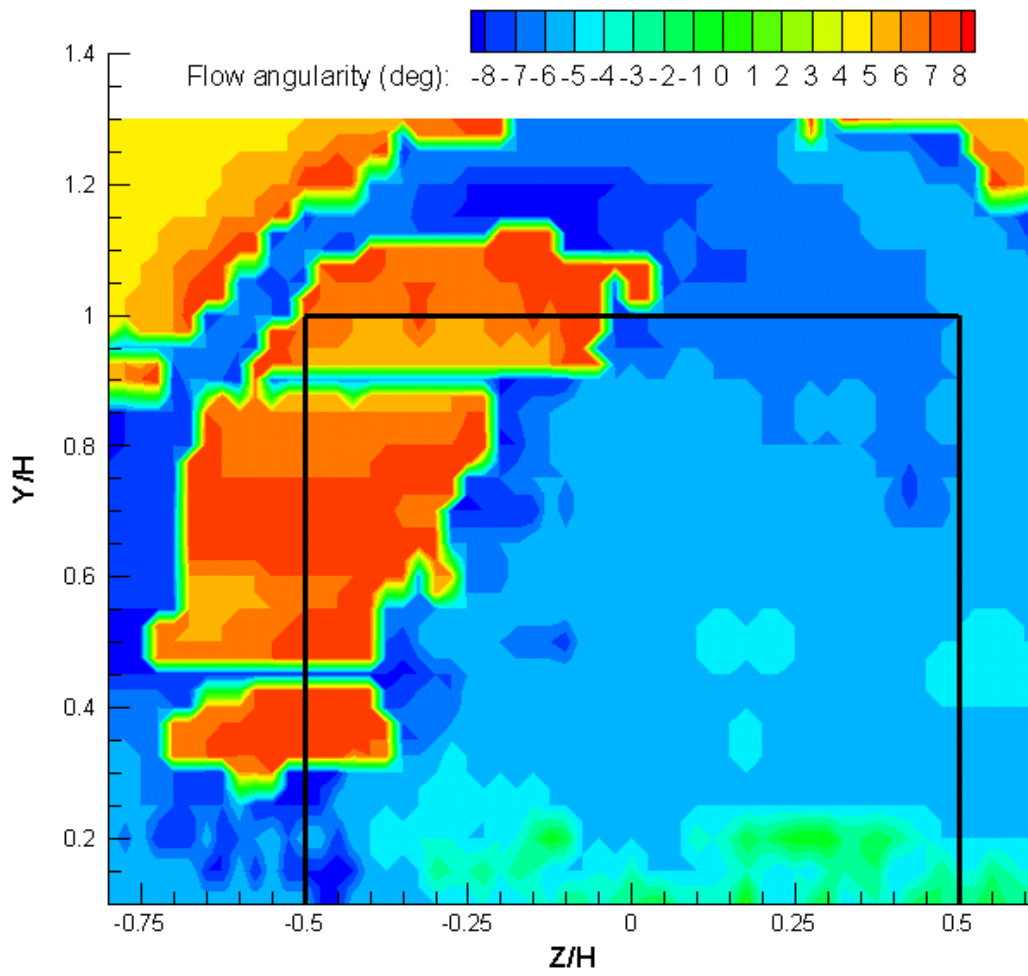


FIGURE D.17 Change in flow angularity in U-V velocity components at  $X/H = 1.5$

D FLOW FIELDS AROUND BUILDINGS OF RECTANGULAR SHAPE

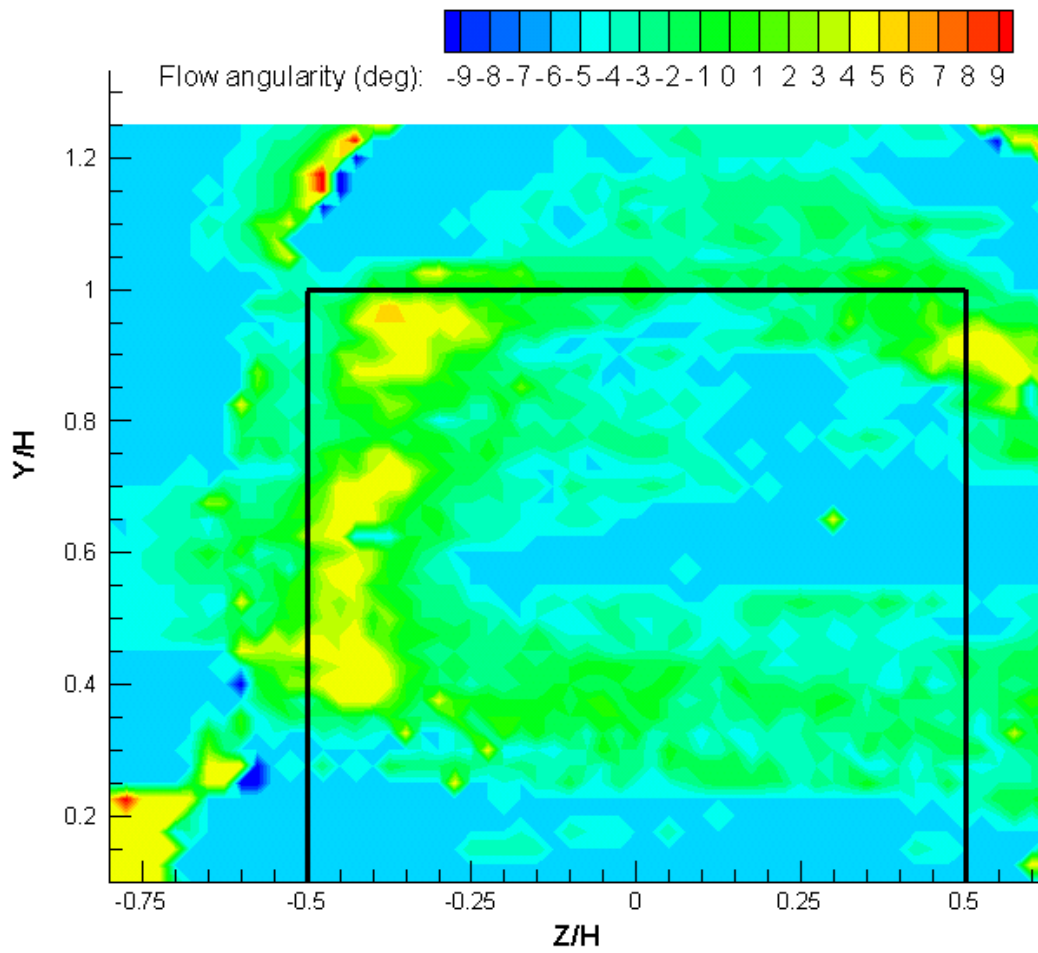


FIGURE D.18 Change in flow angularity in U-V velocity components at  $X/H = 0.75$  behind twin buildings. Only half of the plane of measurement is shown here.

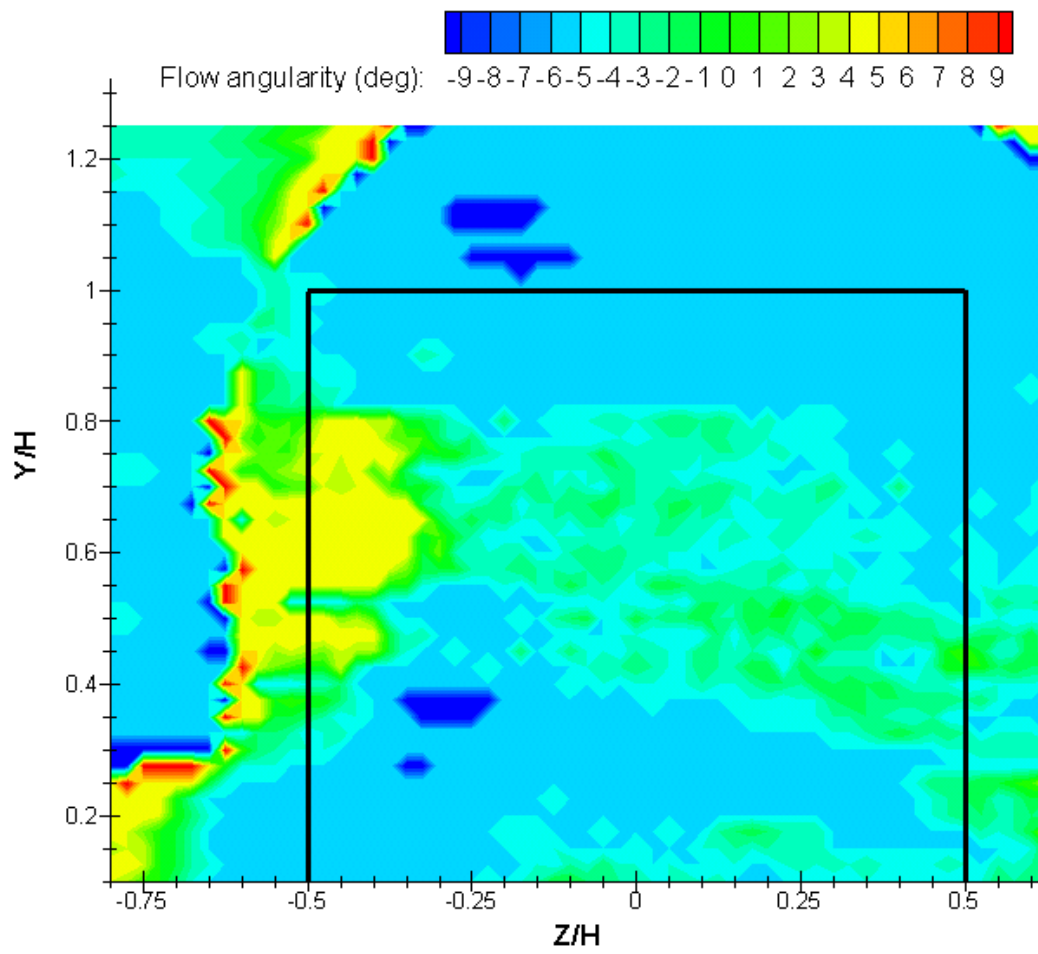


FIGURE D.19 Change in flow angularity in U-V velocity components at  $X/H = 1.0$  behind twin buildings. Only half of the plane of measurement is shown here.



D FLOW FIELDS AROUND BUILDINGS OF RECTANGULAR SHAPE

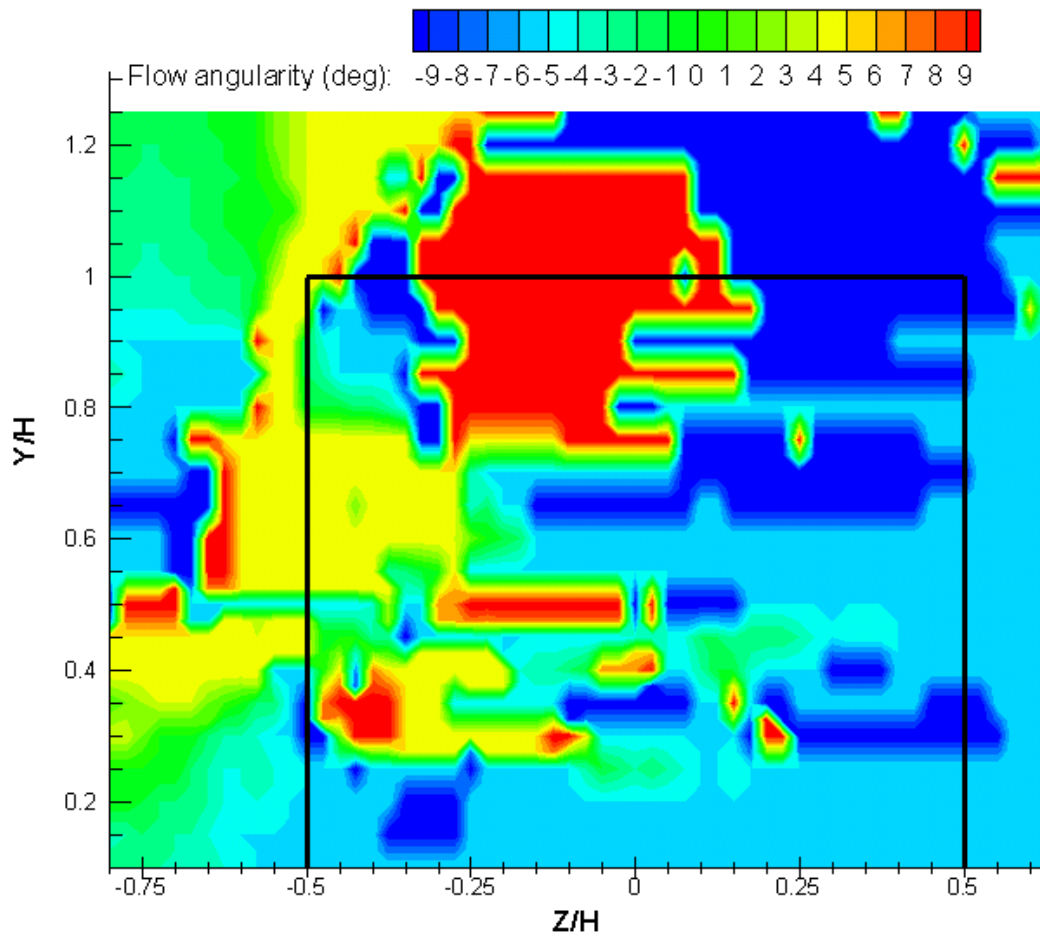


FIGURE D.20 Change in flow angularity in U-V velocity components at  $X/H = 1.5$  behind twin buildings. Only half of the plane of measurement is shown here.

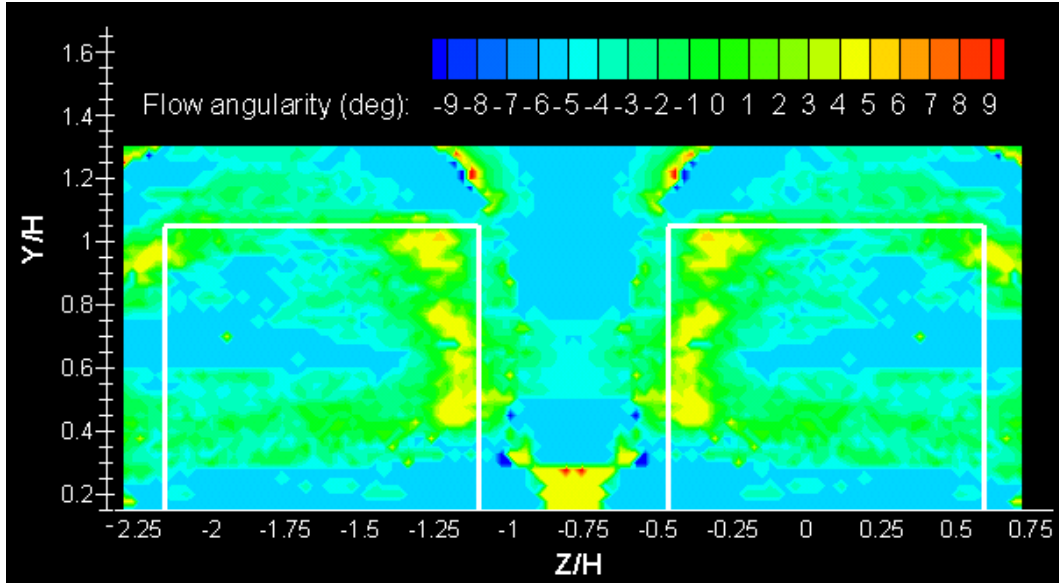


FIGURE D.21 Change in flow angularity in U-V velocity components at  $X/H = 0.75$

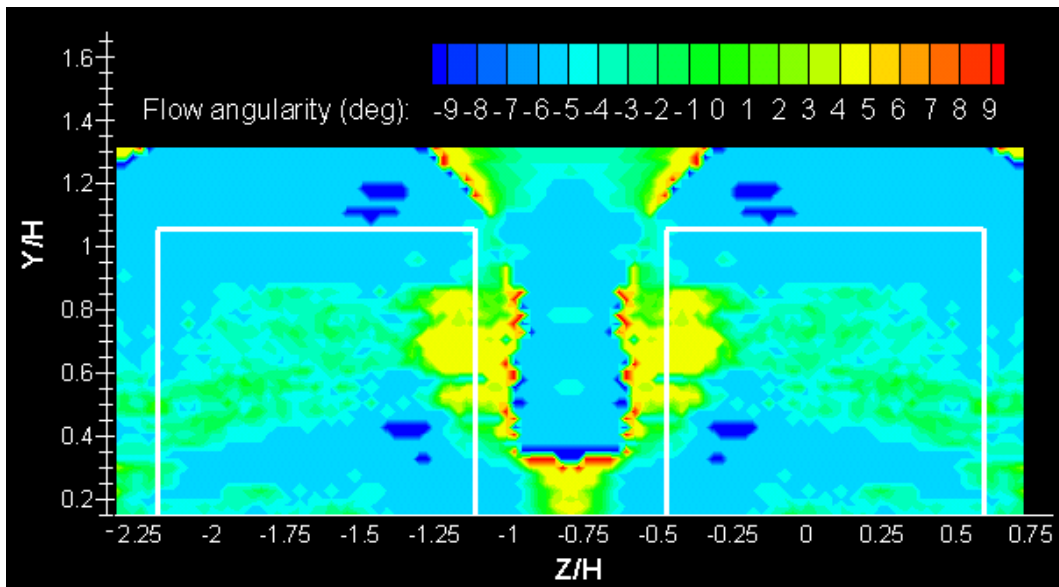


FIGURE D.22 Change in flow angularity in U-V velocity components at  $X/H = 1.0$

D FLOW FIELDS AROUND BUILDINGS OF RECTANGULAR SHAPE

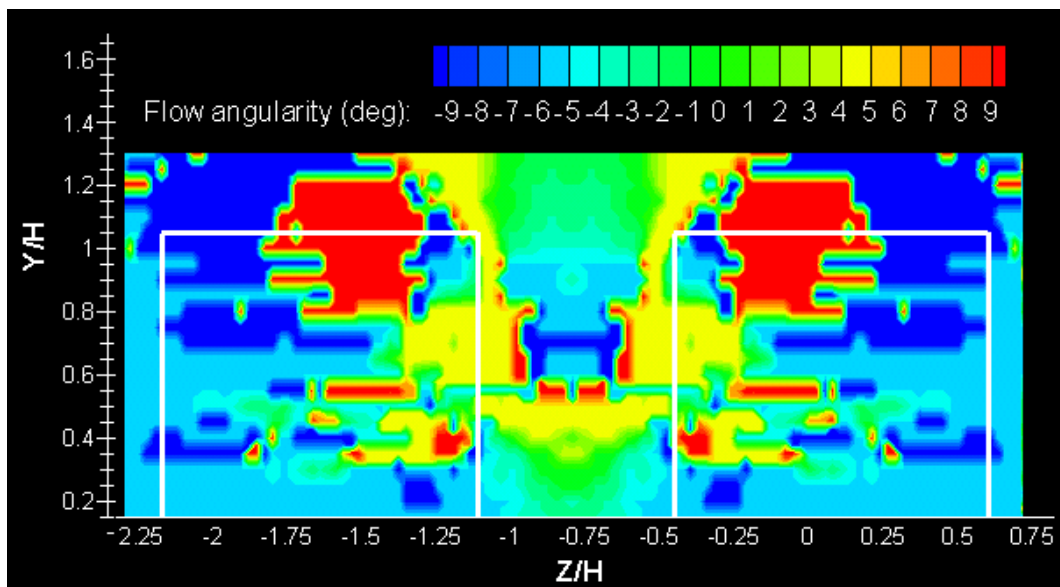


FIGURE D.23 Change in flow angularity in U-V velocity components at  $X/H = 1.5$



# Appendix E

## Wind tunnel of elliptic section

The forces such as lift and drag generated by a wing in real flying environment are different from the forces measured in a wind tunnel due to an effect of enclosure walls. Even in an open tunnel and a closed tunnel, the wall effect is a factor to determine the lift and drag under the same tunnel operation conditions. There are two interesting and important points mentioned by Rosenhead [97] on the interference of a wind tunnel as:

- A magnitude of an interference on any small airfoil testing in an open tunnel having the same magnitude but opposite sign of the same airfoil testing in a closed tunnel.
- In the elliptic tunnel, the airfoil tips are located at the foci points of the tunnel with a uniform interference velocity across a span.

As mentioned in the second point that is the airfoil tips are at the foci points of the elliptic tunnel as seen in Figure E.1. Consequently, a possible maximum wing span ( $2s$ ) giving an approximately true interference should be  $2s = \sqrt{a^2 - b^2}$  due to Eq. E.1 and E.2.

$$\text{The esentricity of ellipse} = \varepsilon = \sqrt{\frac{a^2 - b^2}{a^2}} \quad (\text{E.1})$$

$$\text{Half wing span} = \frac{\mathbf{a}}{2}\varepsilon = \frac{\mathbf{a}}{2}\sqrt{\frac{a^2 - b^2}{a^2}} = \frac{1}{2}\sqrt{a^2 - b^2} \quad (\text{E.2})$$

Furthermore, the interference due to the wall effect produces a correction of angle of attack which is also dependent on how the tunnel major axis orients either in vertical or horizontal planes. This necessary correction factor,  $\Delta\alpha$  is added to the angle of attack and drag coefficient to provide a true value and are calculated [98] by the Eq. E.3 and Eq. E.4 :

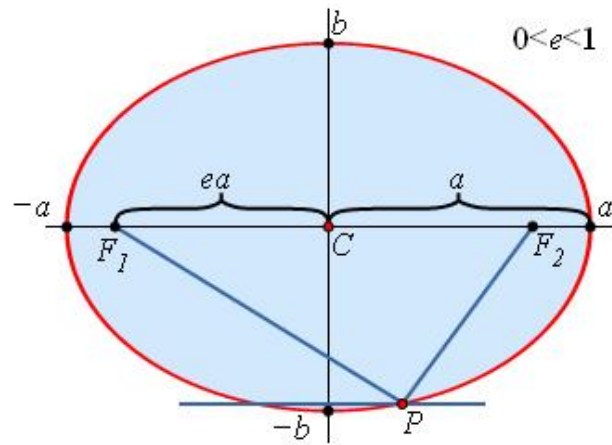


FIGURE E.1 Elements of an elliptic

$$\Delta\alpha = \delta \left( \frac{S}{C} \right) C_L \quad (E.3)$$

$$\Delta C_D = \delta \left( \frac{S}{C} \right) C_L^2 \quad (E.4)$$

According to Rosenhead [97], the correction factor,  $\delta$  for 2 different tunnels and 2 different orientations in Figure E.2 are given in Table E.1 and Table E.2. In Figure E.2, 4 different correction factors are selected to obtain a corrections angle of attack for the lift and drag when the tunnel is oriented either vertically or horizontally. A diagram in Figure E.3 represent the correction factors,  $\delta$  corresponding to a tunnel ratio,  $\lambda$  for a rigid wind tunnel walls. It is clear that the correction factor value reduces as wing span increases in case of width of a tunnel is greater than height of the tunnel i.e.  $\lambda > 1.0$ . In contrast, when the tunnel width is less that the tunnel height i.e.  $\lambda < 1.0$  the correction factor increases as the wing span becomes longer. Whereas the other case, as displayed in Figure E.4 is the case where the tunnel is an open tunnel. The correction factor has a similar trend as in the closed rigid walls tunnel but in the opposite sign as seen in Table E.2.

E

WIND TUNNEL OF ELLIPTIC SECTION

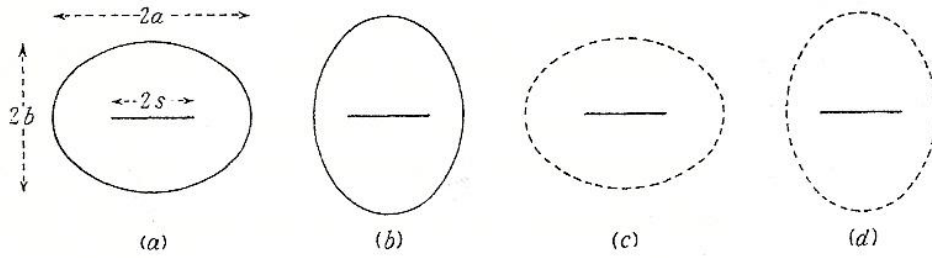


FIGURE E.2 Elements of an elliptic [97]

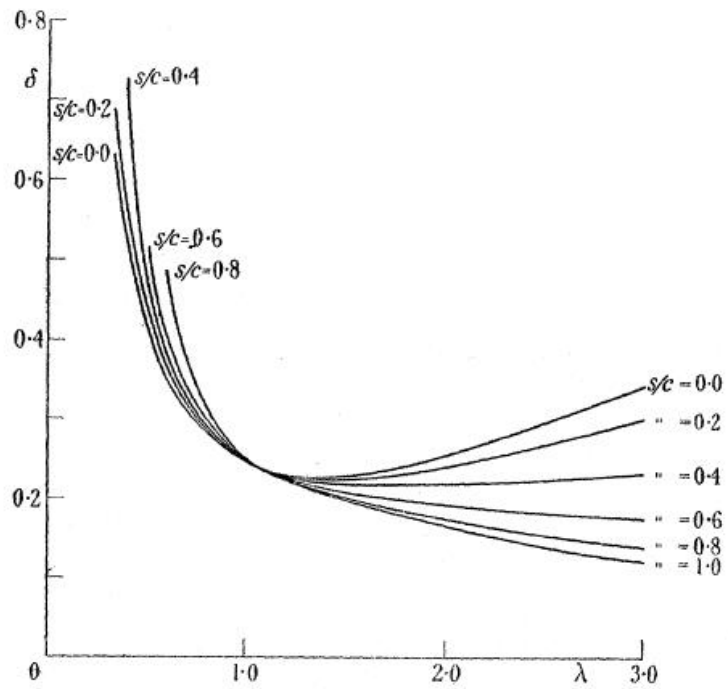


FIGURE E.3 Correction factor plot for a rigid tunnel walls [97]

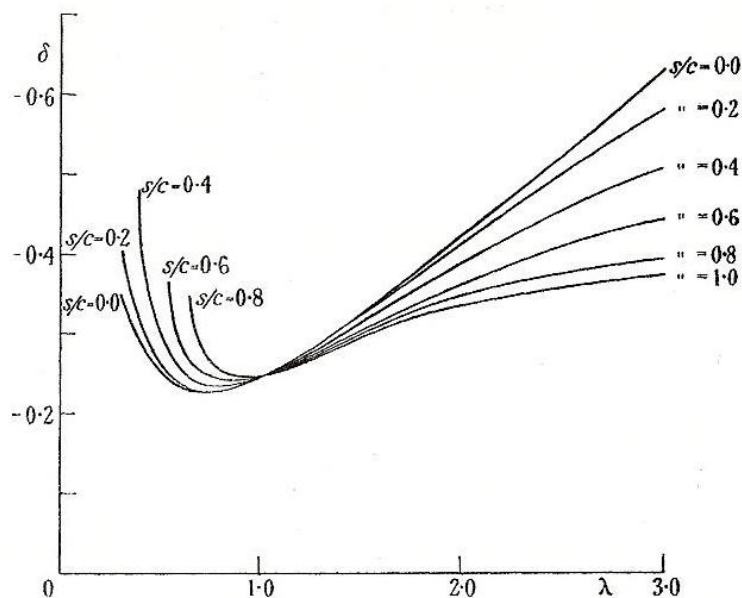


FIGURE E.4 Correction factor plot for an open tunnel [97]

$\lambda$	(1 : 3)	(2 : 5)	(1 : 2)	(2 : 3)	(1 : 1)
$s/c = 0.00$	0.630	0.526	0.4265	0.3311	0.250
$s/c = 0.20$	0.683	0.554	0.4379	0.3339	0.250
$s/c = 0.40$	—	0.718	0.4854	0.3442	0.250
$s/c = 0.60$	—	—	—	0.3673	0.250
$s/c = 0.80$	—	—	—	0.4272	0.250
$s/c = 1.00$	—	—	—	—	0.250

$\lambda$	(3 : 2)	(2 : 1)	(5 : 2)	(3 : 1)
$s/c = 0.00$	0.2306	0.2541	0.2925	0.3365
$s/c = 0.20$	0.2279	0.2445	0.2716	0.3001
$s/c = 0.40$	0.2208	0.2217	0.2281	0.2333
$s/c = 0.60$	0.2118	0.1964	0.1867	0.1783
$s/c = 0.80$	0.2037	0.1761	0.1567	0.1418
$s/c = 1.00$	0.2000	0.1667	0.1428	0.1250

TABLE E.1 The correction factor  $\delta_1$  and  $\delta_2$  for a rigid walls tunnel [97]



$\lambda$	(1 : 3)	(2 : 5)	(1 : 2)	(2 : 3)	(1 : 1)
$s/c = 0.00$	-0.337	-0.293	-0.2541	-0.2306	-0.250
$s/c = 0.20$	-0.388	-0.319	-0.2653	-0.2335	-0.250
$s/c = 0.40$	—	-0.477	-0.3110	-0.2436	-0.250
$s/c = 0.60$	—	—	—	-0.2665	-0.250
$s/c = 0.80$	—	—	—	-0.3264	-0.250
$s/c = 1.00$	—	—	—	—	-0.250

$\lambda$	(3 : 2)	(2 : 1)	(5 : 2)	(3 : 1)
$s/c = 0.00$	-0.3311	-0.4265	-0.5256	-0.6300
$s/c = 0.20$	-0.3283	-0.4164	-0.5032	-0.5860
$s/c = 0.40$	-0.3211	-0.3923	-0.4553	-0.5097
$s/c = 0.60$	-0.3119	-0.3653	-0.4084	-0.4430
$s/c = 0.80$	-0.3038	-0.3434	-0.3733	-0.3965
$s/c = 1.00$	-0.3000	-0.3333	-0.3571	-0.3750

TABLE E.2 The correction factor  $\delta_3$  and  $\delta_4$  for an open tunnel [97]